IOWA STATE UNIVERSITY
Digital Repository

2013

Iridium porphyrins: Catalysis, mechanism, and structural studies

Bernie Joe Anding
Iowa State University

Iridium porphyrins: Catalysis, mechanism, and structural studies

by

Bernie Joe Anding

A dissertation submitted to the graduate faculty

in partial fulfillment of the requirements for the degree of

DOCTOR OF PHILOSOPHY

Major: Organic Chemistry

Program of Study Committee:
L. Keith Woo, Major Professor
Andreja Bakac
William S. Jenks
Aaron D. Sadow
Yan Zhao

Iowa State University
Ames, Iowa
2013

TABLE OF CONTENTS

CHAPTER 5. COMPARISON STUDY OF RHODIUM AND
IRIDIUM PORPHYRIN DIAMINOCARBENE AND N-

LIST OF ABBREVIATIONS

D_{ip}	in-plane displacement
D_{oop}	out-of-plane displacement
DEAD	diethyl azodicarboxylate
EDA	ethyl diazoacetate
ESI	electrospray ionization
Et	ethyl
eq	equation
g	gram
mg	milligram
GC	gas chromatography
GC-MS	gas chromatography coupled with mass spectrometry
HMQC	heteronuclear multiple quantum coherence
HRMS	high-resolution mass spectrometry
IR	infrared
KIE	kinetic isotope effect (k_H/k_D)
kJ/mol	kilojoule per mole
L	liter
Me	methyl
MHz	megahertz

mL	milliliter
μL	microliter
MDA	methyl diazoacetate
MeIm	methyl imidazole
mol	mole
mmol	millimole
μmol	micromole
MPDA	methyl phenyldiazoacetate
NHC	N-heterocyclic carbene
NMR	nuclear magnetic resonance
NOESY	nuclear overhauser effect spectroscopy
NSD	normal-coordinate structural decomposition
OEP	2,3,7,8,12,13,17,18-octaethylporphyrin dianion
Ph	phenyl
PFP	5,10,15,20-tetra(pentafluorophenyl)porphyrin dianion
s	second
TD-DFT	time dependent density functional theory
TEMPO	2,2,6,6-tetramethylpiperidine 1-oxyl
TLC	thin-layer chromatography
THF	tetrahydrofuran
TMP	5,10,15,20-tetramesitylporphyrin dianion

TON   turnover number

TPP   5,10,15,20-tetraphenylporphyrin dianion

TTP   5,10,15,20-tetra(*p*-tolyl)porphyrin dianion

TTPPP   5,10,15,20-tetra(2,4,6-triphenyl)phenylporphyrin dianion

UV/vis   ultra violet and visible

ABSTRACT

Prior to this work, metalloporphyrin catalysts containing iron, ruthenium, osmium, cobalt, and rhodium were shown to be active for carbene transfer reactions. These metalloporphyrin catalysts were typically robust, highly reactive, and capable of inducing high selectivities. Furthermore, derivation at the porphyrin periphery by known routes allows for the development of a wide array of sophisticated chiral catalysts. Despite the promising results with other group 9 metal porphyrin complexes, carbene transfer catalysis with iridium porphyrin complexes had not been reported. The present work describes the development of iridium porphyrin-catalyzed cyclopropanation, C–H insertion, and N–H insertion reactions. These reactions were generally rapid and proceeded in moderate to high yields, at temperatures as low as -78 °C, and with turnover numbers on the order of 10^5. Extensive mechanistic studies revealed that the catalytic cycles proceed through metal-carbene intermediates for cyclopropanation and C–H insertion as well as metal-ylide intermediates to N–H insertion. Although structural studies on these reactive intermediates were not possible, the nature of iridium-carbene intermediates was explored indirectly using diaminocarbenes and N-heterocyclic carbenes (NHCs) as model ligands. Compared to rhodium, iridium seemed to form stronger bonds with these carbene ligands. This finding is consistent with a previously proposed transition state model and rationalizes the observed difference between rhodium and iridium porphyrin catalysts.

CHAPTER 1.   OVERVIEW

Introduction

The development of modern chemical synthesis techniques has allowed chemists the ability to synthesize virtually any organic molecule. This expertise has fueled progress in areas such as pharmaceuticals, electronic devices, molecular machines, and homogenous catalysis. Currently, economic and sustainability goals require the development of new synthetic methods that generate target molecules in fewer steps and with less chemical waste. An example is traditional carbon-carbon cross coupling techniques: Kumada, Negishi, Stille, Suzuki, and Hiyama reactions (Figure 1.1).[1] Despite being vital to the toolbox of a synthetic chemist, all of these methods require the pre-installment of alkyl halide functionalities and generate stoichiometric byproducts, many of which are environmentally hazardous. Considering these reactions, one technique for developing greener methodologies is to replace alkyl halide functionalities with more natural organic moieties, precluding the additional halogenation step and stoichiometric halogenated waste.
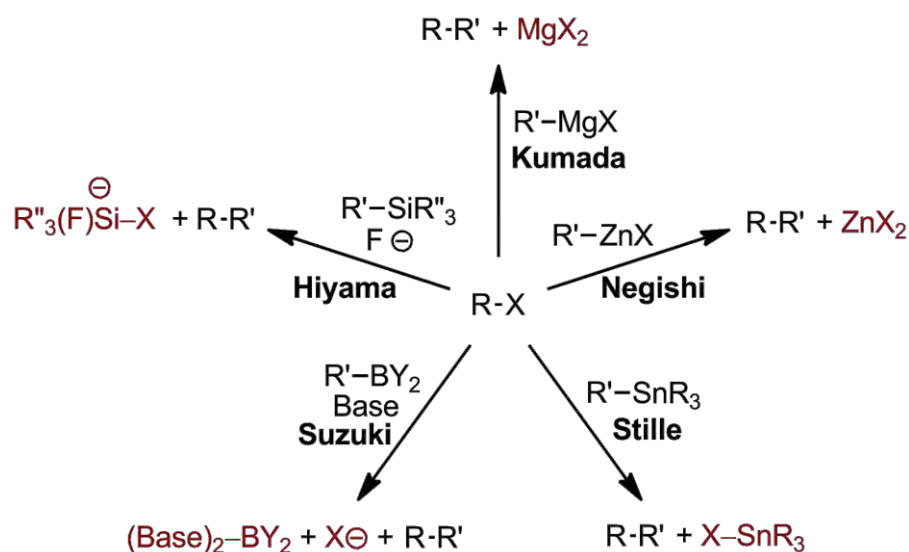
Figure 1.1: Traditional cross-coupling reactions generate stoichiometric waste along with the desired products.

In this regard, carbene transfer reactions are attractive, atom-efficient methods for building complex organic molecules. Carbene transfer reactions involve the insertion of a

carbene fragment (:CR$_2$) to form two new carbon-containing bonds. These reactions are driven by the high reactivity of carbene moieties, allowing them to react with a variety of functional groups. However, as a consequence, free carbene reagents are difficult to isolate and must be formed *in situ* from a carbene precursor. Multiple effective carbene precursors have been discovered.[2-5]

Diazo reagents are the most common because they are highly active and release environmentally benign nitrogen gas as the only byproduct.[6,7] These characteristics make carbene transfer reactions with diazo reagents attractive, green alternatives to traditional carbon bond forming reactions. Diazo reagents are categorized according to reactivity (Figure 1.2).[6,8] The most reactive class contains one electron-donating alkyl or aryl substituent. These diazoalkanes and aryldiazomethanes are so reactive that they are difficult to prepare, unstable, and potentially explosive in their pure form. As a result, diazo reagents with at least one electron-withdrawing substituent, which is generally a carbonyl, are preferred. Diazocarbonyl reagents are safe to handle, can be synthesized by numerous reliable procedures,[6,7] and are versatile for a wide range of reactions. Accordingly, the remainder of this discussion will focus solely on the examples of diazocarbonyl reagent as carbene precursors.

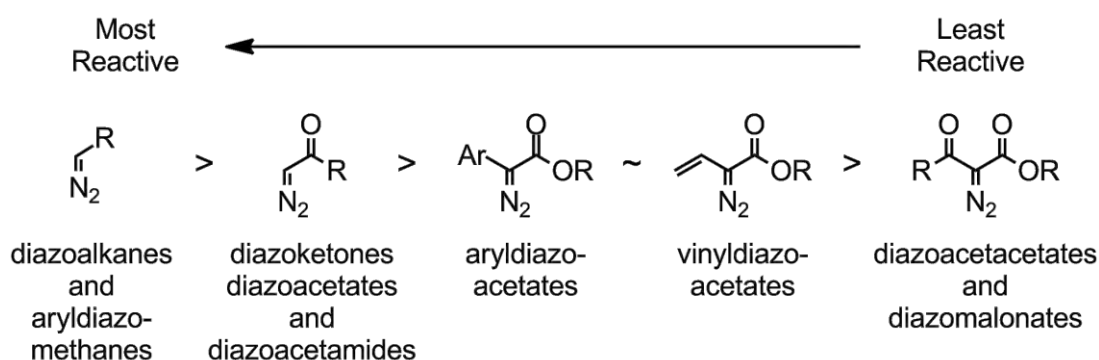**Figure 1.2:** Diazo reagent carbene sources, organized by reactivity.

The first class of diazocarbonyl reagents contains only one electron-withdrawing substituent; their reactivity follows the trend: diazoketones > diazoacetates > diazoacetamides.[6,8] In contrast to diazoalkanes and aryldiazomethanes, these reagents are easy to handle under ambient conditions. For instance, ethyl diazoacetate (EDA) does not

show significant decomposition below 120 °C or when treated with glacial acetic acid at room temperature. These reagents retain high reactivity toward carbene transfer and are commonly employed as model reagents for initial methodological studies. However, due to the lack to steric hindrance, they are prone to carbene dimerization, which can be detrimental to reaction efficiency. To limit carbene dimerization, techniques such as slow addition of the diazocarbonyl reagent are typically employed.

The next class of diazo reagents features a donor aryl, vinyl, or alkyl substituent along with the electron-withdrawing carbonyl functionality.[6,8] These so called donor-acceptor diazo reagents are less susceptible to dimerization, allowing them to be useful for reactions with less reactive substrates where carbene dimerization becomes dominant. Thus, donor-acceptor diazo reagents are more versatile to a wide array of carbene transfer reactions. Vinyldiazoacetates are particularly versatile reagents because they capable of forming bonds at the carbene and the vinyl carbon β to the carbene. The latter is known as vinylogous reactivity. In contrast, the use of alkyldiazoacetates is limited because they are prone to alkene formation by a β-hydride elimination pathway.[7] The final class of diazo reagents is comprised of diazoacetoacetates and diazomalonates, which contain two electron-withdrawing carbonyl substituents. This class is the least reactive; they typically need to be activated by strongly Lewis-acidic catalysts.

The study of carbene transfer reactions with diazocarbonyl reagents dates back to 1885 when Buchner and Curtius demonstrated cycloadditions between EDA and aromatic substrates (Buchner Ring Expansion).[9] The scope of carbene transfer reactions has grown tremendously to include cyclopropanation, X–H insertion (X = C, N, O, S, P, halogens), and ylide generating transformations like the Doyle-Kirmse reaction (2,3-sigmatropic rearrangement) and 1,3-dipolar additions (Figure 1.3).[6,7,10,11] While some of these proceed under purely thermal conditions, the use of a transition metal-catalyst is generally preferred due to an increase in selectivity and reactivity. The development of carbene transfer catalysts, specifically dirhodium(II) complexes, has provided access to several new reactions such as diazo cross-couplings,[12,13] zwitterionic trapping pathways,[14-17] ring expansions,[18-20] and vinylogous couplings with α-vinyldiazoacetate reagents.[21-24] As mentioned above,

vinylogous couplings represent a broad class of transformations where bonds form at the olefinic carbon. Examples include cycloadditions,[25-30] Mukaiyama-Michael additions,[31] X–H insertions,[32,33] and other reactions.[17,19] Overall, carbene transfer reactions with diazocarbonyl reagents offer rapid, atom-economical routes to a wide variety of complex and biologically relevant organic molecules from relatively simple starting materials.[25,34-36]
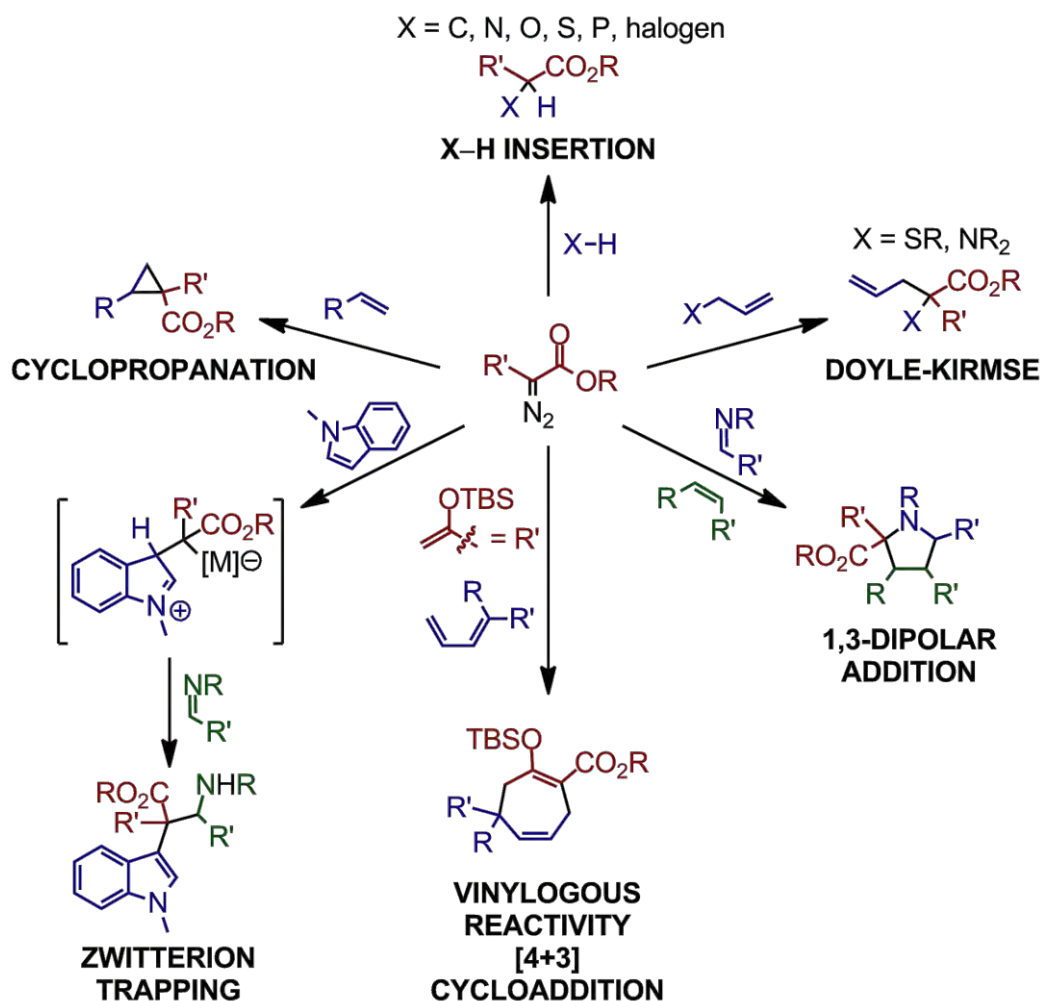
Figure 1.3: A brief representation of the array of complex molecules that can be synthesized via carbene transfer reactions.

Many types of transition metals are capable of catalyzing carbene transfer reactions. The most versatile and effective are dirhodium(II) paddlewheel catalysts.[6] Initial studies by Teyssie and co-workers described the catalytic properties of dirhodium tetraacetate,[37] which is prepared by refluxing rhodium(III) chloride in acetic acid and acetic anhydride.[38] Facile

exchange of the tetraacetate ligands for other carboxylate or carboxamidate provides access to a range of electronically and sterically diverse catalysts. This feature allowed for relatively quick catalyst derivation and the development of highly sophisticated systems that are very efficient, stereoselective, and versatile for a range of carbene transfer reactions. However, dirhodium catalysts also have some disadvantages. Although robust,[39] these catalysts require two precious and expensive rhodium atoms in each complex despite the hypothesis that only one metal-center is active at a time.[40] Additionally, the use of dirhodium catalysts for N–H insertion reactions is limited because the catalysts are poisoned by the amine substrates.[41]

Copper catalysts were also thoroughly explored for carbene transfer reactions.[6,42] Typical protocols generate the active copper catalyst *in situ* by mixing the desired ligand with a copper(I) or copper(II) salt. Copper(I) were determined to be the active species,[43] but due to ease of handling, copper (II) salts are often employed in the presence of a reductant. Similar to dirhodium catalysts, facile ligand screening has allowed for the development of highly selective carbene transfer. The most selective catalysts are those with bi- or tridentate N- and O-based ligands, such as semicorrins, salcyaldamines, and bis-oxazoles. In a couple of instances, copper catalysts exhibited reactivity complimentary to that of dirhodium complexes.[18,28] Copper catalysts selectively generated different products than were formed with dirhodium. This divergent catalyst reactivity further illustrates the value in developing multiple carbene transfer catalysts. Nevertheless, copper catalysts are limited because they generally require high catalyst loadings (5 mol% or greater), and they are not versatile to as many reactions as dirhodium catalysts.[6]

Promising results were also found using metalloporphyrin catalysts.[10] Inspired by biological systems, these macrocyclic complexes are very robust and tunable at the porphyrin periphery, allowing for the development of sophisticated bulky, chiral, and/or surface-linked catalysts. Macrocyclic ligands are especially attractive for their unique ability to selectively form the uncommon product isomers, such as *cis*-cyclopropanes and primary C–H insertion products.[42,44-48] Multiple metalloporphyrin complexes are active toward carbene transfer, including those with iron(II), ruthenium(II), osmium(II), cobalt(II), and rhodium(III).[10]

These catalysts were examined primarily for their activity towards cyclopropanation, X–H insertion reactions, and ylide-forming reactions.

In the next few sections, results for cyclopropanation, C–H insertion, and N–H insertion reactions are reviewed. This provides the necessary background and motivation for studying catalysis with iridium porphyrin complexes. In this regard, previous results with iridium(III) salen catalysts are also discussed.

Cyclopropanation

Cyclopropanation with iron(II), ruthenium(II), and osmium(II) porphyrin catalysts showed similar trends.[10] These catalysts generally gave yields of 60 – 99% for reactions between aryl olefins and aryldiazomethanes,[49] trimethylsilyldiazomethane,[49] diazoketones,[50,51] diazoacetates,[49,52-57] diazoacetamides,[58] diisopropyl diazomethyl phosphonate,[59] aryldiazoacetates,[60,61] and diazoacetoacetates.[56,57] Reactions with diazoacetate reagents formed carbene dimerization products, fumarate and maleates, in significant yields. Most reactions were complete within a few hours using 0.1 mol% to 1.0 mol% catalyst at ambient or slightly elevated temperatures. The most efficient reactions were typically observed with aryl olefin substrates. Although there were a few exceptions,[54,56,57,61-64] aliphatic olefins generally required higher reaction temperatures and were converted in lower yields. Reactions for all substrates were selective for *trans* cyclopropanes with diastereoselectivities as high as 29:1 (*trans*:*cis*).[52] Diastereoselectivity was increased with the use of bulky porphyrin ligands. Despite the many similarities, each of these group 8 metal catalysts showed slight differences in reactivity. For instance, only iron complexes were shown to catalyze Buchner reactions between aromatic rings and aryl diazoacetates. Additionally, cyclopropenation was shown only with osmium.[55,60]

Cobalt(II) and rhodium(III) porphyrin catalysts displayed prominent differences in reactivity. Cobalt(II) complexes, which are the only metalloporphyrin catalysts with a d^7 electron configuration, were remarkable for their ability to efficiently catalyze the cyclopropanation of electron-deficient olefins and aryl olefins.[65] Yields were often greater than 80% with nearly completely *trans* selectivity for reactions with diazoacetates,[66,67] diazosulfones,[68] α-cyanodiazoacetates,[69] and α-nitrodiazoacetates,[70] though reactions with α-

nitrodiazoacetates favored *cis*-cyclopropanes. However, this remarkable catalytic activity required sophisticated porphyrin ligands capable of hydrogen bonding with the intermediate.[68] Catalysts containing traditional TPP and OEP ligands were demonstrated with aryl olefins only and gave 65 – 99% yields with *E*/*Z* ratios ranging from 2.3 to 5.7.

Rhodium(III) catalysts are rare in their ability to generate *cis*-cyclopropanes selectively.[45,71] Diastereomeric ratios (*cis*/*trans*) ranged from 4.9 to 0.73 for reactions between EDA and styrene or aliphatic olefins in the presence Rh(OEP)I or Rh(TTP)I. The use of bulkier porphyrin ligands, such as TMP or the chiral fortress porphyrin, increased the diastereomeric ratio to above 5 with certain substrates.[72,73] Catalyst diastereoselectivity is dependent also on porphyrin electronics, although the nature of this relationship is not well understood.[74,75] Rhodium porphyrin catalysts, compared to the group 8 analogs, were less dependent on the steric and electronic nature of the substrate.[72] Aryl and aliphatic olefins were converted in similar yields, though these yields still varied drastically (31 – 98%). Furthermore, reactions required elevated temperatures (ca. 60 °C) with reactions times often longer than 24 hours.

Cyclopropanation catalyzed by macrocyclic iridium(III) complexes was first reported in 2007.[76] Chiral iridium(III) salen complexes catalyzed the cyclopropanation of aryl olefins with diazoacetate and vinyldiazolactone reagents in 79 – 99% yield and with extremely high diastereo- and enantioselectivity.[44,77] Reactions with acyclic diazoacetates were selective for *cis*-cyclopropanes, whereas those with cyclic vinyldiazolactone produced *trans* cyclopropanes with very high selectivity. Aliphatic di- and tri-substituted olefins were also suitable substrates, albeit at reduced yields. While these results are extraordinary, the reaction mechanism was not investigated, which inhibits the rational design future iridium catalysts.

C–H insertion

Relative to cyclopropanation, insertion of a carbene fragment into a C–H bond is typically less general, lower yielding, and requires more forcing conditions. There are no reports of cobalt porphyrin-mediated C–H insertion reactions, and the only example of a ruthenium-catalyzed insertion is an intramolecular method with sulfonyl hydrazone carbene

precursors.[78,79] With a dinuclear μ-oxo osmium porphyrin catalyst, there is one example of intermolecular C–H insertion between EDA and cyclohexene.[57] C–H insertion proceeded in 43% yield and cyclopropanation byproducts were formed in 49% yield.

More in-depth studies were reported with iron and rhodium porphyrin complexes. Iron complexes with TTP and PFP ligands catalyzed C–H insertion reactions between hydrocarbons and aryldiazoacetates or diazomalonates in 41 – 86% yield.[80] Insertions occurred into both aryl and aliphatic C–H bonds, leading to product mixtures in most cases. With aliphatic substrates, insertion into tertiary C–H bonds was preferred as inductive effects dictate that tertiary C–H bonds are more electron rich than secondary and primary bonds. Forcing conditions were required with 1 – 2 mol% catalyst, high temperatures (80 °C to 110 °C), and long reaction times between 16 hours and 72 hours. Furthermore, the reaction scope limited. Diazoacetates were unsuitable carbene sources, leading only to carbene dimerization products, and high-boiling hydrocarbon substrates were required with THF as the only reported exception. Lastly, due to electronic factors, insertion into primary C–H bonds was rare. The only instances were with toluene and mesitylene, where the primary C–H bond was at the benzylic position and no other aliphatic C–H bonds were available.

Rhodium porphyrin compounds with TTP, TMP, and TDCPP ligands were shown to catalyze C–H insertion reactions between hydrocarbons and diazoacetate reagents at 60 °C.[81] Using TTP, TMP, and TDCPP ligands, insertion reactions carried out at 60 °C gave 5 – 50% yields and 0.12 – 1.25 selectivities (1°/2° normalized per hydrogen). Although these selectivities were modest, they demonstrate that rhodium porphyrins are promising catalysts for primary C–H insertion into linear unactivated aliphatic substrates. Primary selectivity was enhanced by increasing the steric bulk on the porphyrin ligand. As the foremost example, Che and co-workers demonstrated high primary selectivity using the extremely bulky Rh(TTPPP)Me catalyst, with 5,10,15,20-tetra(2,4,6-triphenyl)phenylporphyrin as the ligand.[82] Rh(TTPPP)Me achieved 1°/2° selectivities of 2.7 – 3.2 and 9.8 – 11.4 for insertions into linear unactivated hydrocarbons with EDA and MPDA, respectively. Furthermore, Rh(TTPPP)Me gave increased yields slightly to 48 – 63%, though this may have resulted partially from increasing the reaction temperature to 80 °C.

Iridium salen complexes were also active catalysts for C–H insertion.[83] Insertion into secondary C–H bonds occurred with 83 – 99% yield and high diastereo- and enantioselectivity using methyl and aryl diazoacetates. Similar to the analogous cyclopropanation, this work demonstrated that iridium(III) macrocyclic complexes are promising catalysts but the mechanism was not examined.

N–H insertion

Similar to C–H insertion, there are relatively few examples of metalloporphyrin-catalyzed N–H insertion reactions. Of the previously discussed macrocyclic catalysts, only ruthenium and iron porphyrin complexes were reported to catalyze N–H insertion reactions. Ruthenium catalysts gave yields of 63 – 91% for reactions between EDA and secondary amines.[84,85] An additional example described a Ru(TTP)(CO)-catalyzed insertion of a diazoketone, DON, into aniline in 71% yield.[51] However, inhibitory binding of the amine substrates to the metal limited the scope of these reactions and generally required that the amine be added slowly.

In contrast, iron porphyrin catalysts were not poisoned by amine substrates. Insertion into various aryl and aliphatic N–H bonds with diazoacetates, alkyldiazoacetates, aryldiazoacetates, and diazomalonates occurred generally in greater than 80% yield at low catalyst loadings and without the need for dropwise addition of the amine substrate.[86-90] Moreover, carbene dimerization side products were formed in trace, even with diazoacetates, which obviated the need for excess amine substrate or slow addition of the diazo reagent. Despite these unique advantages of iron porphyrin catalysts, insertion reactions with diazoketones are inconsistent, ranging from 20 to 90% yields.[50,51] In addition, attempts to induce enantioselectivity with chiral iron porphyrin catalysts were unsuccessful.[51]

Mechanistic aspects

For carbene transfer reactions with iron, ruthenium, osmium, and rhodium porphyrin catalysts, the generally accepted mechanism involves a metal-carbene intermediate (Figure 1.4). Initial coordination of the diazo reagent to the metal center generates a diazonium complex. Spectroscopic evidence for a diazonium complex, including a prominent N≡N stretching band at 2338 cm^{-1}, was observed with Rh(TTP)I below -40 °C.[91] Above -20 °C,

evolution of nitrogen gas leads to the formation of an electrophilic metal-carbene complex. Nucleophilic attack of the carbene generates the product and reforms the catalyst.
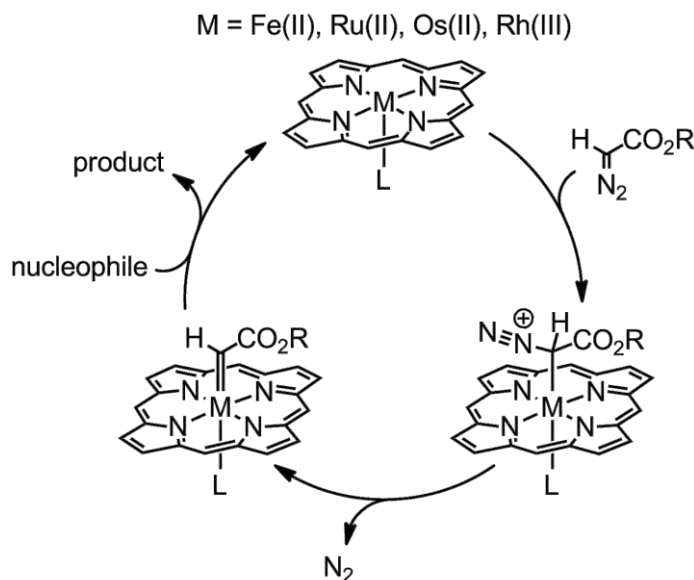

Figure 1.4: The general mechanism for carbene transfer reactions catalyzed by Fe, Ru, Os, and Rh porphyrin catalysts. Porphyrin substituents were omitted for clarity.

Several lines of evidence support the intermediacy of electrophilic metal-carbene complexes. Hammett correlation studies for reactions with *para*-substituted substrates gave ρ values between −0.14 and −1.92, consistent with the buildup of positive charge upon interaction between the substrate and an electrophilic intermediate.[52,54,56,59,61-64] More definitive evidence was provided by stoichiometric carbene transfer from isolable metal-carbene complexes. Remarkably stable iron and ruthenium carbene complexes (**1 – 3**; Figure 1.5) were generated by treating bulky or electron-deficient metalloporphyrin complexes with bulky diazo reagents.[61,64,92] Complexes **1 – 3** were active toward stoichiometric cyclopropanation and C–H insertion, giving yields and selectivities similar to those observed under the analogous catalytic conditions. Osmium-carbene complexes were less reactive than the iron and ruthenium congeners. Sterically unencumbered osmium porphyrin carbene complexes were isolable. For instance, complexes **4** and **5** were isolated after treating [Os(TTP)]₂ or Os(TTP)(CO) with the corresponding diazo reagent.[55,56] They were active toward intra- and intermolecular cyclopropanation but required elevated temperatures, addition of a σ-donor ligand, or longer reaction times than the corresponding catalytic

reaction. Additional studies with mono- and bis-carbene complexes, Os(PFP)(=CPh$_2$) and Os(PFP)(=CPh$_2$)$_2$, revealed that only the bis-carbene complex was active toward stoichiometric transfer,[93] demonstrating that osmium catalysts require a strong σ-donor ligand *trans* to the carbene to activate the complex towards carbene transfer.

Unlike complexes with group 8 metals, stoichiometric carbene transfer with group 9 metal catalysts has not been demonstrated because these metal-carbene complexes are more difficult to isolate. The only group 9 metal-carbene complex that has been isolated was a rhodium diaminocarbene (**6**). The carbene transfer activity of **6** was not examined.[94]
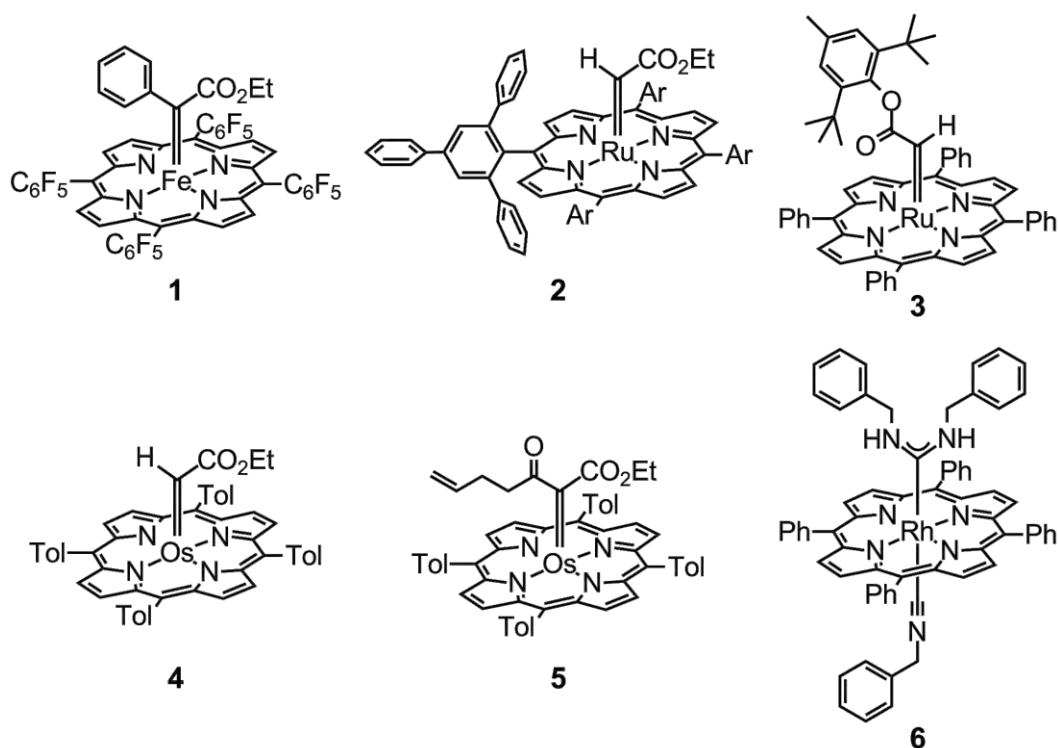

Figure 1.5: Isolated metal-carbene complexes. Complexes **1 – 5** were active for carbene transfer.

A different mechanism was proposed for cobalt(II) porphyrin catalysts. Since cobalt(II) porphyrin complexes have a d^7 rather than d^6 electronic configuration, they are disposed to radical pathways. Accordingly, cobalt(II) carbene ligands were shown to be redox non-innocent where electron transfer from the metal to the carbene forms a radical carbene

complex (Figure 1.6).[95-97] Radical carbenes are relatively nucleophilic, which explains the ability of cobalt catalysts to activate electron-deficient substrates. The intermediacy of radical carbene complexes was supported by DFT studies, EPR spectroscopy, and stoichiometric reactions with ethyl styryldiazoacetate.[97-99]
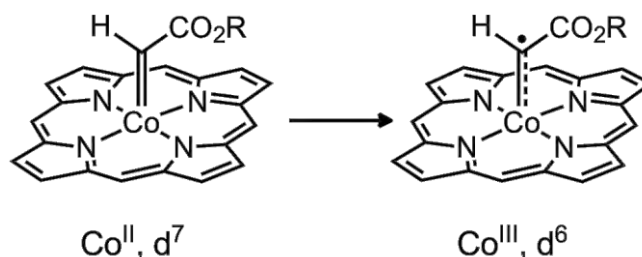

Figure 1.6: Redox non-innocent behavior of carbene ligands. A Fischer-type carbene complex (left) forms a radical carbene complex (right).

Summary and outlook

Macrocyclic complexes are attractive catalysts for carbene transfer reactions. With porphyrin ligands, complexes have the potential to be robust, reactive, and selective catalysts for racemic cyclopropanation, C–H insertion, and N–H insertion reactions. However, metalloporphyrin catalysts still had some limitations. Reactions were often limited to electron-rich or aryl substrates, many catalysts required long reaction times and elevated temperatures, and the best catalysts required sophisticated ligands. Furthermore, most complexes were unable to catalyze N–H insertion reactions due to catalyst poisoning by the amine substrates.

Given the recent successes with chiral iridium(III) salen catalysts, we sought to explore the catalytic activity of iridium(III) porphyrin complexes. We examined iridium catalysts with relatively simple TTP ligands to provide a fair comparison to previous studies with Fe, Ru, Os, Co, and Rh porphyrin catalysts. Compared to these catalysts, iridium porphyrin complexes were extremely robust and reactive catalysts, which could rapidly generate products at −78 °C with turnover numbers on the order of 10^5. In addition, the activity of iridium catalysts was not extinguished by amine substrates, allowing for high yielding N–H insertion reactions. Overall, in conjunction with thorough mechanistic studies, this work

demonstrates that iridium porphyrin complexes are promising catalysts for carbene transfer reactions and provides a basis for the development of future catalysts.

References

1. Larock, R. C. *Comprehensive Organic Transformations : A Guide to Functional Group Preparations*; Wiley: New York, **1999**.

2. Mangion, I. K.; Nwamba, I. K.; Shevlin, M.; Huffman, M. A. *Org. Lett.* **2009**, *11*, 3566.

3. Morandi, B.; Carreira, E. *Angew. Chem. Intl. Ed.* **2010**, *49*, 938.

4. Zhang, J.-L.; Chan, P. W. H.; Che, C.-M. *Tetrahedron Lett.* **2003**, *44*, 8733.

5. Aggarwal, V. K.; de Vicente, J.; Bonnert, R. V. *Org. Lett.* **2001**, *3*, 2785.

6. Doyle, M. P.; McKervey, M. A.; Ye, T. *Modern Catalytic Methods for Organic Synthesis with Diazo Compounds: From Cyclopropanes to Ylides*; Wiley-Interscience: New York, **1998**.

7. Ye, T.; McKervey, M. A. *Chem. Rev.* **1994**, *94*, 1091.

8. Doyle, M. P.; Duffy, R.; Ratnikov, M.; Zhou, L. *Chem. Rev.* **2010**, *110*, 704.

9. Buchner, E.; Curtius, T. *Ber. Dtsch. Chem. Ges.* **1885**, *18*, 2377.

10. Anding, B. J.; Woo, L. K. In *Handbook of Porphyrin Science*; Kadish, K. M., Guilard, R., Smith, K., Eds.; World Scientific Publishing Company: Hackensack, NJ, 2012; Vol. 21, p 145.

11. Padwa, A.; Weingarten, M. D. *Chem. Rev.* **1996**, *96*, 223.

12. Hansen, J. H.; Parr, B. T.; Pelphrey, P.; Jin, Q.; Autschbach, J.; Davies, H. M. L. *Angew. Chem. Intl. Ed.* **2011**, *50*, 2544.

13. Rivilla, I.; Sameera, W. M. C.; Alvarez, E.; Diaz-Requejo, M. M.; Maseras, F.; Perez, P. J. *Dalton Trans.* **2013**, *42*, 4132.

14. Qiu, H. *Nature Chem.* **2012**, *4*, 733.

15. Lian, Y.; Davies, H. M. L. *Org. Lett.* **2012**, *14*, 1934.

16. Lian, Y.; Davies, H. M. L. *Org. Lett.* **2010**, *12*, 924.

17. Lian, Y.; Davies, H. M. L. *J. Am. Chem. Soc.* **2009**, *132*, 440.

18. Xu, X.; Qian, Y.; Zavalij, P. Y.; Doyle, M. P. *J. Am. Chem. Soc.* **2013**, *135*, 1244.

19. Manning, J. R.; Davies, H. M. L. *J. Am. Chem. Soc.* **2008**, *130*, 8602.

20. Manning, J. R.; Davies, H. M. L. *Tetrahedron* **2008**, *64*, 6901.

21. Xu, X.; Zavalij, P. Y.; Hu, W.; Doyle, M. P. *Chem. Commun.* **2012**, *48*, 11522.

22. Xu, X.; Shabashov, D.; Zavalij, P. Y.; Doyle, M. P. *Org. Lett.* **2012**, *14*, 800.

23. Smith, A. G.; Davies, H. M. L. *J. Am. Chem. Soc.* **2012**, *134*, 18241.

24. Valette, D.; Lian, Y.; Haydek, J. P.; Hardcastle, K. I.; Davies, H. M. L. *Angew. Chem. Intl. Ed.* **2012**, *51*, 8636.

25. Lian, Y.; Miller, L. C.; Born, S.; Sarpong, R.; Davies, H. M. L. *J. Am. Chem. Soc.* **2010**, *132*, 12422.

26. Schwartz, B. D.; Denton, J. R.; Lian, Y.; Davies, H. M. L.; Williams, C. M. *J. Am. Chem. Soc.* **2009**, *131*, 8329.

27. Xu, X.; Zavalij, P. Y.; Hu, W.; Doyle, M. P. *J. Org. Chem.* **2013**, *78*, 1583.

28. Qian, Y.; Xu, X.; Wang, X.; Zavalij, P. J.; Hu, W.; Doyle, M. P. *Angew. Chem. Intl. Ed.* **2012**, *51*, 5900.

29. Xu, X.; Zavalij, P. Y.; Doyle, M. P. *Angew. Chem. Intl. Ed.* **2012**, *51*, 9829.

30. Xu, X.; Shabashov, D.; Zavalij, P. Y.; Doyle, M. P. *J. Org. Chem.* **2012**, *77*, 5313.

31. Liu, Y.; Doyle, M. P. *Org. Biomol. Chem.* **2012**, *10*, 6388.

32. Hansen, J. H.; Davies, H. M. L. *Chem. Sci.* **2011**, *2*, 457.

33. Sevryugina, Y.; Weaver, B.; Hansen, J.; Thompson, J.; Davies, H. M. L.; Petrukhina, M. A. *Organometallics* **2008**, *27*, 1750.

34. Davies, H. M. L.; Denton, J. R. *Chem. Soc. Rev.* **2009**, *38*, 3061.

35. Wu, J.; Becerril, J.; Lian, Y.; Davies, H. M. L.; Porco, J. A.; Panek, J. S. *Angew. Chem. Intl. Ed.* **2011**, *50*, 5938.

36. Zhou, J.; Xu, X.; Hu, W.; Briones, J. F.; Davies, H. M. L. *Org. Synth.* **2011**, *88*, 418.

37. Paulissen, R.; Reimlinger, H.; Hayez, E.; Hubert, A. J.; Teyssie, P. *Tetrahedron Lett.* **1973**, *14*, 2233.

38. Rempel, G.; Legzdins, P.; Smith, H.; Wilkinson, G. *Inorg. Synth.* **1971**, *13*, 90.

39. Pelphrey, P.; Hansen, J.; Davies, H. M. L. *Chem. Sci.* **2010**, *1*, 254.

40. Nakamura, E.; Yoshikai, N.; Yamanaka, M. *J. Am. Chem. Soc.* **2002**, *124*, 7181.

41. Aller, E.; Buck, R. T.; Drysdale, M. J.; Ferris, L.; Haigh, D.; Moody, C. J.; Pearson, N. D.; Sanghera, J. B. *J. Chem. Soc., Perkin Trans. 1* **1996**, 2879.

42. Kirmse, W. *Angew. Chem. Intl. Ed.* **2003**, *42*, 1088.

43. Salomon, R. G.; Kochi, J. K. *J. Am. Chem. Soc.* **1973**, *95*, 3300.

44. Suematsu, H.; Kanchiku, S.; Uchida, T.; Katsuki, T. *J. Am. Chem. Soc.* **2008**, *130*, 10327.

45. Callot, H. J.; Metz, F.; Piechocki, C. *Tetrahedron* **1982**, *38*, 2365.

46. Alexander, K.; Cook, S.; Gibson, C. L. *Tetrahedron Lett.* **2000**, *41*, 7135.

47. Doyle, M. P.; Davies, S. B.; Hu, W. *Chem. Commun.* **2000**, 867.

48. Uchida, T.; Katsuki, T. *Synthesis* **2006**, *10*, 1715.

49. Hamaker, C. G.; Mirafzal, G. A.; Woo, L. K. *Organometallics* **2001**, *20*, 5171.

50. Nicolas, I.; Roisnel, T.; Le Maux, P.; Simonneaux, G. *Tetrahedron Lett.* **2009**, *50*, 5149.

51. Le Maux, P.; Nicolas, I.; Chevance, S.; Simonneaux, G. *Tetrahedron* **2010**, *66*, 4462.

52. Wolf, J. R.; Hamaker, C. G.; Djukic, J.-P.; Kodadek, T.; Woo, L. K. *J. Am. Chem. Soc.* **1995**, *117*, 9194.

53. Lo, W.-C.; Che, C.-M.; Cheng, K.-F.; C. W. Mak, T. *Chem. Commun.* **1997**, *0*, 1205.

54. Galardon, E.; Le Maux, P.; Simonneaux, G. *Tetrahedron* **2000**, *56*, 615.

55. Smith, D. A.; Reynolds, D. N.; Woo, L. K. *J. Am. Chem. Soc.* **1993**, *115*, 2511.

56.   Hamaker, C. G.; Djukic, J.-P.; Smith, D. A.; Woo, L. K. *Organometallics* **2001**, *20*, 5189.

57.   Li, Y.; Huang, J.-S.; Zhou, Z.-Y.; Che, C.-M. *Chem. Commun.* **2003**, *0*, 1362.

58.   Gross, Z.; Galili, N.; Simkhovich, L. *Tetrahedron Lett.* **1999**, *40*, 1571.

59.   Paul-Roth, C.; De Montigny, F.; Rethoré, G.; Simonneaux, G.; Gulea, M.; Masson, S. *J. Mol. Catal. A: Chem.* **2003**, *201*, 79.

60.   Mbuvi, H.; Woo, L. *J. Porphyrins Phthalocyanines* **2009**, *13*, 136.

61.   Li, Y.; Huang, J.-S.; Zhou, Z.-Y.; Che, C.-M.; You, X.-Z. *J. Am. Chem. Soc.* **2002**, *124*, 13185.

62.   Wang, S. R.; Zhu, C.-Y.; Sun, X.-L.; Tang, Y. *J. Am. Chem. Soc.* **2009**, *131*, 4192.

63.   Wada, S.; Shimomura, M.; Kikuchi, T.; Yuge, H.; Miyamoto, T. K. *J. Porphyrins Phthalocyanines* **2008**, *12*, 35.

64.   Deng, Q.-H.; Chen, J.; Huang, J.-S.; Chui, S. S.-Y.; Zhu, N.; Li, G.-Y.; Che, C.-M. *Chem. Eur. J.* **2009**, *15*, 10707.

65.   Doyle, M. P. *Angew. Chem. Intl. Ed.* **2009**, *48*, 850.

66.   Chen, Y.; Ruppel, J. V.; Zhang, X. P. *J. Am. Chem. Soc.* **2007**, *129*, 12074.

67.   Ruppel, J. V.; Gauthier, T. J.; Snyder, N. L.; Perman, J. A.; Zhang, X. P. *Org. Lett.* **2009**, *11*, 2273.

68.   Zhu, S.; Ruppel, J. V.; Lu, H.; Wojtas, L.; Zhang, X. P. *J. Am. Chem. Soc.* **2008**, *130*, 5042.

69.   Zhu, S.; Xu, X.; Perman, J. A.; Zhang, X. P. *J. Am. Chem. Soc.* **2010**, *132*, 12796.

70.   Zhu, S.; Perman, J. A.; Zhang, X. P. *Angew. Chem. Intl. Ed.* **2008**, *47*, 8460.

71.   Callot, H. J.; Piechocki, C. *Tetrahedron Lett.* **1980**, *21*, 3489.

72.   Maxwell, J. L.; O'Malley, S.; Brown, K. C.; Kodadek, T. *Organometallics* **1992**, *11*, 645.

73.   O'Malley, S.; Kodadek, T. *Organometallics* **1992**, *11*, 2299.

74.   Tagliatesta, P.; Pastorini, A. *J. Mol. Catal. A: Chem.* **2002**, *185*, 127.

75.   Niino, T.; Toganoh, M.; Andrioletti, B.; Furuta, H. *Chem. Commun.* **2006**, *0*, 4335.

76.   Kanchiku, S.; Suematsu, H.; Matsumoto, K.; Uchida, T.; Katsuki, T. *Angew. Chem. Intl. Ed.* **2007**, *46*, 3889.

77.   Ichinose, M.; Suematsu, H.; Katsuki, T. *Angew. Chem. Intl. Ed.* **2009**, *48*, 3121.

78.   Cheung, W.-H.; Zheng, S.-L.; Yu, W.-Y.; Zhou, G.-C.; Che, C.-M. *Org. Lett.* **2003**, *5*, 2535.

79.   Zheng, S.-L.; Yu, W.-Y.; Xu, M.-X.; Che, C.-M. *Tetrahedron Lett.* **2003**, *44*, 1445.

80.   Mbuvi, H. M.; Woo, L. K. *Organometallics* **2008**, *27*, 637.

81.   Callot, H. J.; Metz, F. *Nouv. J. Chim.* **1985**, *9*, 167.

82.   Thu, H.-Y.; Tong, G. S.-M.; Huang, J.-S.; Chan, S. L.-F.; Deng, Q.-H.; Che, C.-M. *Angew. Chem. Intl. Ed.* **2008**, *47*, 9747.

83.   Suematsu, H.; Katsuki, T. *J. Am. Chem. Soc.* **2009**, *131*, 14218.

84.   Galardon, E.; Le Maux, P.; Simonneaux, G. *J. Chem. Soc., Perkin Trans. 1* **1997**, 2455.

85.   Ho, C.-M.; Zhang, J.-L.; Zhou, C.-Y.; Chan, O.-Y.; Yan, J. J.; Zhang, F.-Y.; Huang, J.-S.; Che, C.-M. *J. Am. Chem. Soc.* **2010**, *132*, 1886.

86.   Baumann, L.; Mbuvi, H.; Du, G.; Woo, L. K. *Organometallics* **2007**, *26*, 3995.

87.   Aviv, I.; Gross, Z. *Synlett* **2006**, 951.

88.   Aviv, I.; Gross, Z. *Chem. Commun.* **2006**, 4477.

89.   Aviv, I.; Gross, Z. *Chem. Eur. J.* **2008**, *14*, 3995.

90.   Mbuvi, H.; Klobukowski, E.; Roberts, G.; Woo, L. K. *J. Porphyrins Phthalocyanines* **2010**, *14*, 284.

91.   Maxwell, J. L.; Brown, K. C.; Bartley, D. W.; Kodadek, T. *Science* **1992**, *256*, 1544.

92.   Le Maux, P.; Roisnel, T.; Nicolas, I.; Simonneaux, G. *Organometallics* **2008**, *27*, 3037.

93.   Li, Y.; Huang, J.-S.; Zhou, Z.-Y.; Che, C.-M. *J. Am. Chem. Soc.* **2001**, *123*, 4843.

94.   Boschi, T.; Licoccia, S.; Paolesse, R.; Tagliatesta, P.; Pelizzi, G.; Vitali, F. *Organometallics* **1989**, *8*, 330.

95.   Penoni, A.; Wanke, R.; Tollari, S.; Gallo, E.; Musella, D.; Ragaini, F.; Demartin, F.; Cenini, S. *Eur. J. Inorg. Chem.* **2003**, 1452.

96.   Johnson, A. W.; Ward, D. *J. Chem. Soc., Perkin Trans. 1* **1977**, 720.

97.   Dzik, W. I.; Xu, X.; Zhang, X. P.; Reek, J. N. H.; de Bruin, B. *J. Am. Chem. Soc.* **2010**, *132*, 10891.

98.   Lu, H.; Dzik, W. I.; Xu, X.; Wojtas, L.; de Bruin, B.; Zhang, X. P. *J. Am. Chem. Soc.* **2011**, *133*, 8518.

99.   Belof, J. L.; Cioce, C. R.; Xu, X.; Zhang, X. P.; Space, B.; Woodcock, H. L. *Organometallics* **2011**, *30*, 2739.

CHAPTER 2.   OLEFIN CYCLOPROPANATION CATALYZED BY IRIDIUM(III) PORPHYRIN COMPLEXES

Bernie J. Anding, Arkady Ellern, and L. Keith Woo

Abstract

Tetratolylporphyrinato (TTP) iridium complexes were shown to be extremely active and robust catalysts for the cyclopropanation of olefins using diazo compounds as carbene sources. Ir(TTP)CH$_3$ (**1**) catalyzed the cyclopropanation of styrene with ethyl diazoacetate (EDA) at -78 ºC and achieved 4.8×10^5 turnovers in three successive reagent additions with no sign of deactivation. High yields and moderate *trans* selectivities were attained for electron rich and sterically unhindered substrates. A Hammett ρ^+ value of -0.23 was determined by competition experiments with *para*-substituted styrenes. Furthermore, competitive cyclopropanation of styrene and styrene-d$_8$ with EDA and **1** demonstrated a moderate inverse secondary isotope effect of 0.86 ± 0.03. These data are consistent with a catalytic cycle that proceeds through a metalloporphyrin carbene intermediate. Carbene transfer to olefin substrates appears to be rate limiting as indicated by kinetic studies. Hexavalent iridium halogenato tetratolylporphyrinato complexes of the form Ir(TTP)X(L), where X = Cl, Br, I, NCS and L = CO, NMe$_3$ (**2 – 6**), and cationic analogues (X = BF$_4$ and L = CO or vacant site (**7**, **8**) also demonstrated high catalytic cyclopropanation activity.

Introduction

Over the past few decades, carbene transfer reactions used to generate new C−C bonds have grown tremendously in synthetic utility.[1-3] Furthermore, carbene moieties generated from diazo reagents provide attractive atom-efficient and environmentally friendly protocols because N$_2$ is the only byproduct. Although many diazo reagents react sluggishly on their

own, various catalysts efficiently assist in formation of carbene intermediates.[4-7] Among the highly active and robust catalysts, metalloporphyrin complexes are particularly versatile for
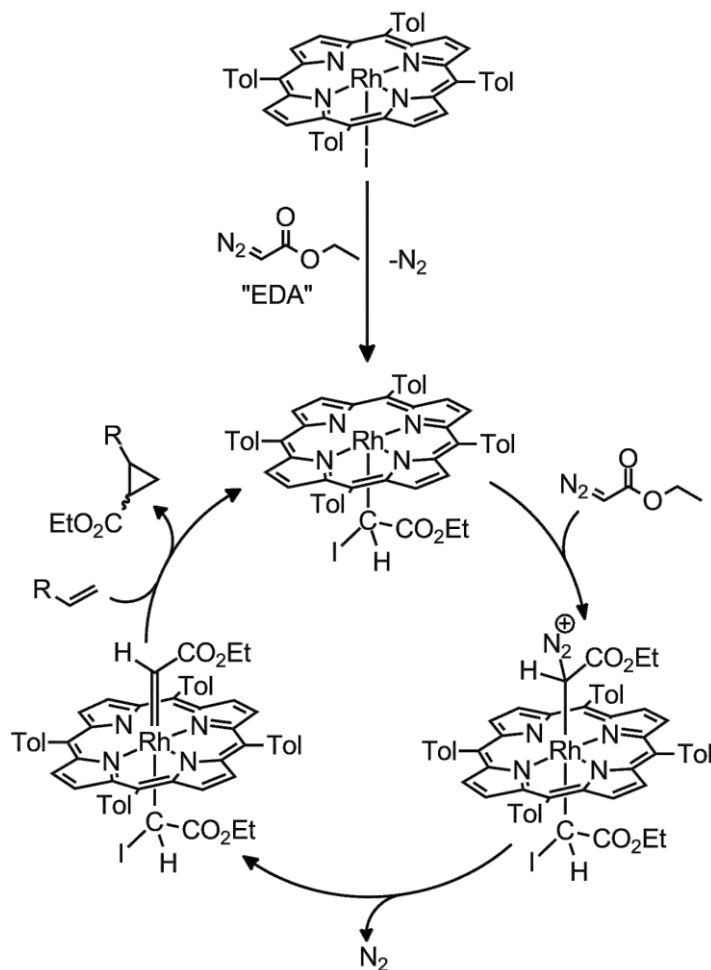

Figure 2.1: Cyclopropanation mechanism for Rh(TTP)I.

the design of stereoselective carbene transfers.[8-10] Metalloporphyrins containing iron,[11] ruthenium,[12] osmium,[13] cobalt,[14,15] and rhodium[15] are all active for catalytic carbene transfer. For example, Fe and Rh complexes exhibit a great breadth of catalytic range, including C−H insertions,[10,16] N−H insertions,[17] olefinations,[18] and cyclopropanations.[11,19] In addition, iron porphyrin catalysts are robust enough to achieve 4300 turnovers,[20] and rhodium adducts furnish cyclopropanation and C−H insertion products with unusual selectivity for *cis*-cyclopropanes and primary insertion products, respectively.[21,22] Despite these notable results

for group 8 and group 9 metals, the reactivity of iridium porphyrins toward carbene transfer has not been reported.

Examples of catalysis by halogenato iridium porphyrins are quite rare in comparison to those for the related rhodium porphyrins. This may be due, in part, to the presence of a kinetically inert CO ligand bound to iridium analogues, yielding a hexavalent complex devoid of an available vacant site.[23] Indeed, the mechanism of cyclopropanation by Rh(TTP)I, reported by Kodadek and co-workers, requires an open site for the initial coordination of the diazo compound (Figure 2.1).[24] Interestingly, the active catalyst was believed to exist primarily as an alkylrhodium complex resulting from initial carbene insertion into the Rh–I bond. Analogous alkyliridium porphyrin compounds, unlike their halogenato counterparts, are pentacoordinate species that appear to be good candidates for catalysis. The present work explores the catalytic activity of alkyliridium porphyrin complexes, as well as other iridium(III) porphyrins, towards transformations with diazo reagents. The work described herein serves as the first examples of carbene transfer catalyzed by iridium porphyrin complexes.

Results and Discussion

The catalytic cyclopropanation activity of both methyl and halogenato iridium tetratolylporphyrinato (TTP) complexes, Ir(TTP)CH$_3$ (**1**) and Ir(TTP)Cl(CO) (**2**) were evaluated. Syntheses of these complexes were reported previously.[25,26] Preliminary reactivity studies showed that methyliridium complex **1** decomposed ethyl diazoacetate (EDA) readily at temperatures as low as -78 ºC to form maleates and fumarates (cis:trans = 6.5:1) in quantitative yield. Reaction intermediates were too transient for spectroscopic observation by ^{1}H NMR. With these initial results, the cyclopropanation of various olefins and EDA using **1** was explored using a protocol similar to that developed for N,N'-bis(salicylidene)ethylenediiminato iridium, Ir(salen).[27] Dropwise addition of EDA to a solution of styrene and **1** at room temperature resulted in instantaneous gas evolution. Cyclopropanes were formed in 35% yield along with a significant amount of diazo dimerization products, diethyl maleate and diethyl fumarate (Table 2.1). The sum of the yields for cyclopropanation and dimerization correspond to complete conversion of EDA.

Lowering the reaction temperature to -78 °C resulted in a significant increase in yield (85%) and stereoselectivity for cyclopropanes, with a corresponding decrease in dimerization of the diazo reagent. This method was cleanly extended to other terminal aryl olefins. In contrast, electron deficient and internal olefins (except indene) required longer reaction times or higher temperatures. Yields for these substrates were lower, especially for those run at room temperature where dimerization becomes dominant. This method was also applicable to less reactive diazo reagents such as methyl 2-phenyldiazoacetate (MPDA; eq 2.1).

(2.1)
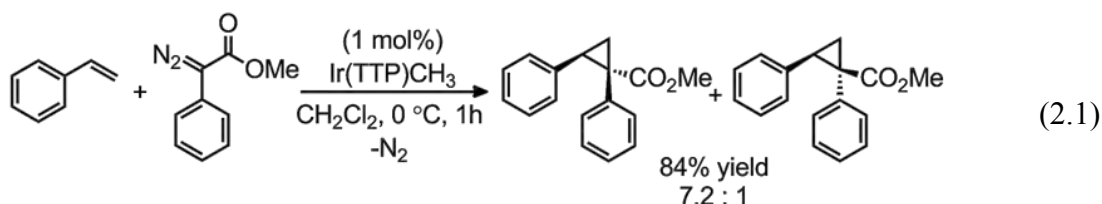
Table 2.1: Cyclopropanation of EDA and alkenes with Ir(TTP)CH$_3$.[a]

Substrate	Solvent	Time (min)	T (°C)	Yield (%)[b]	Trans:Cis[b]
styrene	CH$_2$Cl$_2$	< 5	23	35	5.5 : 1
styrene	CH$_2$Cl$_2$	< 5	-78	85	5.8 : 1
styrene	THF	30	0	80	6.3 : 1
4-methoxystyrene	CH$_2$Cl$_2$	< 5	-78	86	3.4 : 1
4-methylstyrene	CH$_2$Cl$_2$	< 5	-78	84	5.8 : 1
4-bromostyrene	CH$_2$Cl$_2$	< 5	-78	91	7.3 : 1
4-nitrostyrene[c]	CH$_2$Cl$_2$	< 5	-78	84	8.0 : 1
α-methylstyrene	CH$_2$Cl$_2$	< 5	-78	90	2.0 : 1
1-hexene	CH$_2$Cl$_2$	20	-78	60	3.3 : 1
indene	CH$_2$Cl$_2$	30	-78	62	3.2 : 1
cyclohexene	CH$_2$Cl$_2$	< 5	23	14[d]	-[e]
trans-β-methylstyrene	CH$_2$Cl$_2$	< 5	23	31[d]	1[f]
ethyl acrylate	CH$_2$Cl$_2$	< 5	23	12[d]	~10 : 1

[a] Conditions: 1 x 10^{-3} M in Ir(TTP)CH$_3$; Ir(TTP)CH$_3$:EDA:substrate = 1:100:500. [b] Yields and diastereomeric ratios of cyclopropanes as determined by GC. [c] 4-nitrostyrene was not distilled prior to use. [d] Determined by NMR. [e] Isomer not determined. [f] Only one isomer observed.

Reactions catalyzed by **1** displayed a moderate preference for *trans* cyclopropanes. This selectivity was enhanced slightly for reactions run in THF, albeit at higher temperatures and longer reaction times. In comparison to similar catalysts, **1** was more *trans* selective than Rh(TPP)I but less than Fe(TPP)Cl.[20,21] Moreover, analysis of the diastereoselectivity for the *para*-substituted styrenes revealed an influence of substrate electronics on diastereoselectivity. Substrates with electron withdrawing groups at the *para* position displayed a larger preference for *trans* cyclopropanes. Notably, cyclopropanation with *trans*-β-methylstyrene formed only the isomer bearing the phenyl group *anti* to both methyl and ethyl carboxylate as determined by NOESY.

To evaluate catalyst activity further, cyclopropanation was explored at very low catalyst loadings. Using 5.8×10^{-4} mol% of **1** relative to EDA in the presence of excess styrene, diazo conversion and cyclopropanation of styrene were determined after warming to room temperature from -78 °C. For three consecutive diazo additions, EDA was quantitatively consumed to form cyclopropanes with a small amount of diazo dimerization. Cyclopropanation yields were 93%, 92%, and 91% for the first, second, and third additions, respectively. Overall, **1** achieved 4.8×10^{5} turnovers with almost no indication of catalyst deactivation. This TON is nearly two orders of magnitude greater than the values reported for Ru and Rh porphyrin catalysts.[28-30]

Surprisingly, Ir(TTP)Cl(CO) (**2**) also effectively catalyzed the cyclopropanation of olefins with EDA, despite being coordinatively saturated (Table 2.2). The substrate reactivity trends were similar for both **1** and **2**. However, **2** required higher reaction temperatures and longer reaction times. Although **2** was less selective for *trans* cyclopropane products, it was slightly more efficient for the cyclopropanation of more hindered and electron deficient olefins.

Various metalloporphyrin complexes of the form $[Ir(TTP)(L)]^{+}$ or Ir(TTP)X(L), where X is an anionic ligand and L is a neutral ligand, were generated to compare axial ligand effects on catalytic activity. CO ligand substitution was accomplished by adding trimethylamine N-oxide to a CH_2Cl_2 solution of **2** (Figures 2.2). The resulting product was established to be Ir(TTP)Cl(NMe$_3$) (**3**) on the basis of ^{1}H NMR and IR spectroscopies. Protons of the axially

coordinated NMe₃ were strongly shifted upfield due to the porphyrin ring current effect and appeared as a sharp singlet at -2.99 ppm.   Moreover, CO loss was verified by the disappearance of the strong Ir–C≡O stretch at 2050 cm^{-1}.   The molecular structure of **3** (Figure 2.3) was determined by single crystal X-ray analysis.   One molecule of **3** occupied the asymmetric unit of the monoclinic cell together with two molecules of CH_2Cl_2. Presumably, oxidization of CO to CO_2 by trimethylamine N-oxide generated a pentacoordinate chloroiridium complex, which was quickly trapped by the *in situ* generated trimethylamine.[31]   This represents only the second decarbonylation procedure published for Ir(TTP)Cl(CO).[23]

Table 2.2: Cyclopropanation of EDA and alkenes with Ir(TTP)Cl(CO).[a]
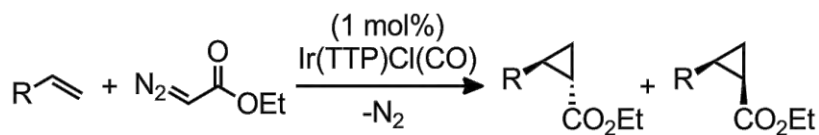
Substrate	Solvent	Time (min)	T (°C)	Yield (%)[b]	Trans:Cis[c]
styrene	CH_2Cl_2	< 5	23	92	4.7 : 1
styrene	CH_2Cl_2	20	0	85	4.9 : 1
styrene	THF	90	23	75	4.3 : 1
α –methylstyrene	CH_2Cl_2	20	0	93	1.8 : 1
1-hexene	CH_2Cl_2	30	0	59	3.5 : 1
indene	CH_2Cl_2	60	0	43	2.5 : 1
cyclohexene	CH_2Cl_2	< 5	23	20[c]	-[d]
trans-β-methylstyrene	CH_2Cl_2	< 5	23	67[c]	1[e]
ethyl acrylate	CH_2Cl_2	< 5	23	24	~10 : 1

[a] Conditions: 1 x 10^{-3} M in Ir(TTP)Cl(CO); Ir(TTP)Cl(CO):EDA:substrate = 1:100:500. [b] Yields and diastereomeric ratios of cyclopropanes as determined by GC. [c] Determined by NMR. [d] Isomer not determined. [e] Only one isomer observed.
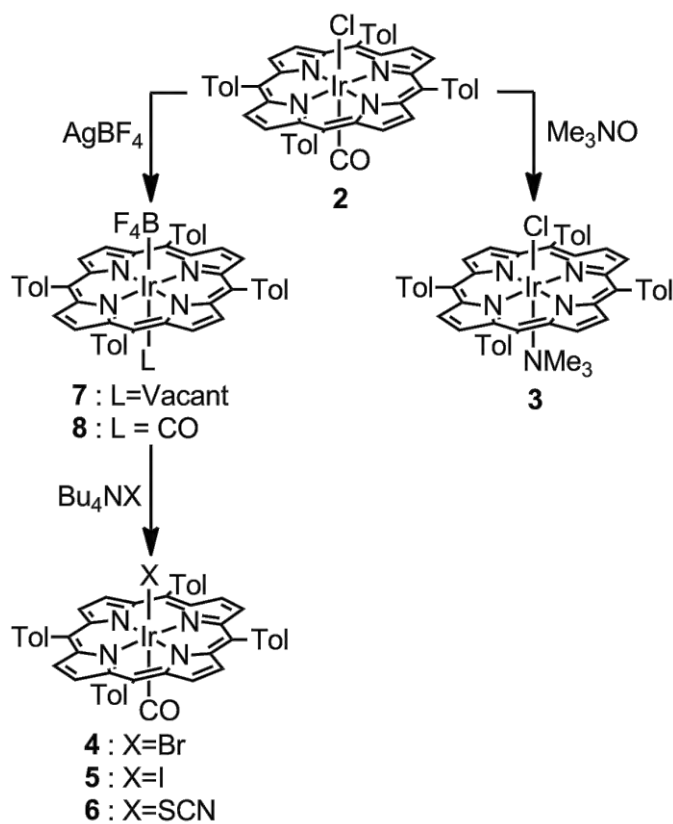
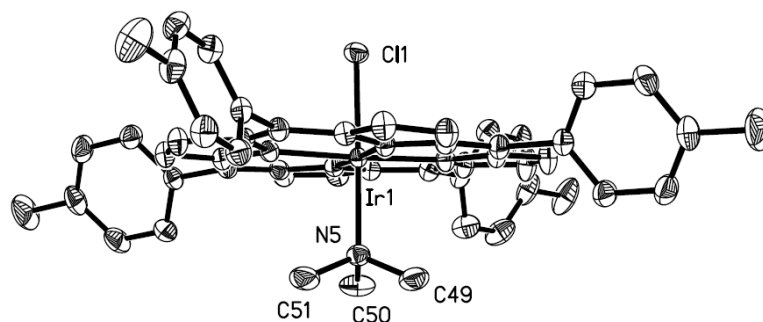**Figure 2.2:** Synthesis of complexes of the form Ir(TTP)X(L).

Figure 2.3: ORTEP[32] of **3** with 50% probability thermal ellipsoids. Selected bond distances (Å): avg. Ir(1)–N(por) = 2.035(4), Ir(1)–Cl(1) = 2.355(1), Ir(1)–N(5) = 2.174(2), avg. N(5)–C = 1.479(6).

Anionic ligand substitution products were generated by chloride abstraction from **2** with silver(I) tetrafluoroborate, followed by anion addition with the appropriate tetrabutylammonium salt. Only minor spectroscopic differences were observed between **2** and Ir(TTP)X(CO) (**4**, X = Br; **5**, X = I; **6**, X = NCS). Compositions and molecular

structures were confirmed by mass spectrometry and single crystal X-ray analysis (Figures 2.4 and 2.5). Selected metrical parameters are given in the figure captions. Complexes **4** and **5** are isostructural and both crystallize in the *I*4/*m* space group with a fourth of the molecule in the asymmetric unit and the Ir atom in a 4/*m* site symmetry. The central Ir atom has typical octahedral coordination with an ideal Ir–N$_4$ equatorial plane (EQP) and displays axial ligand disorder through a mirror plane. For X = NCS, complex **6**, N-coordination of the thioisocyanate ligand to the metal center through nitrogen was confirmed by bond length analysis. Notably, the Ir–N(CS) bond is 0.049(14) Å shorter than that for the shortest reported Ir–N(CS) compound.[33] If no anionic ligand sources were added after chloride abstraction, an inseparable mixture of cationic iridium(III) porphyrin complexes, Ir(TTP)(BF$_4$) (**7**) and Ir(TTP)(BF$_4$)(CO) (**8**), was obtained in variable ratios.[34] Attempts to cleanly isolate either of these cationic complexes failed.
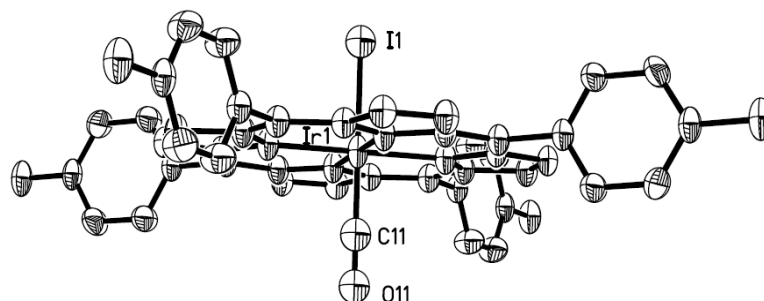
Figure 2.4: ORTEP of **5** showing one of the two configurations disordered by a mirror plane. Thermal ellipsoids are drawn at the 50% probability level. Selected bond distances and angles for **5**: Ir(1)–N$_{pyrrole}$ = 2.048(7), Ir(1)–I(1) = 2.491(2), Ir(1)–C(11) = 1.852(2), C(11)–O(11) = 1.141(2) (Å), I(1)–Ir(1)–C(11) = 180°, I(1)–Ir(1)–N$_4$(EQP) = 90°, C(11)–Ir(1)–N$_4$(EQP) = 90°. Selected bond distances and angles for isostructural **4** (Å): Ir(1)–N$_{pyrrole}$ = 2.047(4), Ir(1)–Br(1) = 2.409(2), Ir(1)–C(11) = 1.855(3), C(11)–O(11) = 1.143(3), Br(1)–Ir(1)–C(11) = 180°, Br(1)–Ir(1)–N$_4$(EQP) = 90°, C(11)–Ir(1)–N$_4$(EQP) = 90°.

Catalytic results, compiled in Table 2.3, show that the activity of hexavalent iridium porphyrin complexes for the cyclopropanation of styrene with EDA was relatively independent of the type of axial ligands. The only neutral species that showed a significant change in reactivity was Ir(TTP)I(CO). In comparison to other halogenato iridium porphyrins, Ir(TTP)I(CO) was considerably more active and diastereoselective, but

cyclopropanation yields were lower due to increased dimerization of the diazo reagent. In contrast, the cationic catalyst mixture (**7**/**8**) was as reactive and efficient toward cyclopropanation, but lower diastereoselectivity was observed. The cationic catalysts were either synthesized and isolated before cyclopropanation or generated *in situ* with silver tetrafluoroborate. Regardless of catalyst preparation, the catalytic efficiency and selectivity were effectively unchanged.
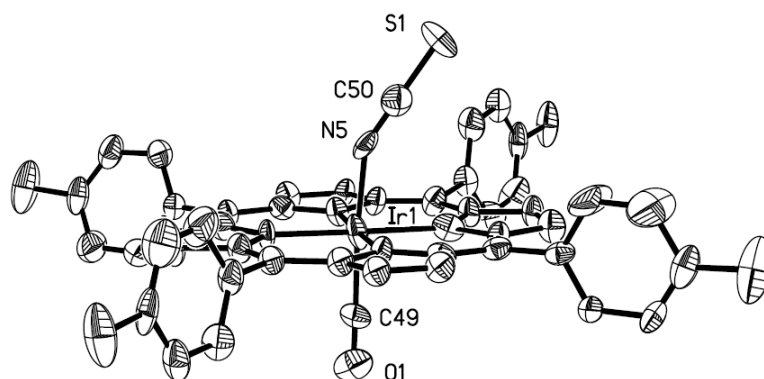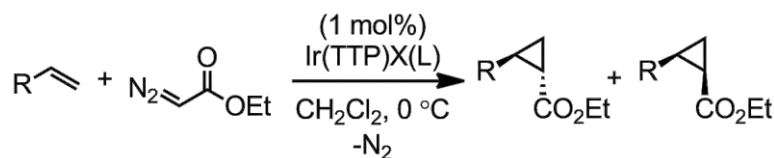

Figure 2.5: ORTEP of **6**. Thermal ellipsoids are drawn at the 50% probability level. Selected bond distances (Å): avg. Ir(1)–$N_{pyrrole}$ = 2.049(12), Ir(1)–N(5) = 1.961(14), N(5)–C(50) = 1.17(2), C(50)–S(1) = 1.664(19), Ir(1)–C(49) = 1.897(14), C(49)–O(1) = 1.153(17).

Table 2.3: Cyclopropanation of EDA and Styrene using various Ir porphyrin catalysts.[a]

Catalyst	Time (min)	Yield (%)	Trans:Cis
Ir(TTP)Cl(CO), **2**	20	85	4.9 : 1
Ir(TTP)Cl(NMe₃), **3**	60	75	5.0 : 1
Ir(TTP)Br(CO), **4**	60	75	4.6 : 1
Ir(TTP)I(CO), **5**	<5	56	5.5 : 1
Ir(TTP)SCN(CO), **6**	120	86	4.5 : 1
Ir(TTP)(BF₄) / Ir(TTP)(BF₄)(CO), **7**/**8**	<5	93	3.3 : 1
2 and AgBF₄[b]	<5	93	3.0 : 1

[a] Conditions: 1 x 10⁻³ M in catalyst; catalyst:EDA:styrene = 1:100:500; reactions run at 0 °C in CH₂Cl₂. Yields and diastereomeric ratios determined by GC. [b] **2** and AgBF₄ were premixed in CH₂Cl₂ and stirred for 30 minutes.

The above results for iridium porphyrin compounds share many similarities with group 8 metalloporphyrin catalysts. Both types of catalysts are *trans* selective and react smoothly with terminal aryl olefins. In addition, yields decrease significantly for electron poor or sterically hindered olefins. This reduction in efficiency was not nearly as drastic for cobalt and rhodium porphyrin catalysts.[19,35] On the basis of these observations, a mechanism similar to that previously proposed for group 8 metalloporphyrins seems likely for the catalytic pathway undertaken for cyclopropanation by Ir(TTP)CH$_3$ (Figure 2.6).[20,24] The initial step involves EDA coordination to form a diazoalkyl complex. Loss of nitrogen forms an intermediate carbene complex, which is susceptible to nucleophilic attack by an alkene. Cyclopropane production regenerates the active catalyst, Ir(TTP)CH$_3$.
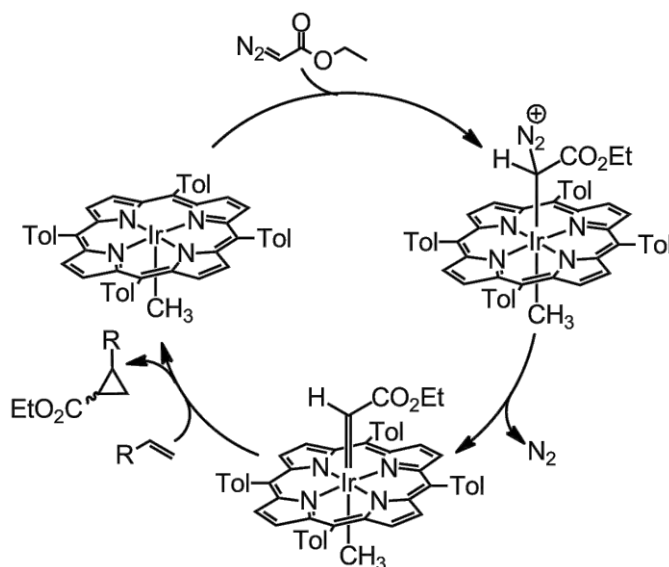
Figure 2.6: Proposed catalytic cycle for cyclopropanation with Ir(TTP)CH$_3$.

Kodadek and coworkers spectroscopically observed the diazoalkyl complex formed from EDA coordination to Rh(TTP)I at temperatures below -20 °C.[36] Unlike Rh(TTP)I, Ir(TTP)CH$_3$ is an extremely active catalyst at temperatures as low as -78 °C. Consequently, intermediate diazoalkyl or carbene complexes were not observed in Ir(TTP)CH$_3$-catalyzed reactions. Additional studies were employed to further explore the catalytic mechanism for Ir(TTP)CH$_3$. Substrate competition reactions were examined to determine the olefin influence on the reaction rate (Table 2.4). Olefins with a broad range of steric and electronic

properties were compared. Significant chemoselectivity was observed between styrene, indene, and cyclohexene. Cyclohexene was completely unreactive in the presence of either styrene or indene. For the competitive cyclopropanation of styrene and indene, products derived from styrene were favored in a ratio of 3.9:1. A comparison of *para*-substituted styrenes demonstrated that more electron rich olefins reacted preferentially. A Hammett correlation with the σ^+ parameter had good linearity with ρ^+ = -0.23 (Figure 2.7). This is indicative of slight positive charge buildup in the transition state. While this ρ^+ value is consistent the mechanism in Figure 2.6, it falls below the range found for iron and ruthenium porphyrin systems (-0.44 to -1.29).[20,30,37,38] In addition, the better correlation with σ^+ instead of σ has been reported for other metalloporphyrin cyclopropanation systems.[30,37]
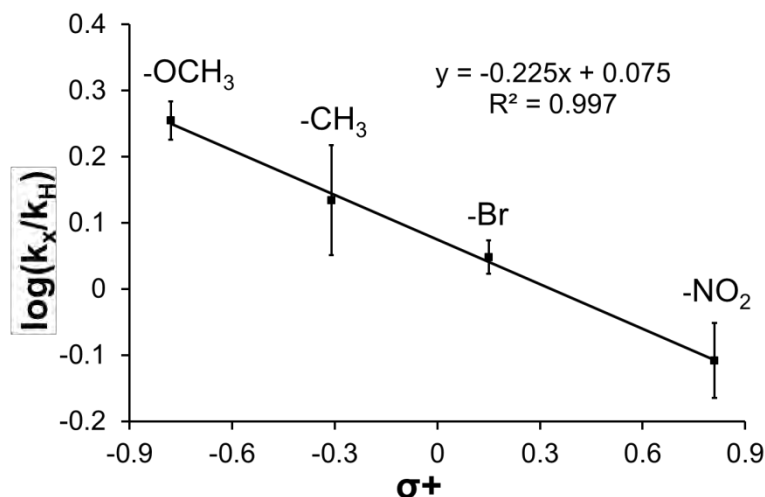
Figure 2.7: Hammett plot for the cyclopropanation of *para*-substituted styrenes with EDA and **1**.

A secondary isotope effect was observed during the competitive cyclopropanation of styrene with styrene-d_8. Complex **1** exhibited an inverse isotope effect of 0.86 ± 0.03, which is comparable to that measured for iron(III) tetrakis(pentafluorophenyl)porphyrin chloride.[20] This suggests that some olefin rehybridization occurs before the transition state of the carbene transfer step. Notably, no secondary isotope effect was observed for rhodium(III) tetramesitylporphyrin chloride.[39] In comparison to the transition state model proposed by Kodadek, Woo, and co-workers,[20] carbene transfers from iridium porphyrins have a later transition state than that for rhodium porphyrins. This implies that iridium carbene species

are more tightly bound and less electropositive, which may rationalize the observed differences in diastereo- and chemoselectivity.

Table 2.4: Cyclopropanation using EDA and Ir(TTP)CH$_3$. Substrate competition reactions.[a]

Substrate A	Substrate B	Ratio of A to B
styrene	indene	3.9
styrene	cyclohexene	only A
indene	cyclohexene	only A
4-methylstyrene	styrene	1.36
4-bromostyrene	styrene	1.12
4-methoxystyrene	styrene	1.80
4-nitrostyrene	styrene	0.78
styrene	styrene-d$_8$	0.85

[a] Conditions: 5 x 10^{-4} M in Ir(TTP)CH$_3$; Ir(TTP)CH$_3$:EDA:substrate A:substrate B = 1:200:1000:1000; reactions allowed to run for 1 h. Yields were determined by GC.

Despite these mechanistic insights, the rate-determining step for cyclopropanation remained unclear. Accordingly, we sought to explore the kinetics for cyclopropanation of styrene and methyl diazoacetate (MDA) in the presence of **1**. MDA was used instead of EDA to simplify monitoring the reaction by ^{1}H NMR. Due to the reactivity of **1** as well as its propensity to catalyze dimerization of the diazo reagent, practical reaction conditions were not trivial to achieve. In order to monitor the reaction by NMR for several half-lives with cyclopropanation as the major product, kinetic experiments were carried out at 273.0 K, with *ca.* 6.4×10^{-4} mol% **1** and excess styrene. However, increasing the amount of styrene from 4.3 to 8.3 equivalents relative to MDA reduced the rate of MDA consumption. We postulated that this inhibition was the result of competitive styrene binding to the catalyst. Indeed, on investigation by visible absorption spectroscopy, the Soret band of **1** was red-shifted by *ca.* 7 nm in the presence of excess styrene, which is suggestive of olefin coordination (Figure 2.19; Appendix A).

To circumvent this complication, the substrate was switched to 1-hexene. Hexene binding to **1** was considerably less substantial as demonstrated by visible absorption

spectroscopy (Figure 2.20; Appendix A). Unfortunately, because hexene is also less reactive than styrene, a significant amount of diazo dimerization was anticipated. Nevertheless, the cyclopropanation of hexene with MDA was studied at 273.0 K to measure the influence of catalyst, diazo reagent, and olefin concentration on reaction rate. Reactions were run with MDA as the limiting reagent, which allowed for the order of MDA to be determined using integrated rate equations. The data was plotted most suitably to the first-order rate law equation, giving a pseudo rate constant, k', of $(2.9 \pm 0.4) \times 10^{-4}$ s^{-1} (Figure 2.8). In addition, the order of **1** was determined by plotting the natural log of k' versus the natural log of the concentration of **1** for a series of reactions at different catalyst concentrations. The slope of the resulting line was 1.02, indicating a first-order dependence on the concentration of **1**. Reactions with different concentrations of hexene demonstrated saturation kinetics with respect to the rate of MDA consumption. The fastest rate was observed using a two-fold excess of hexene (0.14 M) relative to MDA. At higher concentrations of hexene, the rate of MDA consumption decreased marginally, but the rate of formation of cyclopropanation products continued to increase at the expense the dimerization products. Derivations of the rate law equations as well as initial rate data are given in Appendix A.
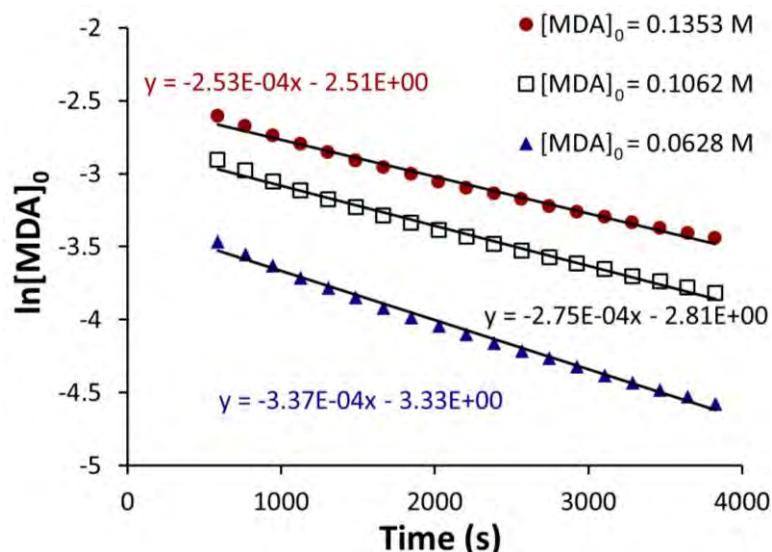
Figure 2.8: First-order integrated rate law plots at 273.0 K for different initial concentrations of MDA with 0.577 M hexene and 5.63×10^{-7} M Ir(TTP)CH$_3$. Data points from the first 400 seconds were omitted in the linear regression to correct for temperature equilibration. The average slope was $(-2.9 \pm 0.4) \times 10^{-4}$ s^{-1}.

The rate dependence on the olefin concentration was further evaluated by comparing kinetic reactions in the presence and absence of 1-hexene. Three sets of reactions were run in tandem to assure nearly equivalent conditions, and the initial rates, determined at less than 10% of reaction (before 500 seconds), were compared (Figure 2.9). The initial rate of MDA consumption was 138 – 151% faster in the presence of hexene than in the absence of hexene. Overall, these experiments clearly demonstrate that the presence of hexene accelerated the rate of MDA consumption.
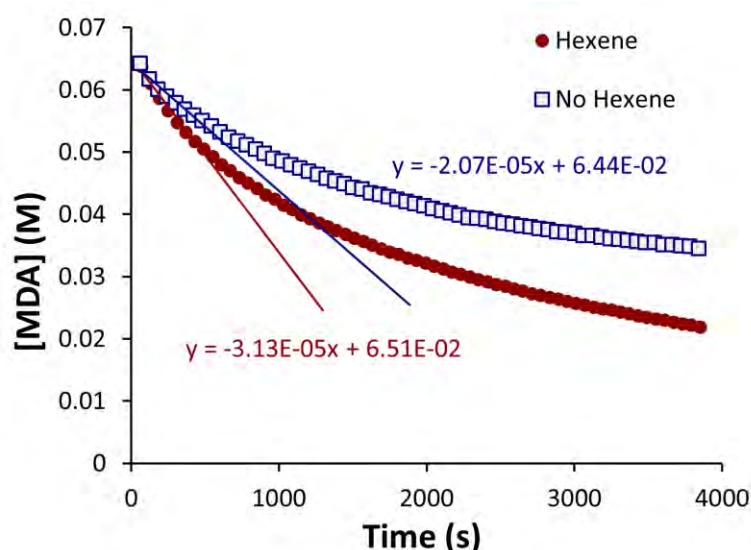
Figure 2.9: A plot of MDA consumption for the reactions of MDA and **1** at 273.0 K in the presence and absence of 1-hexene. Linear regressions were made for the data points between 0 and 500 seconds. The two rates shown represent the first of three sets of reactions.

The pertinent elementary steps for metalloporphyrin-catalyzed transformations with diazo reagents are shown in Figure 2.10. In the analogous system using Rh(TTP)I, Kodadek and co-workers demonstrated that coordination of EDA was rapid and carbene formation was rate-limiting (k_1, $k_{-1} > k_2$).[36] For Ir(TTP)CH$_3$ catalysis, the rate-limiting step must be either carbene formation (k_2) or carbene transfer (k_3, k_4). If k_2 was rate-limiting, the presence of hexene in the reaction would not increase the rate of MDA consumption. In fact, MDA consumption should be inhibited because cyclopropanation would compete with the dimerization pathway and would consume only one equivalent of MDA upon cyclopropanation. This case is not supported by the above kinetic data. Rather, the rate of

MDA consumption increases in the presence of hexene, indicating that carbene transfer must be rate-limiting. In other words, k_3 and k_4 are greater than k_2. Furthermore, since dimerization generally dominates even though hexene is present in excess, k_4 is likely greater than k_3.
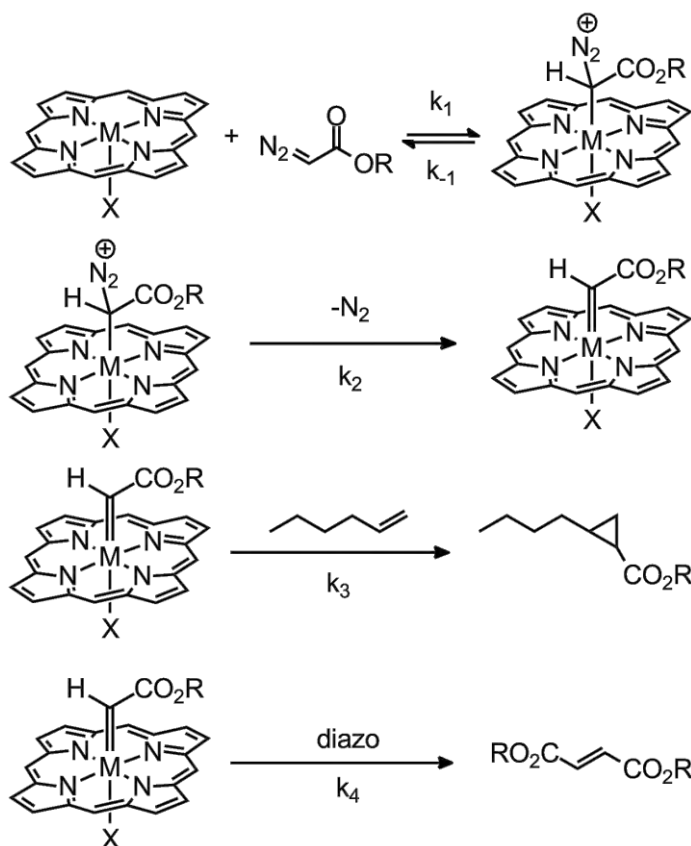

Figure 2.10: Elementary steps for the competitive cyclopropanation/dimerization of alkyl diazoacetate and 1-hexene in the presence of Ir(TTP)CH$_3$ or Rh(TTP)I.

In contrast to the case **1**, the mechanism for cyclopropanation with hexavalent iridium porphyrin complex **2** likely begins with reversible ligand dissociation to provide a vacant site for diazo coordination. Evidence supporting the formation of a heptacoordinate iridium porphyrin complex is limited and therefore seems unlikely in the present system.[40] Assuming only one ligand dissociates, two catalytic pathways are possible (Figure 2.11). CO dissociation would lead to a pathway with a neutral metalloporphyrin, analogous to the mechanism proposed for Ir(TTP)CH$_3$. Alternatively, chloride dissociation to generate a formally cationic metalloporphyrin catalyst could be occurring. The quantitative recovery of

Ir(TTP)Cl(CO) after catalysis suggests that CO dissociation is unlikely. On the other hand, comparing the cyclopropanation reactivity and selectivity of neutral (**1**) and cationic (**7**, **8**) iridium catalysts suggests that the chloride dissociation pathway may not be dominant either.
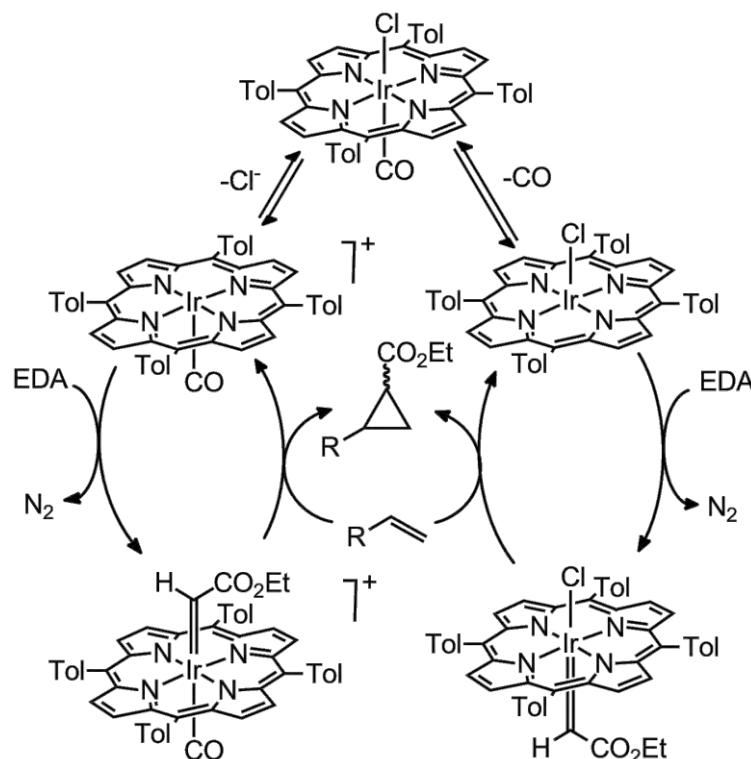
Figure 2.11: Potential routes for Ir(TTP)Cl(CO) catalyzed cyclopropanation.

Conclusions

In summary, a variety of neutral and cationic iridium(III) porphyrin complexes were shown to be exceptionally active catalysts for the cyclopropanation of olefins with diazo compounds. Ir(TTP)CH$_3$ (**1**) was extremely robust for the conversion of EDA, producing cyclopropane TONs of 4.8×10^5 without significant deactivation. Cyclopropanation was explored for a variety of electronically diverse olefins. In general, electron rich and sterically unencumbered substrates reacted the most efficiently. The cyclopropanation mechanism was explored in some depth for catalyst **1**. Competition studies using *para*-substituted styrenes produced a Hammett correlation with $\rho^+ = -0.23$, which indicates buildup of positive charge in the transition state. Using styrene and styrene-d_8, an inverse secondary isotope effect of 0.86 ± 0.03 was observed, suggesting that moderate olefin rehybridization occurs before the

transition state of the carbene transfer step. From these data, the catalytic cycle was proposed to follow a metalloporphyrin carbene pathway similar to that reported for Rh(TTP)I. However, unlike Rh(TTP)I, the rate-limiting step for catalyst **1** appeared to be carbene transfer as determined by kinetics analyses. Similar mechanistic insights for hexacoordinate compounds were not explored due to the ambiguity in competing pathways involving the dissociation of axial ligands. The findings presented herein indicate that significant potential exists for catalysis with iridium porphyrin complexes.

Experimental

General Considerations: All manipulations were performed under a dry nitrogen atmosphere. Ir(TTP)Cl(CO), Ir(TTP)CH$_3$, and Ir(TTP)(BF$_4$)/Ir(TTP)(CO)(BF$_4$) were synthesized according to previously reported methods.[25,26,34] MPDA and MDA were prepared by procedures adapted from the literature.[41,42] All olefin substrates were dried over 4 Å molecular sieves prior to use. The styrene derivatives, except 4-nitrostyrene, were distilled and stored at -20 °C prior to use. Trimethylamine N-oxide was sublimed and stored in an inert-atmosphere glovebox. Methylene chloride and tetrahydrofuran were deoxygenated and dried by passage through columns of reduced copper and alumina. All other chemicals were purchased as reagent grade and used without further purification. NMR spectra were collected using Varian VXR 300 MHz, Varian VXR 400 MHz, or Bruker DRX 400 MHz spectrometers. Kinetic measurements were done using a Bruker DRX 400 MHz spectrometer. ^{1}H NMR peak positions were referenced against residual proton resonances of deuterated solvents (δ, ppm: CDCl$_3$, 7.26; CD$_2$Cl$_2$, 5.33). Gas chromatography was performed using a Shimadzu GC-17a fitted with a HP-5 column (30 m x 0.25 μm). Ratios for kinetic isotope data were determined using a Finnegan Magnum GC-MS fitted with a HP-5 column (30 m x 0.25 μm) and a time-of-flight mass analyzer. Mesitylene was used as an internal standard for GC yield determinations. Column chromatography was performed using silica gel (40 – 63 μm) purchased from Sorbent Technologies. Characterization data for the cyclopropanation products, ethyl 2-phenylcyclopropanecarboxylate,[43] ethyl 2-methyl-2-phenylcyclopropanecarboxylate,[44] ethyl 1,1a,6,6a-tetrahydrocyclopropa[*a*]indene-1-carboxylate,[45] ethyl 2-butylcyclopropanecarboxylate,[44] ethyl bicyclo[4.1.0]heptane-7-carboxylate,[45] ethyl 2-methyl-

3-phenylcyclopropanecarboxylate,[46] diethyl cyclopropane-1,2-dicarboxylate,[47] and methyl 1,2-diphenylcyclopropanecarboxylate,[48] were previously reported. Relative stereochemistry for ethyl 2-methyl-3-phenylcyclopropanecarboxylate was confirmed by NOESY spectroscopy (Figure 2.21; Appendix A).

General cyclopropanation procedure: Catalyst (2 μmol) was weighed as a solid and transferred to a flame-dried Schlenk flask containing a stir-bar. The flask was charged with olefin substrate (1 mmol), CH_2Cl_2 (2.0 mL), and mesitylene (internal standard, 0.144 mmol). If the reaction was carried out 0 °C or -78 °C, it was placed in an ice bath or dry ice/acetone bath, respectively. After allowing 15 minutes for temperature equilibration, reagent grade EDA (0.255 mmol) was added neat, drop-wise via syringe over the course of 30 seconds. During the reaction, aliquots were quenched with pyridine and analyzed by GC. Once the reaction was complete, volatile components were removed *in vacuo*. ^1H NMR ($CDCl_3$) was used to confirm the consumption of EDA. Cyclopropanes could be isolated by column chromatography on silica gel using hexanes and ethyl acetate (40:1) as the eluent system. Catalyst preparations varied slightly for *in situ* generated cationic complexes. In a glovebox, Ir(TTP)Cl(CO) (2 μmol) and excess silver tetrafluoroborate (50 μmol) were dissolved in CH_2Cl_2 (2 mL). The vessel was wrapped in foil and allowed to stir at room temperature for 30 minutes before continuing with the above cyclopropanation protocol.

Experiment to measure catalyst TON: A dry Schlenk flask was charged with Ir(TTP)CH$_3$ (4.13×10^{-6} mmol) from a stock solution (1.00 mL, 4.13×10^{-3} M) in CH_2Cl_2. The porphyrin solution was taken to dryness under an N_2 stream before styrene (7.6 mmol), mesitylene (internal standard 0.2874 mmol), and CH_2Cl_2 (2.0 mL) were added. EDA (0.72 mmol) was added after the mixture was cooled to near -78 °C in an acetone/dry ice bath. The cold bath was removed after 10 minutes and stirring was continued at room temperature for 50 minutes. An aliquot was quenched in pyridine and analyzed by GC. The reaction vessel was again cooled to -78 °C and this method was repeated over the course of three EDA additions. An hour after the final addition, the reaction vessel was quenched with pyridine. Turnover numbers were measured by GC and complete conversion of EDA was observed by ^1H NMR.

General competition experiment: This general method was used for all competition studies including that with styrene-d$_8$. A CH$_2$Cl$_2$-stock solution (200. μL, 4.93 × 10^{-3} M), Ir(TTP)CH$_3$ (0.986 μmol) was transferred to a Schlenk flask and taken to dryness under an N$_2$ stream. Substrate A (0.987 mmol), substrate B, (0.987 mmol), mesitylene (internal standard 0.1437 mmol), and CH$_2$Cl$_2$ (1.0 mL) were added to the flask. The solution was allowed to equilibrate to the desired reaction temperature for 15 minutes. EDA (0.2 mmol) was added dropwise by syringe over the course of 30 seconds. After stirring for 1 hour, the reaction was quenched with pyridine and analyzed by GC.

Setup for Kinetic Measurement Experiments: An NMR tube was charged with **1** (ranging from 1.05 × 10^{-4} to 4.20 × 10^{-4} μmol) from a 5.25 × 10^{-6} M CH$_2$Cl$_2$-stock solution and taken to dryness under reduced vacuum. The tube was taken into a glovebox and loaded with 1-hexene or styrene (ranging from 27.8 to 262 μmol), mesitylene (2.82 μmol), and diluted to a total volume of 420 μL with CD$_2$Cl$_2$. Then, the tube was fitted with a septum, cooled to 273 K and taken to the NMR spectrometer. Spectrometer settings were prepared, included temperature equilibration to 273.0 K, prior to diazo addition. Finally, MDA (ranging from 11.6 to 56.8 umol) in a CD$_2$Cl$_2$-stock solution (dried over molecular sieves), which was chilled in an ice bath, was added quickly. Data collection began *ca.* 1 min after addition. Adding equimolar portions of MDA was challenging, despite storing the stock solution in a -20 °C freezer. Slow volatilization of CD$_2$Cl$_2$ caused the MDA stock concentration to fluctuate over the course of a couple weeks. Because MDA and all the products could be monitored during the reaction, data were normalized to the total mass balance of MDA and its products.

Ir(TTP)Cl(NMe$_3$) (3): In a glovebox, Ir(TTP)Cl(CO) (34.3 mg, 0.0371 mmol) and trimethylamine N-oxide (15 mg, 0.20 mmol) were dissolved in CH$_2$Cl$_2$ (5 mL) and stirred at room temperature for 1 day. Volatile components were removed *in vacuo*. Crystals were grown by slow evaporation from CH$_2$Cl$_2$/MeOH and separated from solution by decanting the solvent to give **3** in 87% yield (30.8 mg, 0.0322 mmol). ^{1}H NMR (CDCl$_3$): δ 8.71 (s, 8H), 8.15 (d, *J* = 7.2 Hz, 4H), 8.02 (d, *J* = 7.2 Hz, 4H), 7.56 (t, *J* = 6.0 Hz, 8H), 2.74 (s, 12H). UV-vis (CH$_2$Cl$_2$): λ$_{max}$ (log ε) 412 (5.34), 522 (4.21), 555 (3.47).

Ir(TTP)Br(CO) (4): All Ir(TTP)X(CO) adducts were synthesized using the following procedure with the appropriate tetrabutylammonium salts. Halide abstraction was performed similarly to a previously reported method.[34] In a glovebox, a reaction vessel was charged with Ir(TTP)Cl(CO) (14 mg, 0.015 mmol), excess silver tetrafluoroborate (20 mg, 0.1 mmol), and CH_2Cl_2 (3 mL). The vessel was wrapped in foil and stirred for 2 days at ambient temperature. The resulting solids were removed by filtration. Excess tetrabutylammonium bromide (5 – 10 equivalents) was added to the filtrate and the mixture was stirred overnight. An aqueous workup and extraction in CH_2Cl_2 afforded **4** as a moderately pure, red solid. Purification by column chromatography on silica gel eluting with hexanes and CH_2Cl_2 (1:2) yielded **4** in 54% yield (7.8 mg, 8.1 x 10^{-3} mmol). X-ray quality single crystals were grown by slow evaporation from CH_2Cl_2. Anal. Calcd for $C_{49}H_{36}BrIrN_4O$: C, 60.74; H, 3.74; N, 5.78. Found: C, 61.26; H, 3.81; N, 5.71. ^{1}H NMR (CDCl3): δ 8.93 (s, 8H), 8.12 (t, J = 7.5 Hz, 8H), 7.56 (d, J = 6.0 Hz, 8H), 2.1 (s, 12H). UV-vis (CH_2Cl_2): λ_{max} (log ε) 424 (5.59), 535 (4.39), 570 (3.88).

Ir(TTP)I(CO) (5): Substitute tetrabutylammonium iodide in the procedure outlined for **4**. Ir(TTP)Cl(CO) (17.2 mg, 0.0186 mmol) led to **5** in 45% yield (8.5 mg) after column chromatography. ^{1}H NMR (CDCl3): δ 8.92 (s, 8H), 8.11 (m, 8H), 7.57 (t, J = 6.6 Hz, 8H), 2.71 (s, 12H). UV-vis (CH_2Cl_2): λ_{max} (log ε) 422 (5.51), 533 (4.36), 569 (3.82).

Ir(TTP)(SCN)(CO) (6): Substitute tetrabutylammonium thiocyanate in the procedure outlined for **4**. Ir(TTP)Cl(CO) (27.5 mg, 0.0297 mmol) led to **6** in 72% yield (20.2 mg). Anal. Calcd for $C_{50}H_{36}IrN_5OS \cdot 1/2H_2O$: C, 62.81; H, 3.90; N, 7.32. Found: C, 62.26; H, 3.34; N, 7.13. ^{1}H NMR (CDCl3): δ 8.98 (s, 8H), 8.13 (dd, J = 15.2 Hz, 7.6 Hz, 8H), 7.60 (t, J = 6.4 Hz, 8H), 2.73 (s, 12H). UV-vis (CH_2Cl_2): λ_{max} (log ε) 420 (5.59), 531 (4.42), 566 (3.84).

X-Ray Single Crystal Structure Determination: The crystal evaluation and data collection were performed at 173 K on a Bruker APEX II CCD diffractometer using Mo K_α (λ = 0.71073 Å). Full sphere data with 0.3° frame width were collected until a resolution of 0.74 Å. The absorption correction was based on a fit of a spherical harmonic function to the empirical transmission surface as sampled by multiple equivalent measurements.[49] Structures were solved using direct methods and were refined in full-matrix anisotropic

approximation for all non-hydrogen atoms. All hydrogen atoms were placed in the structure factor calculation at idealized positions and refined using a "riding model". The $U_{iso}(H)$ values were set at 1.5 times the U_{eq} value of the carrier atom. All calculations were performed using the APEX II software package.[50,51] In complexes **4** and **5**, the axial ligands were disordered by inversion and distances in these ligands were constrained during refinement.

References

1.   Che, C.-M.; Zhou, C.-Y.; Wong, E. In *Topics in Organometallic Chemistry*; Plietker, B., Ed.; Springer Berlin / Heidelberg: 2011; Vol. 33, p 111.

2.   Lu, H.; Zhang, X. P. *Chem. Soc. Rev.* **2011**, *40*, 1899.

3.   Nicolas, I.; Le Maux, P.; Simonneaux, G. *Coord. Chem. Rev.* **2008**, *252*, 727.

4.   Davies, H. M. L.; Panaro, S. A. *Tetrahedron* **2000**, *56*, 4871.

5.   Doyle, M. P.; Duffy, R.; Ratnikov, M.; Zhou, L. *Chem. Rev.* **2010**, *110*, 704.

6.   Diaz-Requejo, M. M.; Belderrain, T. R.; Nicasio, M. C.; Perez, P. J. *Dalton Trans.* **2006**, 5559.

7.   Caballero, A.; Prieto, A.; Díaz-Requejo, M. M.; Pérez, P. J. *Eur. J. Inorg. Chem.* **2009**, *2009*, 1137.

8.   Doyle, M. P. *Angew. Chem. Intl. Ed.* **2009**, *48*, 850.

9.   Ferrand, Y.; Le Maux, P.; Simonneaux, G. *Org. Lett.* **2004**, *6*, 3211.

10.   Thu, H.-Y.; Tong, G. S.-M.; Huang, J.-S.; Chan, S. L.-F.; Deng, Q.-H.; Che, C.-M. *Angew. Chem. Intl. Ed.* **2008**, *47*, 9747.

11.   Hamaker, C. G.; Mirafzal, G. A.; Woo, L. K. *Organometallics* **2001**, *20*, 5171.

12.   Zhou, C.-Y.; Che, C.; Zhou *Synlett* **2010**, *2010*, 2681.

13.   Che, C.-M.; Huang, J.-S. *Coord. Chem. Rev.* **2002**, *231*, 151.

14.   Xu, X.; Lu, H.; Ruppel, J. V.; Cui, X.; Lopez de Mesa, S.; Wojtas, L.; Zhang, X. P. *J. Am. Chem. Soc.* **2011**, *133*, 15292.

15.   Intrieri, D.; Caselli, A.; Gallo, E. *Eur. J. Inorg. Chem.* **2011**, n/a.

16. Mbuvi, H. M.; Woo, L. K. *Organometallics* **2008**, *27*, 637.

17. Mbuvi, H.; Klobukowski, E.; Roberts, G.; Woo, L. K. *J. Porphyrins Phthalocyanines* **2010**, *14*, 284.

18. Cheng, G.; Mirafzal, G. A.; Woo, L. K. *Organometallics* **2003**, *22*, 1468.

19. Callot, H. J.; Metz, F.; Piechocki, C. *Tetrahedron* **1982**, *38*, 2365.

20. Wolf, J. R.; Hamaker, C. G.; Djukic, J.-P.; Kodadek, T.; Woo, L. K. *J. Am. Chem. Soc.* **1995**, *117*, 9194.

21. Callot, H. J.; Piechocki, C. *Tetrahedron Lett.* **1980**, *21*, 3489.

22. Callot, H. J.; Metz, F. *Tetrahedron Lett.* **1982**, *23*, 4321.

23. Sadasivan, N. *J. Inorg. Nucl. Chem.* **1968**, *30*, 591.

24. Bartley, D. W.; Kodadek, T. *J. Am. Chem. Soc.* **1993**, *115*, 1656.

25. Ogoshi, H.; Setsune, J.; Yoshida, Z. *J. Organomet. Chem.* **1978**, *159*, 317.

26. Yeung, S. K.; Chan, K. S. *Organometallics* **2005**, *24*, 6426.

27. Kanchiku, S.; Suematsu, H.; Matsumoto, K.; Uchida, T.; Katsuki, T. *Angew. Chem. Intl. Ed.* **2007**, *46*, 3889.

28. Berkessel, A.; Kaiser, P.; Lex, J. *Chem. Eur. J.* **2003**, *9*, 4746.

29. O'Malley, S.; Kodadek, T. *Tetrahedron Lett.* **1991**, *32*, 2445.

30. Che, C.-M.; Huang, J.-S.; Lee, F.-W.; Li, Y.; Lai, T.-S.; Kwong, H.-L.; Teng, P.-F.; Lee, W.-S.; Lo, W.-C.; Peng, S.-M.; Zhou, Z.-Y. *J. Am. Chem. Soc.* **2001**, *123*, 4119.

31. Shvo, Y.; Hazum, E. *J. Chem. Soc., Chem. Commun.* **1975**, 829.

32. Burnett, M. N.; Johnson, C. K. ORTEP-III: Oak Ridge Termal Ellipsoid Plot Program for Crystal Structure Illustrations, Oak Ride National Laboratory Report ORNL-6895, 1996.

33. Rohde, J. *Z. Anorg. Allg. Chem.* **1997**, *623*, 1774.

34. Song, X.; Chan, K. S. *Organometallics* **2007**, *26*, 965.

35.   Chen, Y.; Ruppel, J. V.; Zhang, X. P. *J. Am. Chem. Soc.* **2007**, *129*, 12074.

36.   Maxwell, J. L.; Brown, K. C.; Bartley, D. W.; Kodadek, T. *Science* **1992**, *256*, 1544.

37.   Lai, T.-S.; Chan, F.-Y.; So, P.-K.; Ma, D.-L.; Wong, K.-Y.; Che, C.-M. *Dalton Trans.* **2006**, 4845.

38.   Galardon, E.; Le Maux, P.; Simonneaux, G. *Tetrahedron* **2000**, *56*, 615.

39.   Brown, K. C.; Kodadek, T. *J. Am. Chem. Soc.* **1992**, *114*, 8336.

40.   Cheung, C. W.; Chan, K. S. *Organometallics* **2008**, *27*, 3043.

41.   Zhao, W.-J.; Yan, M.; Huang, D.; Ji, S.-J. *Tetrahedron* **2005**, *61*, 5585.

42.   Searle, N. E. *Org. Synth.* **1956**, *36*.

43.   Chen, Y.; Fields, K. B.; Zhang, X. P. *J. Am. Chem. Soc.* **2004**, *126*, 14718.

44.   Barrett, A. G. M.; Braddock, D. C.; Lenoir, I.; Tone, H. *J. Org. Chem.* **2001**, *66*, 8260.

45.   Rosenberg, M. L.; Krivokapic, A.; Tilset, M. *Org. Lett.* **2009**, *11*, 547.

46.   Feldman, K. S.; Simpson, R. E. *J. Am. Chem. Soc.* **1989**, *111*, 4878.

47.   Doyle, M. P.; Dorow, R. L.; Tamblyn, W. H. *J. Org. Chem.* **1982**, *47*, 4059.

48.   Tarwade, V.; Liu, X.; Yan, N.; Fox, J. M. *J. Am. Chem. Soc.* **2009**, *131*, 5382.

49.   Blessing, R. *Acta Crystallogr., Sect. A* **1995**, *51*, 33.

50.   Sheldrick, G. M. *Acta. Cryst.* **2008**, *A64*, 112.

51.   ; APEX2 Version 2.2. Bruker AXS Inc.: Madison, WI, USA, 2007.

Appendix A

Kinetics Data
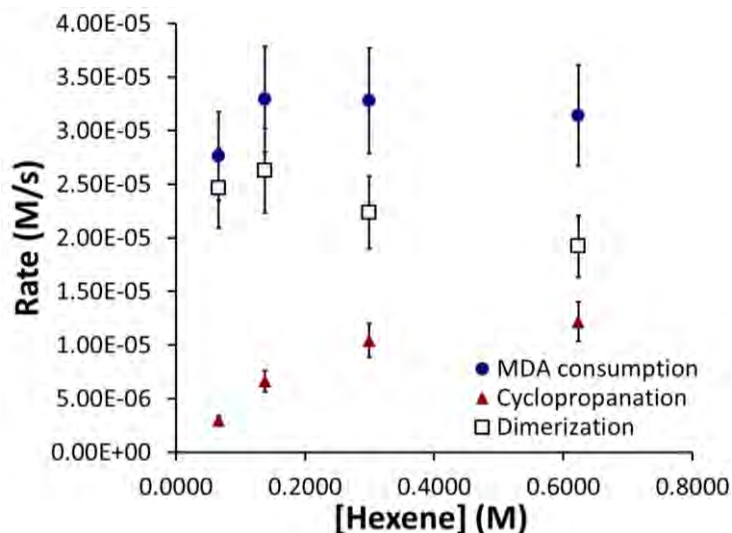
Figure 2.12: Rate dependence on hexene. Conditions: 5.63×10^{-7} M Ir(TTP)CH$_3$ and 0.0681−0.0755 M MDA in CD$_2$Cl$_2$ at 273.0 K with mesitylene as the internal standard (0.0110 M). The concentration of hexene was varied from 0.0662 to 0.6233 M. Error was estimated at 15%. Since saturation kinetics was observed, no further kinetic analysis was attempted.
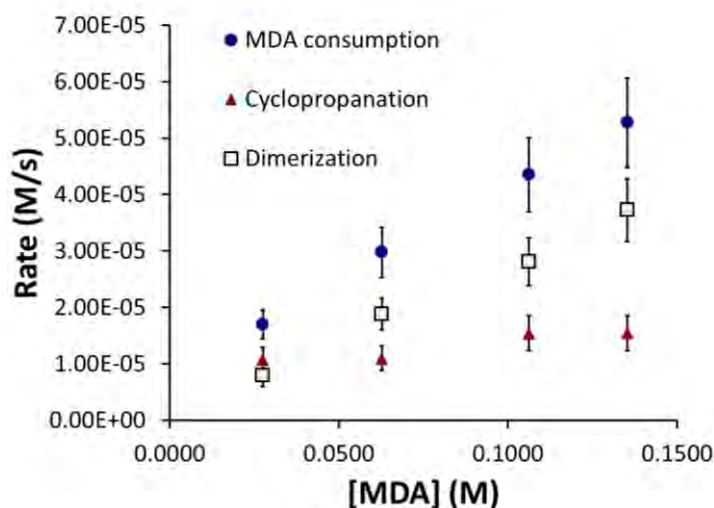
Figure 2.13: Rate dependence on MDA. Conditions: 5.63×10^{-7} M Ir(TTP)CH$_3$ and 0.56–0.58 M hexene in CD$_2$Cl$_2$ at 273.0 K with mesitylene as the internal standard (0.0110 M). The concentration of MDA was varied between 0.0275 and 0.1353 M. Error was estimated at 15%.

The order of MDA was derived from rate equations 2.2 – 2.4. Individual reactions were plotted using the zeroth, first, and second order derivations of equation 2.3 and k' were determined for each. The value of k' varied drastically for the zeroth and second order plots (2.8×10^{-5} to 5.3×10^{-5} Ms^{-1} and 0.0068 to 0.019 $M^{-1}s^{-1}$, respectively). In contrast, k' for the first order plots were relatively constant at $2.9 \times 10^{-4} \pm 0.4 \times 10^{-4}$ s^{-1}, suggesting that the reaction is first-order with respect to MDA.

$$Rate = k[MDA]^m[hexene]^n[Ir(TTP)CH_3]^p \tag{2.2}$$

$$Rate = k'[MDA]^m = \frac{-d[MDA]}{dt} \tag{2.3}$$

$$k' = k[hexene]^n[Ir(TTP)CH_3]^p \tag{2.4}$$
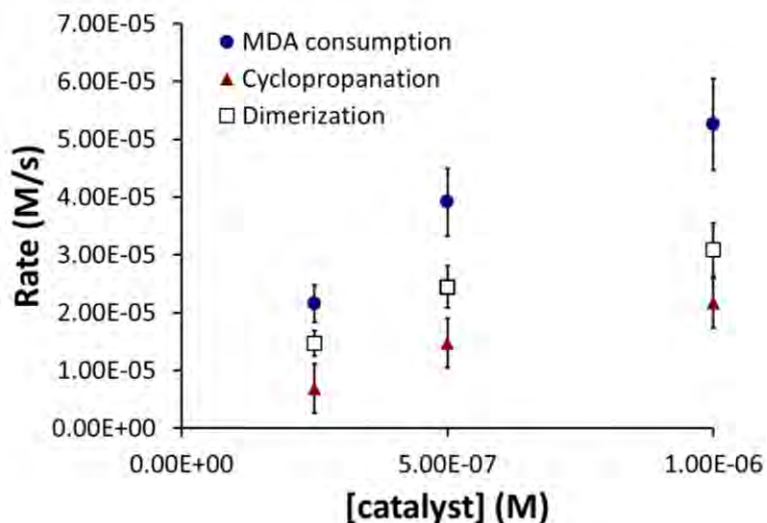
Figure 2.14: Rate dependence on Ir(TTP)CH$_3$. Conditions: 0.494 M hexene and 0.0548−0.0645 M MDA in CD$_2$Cl$_2$ at 273.0 K with mesitylene as the internal standard (0.0110 M). The concentration of Ir(TTP)CH$_3$ was varied between 2.50×10^{-7} and 1.00×10^{-6} M. Error was estimated at 15%.

The order of Ir(TTP)CH$_3$ was determined using equation 2.5, which was derived from equation 2.4. For each of the three individual reactions, k' was determined using the first-order derivation of equation 2.3. Then, the natural log of the k' values were plotted against the natural log of the concentration of Ir(TTP)CH$_3$, rendering the order of Ir(TTP)CH$_3$ (p) as the slope. The slope of $p = 1.018$ indicates that the reaction is first-order with respect to Ir(TTP)CH$_3$.

$$\ln(k') = \ln(k) + n\ln([hexene]) + p\ln([Ir(TTP)CH_3]) \tag{2.5}$$

ln[Ir(TTP)CH$_3$]

y = 1.018E+00x + 7.270E+00

ln(k')
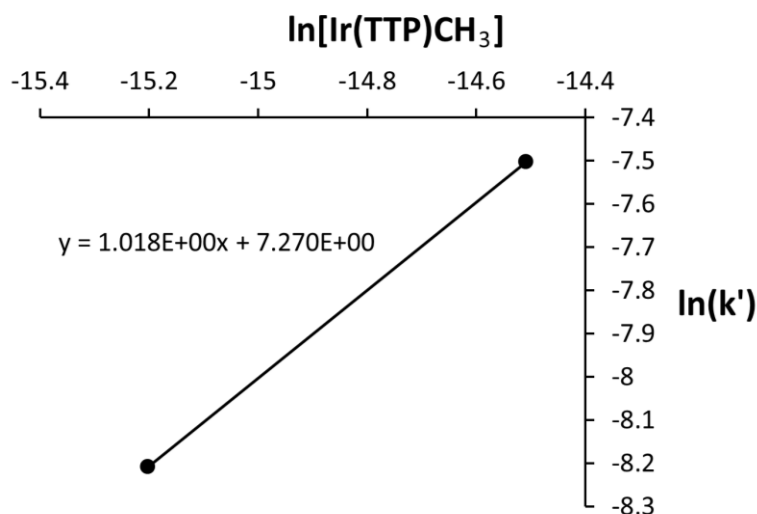
Figure 2.15: Determination of the catalyst order by the differential rate method. The data for the reaction using the largest amount of catalyst, [Ir(TTP)CH$_3$] = 1.00×10^{-6} M, was omitted because the reaction was too fast. By the time the first data point was acquired (ca. 50 seconds), the reaction was nearly half complete. Therefore, initial rate data could not be collected for this case.

[MDA]

● Hexene
□ No Hexene

y = -1.552E-05x + 6.308E-02

y = -2.510E-05x + 6.354E-02

Time (s)
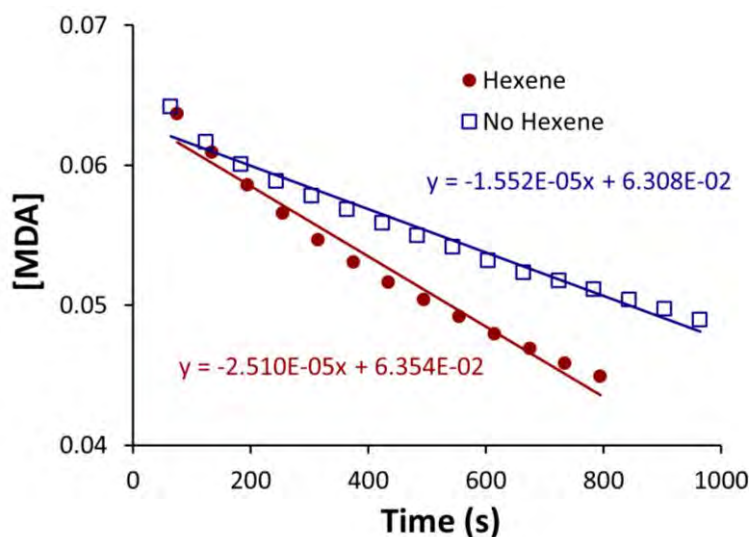
Figure 2.16: Initial rate data for MDA reactions in the presence and absence hexene: first trial. Conditions: Ir(TTP)CH$_3$ (5.63×10^{-7} M) and 1-hexene (0 or 0.671 M) in 4.20×10^2 μL CD$_2$Cl$_2$ were treated with [MDA] (0.0874-0.115 M, variation resulted from error) at 273.0 K.
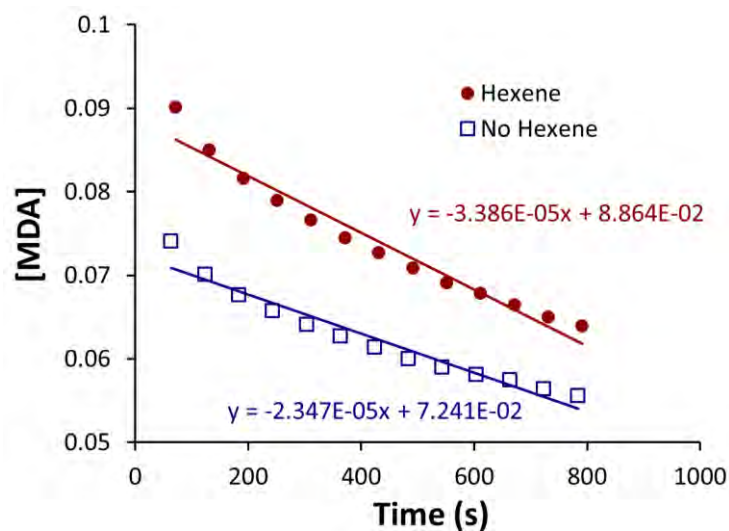
Figure 2.17: Initial rate data for MDA reactions in the presence and absence hexene: second trial. Conditions: Ir(TTP)CH$_3$ (5.63 × 10^{-7} M) and 1-hexene (0 or 0.671 M) in 4.20 × 10^2 μL CD$_2$Cl$_2$ were treated with [MDA] (0.0874-0.115 M, variation resulted from error) at 273.0 K.
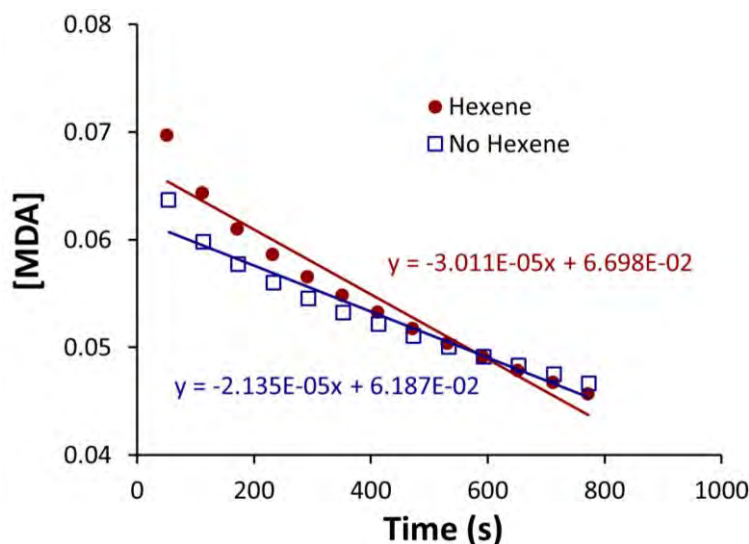
Figure 2.18: Initial rate data for MDA reactions in the presence and absence hexene: third trial. Conditions: Ir(TTP)CH$_3$ (5.63 × 10^{-7} M) and 1-hexene (0 or 0.671 M) in 4.20 × 10^2 μL CD$_2$Cl$_2$ were treated with [MDA] (0.0874-0.115 M, variation resulted from error) at 273.0 K.

The initial rate was determined using data points from the first 500 seconds of the reaction. The concentration of MDA varied due to volatilization of the stock solution. Although the concentration of MDA has a first-order effect on the reaction rate, the error due to variations in the MDA concentration could not account for the observed rate enhancement.

Olefin Binding Studies

Ir(TTP)CH$_3$ (38.0 nmol from a 3.83 $\times$ 10^{-3} M stock solution of Ir(TTP)CH$_3$) was dissolved in CH$_2$Cl$_2$ (2.0 mL). First, a spectrum of Ir(TTP)CH$_3$ was obtained. Then, the sample was charged with 0.5 mL of either styrene (4.4 $\times$ 10^6 nmol) or 1-hexene (4.0 $\times$ 10^6 nmol). Shifts in the Soret band were monitored. For styrene, the Soret shifted from 406 to 415 nm. 1-Hexene shifted the Soret from 407 to 410 nm. In essence, both olefins coordinate to Ir(TTP)CH$_3$ to some extent, but styrene binds more strongly. It should be noted that the ratio for olefin to Ir(TTP)CH$_3$ under these conditions is (1.1 $\times$ 10^5 : 1). Under cyclopropanation conditions, the olefin to catalyst ratio was (1.2 $\times$ 10^6 : 1).
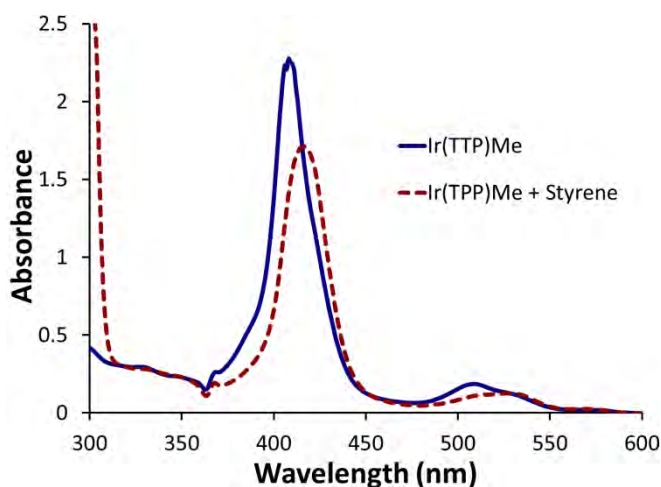
Figure 2.19: Styrene binding to Ir(TTP)CH$_3$.
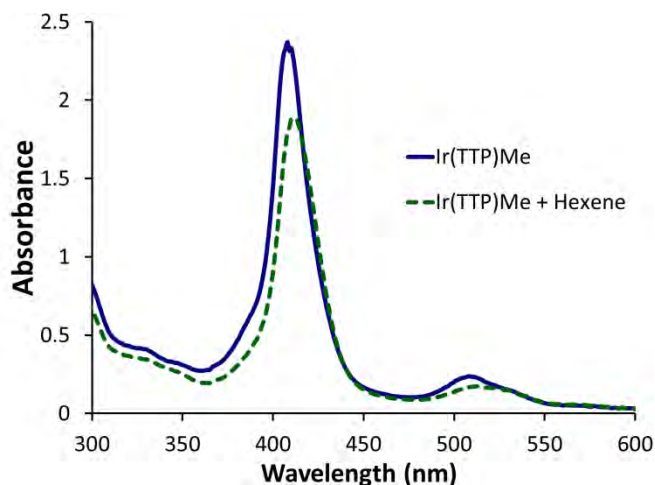
Figure 2.20: Hexene binding to Ir(TTP)CH$_3$.

Characterization Data
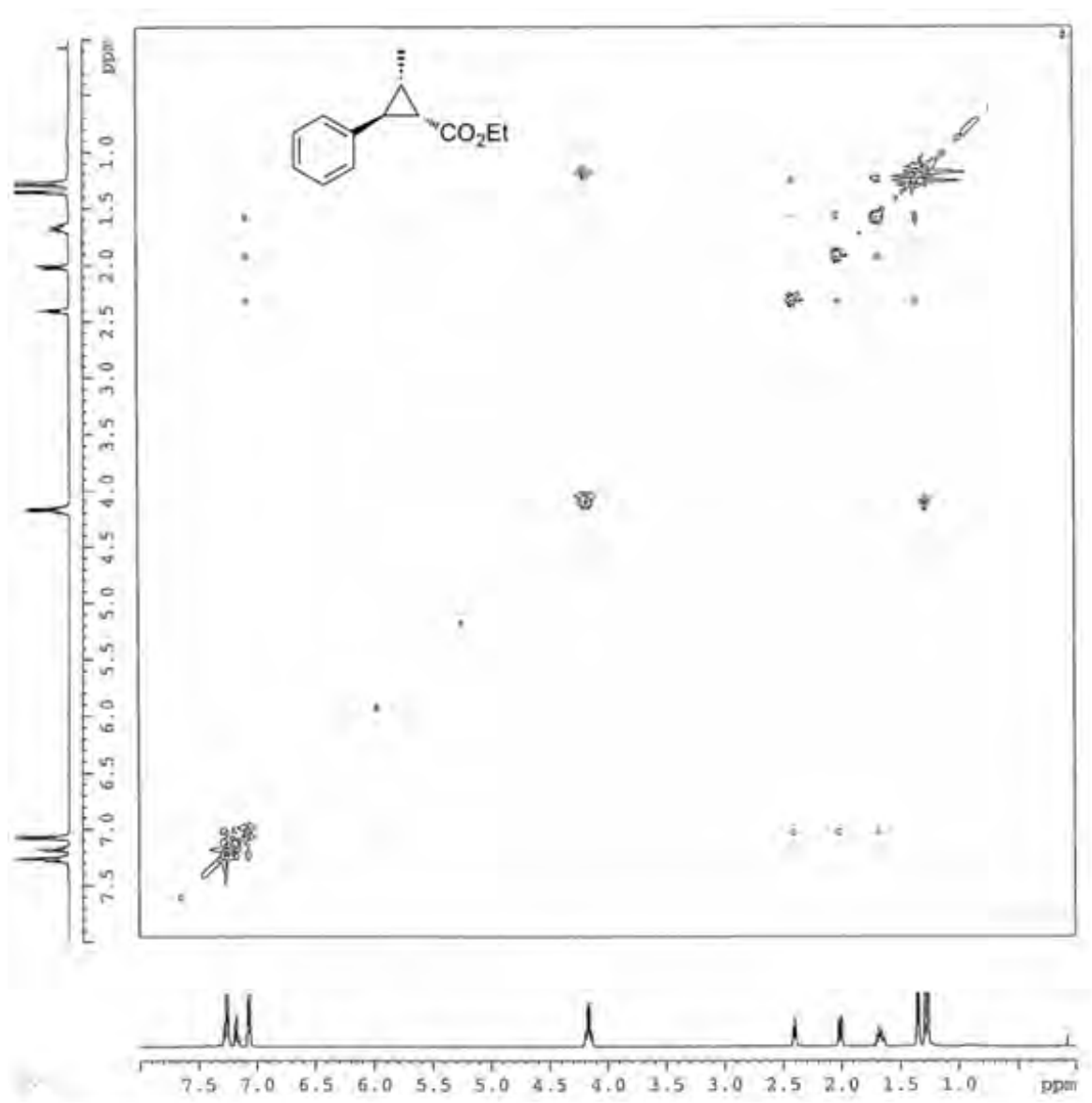
Figure 2.21: NOESY spectrum for ethyl 2-methyl-3-phenylcyclopropanecarboxylate.

Crystal Data

Table 2.5: Crystal data and structure refinement for complexes **3** and **6**.

	Complex **3**	Complex **6**
empirical formula	$C_{51}H_{45}ClIrN_5 \cdot 2CH_2Cl_2$	$C_{50}H_{36}IrN_5OS$
formula weight	1125.42	947.10
temperature	173(2) K	153(2) K
wavelength	0.71073 Å	0.71073 Å
cryst. syst., space group	monoclinic, P 1 21/c 1	monoclinic, P 1 21 1
unit cell dimensions	a = 13.0353(11) Å b = 15.4171(13) Å c = 24.578(2) Å α = 90° β = 102.0610(10)° γ = 90°	a = 9.9086(11) Å b = 9.2532(10) Å c = 22.278(2) Å α = 90° β = 95.895(2)° γ = 90°
volume	4830.3(7) Å^3	2031.8(4) Å^3
Z, calculated density	4, 1.548 Mg/m^3	2, 1.548 Mg/m^3
absorption coefficient	3.083 mm^{-1}	3.382 mm^{-1}
F(000)	2256	944
crystal size	0.32 x 0.32 x 0.25 mm^3	0.18 x 0.18 x 0.12 mm
θ range for data collection	1.57 to 29.50°	0.92 to 28.93°
limiting indices	$-18 \leq h \leq 18$ $-21 \leq k \leq 21$ $-34 \leq l \leq 33$	$-13 \leq h \leq 13$ $-12 \leq k \leq 12$ $-29 \leq l \leq 29$
reflections collected/unique	51968/13362 [R(int) = 0.0256]	21076/10026 [R(int) = 0.0438]
completeness to θmax	100.0 %	99.4 %
absorption correction	multi-scan	multi-scan
max and min transmission	0.5128 and 0.4387	0.6870 and 0.5812
data/restraints/parameters	13362/0/584	10026/17/516
goodness-of-fit on F^2	1.080	1.126
final R indices [I > 2σ(I)]	R1 = 0.0240 wR2 = 0.0606	R1 = 0.0764 wR2 = 0.1633
R indices (all data)	R1 = 0.0303 wR2 = 0.0645	R1 = 0.0820 wR2 = 0.1681
largest diff. peak and hole	1.218 and -1.182 e Å^{-3}	6.415 and -5.993 e Å^{-3}

Table 2.6: Crystal data and structure refinement for complexes **4** and **5**.

	Complex **4**	Complex **5**
empirical formula	$C_{49}H_{36}BrIrN_4O$	$C_{49}H_{36}IIrN_4O$
formula weight	968.93	1015.92
temperature	173(2) K	173(2) K
wavelength	0.71073 Å	0.71073 Å
cryst. syst., space group	tetragonal, I 4/m	tetragonal, I 4/m
unit cell dimensions	a = 14.6430(7) Å b = 14.6430(7) Å c = 9.6955(5) Å α = 90° β = 90° γ = 90°	a = 14.6955(5) Å b = 14.6955(5) Å c = 9.7922(4) Å α = 90° β = 90° γ = 90°
volume	2078.88(18) Å^3	2114.70(13) Å^3
Z, calculated density	2, 1.548 Mg/m^3	2, 1.595 Mg/m^3
absorption coefficient	4.213 mm^{-1}	3.927 mm^{-1}
F(000)	956	992
crystal size	0.23 x 0.23 x 0.11 mm^3	0.25 x 0.23 x 0.14 mm^3
θ range for data collection	2.78 to 30.48°	1.96 to 30.56°
limiting indices	$-20 \leq h \leq 20$ $-20 \leq k \leq 2$ $-13 \leq l \leq 13$	$-20 \leq h \leq 20$ $-20 \leq k \leq 20$ $-13 \leq l \leq 13$
reflections collected/unique	11561/1653 [R(int) = 0.0369]	12040/1685 [R(int) = 0.0330]
completeness to θmax	98.4 %	98.5 %
absorption correction	multi-scan	multi-scan
max and min transmission	0.6543 and 0.4441	0.6093 and 0.4401
data/restraints/parameters	1653/3/81	1685/3/81
goodness-of-fit on F^2	1.154	1.346
final R indices [I > 2σ(I)]	R1 = 0.0282 wR2 = 0.0760	R1 = 0.0471 wR2 = 0.1362
R indices (all data)	R1 = 0.0282 wR2 = 0.0760	R1 = 0.0477 wR2 = 0.1366
largest diff. peak and hole	1.833 and -3.945 e Å^{-3}	2.045 and -5.037 e Å^{-3}

Table 2.7: Selected distances and angles for complexes 3 and 6.

Complex **3**		Complex **6**	
Ir(1)–Cl(1)	2.355(1)	Ir(1)–N(5)	1.95(1)
Ir(1)–N(5)	2.174(2)	N(5)–C(50)	1.19(2)
Ir(1)–N(1)	2.031(2)	C(50)–S(1)	1.61(2)
Ir(1)–N(2)	2.040(2)	Ir(1)–C(49)	1.91(1)
Ir(1)–N(3)	2.034(2)	C(49)–O(1)	1.14(2)
Ir(1)–N(4)	2.036(2)	Ir(1)–N(1)	2.032(9)
N(5)–C(49)	1.461(4)	Ir(1)–N(2)	2.031(9)
N(5)–C(50)	1.489(3)	Ir(1)–N(3)	2.076(12)
N(5)–C(51)	1.486(4)	Ir(1)–N(4)	2.068(9)
Ir(1) out of plane	0.060[a]	Ir(1) out of plane	0.047[b]
N(1)–Ir(1)–Cl(1)	87.01(5)	N(1)–Ir(1)–N(5)	93.7(4)
N(2)–Ir(1)–Cl(1)	89.64(6)	N(2)–Ir(1)–N(5)	90.9(4)
N(3)–Ir(1)–Cl(1)	90.61(6)	N(3)–Ir(1)–N(5)	85.2(4)
N(4)–Ir(1)–Cl(1)	88.66(5)	N(4)–Ir(1)–N(5)	87.4(4)
N(1)–Ir(1)–N(5)	92.06(8)	N(1)–Ir(1)–C(49)	90.2(5)
N(2)–Ir(1)–N(5)	90.64(7)	N(2)–Ir(1)–C(49)	90.4(4)
N(3)–Ir(1)–N(5)	90.32(8)	N(3)–Ir(1)–C(49)	90.8(5)
N(4)–Ir(1)–N(5)	91.07(7)	N(4)–Ir(1)–C(49)	91.2(4)
N(1)–Ir(1)–N(3)	177.60(8)	N(1)–Ir(1)–N(3)	178.7(4)
N(2)–Ir(1)–N(4)	178.26(7)	N(2)–Ir(1)–N(4)	178.0(4)
Cl(1)–Ir(1)–N(5)	179.03(5)	C(49)–Ir(1)–N(5)	175.8(6)
Ir(1)–N(5)–C(49)	112.7(2)	Ir(1)–C(49)–O(1)	178(1)
Ir(1)–N(5)–C(50)	112.6(2)	Ir(1)–N(5)–C(50)	151(1)
Ir(1)–N(5)–C(51)	112.2(2)	N(5)–C(50)–S(1)	179(1)
C(49)–N(5)–C(50)	106.0(2)		
C(49)–N(5)–C(51)	106.1(2)		
C(50)–N(5)–C(51)	106.9(2)		

a) Toward N(5). b) Toward C(49).

Table 2.8: Selected distances and angles for complexes 4 and 5.

Complex **4**		Complex **5**	
Ir(1)–Br(1)[a]	2.409(2)	Ir(1)–I(5)[a]	2.491(2)
Ir(1)–C(11)[a]	1.855(3)	Ir(1)–C(11)[a]	1.852(2)
C(11)–O(11)[a]	1.143(3)	C(11)–O(11)[a]	1.141(2)
Ir(1)–N(1)	2.047(4)	Ir(1)–N(1)	2.048(7)
Br(1)–Ir(1)–C(11)	180	I(1)–Ir(1)–C(11)	180
N(1)–Ir(1)–N(1A)	90	N(1)–Ir(1)–N(1A)	90

a) Due to axial ligand disorder, these lengths were approximated.

CHAPTER 3. C–H INSERTION CATALYZED BY TETRATOLYLPORPHYRINATO METHYLIRIDIUM VIA A METAL-CARBENE INTERMEDIATE

Bernie J. Anding, Jakoah Brgoch, Gordon J. Miller, and L. Keith Woo

Abstract

C–H insertion reactions between different substrates and diazo reagents were catalyzed by tetratolylporphyrinato methyliridium (Ir(TTP)CH$_3$). The highest yields were achieved for reactions between the bulky diazo reagent methyl 2-phenyldiazoacetate (MPDA) and substrates containing electron rich C–H bonds. An intermediate metalloporphyrin complex was identified as a metal-carbene complex, Ir(TTP)(=C[Ph]CO$_2$CH$_3$)(CH$_3$) (**12**), using ^{1}H NMR and UV/vis absorption spectroscopy. The presence of **12** was further supported by computationally modeling the absorption spectra with time-dependent DFT (TD-DFT) (6-31G(d,p)/SBKJC basis set, PBE0 functional). Kinetic studies for C–H insertion reactions using different substrates showed substantial differences in the rate of MPDA consumption, suggesting that carbene transfer is rate-limiting. Furthermore, primary kinetic isotope effects of 3.7 ± 0.3 and 2.7 ± 0.4 were measured using toluene and cyclohexane, respectively. These data are consistent with a mechanism that involves direct C–H insertion rather than a radical rebound pathway.

Introduction

Selective functionalization of unactivated carbon-hydrogen bonds is still a great challenge in synthetic chemistry. Insertion of carbene fragments, generated from diazo reagents, into C–H bonds using transition metal catalysts provides a promising, atom-

economical method to accomplish this goal. High selectivities were found using Cu, Ni, and Rh catalysts for intramolecular C−H insertion reactions.[1,2] However, general and selective catalysts for intermolecular insertions are rare. Among the promising candidates, rhodium(III) porphyrin catalysts are particularly appealing because they have demonstrated unique selectivity for intermolecular carbene insertion into the primary C−H bonds of simple aliphatic compounds.[3] The most selective catalyst utilized the bulky tetra(2,4,6-triphenylphenyl)porphyrin (TTPPP).[4] In the presence of Rh(TTPPP)I, the reaction between octane and methyl 2-phenyldiazoacetate (MPDA) generated insertion products in 55% yield, with primary insertion favored over secondary insertion in a ratio of 10.5:1. Recently, intermolecular C−H insertion was also accomplished in high yield and enantioselectivity using iridium(III) complexes with chiral N,N'-bis(salicylidene)ethylenediiminato (salen) and D_4-symmetric Halterman porphyrin ligands.[5,6] At low temperatures, the Ir(III) complexes catalyzed the insertion of alkyl and aryldiazoacetates into the C−H bonds of THF and cyclohexadiene in good yields and with 81 − 99% ee values. These promising results prompted us to explore further the scope and mechanism for C−H insertion catalyzed by the iridium(III) porphyrin complex, (5,10,15,20-tetratolylporphyrinato)methyliridium (Ir(TTP)CH$_3$).

Results and Discussion

Optimization studies were carried out in neat cyclohexane with 1.0 mol% Ir(TTP)CH$_3$. Initial reactions with ethyl diazoacetate (EDA) failed to generate the desired insertion product, **9a**. Instead, the only observed products resulted from dimerization of the diazo reagent to afford diethyl fumarate and diethyl maleate, **10** (Table 3.1). Attempts to decrease dimerization by lowering reaction temperature failed, which was due in part to the low solubility of Ir(TTP)CH$_3$ in cyclohexane. Changing the diazo reagent to MPDA, which is more resistant to dimerization, afforded C−H insertion products in low yields at room temperature. The major product of this reaction, azine **11**, resulted from MPDA dimerization. The structure of the Z,Z-isomer of **11** was verified by an analysis of single crystal X-Ray diffraction data with metrical parameters that matched published molecular structures.[7,8] High yields of **9b** were achieved using elevated temperatures and dropwise

addition of MPDA. Increasing the catalyst loading to 5.0 mol% also significantly increased the yield of product **9b**, but such a high catalyst loading is not practical given the cost of Ir(TTP)CH$_3$. Attempts to catalyze C–H insertion with Ir(TTP)Cl(CO) under these conditions yielded trace amounts of **9b** and incomplete MPDA conversion.

Table 3.1: Optimization of cyclohexane C–H insertion using Ir(TTP)CH$_3$.[a]

EDA : R$_1$ = H, R$_2$ = Et   **9a:** R$_1$ = H, R$_2$ = Et
MPDA : R$_1$ = Ph, R$_2$ = Me   **9b:** R$_1$ = Ph, R$_2$ = Me   **10**   **11**

Diazo Reagent	Temperature (°C)	Yield **9** (%)[e]	Yield dimers (%)[f]
EDA	0	0	100
MPDA[b]	0	trace	31
MPDA	80	28	68
MPDA[c]	80	74	14
MPDA[c,d]	80	94	3

[a] Conditions: Ir(TTP)CH$_3$ (1.0 mol%) and diazo reagent (0.30 mmol) in cyclohexane (4.5 mL). [b] Unreacted MPDA remained (24% determined by NMR). [c] Dropwise addition of MPDA. [d] Using 5.0 mol% catalyst. [e] Isolated yields. [f] Determined by NMR.

The optimized method was extended to several other substrates (Table 3.2). Treating Ir(TTP)CH$_3$ with MPDA in refluxing pentane afforded azine **11** in nearly quantitative yields. With the higher boiling octane, C–H insertion products were isolated in 37% yield. Insertion occurred preferentially into secondary (C$_2$ and C$_3$, 18%) carbons, but a considerable amount of primary insertion (7%) was also observed. Although the selectivity was modest, Ir(TTP)CH$_3$ was more selective for primary insertion than that for the previously reported Rh(TTP)I.[9] Extending this method to toluene and cyclohexadiene gave good yields of the products corresponding to benzylic and allylic C–H insertion, respectively. Products corresponding to vinyl or aryl C–H insertion were not detected. Furthermore, unlike reactions with Fe(TPP)Cl, there were no signs of competitive cyclopropanation or Büchner additions.[10] THF was also a suitable substrate for C–H insertion. In this case, the products corresponding to α-C–H insertion were isolated in 75% yield with a moderate selectivity for the *anti*-isomer. No β-insertion products or ring-opened ethers were identified. In all cases,

as the reaction temperature was decreased, yields of the insertion products decreased, the formation of azine **11** increased, and catalyst decomposition was more evident. This effect was more pronounced with octane and toluene than with THF and cyclohexadiene. Additionally, trace water contamination, specifically with THF, generated considerable amounts of the competitive O–H insertion product, methyl 2-hydroxy-2-phenylacetate.

Table 3.2: C–H insertion of various substrates using MPDA and Ir(TTP)CH$_3$.[a]

Substrate	Major Product	Yield (%)[b]	Selectivity
	azine **11**	trace	n/a
		37	1 : 2.5 : 1.6[d]
		63	n/a
		56 (76)[c]	n/a
		75	3.8 : 1[e]

[a] Conditions: A solution of MPDA (0.12 mmol) and substrate (1.0 mL) was added dropwise to a refluxing solution of Ir(TTP)CH$_3$ (1.0 mol%) and substrate (4.5 mL) over the course of 2 hours. [b] Isolated yields. [c] Yield determined by NMR. [d] C$_1$:C$_2$+C$_3$:C$_4$, normalized by the number of hydrogen atoms. [e] *anti*:*syn*.

Addition of MPDA in the above reactions, specifically those with cyclohexane, octane, and toluene, resulted in a temporary color change from orange to greenish brown, indicating the presence of an observable intermediate. This intermediate was investigated by UV/vis absorption spectroscopy for the reaction between a cyclohexane solution of Ir(TTP)CH$_3$ and MPDA over three consecutive additions of the diazo reagent. The Soret band of Ir(TTP)CH$_3$ was observed at 404 nm. After the first addition of MPDA (5.7 equivalents), the peak at 404

nm was immediately consumed and three new bands were formed at 375, 417, and 443 nm (Figure 3.1). The intermediate bands endured for approximately five minutes before reverting back to the single Soret peak of Ir(TTP)CH$_3$. The conversion between Ir(TTP)CH$_3$ and intermediate bands occurred too rapidly to observe isosbestic behavior. Furthermore, catalyst solubility seemed to increase throughout the reaction. Addition of a second portion of MPDA resulted in similar behavior, except that the band at 417 nm was larger throughout the reaction relative to other peaks (Figure 3.11; Appendix B). The resulting equilibrated solution displayed a significant shoulder at 417 nm, which seemed to form at the expense of Ir(TTP)CH$_3$. Finally, with the third addition of MPDA, the band at 417 nm was dominant and persisted indefinitely (Figure 3.12; Appendix B). This resulting metalloporphyrin was unreactive with further additions of MPDA and prolonged heating, indicating it is a product of catalyst decomposition. The catalyst TON was between 11.4 and 17.1 under these conditions.
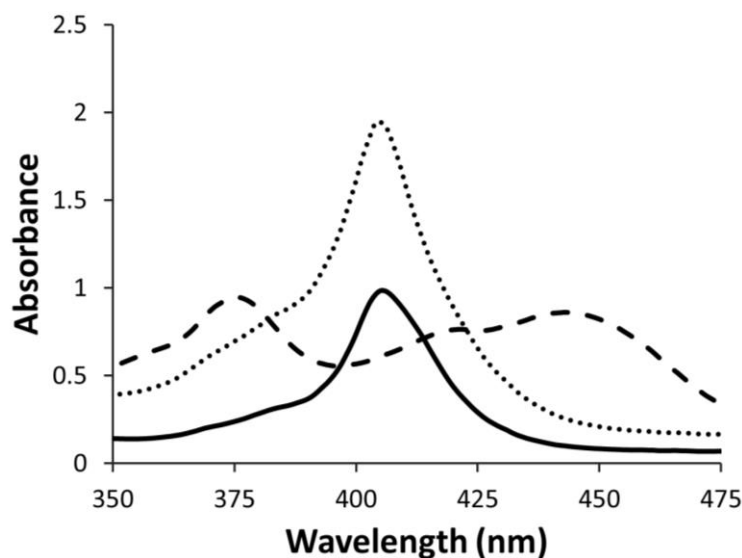
Figure 3.1: Absorption spectra for the treatment of Ir(TTP)CH$_3$ with 5.6 equivalents of MPDA. The selected spectra depict Ir(TTP)CH$_3$ before MPDA addition (solid), the intermediate at 210 seconds after MPDA addition (dashed), and the return to Ir(TTP)CH$_3$ 300 seconds after MPDA addition (dotted).

In analogy to the mechanism proposed for iridium porphyrin-catalyzed cyclopropanation,[11] the observed intermediate was believed to be the metal-carbene complex, Ir(TTP)(=C[Ph]CO$_2$CH$_3$)(CH$_3$), **12**. To validate that the changes observed in the absorption

spectra arose from the formation of a carbene complex, time dependent density functional theory (TD-DFT) was used to calculate the absorption spectra for both Ir(TTP)CH$_3$ and **12**. All calculations were carried out using *GAMESS*[12-15] with a mixed basis set, including 6-31G(d,p) for the main group elements, the SBJKC effective core potential for the iridium atom,[16-18] and the hybrid functional PBE0,[19,20] which has been shown to reasonably represent the electronic structure of porphyrin systems.[21,22] Accordingly, structural optimizations via DFT calculations provided reasonable ground-state geometries (optimized structures and selected metrical parameters provided in Appendix B). For example, the calculated geometrical parameters for Ir(TTP)CH$_3$ are consistent with the reported crystallographic structure of Ir(TTP)CH$_3$•H$_2$O.[23] Specifically, the calculated Ir–CH$_3$ bond length, 2.037 Å, agrees with the reported distance of 2.059(11) Å. Upon coordination of the carbene ligand, the Ir–CH$_3$ bond in **12** lengthened to 2.123 Å due to the *trans* influence exerted by the carbene ligand.[24] The calculated Ir–C carbene bond length was 2.045 Å, which is slightly long compared to the metal-carbene complexes of group 8 metalloporphyrins. Previous studies of similar systems report M–C bond lengths ranging from 1.767(3) to 2.035(2) Å.[24-26] Considering the high carbene transfer reactivity of iridium porphyrin complexes compared to that of group 8 metal complexes,[5,11] a slightly elongated Ir–C carbene bond is reasonable. Coordination of the carbene ligand also caused noticeable distortion to the porphyrin core. The out-of-plane displacement (D_{oop}) and in-plane displacement (D_{ip}) were calculated by normal-coordinate structure decomposition (NSD) analysis (Tables 3.4 and 3.5; Appendix B).[27,28] Results for complex **12** showed D_{oop} = 0.5154 and D_{ip} = 0.1430. The most prominent distortions were ruffling (B_{1u}) and doming (A_{1g}) out-of-plane displacements. Deformations were considerably less significant for Ir(TTP)CH$_3$, which had D_{oop} = 0.1071 and D_{ip} = 0.2598. In general, the distortions exhibited by Ir(TTP)CH$_3$ and **12** are relatively small compared to other metalloporphyrin systems.[29]

The calculated electronic spectra of Ir(TTP)CH$_3$ and **12** are shown in Figure 3.2. The main absorption band of Ir(TTP)CH$_3$, arising from a π to π^* transition, occurred as one large peak centered at 371 nm, which was consistent with the experimentally observed transition at 404 nm. The calculated spectrum of **12** showed transitions at 357, 366, and 427 nm. Similar

spectral changes were reported for other 6-coordinate alkyl Ir porphyrin complexes with neutral donor ligands *trans* to the alkyl group.[30] The resolution of the experimental spectrum likely coalesces the bands at 357 and 366 nm into one peak. Thus, the calculated spectrum is in good agreement with the observed peaks of the intermediate complex at 375 and 445 nm. Overall, TD-DFT modeling of Ir(TTP)CH$_3$ and **12** adequately reproduced the observed absorption spectra, providing additional evidence in support of a metal-carbene intermediate.
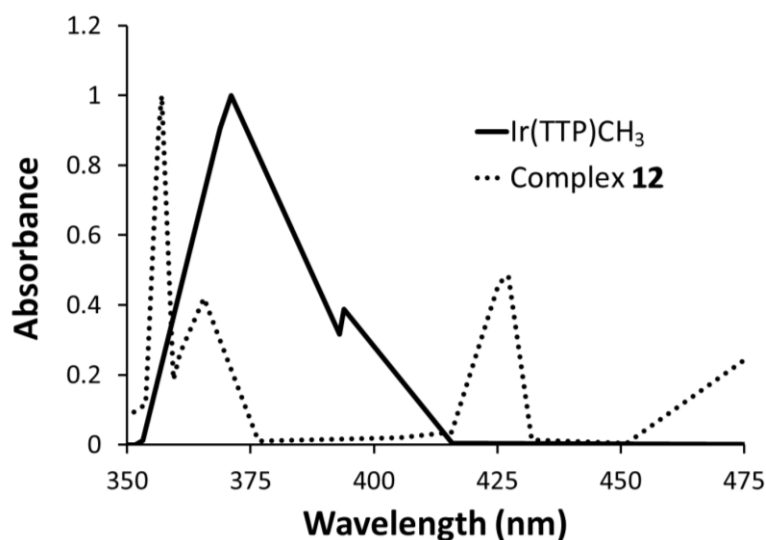
Figure 3.2: TD-DFT absorption spectra for Ir(TTP)CH$_3$ (bold) and **12** (dotted).

The intermediate carbene complex was also investigated by ^{1}H NMR. Addition of MPDA (*ca.* 5 equivalents) to a solution of Ir(TTP)CH$_3$ in benzene-d_6 resulted in the complete formation of a new metalloporphyrin complex as indicated by the clean singlets for the porphyrin β-pyrrole and Ir−CH$_3$ protons at 8.83 ppm and -4.80 ppm, respectively (Figure 3.14; Appendix B). The Ir−CH$_3$ protons were shifted significantly downfield from those of Ir(TTP)CH$_3$ (-5.92 ppm). Furthermore, the appearance of new phenyl proton signals [6.55 (t, *J* = 7.6 Hz, 1H), 5.92 (t, *J* = 7.6 Hz, 2H), 3.93 (d, *J* = 7.6 Hz, 2H)] and a new methyl singlet at 2.19 ppm (3H) suggested that the carbene fragment derived from MPDA was coordinated to iridium; the carbene signals were strongly shifted upfield due to the porphyrin ring current effect. After 20 hours, the major remaining porphyrin species was Ir(TTP)CH$_3$. MPDA had been completely consumed, forming azine **11** as the predominant product. Despite numerous efforts, including attempts with chromium(III) acetylacetonate, a signal corresponding to the

putative carbene carbon of the intermediate was not located by ^{13}C NMR. Difficulty locating the carbene signal for MPDA is documented,[31] and coupling to iridium, a spin active nuclei, would further reduce the carbene signal-to-noise ratio. Unfortunately, numerous attempts to isolate the intermediate, including lyophilization from benzene, also failed.

A kinetic study of the reaction between 4.9 equivalents of MPDA and 1.0 equivalent of Ir(TTP)CH$_3$ at 300.0 K revealed first-order consumption of MPDA with a rate constant, $k = 8.0 \pm 0.3$ s^{-1}. In the presence of up to 55.3 equivalents of toluene or cyclohexane, the rate of MPDA consumption was unchanged, and the major product was azine **11**. Apparently, a second equivalent of MPDA was more effective at trapping the intermediate than toluene or cyclohexane. In contrast, reactions run in the presence of 11.1 equivalents of cyclohexadiene afforded primarily C−H insertion products and completely consumed MPDA in less than 60 seconds, demonstrating that the rate of MPDA consumption is dependent on the nature of the substrate.

The above data supports a catalytic cycle involving a metal-carbene intermediate (Figure 3.3), analogous to related C−H insertion and cyclopropanation systems.[2,11,24,25,32] Coordination of MPDA to Ir(TTP)CH$_3$ initially generates a diazonium complex, which forms metal-carbene complex **12** after loss of dinitrogen. While the observed intermediate may conceivably be the diazonium complex,[33] UV/vis absorption spectroscopy, TD-DFT, and kinetic studies all support carbene complex **12** as the observed intermediate. Furthermore, an N≡N stretch corresponding to a diazonium intermediate was not observed by IR spectroscopy. After carbene formation, subsequent nucleophilic attack at the carbene carbon with a C−H bond results in product formation. Insight into the mechanism of carbene transfer was gained from kinetic isotope studies. Separate competition reactions between toluene/toluene-d_8 and cyclohexane/cyclohexane-d_{12} revealed kinetic isotope effects (KIE) of 3.7 ± 0.3 and 2.7 ± 0.4, respectively. These values support a mechanism involving direct C−H insertion rather than a radical rebound pathway, which exhibits a larger KIE, typically between 7 and 12.[9] Direct C−H insertion may be most accurately described as a concerted, nonsynchronous hydride transfer and C−C bond formation.[34,35]
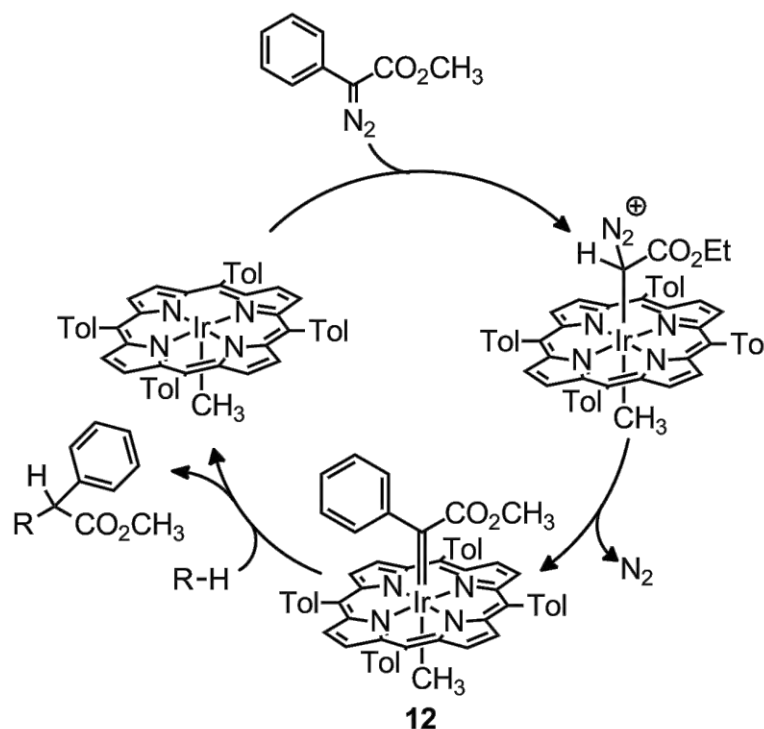
Figure 3.3: Proposed catalytic cycle for C–H Insertion of hydrocarbons using MPDA and Ir(TTP)CH₃.

Conclusions

In summary, C–H insertion catalyzed by Ir(TTP)CH₃ was examined using different substrates and diazo reagents. The highest yields were found using MPDA and substrates with electron rich C–H bonds, such as THF and cyclohexadiene. Mechanistic studies and spectroscopic examination of the reaction intermediate suggests that C–H insertion proceeds through a metal-carbene intermediate and that carbene transfer is the rate-limiting step.

Experimental

General Considerations: All manipulations were performed under a dry nitrogen atmosphere. Most substrates were dried over 4 Å molecular sieves, freeze-pump-thawed, and run through a plug of activated alumina under a glovebox atmosphere. THF was deoxygenated and dried by passage through columns of reduced copper and alumina. Ir(TTP)CH₃ and MPDA were prepared according to previously reported methods.[36-38]

Absorption spectra were collected using a Hewlett-Packard/Agilent Technologies 8453 UV-Vis spectrophotometer. General NMR spectra were collected using Varian VXR 300 MHz and Varian VXR 400 MHz spectrometers and kinetic measurements were done using a Bruker DRX 400 MHz spectrometer. ^{1}H NMR peak positions were referenced against residual proton resonances of deuterated solvents (δ, ppm: CDCl$_3$, 7.26; C$_6$D$_6$, 7.16). Ratios for kinetic isotope data were determined using a Finnegan Magnum GC-MS fitted with a HP-5 column (30m x 0.25μm) and a time-of-flight mass analyzer. Column chromatography was performed using silica gel (40 – 63 μm) purchased from Sorbent Technologies. Characterization data for the C–H insertion products was previously reported.[4,6,39]

Computational Details: The ground-state geometries of Ir(TTP)CH$_3$, MPDA, and **12** were determined without any symmetry constraints using the program *GAMESS*.[12-15] Exchange and correlation were treated by the hybrid density functional PBE0 and included a mixed basis set. All main group elements were calculated with the 6-31G(d,p) basis set while an effective core potential (SBKJC) was utilized for Ir. The electronic absorption spectra were calculated by the time-dependent density functional (TD-DFT) method implemented within the *GAMESS* code. The effects of hexane as a solvent were handled using the polarizable continuum model (PCM).[40-43]

General C–H insertion procedure: A CH$_2$Cl$_2$-stock solution of Ir(TTP)CH$_3$ (216 μL from a 5.34×10^{-3} M stock solution, 1.15 μmol) was transferred to a side-arm, round-bottom flask and taken to dryness under a nitrogen stream. Substrate (4.5 mL) was added and the solution was taken to reflux. Meanwhile, a solution of MPDA (0.115 mmol) and substrate (1.0 mL) was prepared in a dry round-bottom flask. The MPDA solution was added dropwise to the Ir(TTP)CH$_3$ solution over the course of 2 hours using a syringe pump. After MPDA addition and after the color reverted back to orange, volatiles were removed *in vacuo*. Products were isolated by column chromatography on silica gel using hexanes and ethyl acetate (40:1) as the eluent system.

Observation of complex 12 by UV/vis absorption spectroscopy: Ir(TTP)CH$_3$ (0.0768 μmol) from a 3.84×10^{-3} M CH$_2$Cl$_2$-stock solution was taken to dryness in a 1-mm path length cuvette and then dissolved in cyclohexane (0.3 mL). A UV/vis spectrum of the

starting material was collected at this point. Then, MPDA from a cyclohexane-stock solution (0.011 M, 40 µL, 0.44 µmol) was added and a UV/vis spectrum was obtained every 30 seconds until equilibrium was reached (*ca.* 6 minutes). This process was repeated two more times until only an unreactive metalloporphyrin complex, with a Soret peak at 417 nm, remained.

Observation of 12 by ^{1}H NMR spectroscopy: Solid Ir(TTP)CH$_3$ (5.7 mg, 6.5 µmol) was transferred into a medium-walled NMR tube and dissolved in *ca.* 0.5 mL C$_6$D$_6$. The solution was treated with MPDA (3.5 µL, 22.3 µmol); spectra were acquired immediately and after 20 hours. ^{1}H NMR (C$_6$D$_6$): δ 8.83 (s, 8H), 8.14 (d, J = 7.6 Hz, 4H), 7.93 (m, 4H, overlapping with a signal from azine **11**), 7.31 (d, J = 7.6 Hz, 4H), 7.18 (d, J = 7.6 Hz, 4H, obsured by the residual solvent signal), 6.55 (t, J = 7.6 Hz, 1H), 5.92 (t, J = 7.6 Hz, 2H), 3.93 (d, J = 7.6 Hz, 2H), 2.38 (s, 12H), 2.19 (s, 3H), and -4.80 (s, 3H).

Kinetic measurement experiments: A CH$_2$Cl$_2$-stock solution of Ir(TTP)CH$_3$ (400. µL, 4.26×10^{-3} M, 1.70 µmol) was transferred to a medium-walled NMR tube and taken to dryness at 45 °C. In a glovebox, the tube was loaded with triphenylmethane as an internal standard (9.96 µmol), substrate (ranging from 0 to 94 µmol), and diluted to a total volume of 420 µL with C$_6$D$_6$. The tube was fitted with a septum and taken to the NMR spectrometer, where the temperature was equilibrated to 300.0 K. prior to diazo addition. Then, MPDA (8.40 µmol) from a 0.240 M, room-temperature C$_6$D$_6$-stock solution was added and reaction progress was monitored at 60-second intervals.

Procedure for kinetic isotope studies: A CH$_2$Cl$_2$-stock solution of Ir(TTP)CH$_3$ (100 µL from a 3.83×10^{-3} M stock solution, 0.383 µmol) was transferred to a round-bottom flask fitted with a side-arm and taken to dryness under a nitrogen stream. Ir(TTP)CH$_3$ was dissolved in 1.8 mL of a premixed solution of substrate (1.0 mL) and deuterated substrate (1.0 mL), where the substrates are either toluene or cyclohexane. In a separate round-bottom flask, MPDA was dissolved in the remained 0.2 mL of the mixed substrate solution. Then, to a refluxing solution of Ir(TTP)CH$_3$, the MPDA solution was added manually dropwise. After each drop, the color of the solution was allowed to revert back to orange before the

next drop of MPDA solution was added. Once MPDA addition was complete and the color returned to orange, the product mixture was analyzed by GC-MS.

References

1. Diaz-Requejo, M. M.; Perez, P. J. *Chem. Rev.* **2008**, *108*, 3379.

2. Doyle, M. P.; Duffy, R.; Ratnikov, M.; Zhou, L. *Chem. Rev.* **2009**, *110*, 704.

3. Callot, H. J.; Metz, F. *Tetrahedron Lett.* **1982**, *23*, 4321.

4. Thu, H.-Y.; Tong, G. S.-M.; Huang, J.-S.; Chan, S. L.-F.; Deng, Q.-H.; Che, C.-M. *Angew. Chem. Intl. Ed.* **2008**, *47*, 9747.

5. Wang, J.-C.; Xu, Z.-J.; Guo, Z.; Deng, Q.-H.; Zhou, C.-Y.; Wan, X.-L.; Che, C.-M. *Chem. Commun.* **2012**, *48*, 4299.

6. Suematsu, H.; Katsuki, T. *J. Am. Chem. Soc.* **2009**, *131*, 14218.

7. Lai, E. C. K.; Mackay, D.; Taylor, N. J.; Watson, K. N. *Can. J. Chem.* **1988**, *66*, 2839.

8. Glaser, R.; Chen, G. S.; Barnes, C. L. *J. Org. Chem.* **1993**, *58*, 7446.

9. Callot, H. J.; Metz, F. *Nouv. J. Chim.* **1985**, *9*, 167.

10. Mbuvi, H.; Woo, L. *J. Porphyrins Phthalocyanines* **2009**, *13*, 136.

11. Anding, B. J.; Ellern, A.; Woo, L. K. *Organometallics* **2012**, *31*, 3628.

12. Schmidt, M.; Baldridge, K. K.; Boatz, J. A.; Elbert, S. T.; Gordon, M. S.; Jensen, J. H.; Koseki, S.; Matsunaga, N.; Nguyen, K. A. *J. Comput. Chem.* **1993**, *14*, 1347. Computer code GAMESS available at: http://www.msg.ameslab.gov/GAMESS/GAMESS.html.

13. Gordon, M.; Dykstra, C. E. *Advances in electronic structure theory: GAMESS a decade later. Theory and Applications of Computational Chemistry : The First Forty Years*, **2005**.

14. Casida, M. *Comput. Theor. Chem.* **1996**, *4*, 391.

15. Casida, M. In *Recent Advances in Density Functional Methods*; Chong, D. P., Ed.; World Scientific: Singapore, **1995**; Vol. 1.

16. Cundari, T. R.; Stevens, W. J. *J. Chem. Phys.* **1993**, *98*, 5555.

17.   Stevens, W. J.; Krauss, M.; Basch, H.; Jasien, P. G. *Can. J. Chem.* **1992**, *70*, 612.

18.   Stevens, W. J.; Basch, H.; Krauss, M. *J. Chem. Phys.* **1984**, *81*, 6026.

19.   Ernzerhof, M.; Scuseria, G. E. *J. Chem. Phys.* **1999**, *110*, 5029.

20.   Adamo, C.; Barone, V. *J. Chem. Phys.* **1999**, *110*, 6158.

21.   Quartarolo, A.; Lanzo, I.; Sicilia, E.; Russo, N. *Phys. Chem. Chem. Phys.* **2009**, *11*, 4586.

22.   Petit, L.; Quartarolo, A.; Adamo, C.; Russo, N. *J. Phys. Chem. B* **2006**, *110*, 2398.

23.   Song, X.; Chan, K.-S. *J. Chin. Chem. Soc.* **2009**, *56*, 667.

24.   Li, Y.; Huang, J.-S.; Zhou, Z.-Y.; Che, C.-M. *J. Am. Chem. Soc.* **2001**, *123*, 4843.

25.   Li, Y.; Huang, J.-S.; Zhou, Z.-Y.; Che, C.-M.; You, X.-Z. *J. Am. Chem. Soc.* **2002**, *124*, 13185.

26.   Li, Y.; Huang, J. S.; Xu, G. B.; Zhu, N. Y.; Zhou, Z. Y. *Chem. Eur. J.* **2004**, *10*, 3486.

27.   Jentzen, W.; Ma, J.-M.; Shelnutt, J. A. *Biophys. J.* **1988**, *74*, 753.

28.   Sun, L.; Jentzen, W.; Shelnutt, J. A.   The Normal Coordinate Structural Decomposition   Engine. http://jasheln.unm.edu/jasheln/content/nsd/NSDengine/start.htm.

29.   Jentzen, W.; Song, X.-Z.; Shelnutt, J. A. *J. Phys. Chem. B* **1997**, *101*, 1684.

30.   Kadish, K. M.; Cornillon, J. L.; Mitaine, P.; Deng, Y. J.; Korp, J. D. *Inorg. Chem.* **1989**, *28*, 2534.

31.   Tayama, E.; Yanaki, T.; Iwamoto, H.; Hasegawa, E. *Eur. J. Org. Chem.* **2010**, *2010*, 6719.

32.   Bartley, D. W.; Kodadek, T. *J. Am. Chem. Soc.* **1993**, *115*, 1656.

33.   Maxwell, J. L.; Brown, K. C.; Bartley, D. W.; Kodadek, T. *Science* **1992**, *256*, 1544.

34.   Nakamura, E.; Yoshikai, N.; Yamanaka, M. *J. Am. Chem. Soc.* **2002**, *124*, 7181.

35.   Mbuvi, H. M.; Woo, L. K. *Organometallics* **2008**, *27*, 637.

36.   Yeung, S. K.; Chan, K. S. *Organometallics* **2005**, *24*, 6426.

37.   Ogoshi, H.; Setsune, J.; Yoshida, Z. *J. Organomet. Chem.* **1978**, *159*, 317.

38.   Zhao, W.-J.; Yan, M.; Huang, D.; Ji, S.-J. *Tetrahedron* **2005**, *61*, 5585.

39.   Davies, H. M. L.; Hansen, T. *J. Am. Chem. Soc.* **1997**, *119*, 9075.

40.   Tomasi, J.; Mennucci, B.; Cammi, R. *Chem. Rev.* **2005**, *105*, 2999.

41.   Cramer, C. J.; Truhlar, D. G. *Chem. Rev.* **1999**, *99*, 2161.

42.   Tomasi, J.; Persico, M. *Chem. Rev.* **1994**, *94*, 2027.

43.   Miertus, S.; Scrocco, E.; Tomasi, J. *Chem. Phys.* **1981**, *55*, 117.

Appendix B

Computationally Optimized Structures
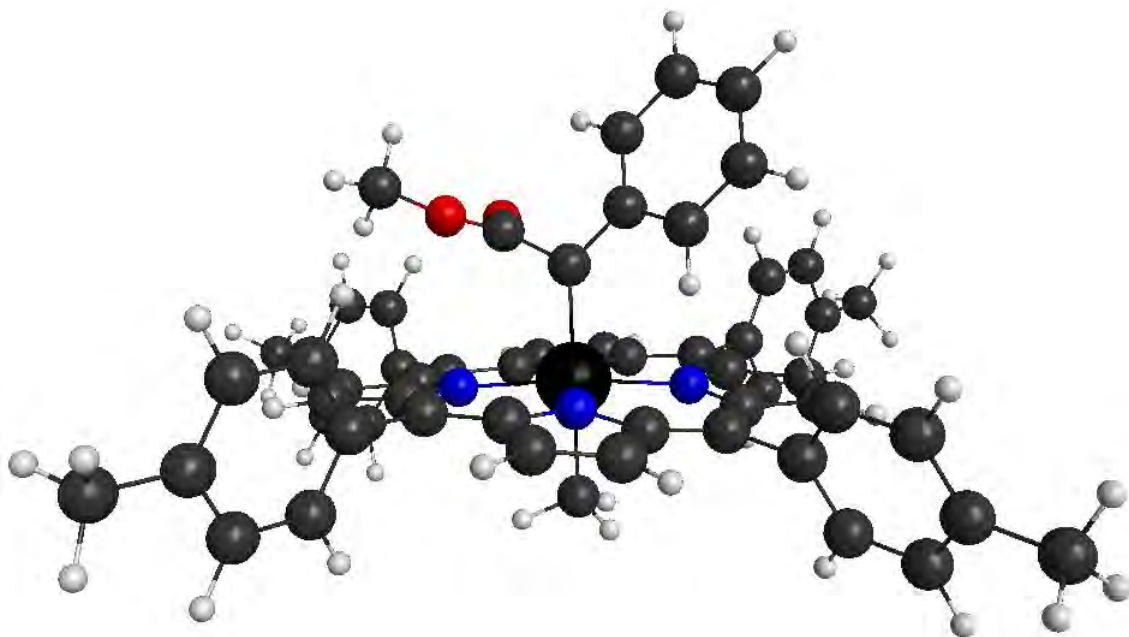
Figure 3.4: The structure of complex **12** as optimized by DFT. Grey sphere = carbon, white sphere = hydrogen, blue sphere = nitrogen, red sphere = oxygen, black sphere = iridium.
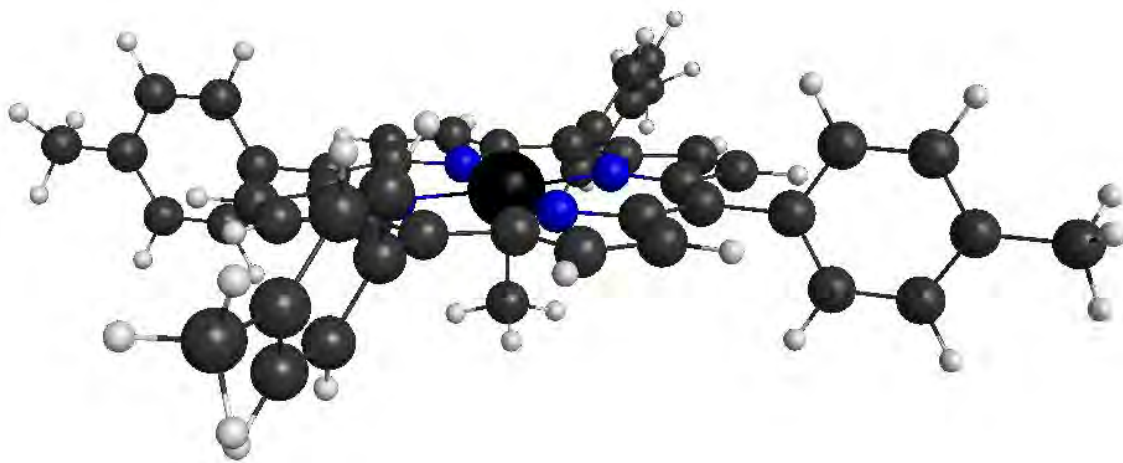
Figure 3.5: The structure of Ir(TTP)CH$_3$ as optimized by DFT. Grey sphere = carbon, white sphere = hydrogen, blue sphere = nitrogen, black sphere = iridium.
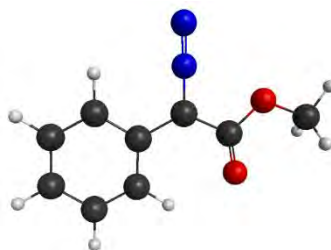
Figure 3.6: The structure of MPDA as optimized by DFT. Grey sphere = carbon, white sphere = hydrogen, blue sphere = nitrogen, red sphere = oxygen.

Table 3.3: Selected bond distances and angles for the optimized structures of MPDA, Ir(TTP)CH$_3$, and complex **12**.

MPDA		Ir(TTP)CH$_3$		Complex **12**	
C−N	1.312 Å	Ir−C(methyl)	2.058 Å	Ir−C(methyl)	2.123 Å
N−N	1.133 Å	Ir−N(pyrrole)	2.045 Å [a]	Ir−C(carbene)	2.045 Å
C−O	1.214 Å	N−Ir−N	89.94°[a]	Ir−N(pyrrole)	2.051 Å [a]
C(Ph)−C−N	117.90°			C−O	1.216 Å
C(O)−C−N	114.81°			C−Ir−C	176.22°
				C(O)−C−Ir	115.24°
				C(Ph)−C−Ir	132.11°
				N−Ir−N	89.55°[a]

a) An average of the four pyrrole moieties.

NSD Data

Table 3.4: Out-of-plane distortion for Ir(TTP)CH$_3$ and complex **12** as determined by NSD analysis from the minimum basis set of core atoms in the porphyrin ring.

	D_{oop}	B_{2u}, *sad*	B_{1u}, *ruf*	A_{2u}, *dom*	$E_g(x)$, *wav(x)*	$E_g(y)$, *wav(y)*	A_{1u}, *prop*
Ir(TTP)CH$_3$	0.1071	-0.0088	0.0818	0.0237	0.0410	0.0496	0.0002
Complex **12**	0.5154	-0.0927	-0.4513	-0.2309	-0.0039	0.0032	0.0072

Table 3.5: In-plane distortion for Ir(TTP)CH$_3$ and complex **12** as determined by NSD analysis from the minimum basis set of core atoms in the porphyrin ring.

	D_{ip}	B_{2g}, *m-str*	B_{1g}, *n-str*	A_{2g}, *rot*	$E_u(x)$, *trn*	$E_u(y)$, *trn*	A_{1g}, *bre*
Ir(TTP)CH$_3$	0.2598	0.0216	0.0014	-0.0007	-0.0009	0.0010	0.2589
Complex **12**	0.1430	-0.0001	0.0118	0.0005	0.0009	-0.0074	0.1423

TD-DFT Data
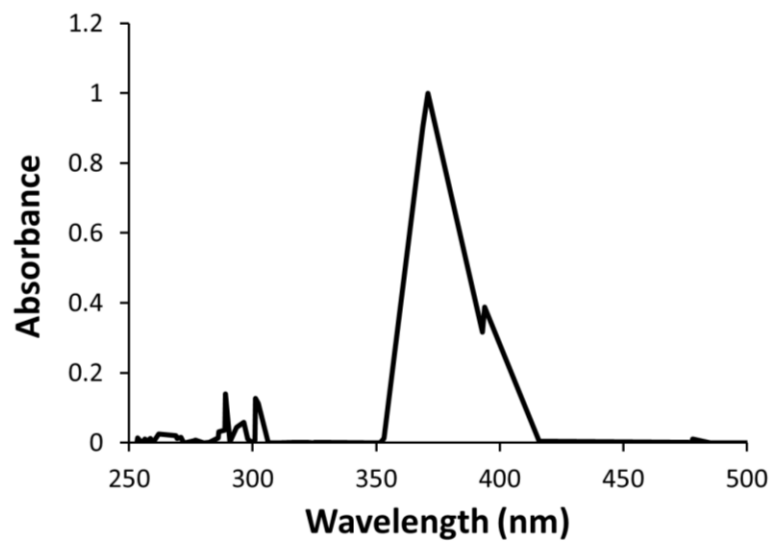
Figure 3.7: TD-DFT absorption spectrum of Ir(TTP)CH$_3$.
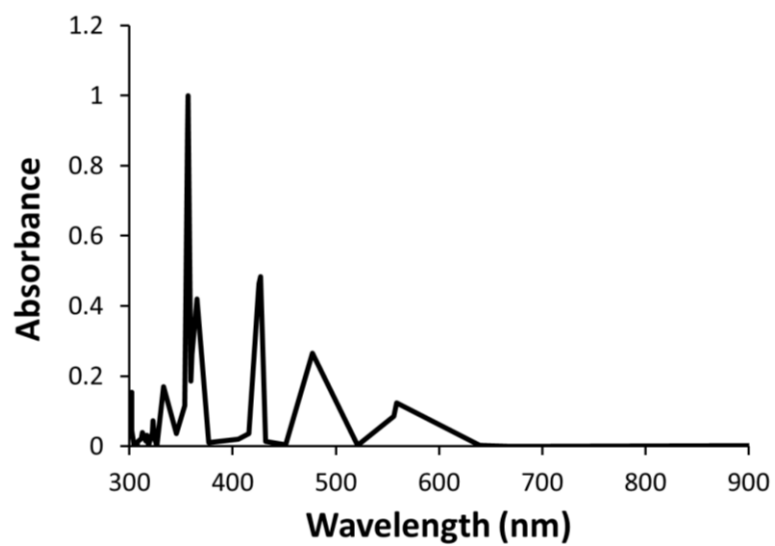
Figure 3.8: TD-DFT absorption spectrum of complex **12**.

Experimental Absorption Spectra
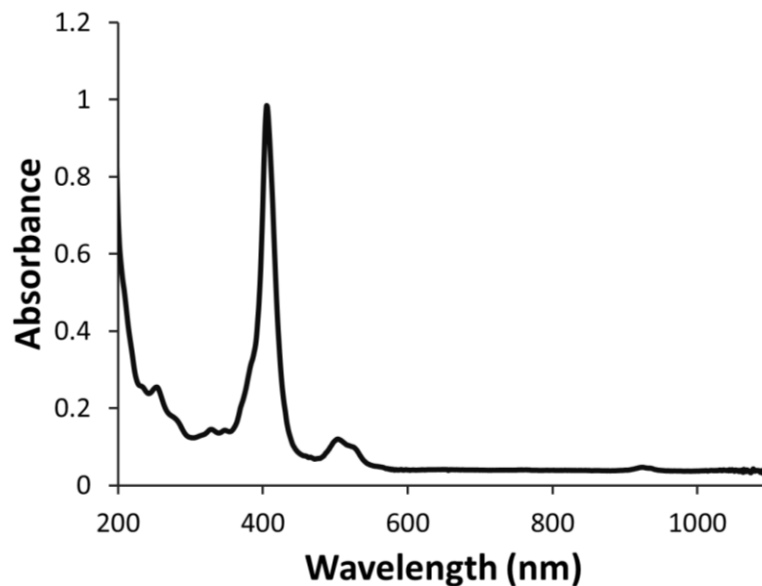
Figure 3.9: The full experimental absorption spectrum of Ir(TTP)CH$_3$ in cyclohexane.
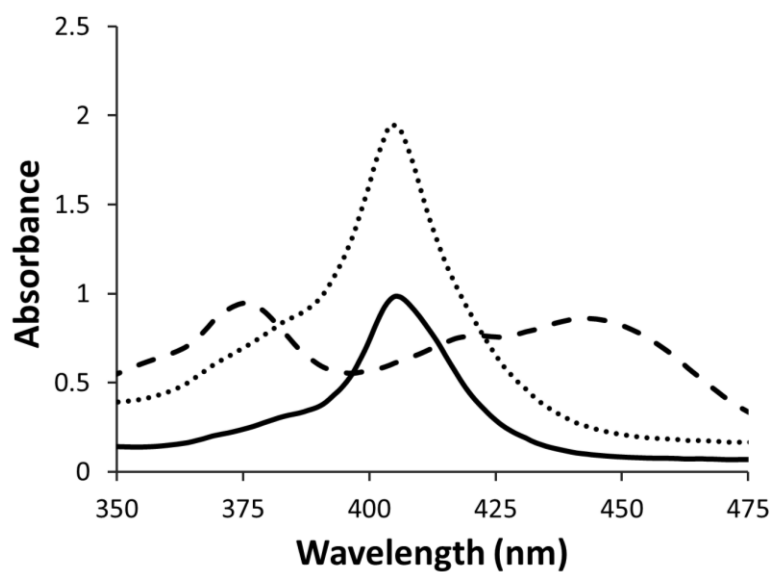
Figure 3.10: Soret region of the absorption spectra during the first addition of MPDA (5.6 equiv.) to Ir(TTP)CH$_3$ in cyclohexane. The selected spectra depict Ir(TTP)CH$_3$ before MPDA addition (solid), the intermediate at 210 seconds after MPDA addition (dashed), and the final persisting solution formed 300 seconds after MPDA addition (dotted).
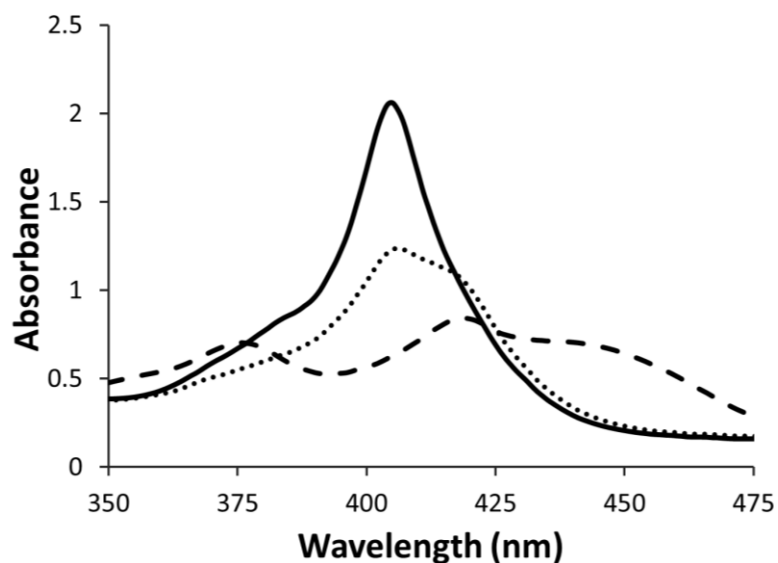
Figure 3.11: Soret region of the absorption spectra during the second addition of MPDA (an additional 5.6 equiv., which gave a total of 11.2 equiv.). The selected spectra depict Ir(TTP)CH$_3$ before MPDA addition (solid), the intermediate at 30 seconds after MPDA addition (dashed), and the final persisting solution formed 330 seconds after MPDA addition (dotted).
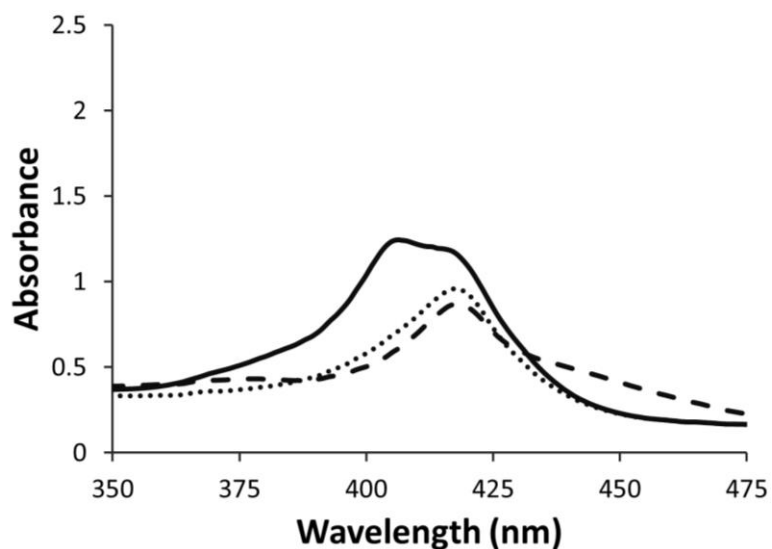
Figure 3.12: Soret region of the absorption spectra during the third addition of MPDA (an additional 5.6 equiv., which gave a total of 16.7 equiv.). The selected spectra depict the initial solution before MPDA addition (solid), the intermediate at 30 seconds after MPDA addition (dashed), and the final persisting solution formed 300 seconds after MPDA addition (dotted).
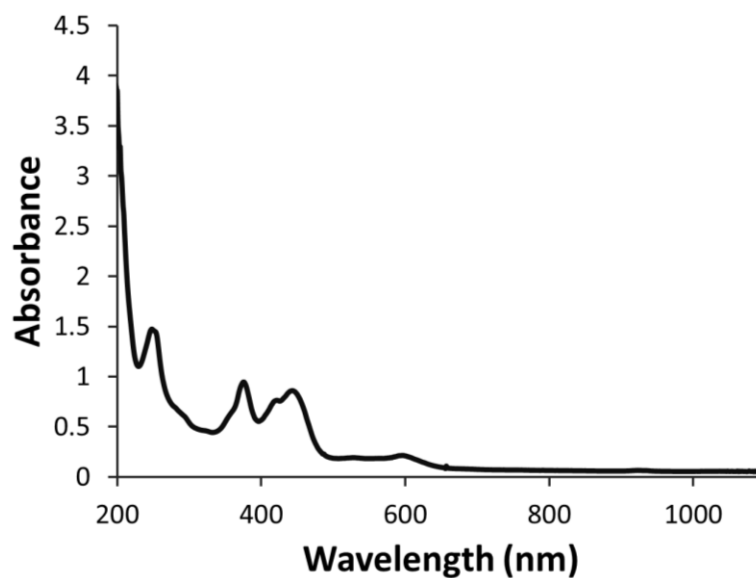
Figure 3.13: The full spectrum of intermediate **12** in cyclohexane. This spectrum was acquired 210 seconds after the first addition of MPDA to Ir(TTP)CH$_3$ in cyclohexane.

Proton NMR Spectrum of Intermediate 12
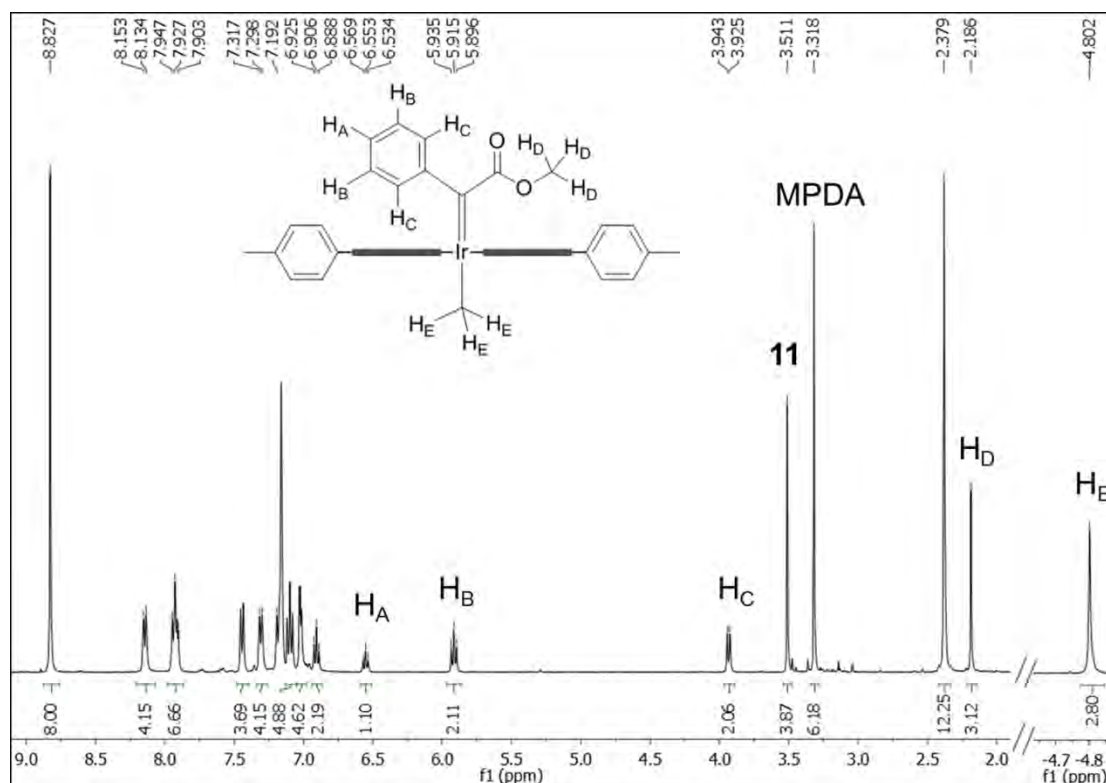
Figure 3.14: ^{1}H NMR spectrum resulting from the reaction between MPDA (3.43 equiv.) and Ir(TTP)CH$_3$. The spectrum was acquired ten minutes after the addition of MPDA.

Kinetics Data
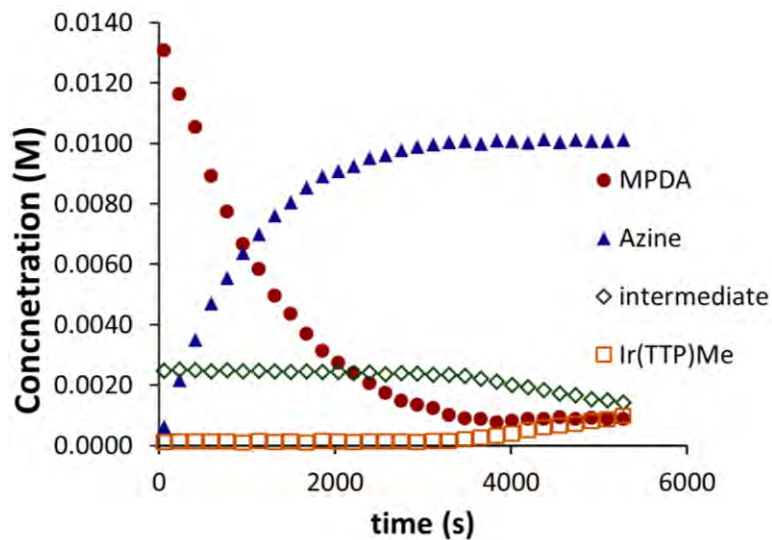
Figure 3.15: Kinetic plot for the reaction of MPDA (0.0200 M) with Ir(TTP)CH$_3$ (0.00405 M) in C$_6$D$_6$. Similar plots were obtained for reaction run in the presence of cyclohexane (0.044 M) or toluene (0.045 M or 0.22 M).
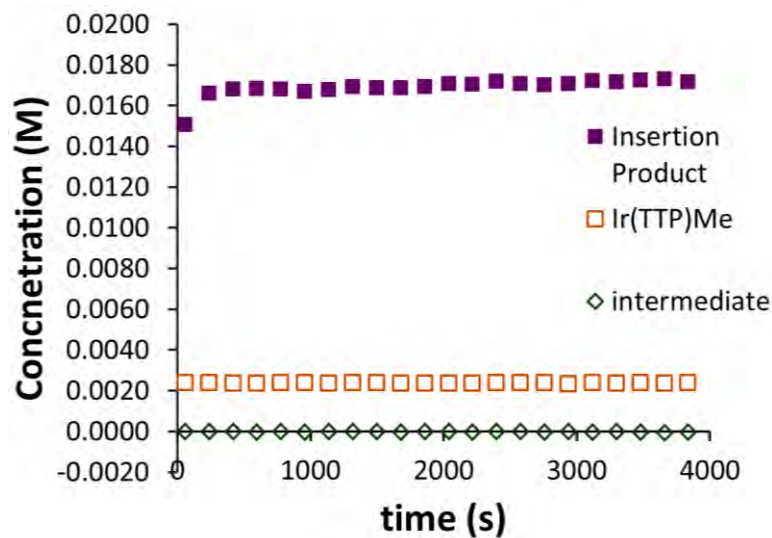
Figure 3.16: Kinetic plot for the reaction of MPDA (0.0200 M), Ir(TTP)CH$_3$ (0.00405 M), and cyclohexadiene (0.045 M) in C$_6$D$_6$.

CHAPTER 4.   IRIDIUM PORPHYRIN CATALYZED N–H INSERTION REACTIONS: SCOPE AND MECHANISM

Bernie J. Anding and L. Keith Woo

Abstract

Ir(TTP)CH3 catalyzed the N–H insertion reactions between ethyl diazoacetate (EDA) or methyl phenyldiazoacetate (MPDA) and a variety of aryl, aliphatic, primary, and secondary amines to generate substituted glycine esters with modest to high yields. Aniline substrates generally gave yields above 80%, with up to 105 catalyst turnovers, and without slow addition of the diazo reagent. Good yields were also achieved with aliphatic amines, though higher catalyst loadings and slow addition of the amine were necessary in some cases. Primary amines reacted with EDA to generate both single and double-insertion products, either of which could be produced selectively in high yield with the proper choice of stoichiometric ratios and reaction temperature. Notably, mixed trisubstituted amines, RN(CH2CO2Et)(CHPhCO2Me), were generated from the insertion of one equivalent of EDA and one equivalent of MPDA into primary amines. The N-H insertion mechanism was examined using substrate competition studies, trapping experiments, and multiple spectroscopic techniques. Substrate competition studies using pairs of amines with EDA or MPDA revealed Hammett correlations with respective slopes of $\rho = 0.15$ and $\rho^+ = -0.56$ as well as kinetic isotope ratios of $k_H/k_D = 1.0 \pm 0.2$ and 2.7 ± 0.2. Competitive amine binding to the catalyst was demonstrated by kinetics and equilibrium binding studies. Equilibrium binding constants ranged from $10^2 - 10^5$. Monitoring the reaction by absorption spectroscopy revealed a transient metalloporphyrin complex. The lifetime of this species was dependent on the nature of the amine substrate, which suggests that the catalytic cycle proceeds through a metal-ylide intermediate.

Introduction
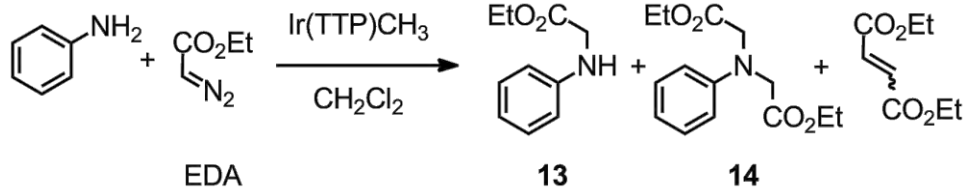
N–H insertion reactions of diazocarbonyl compounds are atom-efficient and rapid routes to an array of synthetically and biologically important nitrogen-containing compounds.[1-5] Studies over the last few decades demonstrate that N–H insertions occur under thermal and transition metal-catalyzed conditions.[6] Under catalyst-free conditions, donor/acceptor carbenes inserted into aliphatic and aryl amines in 53 – 96% yield, but the reactions required refluxing temperatures in trifluorotoluene, an expensive and high-boiling solvent.[7] A similar method with toluene solvent afforded significantly reduced yields in the range of 15 – 60%.[8] More efficient mild conditions were achieved using transition metal catalysts containing rhodium,[9-14] copper,[3,15-18] rhenium,[19] ruthenium,[20-23] and iron.[22-27] Although sophisticated rhodium and copper systems have been developed, these catalysts are poisoned by Lewis basic amines, which typically limits their use to amides, carbamates, and anilines.[14] Furthermore, most catalysts require long reaction times, high catalyst loadings, and dropwise addition of the diazo reagent to avoid dimerization byproducts. As a notable exception, iron porphyrins were not poisoned by amine substrates, efficient at low catalyst loadings, and did not require slow addition of the diazo reagent.[26] Nonetheless, more effective, efficient, and selective N–H insertion catalysts are still needed.[25]

Mangion and coworkers were the first to report the use of an iridium catalyst, [Ir(COD)Cl]$_2$, for N–H insertions.[28] In their work, reactions between anilines and sulfoxonium ylides generated glycine esters in 76 – 93% yield at ambient temperatures. Insertions into aliphatic amines were also observed, albeit only for intramolecular conversions at elevated temperatures. Although this serves as the first reported example of iridium-catalyzed N–H insertions, there is precedent for macrocyclic iridium complexes as catalysts for carbene transfer reactions including cyclopropanation,[29-31] C–H insertion,[29,32-34] and Si–H insertion.[29,35] These catalysts are often reactive at temperatures lower than -40 °C and robust, with turnover numbers (TONs) as high as 4.8×10^5. The present work provides the first account of a macrocyclic iridium complex, Ir(TTP)CH$_3$ (TTP = tetratolylporphyrinato dianion), toward N–H insertion reactions using amines and diazo reagents.

Results and Discussion

N–H insertion using catalytic Ir(TTP)CH$_3$ was initially studied for the reaction between aniline and ethyl diazoacetate (EDA) (Table 4.1). Treating a CH$_2$Cl$_2$ solution of Ir(TTP)CH$_3$ and aniline with 1.1 equiv. of EDA at ambient temperature generated a mixture of single (**13**) and double (**14**) N–H insertion products in 70% and 25% yield, respectively, in less than 2 h. The only observed byproducts were diethyl maleate and diethyl fumarate, which resulted from dimerization of EDA. Similar to iron N–H insertion catalysts,[26] dimerization yields were unaffected by the rate of EDA addition so dropwise addition of EDA was unnecessary. Changing the stoichiometric ratios of the reactants, however, significantly altered the product distribution. Increasing the amount of aniline favored the formation of single-insertion product **13** while decreasing the amount of double-insertion and dimerization. In contrast, double-insertion product **14** and butenedioates were generated preferentially for reactions where aniline was the limiting reagent. Proper choice of stoichiometric ratios could produce either **13** in 93% yield or **14** in 94% yield. Reaction temperature also influenced selectivity; starting the reaction at -78 °C and then allowing it warm to ambient temperature gave a modest increase in single-insertion (Table 4.1, entries 1 – 2). For all conditions, low catalyst loadings (0.06 mol%) were sufficient to effect the reaction with high yields. Turnover numbers as high as 10^5 were observed without any indication of catalyst deactivation.

Based on the above results, two separate Ir(TTP)CH$_3$-catalyzed procedures were developed to optimize the selective formation of either the single or double-insertion product. To generate single-insertion products, reactions were run at -78 °C using a two-fold excess of amine relative to EDA. High single-insertion yields were found for reactions between aryl amines and EDA (Table 4.2). Double-insertion occured in less than 10% yield with all aryl substrates except for *p*-cyanoaniline, where the diglycyl ester was generated in 20% yield. Reactions with aliphatic amines required higher temperatures and catalyst loadings between 0.25 and 0.50 mol%. Single-insertion products were formed in good yields for benzylamine and *n*-butylamine, but reactions with *t*-butylamine generated the single-insertion product in modest yield and with little selectivity. Attempts to insert EDA into an amide N–H bond also resulted in low yields and selectivity.

Table 4.1: N–H Insertion of EDA and aniline catalyzed by Ir(TTP)CH$_3$.[a]

Entry	Aniline Equivalents	Yield (%)[c]		
		13	**14**	Dimers
1	1.1	70	25	5
2	1.1[b]	76	19	5
3	2.0	87	10	3
4	3.0	93	5	2
5	0.5	32[d]	61[d]	18
6	0.25	3[d]	94[d]	48

[a] Conditions: Ir(TTP)CH$_3$ (0.06 mol%), aniline, and CH$_2$Cl$_2$ (2.0 mL) were treated with EDA (150 μmol). Yields were determined by NMR. [b] Reaction started at -78 °C and allowed to warm to ambient temperature over 2 h. [c] Yield based on EDA. [d] Yields based on aniline.

This method was also extended to methyl phenyldiazoacetate (MPDA). With aryl amines and amides, single-insertion products were generated in good yields (Table 4.2). However, reactions with aliphatic amines were sluggish and low-yielding over a *ca.* 24 h time frame, suggesting that these amines were poisoning the catalyst and preventing MPDA coordination. Accordingly, the order of additions was altered so that MPDA was allowed to interact with Ir(TTP)CH$_3$ before slow addition of the amine. This method works for MPDA because its rate of dimerization is slow, whereas EDA under these conditions would completely dimerize.[31,36] The initial catalyst solution darkened from orange to dark green, on addition of MPDA, signifying the formation of a metal-carbene intermediate.[32] Subsequent dropwise addition of the amine quickly quenched this intermediate and turned the solution color back to orange. The reaction color was allowed to revert back to dark green before the next aliquot of amine was added. Using this technique, single-insertion products were generated in 87% and 79% yields for *t*-butylamine and benzylamine, respectively. Double-insertion products were not observed for any reactions with MPDA.

Table 4.2: Single-insertion into primary amines using catalytic Ir(TTP)CH$_3$.[a]

Amine	Diazo Reagent	Yield (%)		
		Single	Double	Dimers
aniline	EDA	92	7	1
p-toluidine	EDA	88	8	4
p-anisidine	EDA	87	8	5
p-chloroaniline	EDA	87	7	6
p-bromoaniline	EDA	89	8	3
p-cyanoaniline	EDA	77	20	3
p-nitroaniline	EDA	85	6	9
benzylamine[b]	EDA	85	15	0
t-butylamine[b]	EDA	38	27	35
n-butylamine[c,d]	EDA	76	18	6
acetamide[e]	EDA	11	12	59
aniline[b,c,f]	MPDA	88	0	trace
t-butylamine[b,c,f]	MPDA	31	0	32
t-butylamine[b,e,f,g]	MPDA	87	0	4
benzylamine[c,d,f]	MPDA	30	0	trace
benzylamine[b,e,f,g]	MPDA	79	0	trace
acetamide[b,e,f]	MPDA	72	0	trace

[a] Conditions: Ir(TTP)CH$_3$ (0.07 mol%) and amine (2.0 equiv.) were dissolved in CH$_2$Cl$_2$ (2.0 mL) and treated with EDA (1.0 equiv., 150 μmol). Yields were determined by NMR. [b] 0.25 mol% catalyst loading. [c] Run at ambient temperature for *ca.* 24 h. [d] 0.5 mol% catalyst loading. [e] Refluxing. [f] Using 1.1 equiv. of amine. [g] Ir(TTP)CH$_3$, MPDA, and CH$_2$Cl$_2$ were treated with amine dropwise.

For the above reactions with aryl amines, prolonged stirring of the reaction mixture (> 8 h) led to the formation of imine esters resulting from oxidation of the single-insertion products (Eq. 4.1). Similar oxidations have been shown with other late metal catalysts.[37,38] The oxidation of monoglycine **13** was briefly investigated under various conditions. Heating **13** in the presence of catalytic Ir(TTP)CH$_3$ at 55 °C for 36 hours under air produced imine **15** in 19% yield. Under the same conditions without Ir(TTP)CH$_3$, no oxidation was observed.

The amount of oxidation was increased slightly by heating under an O_2 atmosphere, but the yield was never greater than 25%.

(4.1)
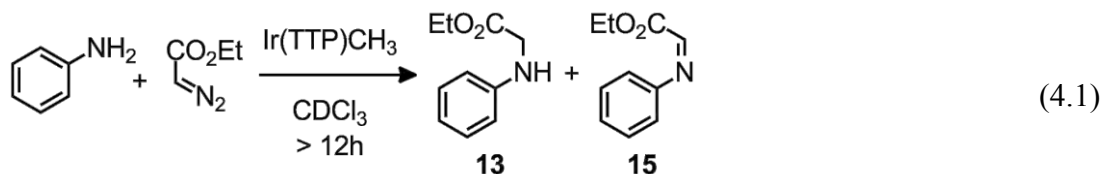
Table 4.3: Double-insertion into primary amines using catalytic Ir(TTP)CH$_3$.[a]

Amine	Yield (%)	
	Single	Double
aniline	3	97
p-toluidine	2	98
p-anisidine	3	97
p-chloroaniline	2	98
p-bromoaniline	2	98
p-cyanoaniline	3	96
p-nitroaniline	9	83
benzylamine	11	89
n-butylamine	22	78
t-butylamine	1	24
acetamide	21	21
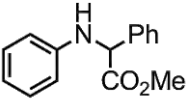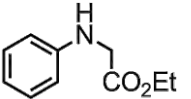
[a] Conditions: Ir(TTP)CH$_3$ (0.07 mol%) and amine (1.0 equiv., 38 μmol) were dissolved in CH$_2$Cl$_2$ (2.0 mL) and given EDA dropwise (4.0 equiv.). Reactions were stirred for 1 to 4 h at ambient temperature. Yields determined by NMR.

Double-insertion products were generated selectively at ambient temperature with a four-fold excess of diazo reagent to amine. Reactions between EDA and aryl amines afforded double-insertion products in high yields. Good yields were also found for benzylamine and *n*-butylamine, albeit with slightly more single-insertion product formation relative to that for aryl amines (Table 4.3). However, reactions with *t*-butylamine and acetamide showed little selectivity for single versus double insertion and produced modest yields with significant

amounts of dimerization of the diazo reagent. For most of the double-insertion reactions, consumption of the amine substrate was quantitative and dimerization of EDA did not diminish insertion yields, indicating that N−H insertion occured preferentially over dimerization. This is noteworthy given the propensity of EDA to dimerize during cyclopropanation and C−H insertion reactions, which are typically carried out using excess substrate.[31,32] In addition, some of the reactions for double-insertion exhibited a fleeting color change, signifying the presence of an observable intermediate.

Table 4.4: N−H Insertion into secondary amines using catalytic Ir(TTP)CH$_3$.[a]
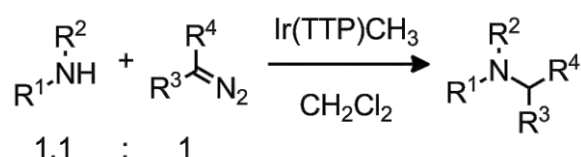
Amine	Diazo Reagent	Yield (%)	
		Insertion	Dimerization
piperidine	EDA	77[b]	23
N-methylaniline	EDA	84	16
N-ethylaniline	EDA	79	21
N-isopropylaniline	EDA	61	39
N-isopropylaniline	EDA	86[c]	14
16	EDA	0	100
N-methylaniline	MPDA	79	trace
13	MPDA	82[d]	trace

[a] Conditions: Ir(TTP)CH$_3$ (0.07 mol%) and amine (1.1 equiv.) were dissolved in CH$_2$Cl$_2$ (2.0 mL). The diazo reagent (1.0 equiv., 150 μmol) was added dropwise over 30 seconds. Reactions were run at ambient temperature for 1 – 4 h. Yields determined by NMR. [b] Catalyst loading of 1.0 mol%. [c] Using 2.0 equiv. of N-isopropylaniline. [d] Using 0.25 mol% catalyst loading at reflux.

Ir(TTP)CH$_3$ was also capable of catalyzing N−H insertion with secondary amines (Table 4.4). Reactions with N-alkylanilines or piperidine and EDA gave insertion products in good yield, albeit at higher catalyst loadings (1.0 mol%) for piperidine. A correlation between

steric bulk and N–H insertion efficiency was found for the reactions with N-alkylanilines. As the bulk of the N-alkyl substituent was increased, reactions proceeded faster as indicated by rapid gas evolution after EDA addition, but insertion yields decreased and the amount of EDA dimerization increased. For example, reactions with 1.1 equivalents of N-methylaniline afforded insertion products in 84% yield, whereas the same conditions with N-isopropylaniline gave the insertion product in 61% yield. The yield for N-isopropylaniline was increased to 86% using a two-fold excess of substrate. Following the same trend, attempts to generate a mixed glycine ester by treating **16**, the single-insertion product from the reaction of aniline with MPDA, with EDA failed. Compound **16** was too sterically encumbered, leading to rapid and quantitative dimerization of EDA. As an alternative approach to synthesizing mixed glycine esters, insertions into secondary amines were briefly examined with MPDA. MPDA reacted with N-alkylanilines and compound **16** to generate the corresponding trisubstituted amines in *ca.* 80% yields (Table 4.4). The latter serves as the first reported method to generate a mixed glycine ester from EDA and MPDA.

Reactivity trends indicated that amine substrates poison the catalyst. The extent of this poisoning was elucidated further by kinetics studies. The dependence of reaction rate on amine concentration was measured for the reaction between aniline, methyl diazoacetate (MDA), and catalytic Ir(TTP)CH$_3$ at 300.0 K (Figure 4.1). As the amine concentration was increased, the rate constant for MDA consumption decreased considerably. The rate constant is quite sensitive to changes at low aniline concentrations, but this inhibition effect appeared to saturate at high aniline concentrations, thus allowing the catalyst to tolerate high amine concentrations without deactivating completely. In a similar study, the influence of substrate bulk on reaction rate was examined by comparing the rate of MDA consumption for aniline, N-methylaniline, N-ethylaniline, and N-isopropylaniline. Increasing the bulk of the N-alkyl substituent presumably inhibited its binding to the Ir center and led to a dramatic increase in the rate of MDA consumption (Figure 4.2), which was consistent with the reactivity trends previously discussed for secondary amines (Table 4.4). Substrate electronics also influenced reaction rate (Figure 4.7; Appendix C), as observed indirectly during Hammett correlation experiments (*vide infra*). Using *para*-substituted aniline substrates and MDA, it was found that reactions with electron-withdrawing substrates consumed MDA faster than those with

electron-donating substrates. This electronic effect seemed to be less drastic than the steric effect.
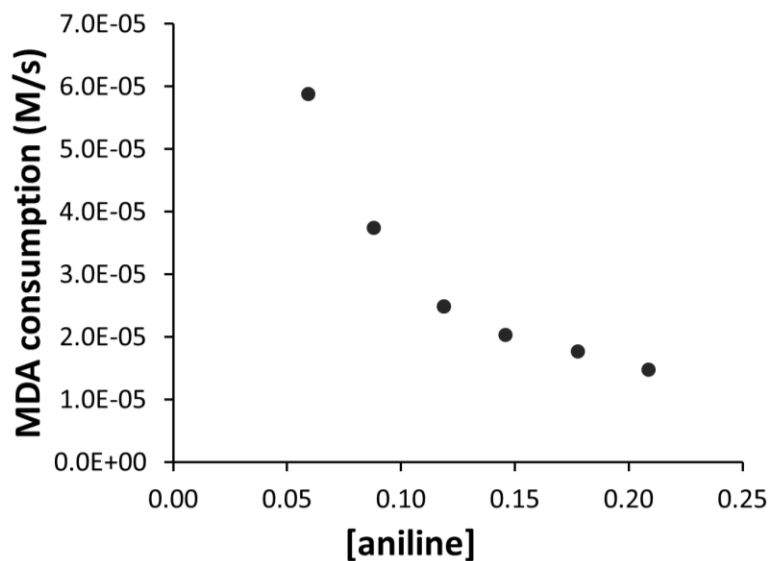
Figure 4.1: Rate comparison of MDA consumption for reactions with Ir(TTP)CH$_3$ (8.92 × 10^{-6} M), MDA (0.117 M), and varying amounts of aniline (0.0595–0.209 M) in CD$_2$Cl$_2$ at 300.0 K.
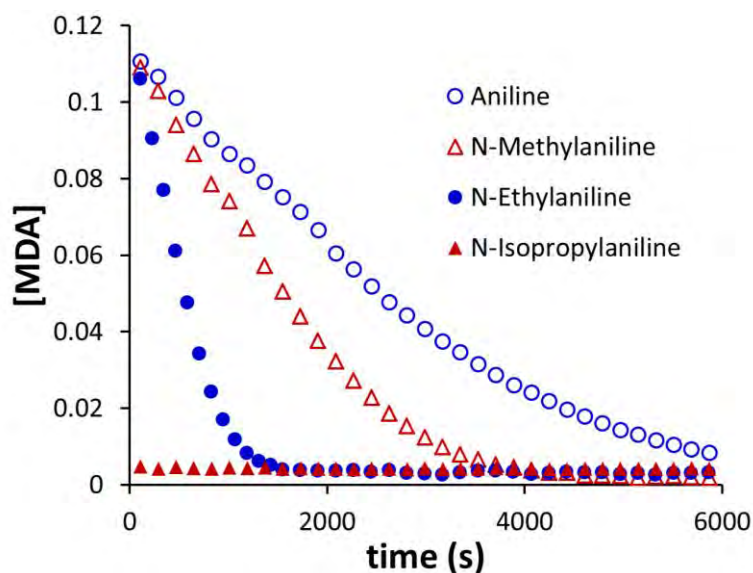
Figure 4.2: The effect of substrate steric on the rate of MDA consumption for reactions with Ir(TTP)CH$_3$ (8.92 × 10^{-6} M), MDA (0.117 M), and amine (0.119 M) in CD$_2$Cl$_2$ at 300.0 K.

Coordination of amine substrates to Ir(TTP)CH$_3$ was explored further by absorption spectroscopy using a UV/vis titration method similar to that reported previously.[39] To evaluate the influence of amine electronics and sterics on ligand binding, equilibrium constants were obtained for several *para*-substituted and N-alkyl-substituted aniline compounds (Table 4.5). Comparing N-alkylaniline compounds showed that log K dramatically decreased as the bulk of the alkyl group was increased, demonstrating that ligand bulk has a significant impact on binding. There was a similar relationship between log K and the electronic character of the amine. Anilines with electron-donating substituents at the *para*-position had larger equilibrium constants. Overall, the observed trends in ligand binding are consistent with the kinetics results. Amines with lower binding constants result in faster MDA consumption under N–H insertion conditions, providing additional evidence that competitive amine binding to the Ir center inhibits the catalysis. The values of these log K values are reasonable compared to those previously reported for binding between Ir(OEP)(C$_3$H$_7$) and amines.[39]

Table 4.5: Equilibrium binding constants for the coordination of amines to Ir(TTP)CH$_3$ at 23 °C.
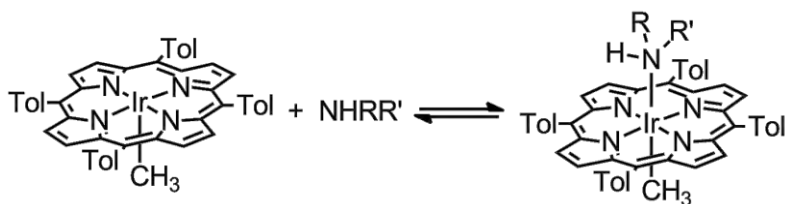
Amine	log(K)
aniline	4.4 ± 0.1
N-methylaniline	4.0 ± 0.1
N-ethylaniline	2.7 ± 0.4
N-isopropylaniline	2.0 ± 0.1
p-anisidine	5.4 ± 0.4
p-toluidine	5.0 ± 0.1
p-chloroaniline	4.4 ± 0.1
p-cyanoaniline	3.4 ± 0.1

Substrate competition reactions were examined to gain further insight into the reaction mechanism. In the presence of EDA and catalytic Ir(TTP)CH$_3$, competitive reactions between aniline and a series of *para*-substituted anilines generated a Hammett correlation with slope $\rho = 0.15$ (Figure 4.3), suggesting the slight buildup of negative charge during the reaction. This result was unexpected because similar reactions involving EDA and a metalloporphyrin catalyst, including Fe(TPP)Cl-catalyzed N–H insertion, produced Hammett correlations with a negative ρ value.[23,27] As a comparison, a similar correlation study was conducted using insertions of MPDA into amines with Ir(TTP)CH$_3$ as the catalyst. This study revealed a Hammett correlation with a negative slope $\rho^+ = -0.56$, consistent with the previous study using Fe(TPP)Cl ($\rho^+ = -0.66$).[27] A better Hammett fit for the MPDA reactions was obtained using σ^+ values ($R^2 = 0.93$) rather than the standard σ values ($R^2 = 0.86$).
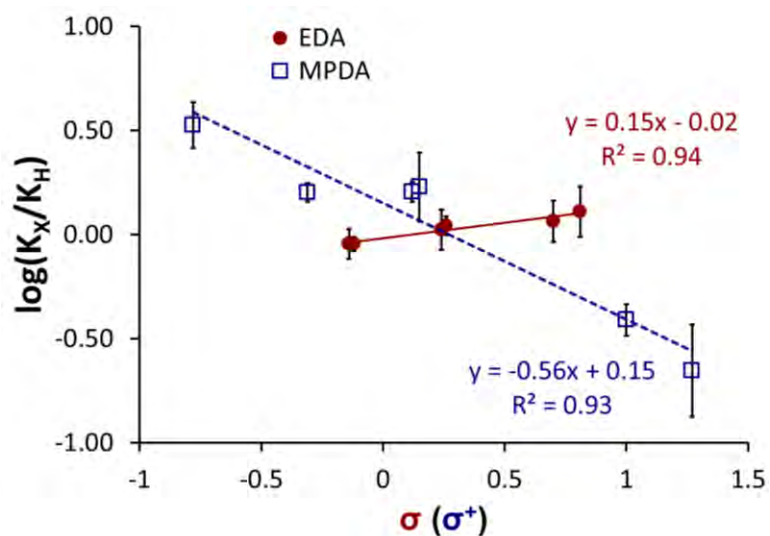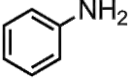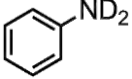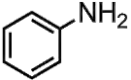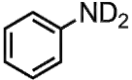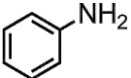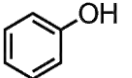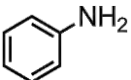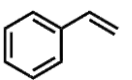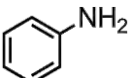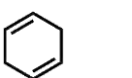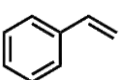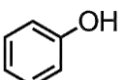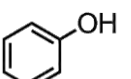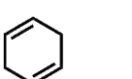
Figure 4.3: Hammett plots for the reactions between *para*-substituted anilines and EDA or MPDA in the presence of catalytic Ir(TTP)CH$_3$. Substrates include *p*-anisidine, *p*-toluidine, *p*-chloroaniline, *p*-bromoaniline, *p*-cyanoaniline, and *p*-nitroaniline. The EDA series was fit to standard σ values whereas the MPDA series gave the best fit with σ^+ values.

Kinetic isotope effects (KIEs) were examined using aniline and C$_6$H$_5$ND$_2$ in the presence of Ir(TTP)CH$_3$ (Table 4.6). For reactions with EDA, no KIE was observed. However, MPDA produced a KIE (2.7 ± 0.2) consistent with similar systems where proton transfer was rate-limiting.[16,40] This study, along with the Hammett correlation results, demonstrated that

Table 4.6: Substrate competition studies using catalytic Ir(TTP)CH$_3$.[a]

$$\text{Sub}_A\text{–X} + \text{Sub}_B\text{–X} + \underset{R^1}{\overset{R^2}{\diagdown}}{\diagup}N_2 \xrightarrow[\text{CH}_2\text{Cl}_2]{\overset{0.07\ \text{mol\%}}{\text{Ir(TTP)CH}_3}} \text{Sub}_A\overset{R^1\ R^2}{\diagup\!\diagdown}X + \text{Sub}_B\overset{R^1\ R^2}{\diagup\!\diagdown}X$$

$$5\quad:\quad 5\quad:\quad 1$$

Substrate A	Substrate B	Diazo Reagent	Yield (%) A	Yield (%) B
aniline (NH$_2$)	aniline-d$_2$ (ND$_2$)	EDA	51	49
aniline (NH$_2$)	aniline-d$_2$ (ND$_2$)	MPDA	30[b]	11
aniline (NH$_2$)	phenol (OH)	EDA	100	0
aniline (NH$_2$)	styrene	EDA	100	0
aniline (NH$_2$)	1,4-cyclohexadiene	EDA	100	0
styrene	phenol (OH)	EDA	72[c]	3
phenol (OH)	1,4-cyclohexadiene	EDA	40[c]	7

[a] Conditions: Ir(TTP)CH$_3$ (0.07 mol%), substrate A (5.0 equiv.), substrate B (5.0 equiv.), and CH$_2$Cl$_2$ (2.0 mL) were treated with diazo reagent (120 μmol) at ambient temperature. Yields determined by NMR. [b] Reaction generated a significant amount of an undetermined side-product. [c] Diethyl maleate and diethyl fumarate were the only other reaction products.

reactions with EDA are less sensitive to the nature of the amine substrate than those with MPDA. Other competition reactions were investigated to explore the relative rate of N–H insertion reactions compared to cyclopropanation, C–H insertion, and O–H insertion. The substrates chosen to represent each reaction were among the most efficient for their respective reactions: styrene (cyclopropanation) and 1,4-cyclohexadiene (C-H insertion).[31,32] Since O–H insertion had not been previously reported for Ir(TTP)CH$_3$, phenol was chosen based on its reactions with Fe(TPP)Cl.[24] For reactions involving aniline, N–H insertion was heavily favored producing compound **13** in quantitative yields regardless of the other substrate. This result is in contrast with dirhodium catalysts for which O–H insertion is

favored over N–H insertion.[14] The other competition reactions generated a mixture a products along with significant amounts of dimerization materials (Table 4.6). Overall, these results indicate the following reactivity trend: N–H insertion >> cyclopropanation > O–H insertion > C–H insertion.
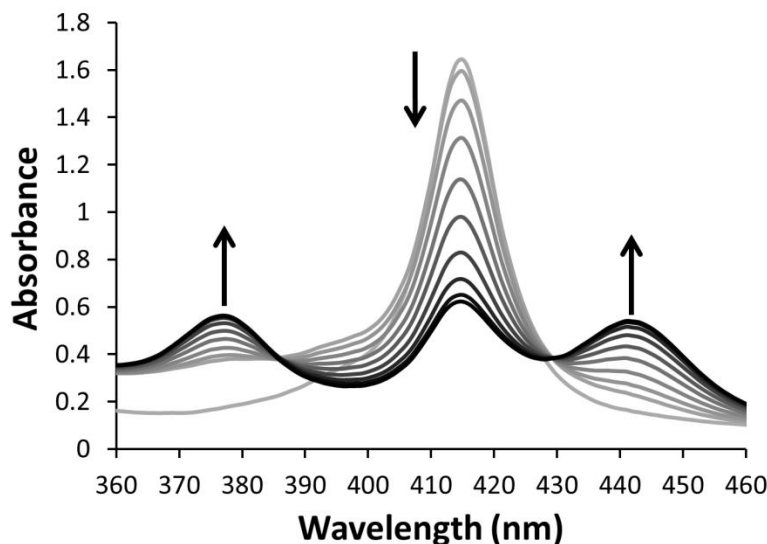
Figure 4.4: Absorption spectra for the reaction between aniline (27 μmol) and EDA (105 μmol) in the presence of Ir(TTP)CH$_3$ (0.075 μmol, 7.5×10^{-5} M in CH$_2$Cl$_2$) over 105 seconds. The spectra shown depict the solution absorbance before EDA was added (light gray) and the reaction progress from initial EDA addition toward the maximum absorbance of the intermediate bands (gray to black).

As mentioned above, double-insertion reactions exhibited a transient color change, implying the involvement of an intermediate species. This intermediate was investigated by absorption spectroscopy for the reaction between aniline and a four-fold excess of EDA in the presence of 0.28 mol% Ir(TTP)CH$_3$. The Soret band of Ir(TTP)CH$_3$ in CH$_2$Cl$_2$, which initially displayed a λ_{max} at 407 nm, red-shifted to 415 nm after addition of aniline to signify the formation of hexacoordinate Ir(TTP)CH$_3$(aniline). EDA was added subsequently and reaction progress was monitored every ten seconds. Over the course of 105 seconds, the band at 415 nm was partially consumed to give rise to two bands at 377 nm and 441 nm (Figure 4.4). These intermediate bands returned to a single band at 415 nm over the course of minutes. Isosbestic behavior was followed for a majority of the reaction, except immediately after EDA addition and near the end when aniline consumption was nearly

complete. This deviation from isosbestic behavior indicates that the transition from Ir(TTP)CH$_3$(aniline) to the intermediate is not a smooth process, suggesting that aniline must first dissociate from the hexacoordinate resting state in order for EDA to react with Ir(TTP)CH$_3$ and form the intermediate. Interestingly, repeating this procedure using a 1:2 ratio of aniline to EDA did not produce a change in the 415-nm band (Figure 4.18; Appendix C). A second addition of EDA, making an effective overall four-fold excess of EDA to aniline, was required to reproduce the intermediate spectrum. Attempts to detect the intermediate complex by ^{1}H NMR spectroscopy failed. Furthermore, an intermediate was not observed under similar conditions with MPDA.

The bands shown in Figure 4 are very similar to the 375 and 443-nm bands observed previously for the metal–carbene complex formed from Ir(TTP)CH$_3$ and MPDA.[32] The intermediate spectrum observed here may represent a metal–carbene complex, but the alternative of an aniline-stabilized metal–carbene complex or a metal–ylide complex, similar to those shown for osmium porphyrins,[41] is also possible. Further insight was gained by monitoring the formation and lifetimes of intermediate complexes for reactions with different *para*-substituted aniline compounds. Reaction progress for each substrate was compared by plotting the intensity of the intermediate band at 441 nm verses time (Figure 4.5). Bands corresponding to an intermediate were not observed with *p*-cyanoaniline; only a slight broadening of the Ir(TTP)CH$_3$(L) Soret band occurred. With all other aniline substrates, the rate of formation of the intermediate slowed and the lifetime of the intermediate was prolonged as the *para*-substituents became more electron rich. The formation trend is consistent with electron-rich amines binding more strongly to Ir and delaying the appearance of the intermediate, due to slower amine dissociation. However, the metal binding trend does not explain the short intermediate lifetime for electron-deficient substrates *p*-chloroaniline and *p*-cyanoaniline. If a metal-carbene complex was the intermediate, electron-deficient substrates would nucleophilically attack and consume the intermediate more slowly than electron-rich substrates. Moreover, if amine substrates were participating only in metal binding, one would expect similar intermediate profiles for aniline and *p*-chloroaniline given their similar binding constants (Table 4.5). A more likely explanation is that the aniline substrates are stabilizing the intermediate species. This implies that the substrate must be

bound in the intermediate, and strongly implicates a metal–ylide intermediate, similar to those suggested for related N–H insertion catalysts.[16,26]
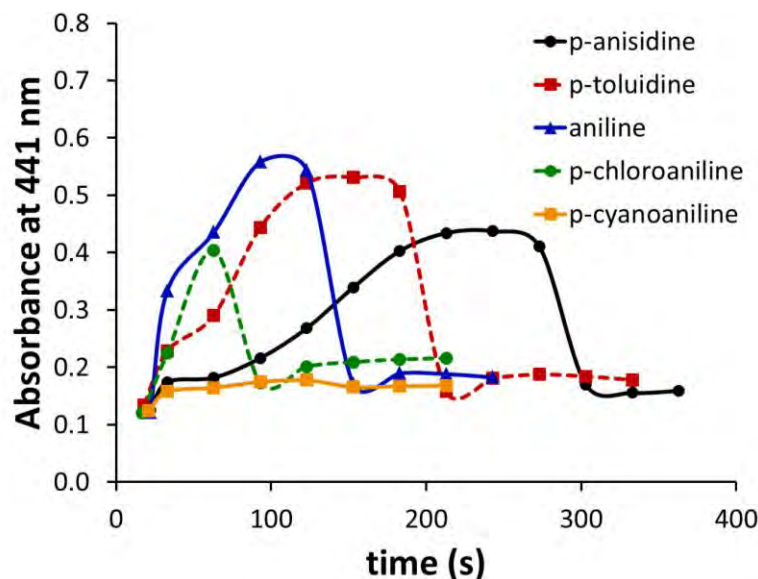

Figure 4.5: Formation of the intermediate after EDA addition, as monitored by the plot of the intermediate band at 441 nm verses time. Reaction conditions: Ir(TTP)CH$_3$ (7.24 × 10^{-5} M), EDA (0.105 M), and various aniline substrates (0.026 M). Data points were collected at 30 second intervals.

Trapping experiments were conducted to probe the involvement of metal–ylide intermediates. In a previous study, Aviv and Gross found that treating aniline with EDA in the presence of catalytic Fe(TPP)Cl and stoichiometric diethyl azodicarboxylate (DEAD) generated compound **18** as the sole product (Eq. 4.2).[26] Compound **18** formed as a result of DEAD trapping the free ylide intermediate (**17**). Using catalytic Ir(TTP)CH$_3$ under the same conditions, the N–H insertion product **13** was generated without any trace of compound **18**. The same result was found using a variety of different stoichiometric ratios, indicating that a free ylide compound is either short-lived or not formed under any of the present reaction conditions. An alternative trapping experiment was attempted with diallylamine as the substrate. The allyl moieties can trap metal–ylide intermediates via a rapid intramolecular 2,3-sigmatropic rearrangement.[26] Treating diallylamine with an equimolar amount of EDA in the presence of catalytic Ir(TTP)CH$_3$, at ambient temperature, generated primarily N–H insertion product **19** along with small amounts of compound **20**, presumably formed as a

result of a tandem N–H insertion and 2,3-sigmatropic rearrangement (Eq. 4.3). Monitoring the reaction by ^{1}H NMR revealed that compound **19** formed initially and compound **20** grew in slowly as diallylamine became scarce. Addition of excess EDA at the end of the reaction resulted in continued production of **20** at the expense of compound **19**. Throughout the reaction, the secondary amine corresponding to 2,3-sigmatropic rearrangement of diallylamine was never observed. It can be concluded that compound **20** formed by initial N–H insertion followed by 2,3-sigmatropic rearrangement, demonstrating that proton transfer occurred preferentially to intramolecular sigmatropic rearrangement. Regardless, the fact that tertiary allylic amines undergo a 2,3-sigmatropic rearrangement further supports the potential for metal–ylide intermediates.

(4.2)

(4.3)
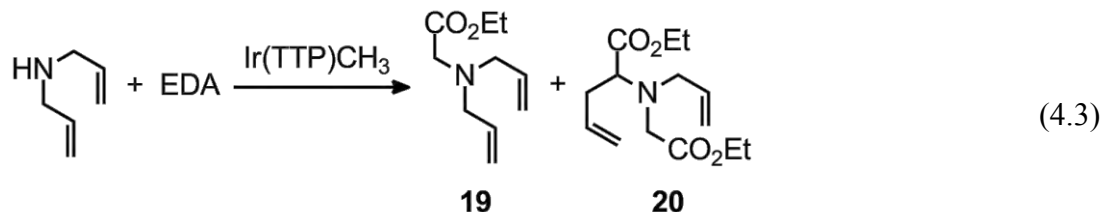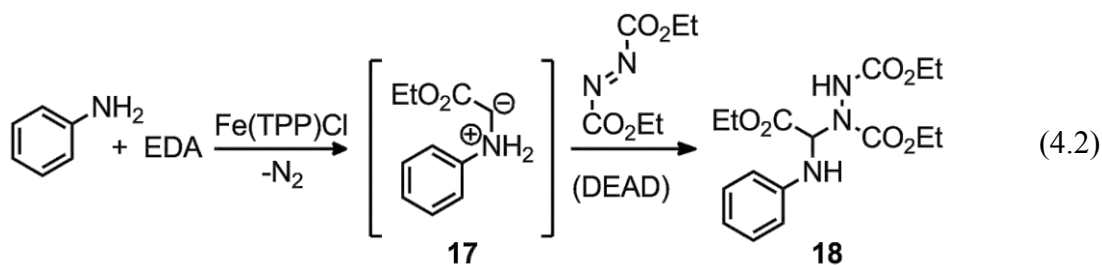
Under ambient light, Ir(TTP)CH$_3$ is sensitive to photolytic cleavage of the Ir–CH$_3$ bond, which generates Ir(TTP)Cl(CO) in the presence of halogenated solvents.[42] To ensure that this is not significant during N–H insertion, photolysis of Ir(TTP)CH$_3$ and Ir(TTP)CH$_3$(aniline) was examined by absorption spectroscopy using both ambient and sun lamp light sources. With either light source, photolysis of Ir(TTP)CH$_3$ in CH$_2$Cl$_2$ generated Ir(TTP)Cl(CO) as indicated in a shift of the Soret band from 407 to 421 nm. Conversion was quantitative and complete in less than 15 minutes using the sun lamp. In contrast, radiating Ir(TTP)CH$_3$(aniline) under the same conditions did not lead to a shift in the Soret band (Figures 4.26 and 4.27; Appendix C), demonstrating that the photolytic cleavage of the Ir–CH$_3$ bond is drastically inhibited in the presence of amines. In addition, attempts were made

to trap transient radical intermediates under N–H insertion conditions using 2,2,6,6-tetramethylpiperidine 1-oxyl (TEMPO). N–H insertion reactions carried out in the presence of TEMPO showed no qualitative change in the reaction rate or product distribution, indicating further that species with radical character were not substantial during the reaction.
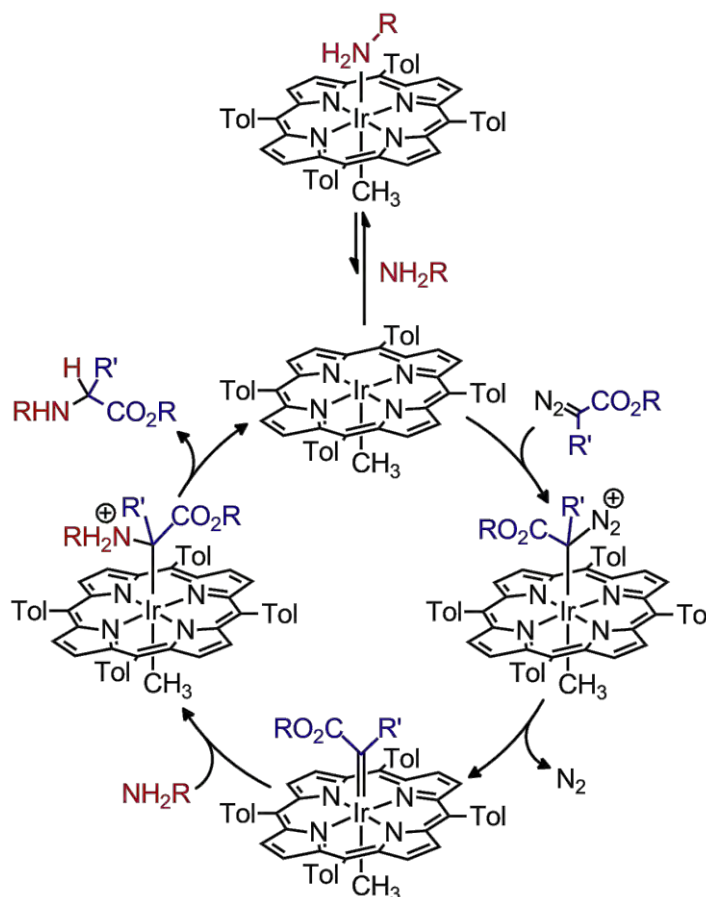
Figure 4.6: The proposed catalytic cycle for N–H insertion reactions catalyzed by Ir(TTP)CH$_3$.

The above evidence supports the catalytic cycle shown in Figure 4.6, which is analogous to the stepwise mechanism proposed for a copper catalyst involving a simultaneous proton transfer and catalyst dissociation step.[16] Initially, the diazo reagent and the amine substrate compete for binding to the vacant site of Ir(TTP)CH$_3$. Amine binding forms an inactive hexavalent complex whereas binding of the diazo reagent to Ir(TTP)CH$_3$ produces a diazonium complex. Once formed, the diazonium complex loses dinitrogen to form a metal–carbene complex, as was shown for the analogous Ir-catalyzed C–H insertion reactions.[32]

Amine substrates react with the electrophilic metal–carbene complex to form a metal–ylide intermediate, which is supported by absorption spectroscopy studies. Although the above data cannot determine if metal-ylide formation is stepwise or concerted (*i.e.* whether or not a metal-carbene complex truly forms), this process must be rapid as indicated by the drastic chemoselectivity between different substrates such that N–H insertion is strongly favored over carbene dimerization, cyclopropanation, C–H insertion, and O–H insertion (Tables 4.4 and 4.6, *vide supra*). Once the metal–ylide complex is formed, proton transfer produces the glycine ester product and regenerates Ir(TTP)CH$_3$. Since attempts to trap a free ylide compound with DEAD were unsuccessful, proton transfer apparently occurs simultaneously with ylide dissociation from the metal center. Kinetic isotope effect studies, where amine substrate is present in excess, support a rate-limiting proton transfer for reactions with MPDA but not for those with EDA. However, the observation of a metal-ylide intermediate under conditions of excess EDA implies that the rate-limiting step changes depending on the reaction conditions.

Conclusions

Ir(TTP)CH$_3$ catalyzed the N–H insertion reactions of various aryl, aliphatic, primary, and secondary amines with diazoacetate reagents. Reactions with aryl amines produced the highest yields with up to 10^5 catalyst turnovers and without the need for slow addition of the diazo reagent. Although competitive amine binding to the catalyst was demonstrated, insertions with aliphatic amines still proceeded with good yields in many cases. Slow addition of the amine was required only for reactions between aliphatic amines and MPDA. Mixed glycine ester products, RN(CH$_2$CO$_2$Et)(CHPhCO$_2$Me), were generated for the first time using an N–H insertion protocol.[43,44] In general, mechanistic studies support a stepwise mechanism with a metal-ylide intermediate, where proton transfer is simultaneous with ylide dissociation from the iridium center.

Experimental

General Considerations: Unless noted otherwise, all manipulations were performed under a dry nitrogen atmosphere. Substrates were reagent grade and used without purification for catalytic reactions. For quantitative analyses, aniline substrates containing

colored impurities, specifically *p*-toluidine, were recrystallized from ethyl acetate. Ir(TTP)CH$_3$ and MPDA were prepared according to previously reported methods.[45-47] C$_6$H$_5$ND$_2$ was prepared by treating aniline with D$_2$O. CH$_2$Cl$_2$ was dried and deoxygenated by passage through columns of alumina and reduced copper. For kinetics reactions, CDCl$_3$ was dried over molecular sieves, deoxygenated by three freeze-pump-thaw cycles, and passed through a plug of activated alumina under a glovebox atmosphere. Absorption spectra were collected using a Hewlett-Packard/Agilent Technologies 8453 UV-Vis spectrophotometer. General NMR spectra were collected using Varian VXR 300 MHz and Varian VXR 400 MHz spectrometers and kinetic measurements were done using a Bruker DRX 400 MHz spectrometer. ^{1}H NMR peak positions were referenced against residual proton resonances of deuterated solvents (δ, ppm: CDCl$_3$, 7.26 (^{1}H) and 77.16 (^{13}C)). Gas chromatography was performed on an HP-6890 instrument fitted with a HP-5 capillary column (30 m length, 0.25 mm internal diameter, 0.25 μm film thickness). Column chromatography was performed using silica gel (40 – 63 μm) purchased from Sorbent Technologies. Characterization data for most N–H insertion products were previously reported.[26,27,48-55]

Procedure for single-insertion into primary amines: Method A: A CH$_2$Cl$_2$-stock solution of Ir(TTP)CH$_3$ (4.25 × 10^{-3} M stock solution, between 0.07 to 0.50 mol%) was transferred to a side-arm, round-bottom flask and taken to dryness under a nitrogen stream. The catalyst was dissolved in CH$_2$Cl$_2$ (2.0 mL) and amine substrate (373 μmol). The solution was cooled to -78 °C in a dry ice/acetone bath and then treated with the diazo reagent (154 μmol). Reactions were allowed to warm to ambient temperature over the course of 1 – 2 hours and volatiles were removed *in vacuo* after the diazo reagent was fully consumed, which required 2 to 24 hours depending on the substrate. Reaction progress could be monitored by TLC or GC. Yields were determined by ^{1}H NMR using mesitylene as the internal standard (57.5 μmol). Samples could be purified by column chromatography on silica gel using an eluent system of ethyl acetate and hexanes. Method B: Used for reactions between MPDA and aliphatic amines benzylamine and *t*-butylamine. Two separate solutions were prepared under nitrogen atmosphere. The first contained Ir(TTP)CH$_3$ (0.391 μmol) and CH$_2$Cl$_2$ (2.0 mL) and the second contained CH$_2$Cl$_2$ (1.0 mL) and amine substrate (165 μmol).

The former was heated to reflux and then treated with MPDA (154 μmol). After rapidly turning a dark green color, it was treated with the amine solution dropwise. Each drop caused the color to change briefly to a light orange before returning to dark green. Once all the amine solution was added and the reaction solution maintained a light orange color, volatiles were removed and the residue was analyzed by ^{1}H NMR.

Procedure for double-insertion into primary amines: CH_2Cl_2-stock solutions of Ir(TTP)CH$_3$ (26 μL from a 4.25×10^{-3} M stock solution, 0.111 μmol) and amine substrate (*ca.* 1 M, 38.5 μmol) were transferred to a side-arm, round-bottom flask and taken to dryness under a nitrogen stream. The solids were dissolved in CH_2Cl_2 (2.0 mL) and then given the diazo reagent (154 μmol) dropwise over 30 seconds. After the diazo reagent was fully consumed, which generally required 1 to 4 hours stirring at ambient temperature, volatiles were removed *in vacuo*. Yields were determined by ^{1}H NMR using mesitylene as the internal standard (57.5 μmol).

Procedure for insertion into secondary amines: A portion of Ir(TTP)CH$_3$ (4.25×10^{-3} M stock solution, between 0.07 to 0.50 mol%) was taken to dryness under a nitrogen stream and then dissolved in CH_2Cl_2 (2.0 mL) and amine (162 μmol). The solution was treated with diazo reagent (154 μmol) and stirred at ambient temperature unless otherwise noted until the diazo reagent was completely consumed (1 – 4 hours). Volatiles were removed *in vacuo*. Yields were determined by ^{1}H NMR using mesitylene (57.5 μmol) as the standard.

Amine N-H insertion competition reactions: A vessel was prepared containing Ir(TTP)CH$_3$ (0.118 μmol), both amine substrates (778 μmol each), and CH_2Cl_2 (4.0 mL). The diazo reagent (154 μmol) was added and the solution was stirred at ambient temperature until the diazo reagent was completely consumed, which generally took 12 to 48 hours. For samples that were analyzed by ^{1}H NMR, which include those for the Hammett correlation study with EDA, the solution was then stirred with D_2O (ca. 2 mL) for 12 hours. The organic portion was separated, taken to dryness *in vacuo*, and analyzed by ^{1}H NMR using mesitylene (57.5 μmol) as the standard. Reactions investigating the Hammett relationship with MPDA were analyzed by GC using hexadecane (68.3 μmol) as the standard. Products from reactions

investigating KIE were purified by column chromatography on silica gel using an ethyl acetate/hexanes eluent (1:10 for products formed from EDA and 1:30 for products formed from MPDA). The purified materials were stirred with D_2O (2.0 mL) for *ca.* 12 hours, taken to dryness, and analyzed by ^1H NMR.

UV-vis observation of ylide intermediate: In a 1-mm path length cell under air, $Ir(TTP)CH_3$ (17 μL from a 4.26×10^{-3} M stock solution in CH_2Cl_2, 0.0724 μmol) and amine (61 μL from a 0.426 M stock solution in CH_2Cl_2, 26.0 μmol) were diluted to 1.0 mL in CH_2Cl_2. A spectrum at time (t = 0) was acquired. Then, EDA (105 μmol) was added quickly. An absorption spectrum was acquired as quickly as possible (t = *ca.* 20 s) and then at 30 second intervals starting at t = 30 s.

TEMPO and DEAD trapping experiments: $Ir(TTP)CH_3$ from a CH_2Cl_2-stock solution (4.25×10^{-3} M stock solution, between 0.07 mol%) was taken to dryness under a nitrogen stream and then dissolved in CH_2Cl_2 (2.0 mL), amine (120 μmol), and DEAD (or TEMPO where applicable, 120 μmol). Reactions were treated with EDA (119 μmol) at ambient temperature. Products were analyzed by ^1H NMR.

Kinetics reactions: A portion of $Ir(TTP)CH_3$ from a CH_2Cl_2-stock solution (6.57×10^{-5} M, $2.34 - 6.97 \times 10^{-3}$ μmol) was collected in a medium-walled NMR tube and taken to dryness. Under a glovebox atmosphere, the tube was charged with aniline (from a $CDCl_3$-stock solution, $25.0 - 87.8$ μmol), mesitylene standard (40.0 μL from a 5.06×10^{-2} M $CDCl_3$-stock solution, 2.02 μmol), and diluted to 4.20×10^2 μL with $CDCl_3$. The tube was fitted with a septum and taken to the NMR instrument. After the instrument was tuned and the temperature equilibrated at 300.0 K, MDA (29.0 μL from a 1.70 M $CDCl_3$-stock solution, 49.3 μmol) was added and the reaction was monitored by spectra acquired at 60 second intervals.

Determination of amine binding constants: For all spectra, samples were prepared in a 1-mm path length cell and in benzene, rather than CH_2Cl_2, to avoid photolysis of the Ir–CH₃ bond. Molar extinction coefficients were determined by generating Beer's Law plots for $Ir(TTP)CH_3$ and the coordination complexes formed with $Ir(TTP)CH_3$ and N-alkylanilines,

para-substituted anilines, or pyridine. For these samples, concentrations of Ir(TTP)CH$_3$ ranged from 8.80×10^{-6} to 1.09×10^{-4} M in benzene, and coordination complexes were examined in 0.1 M solutions of the respective amine. After determination of all the molar extinction coefficients, equilibrium constants were measured for solutions with known initial concentrations of Ir(TTP)CH$_3$ (4.00×10^{-5} to 5.27×10^{-5} M) and amine (4.68×10^{-5} to 1.83×10^{-2} M).

Ethyl 2-(isopropyl(phenyl)amino)acetate: Purification by column chromatography on silica gel (1:40 ethyl acetate to hexanes) gave the product as a light yellow oil (59.9 mg, 77% yield). ^{1}H NMR (CDCl$_3$, 400 MHz): δ 7.22 (t, J = 7.2 Hz, 2H), 6.72 (t, J = 7.2 Hz, 1H), 6.69 (d, J = 7.2 Hz, 2H), 4.24 – 4.14 (m, 3H), 3.92 (s, 2H), 1.27 (t, J = 6.8 Hz, 3H), 1.21 (d, J = 6.4 Hz, 6H). ^{13}C{^{1}H} NMR (CDCl$_3$, 300 MHz): δ 172.39, 148.61, 129.39, 117.18, 112.76, 61.11, 48.12, 46.94, 20.11, 14.38. HRMS (ESI): calcd for C$_{13}$H$_{19}$NO$_2$ (M + H)$^+$ m/z = 222.1489, found m/z = 222.1488.

Methyl 2-((2-ethoxy-2-oxoethyl)(phenyl)amino)-2-phenylacetate: Purification by column chromatography on silica gel (1:20 ethyl acetate to hexanes) gave the product as a light yellow oil (36.7 mg, 73% yield). ^{1}H NMR (CDCl$_3$, 400 MHz): δ 7.36 (s, 5H), 7.27 (t, J = 8.0 Hz, 2H), 6.86 (t, J = 8.0 Hz, 1H), 6.81 (d, J = 8.0 Hz, 2H), 5.71 (s, 1H), 4.06 (ABq, J_{AB} = 18.4 Hz, Δv_{AB} = 22.7 Hz, 2H), 4.00 (q, J = 7.0 Hz, 2H), 3.79 (s, 3H), 1.12 (t, J = 7.0 Hz, 3H). ^{13}C{^{1}H} NMR (CDCl$_3$, 300 MHz): δ 172.42, 171.13, 148.80, 135.06, 129.42, 129.09, 128.84, 128.65, 119.30, 114.16, 65.37, 60.77, 52.35, 50.59, 14.20. HRMS (ESI): calcd for C$_{19}$H$_{21}$NO$_4$ (M + H)$^+$ m/z = 328.1544 and (M + Na)$^+$ m/z = 350.1363, found m/z = 328.1549 and 350.1368.

Ethyl 2-(diallylamino)acetate (19): Ir(TTP)CH$_3$ (4.26×10^{-3} M stock solution, between 0.02 mol%) was taken to dryness under a nitrogen stream and then dissolved in CH$_2$Cl$_2$ (2.0 mL) and diallylamine (983 μmol). The solution was treated with EDA (490 μmol) and stirred overnight at ambient temperature. Removal of volatiles *in vacuo* and purification by column chromatography on silica gel (1:20 ethyl acetate to hexanes) gave the product as a light yellow oil (49.2 mg, 60% yield). ^{1}H NMR (CDCl$_3$, 400 MHz): δ 5.85 (ddt, J_{ab} = 16.8 Hz, J_{ac} = 10.0 Hz, J_{ad} = 6.4 Hz, 2H), 5.21 – 5.13 (m, 4H), 4.15 (q, J = 7.2 Hz, 2H), 3.30 (s,

2H), 3.23 (d, J = 6.4 Hz, 4H), 1.25 (t, J = 7.2 Hz, 3H). $^{13}C\{^1H\}$ NMR (CDCl$_3$, 300 MHz): δ 171.45, 135.33, 118.35, 60.47, 57.35, 54.00, 14.39. HRMS (ESI): calcd for C$_{10}$H$_{17}$NO$_2$ (M + H)$^+$ m/z = 184.1332, found m/z = 184.1331.

Ethyl 2-(allyl(2-ethoxy-2-oxoethyl)amino)pent-4-enoate (20): Ir(TTP)CH$_3$ (4.26 × 10^{-3} M stock solution, between 0.02 mol%) was taken to dryness under a nitrogen stream and then dissolved in CH$_2$Cl$_2$ (2.0 mL) and diallylamine (487 μmol). The solution was cooled to -78 °C in a dry ice/acetone bath, treated with EDA (490 μmol), and allowed to warm to ambient temperature over 1 hour. This process was repeated for a second addition of EDA (980 μmol total). Removal of volatiles *in vacuo* and purification by column chromatography on silica gel (1:30 ethyl acetate to hexanes) gave the product as a clear oil (23.8 mg, 29% yield). ^{1}H NMR (CDCl$_3$, 400 MHz): δ 5.81 (m, 2H), 5.22 – 5.02 (m, 4H), 4.14 (m, 4H), 3.54 (m, 2H), 3.42-3.38 (m, 2H), 3.29-3.23 (m, 1H), 2.46 (m, 2H), 1.25 (m, 6H). $^{13}C\{^1H\}$ NMR (CDCl$_3$, 300 MHz): δ 172.50, 171.85, 135.75, 134.48, 117.99, 117.18, 63.64, 60.50, 60.37, 55.53, 51.67, 34.87, 14.49, 14.30. HRMS (ESI): calcd for C$_{14}$H$_{23}$NO$_4$ (M + Na)$^+$ m/z = 292.1519, found m/z = 292.1530.

References

1. Bartrum, H. E.; Blakemore, D. C.; Moody, C. J.; Hayes, C. J. *Chem. A. Eur. J.* **2011**, *17*, 9586.

2. Shi, B.; Blake, A. J.; Campbell, I. B.; Judkins, B. D.; Moody, C. J. *Chem. Commun.* **2009**, 3291.

3. Lee, E. C.; Fu, G. C. *J. Am. Chem. Soc.* **2007**, *129*, 12066.

4. Wang, Y.; Zhu, S. *Org. Lett.* **2003**, *5*, 745.

5. Deng, G.; Jiang, N.; Ma, Z.; Wang, J. *Synlett* **2002**, *11*, 1913.

6. Nicoud, J.-F.; Kagan, H. B. *Tetrahedron Lett.* **1971**, *12*, 2065.

7. Hansen, S. R.; Spangler, J. E.; Hansen, J. H.; Davies, H. M. L. *Org. Lett.* **2012**, *14*, 4626.

8. Saito, H. *Tetrahedron Lett.* **2012**, *53*, 6662.

9.   Belof, J. L.; Cioce, C. R.; Xu, X.; Zhang, X. P.; Space, B.; Woodcock, H. L. *Organometallics* **2011**, *30*, 2739.

10.   Saito, H.; Uchiyama, T.; Miyake, M.; Anada, M.; Hashimoto, S. *Heterocycles* **2010**, *81*, 1149.

11.   Shi, B.; Blake, A. J.; Lewis, W.; Campbell, I. B.; Judkins, B. D.; Moody, C. J. *J. Org. Chem.* **2009**, *75*, 152.

12.   Bashford, K. E.; Cooper, A. L.; Kane, P. D.; Moody, C. J.; Muthusamy, S.; Swann, E. *J. Chem. Soc., Perkin Trans. 1* **2002**, 1672.

13.   Yang, M.; Wang, X.; Li, H.; Livant, P. *J. Org. Chem.* **2001**, *66*, 6729.

14.   Aller, E.; Buck, R. T.; Drysdale, M. J.; Ferris, L.; Haigh, D.; Moody, C. J.; Pearson, N. D.; Sanghera, J. B. *J. Chem. Soc., Perkin Trans. 1* **1996**, 2879.

15.   Zhu, S.-F.; Zhou, Q.-L. *Acc. Chem. Res.* **2012**, *45*, 1365.

16.   Zhu, S.-F.; Xu, B.; Wang, G.-P.; Zhou, Q.-L. *J. Am. Chem. Soc.* **2011**, *134*, 436.

17.   Morilla, M. E.; Diaz-Requejo, M. M.; Belderrain, T. R.; Nicasio, M. C.; Trofimenko, S.; Perez, P. J. *Chem. Commun.* **2002**, 2998.

18.   Bachmann, S.; Fielenbach, D.; Jorgensen, K. A. *Org. Biomol. Chem.* **2004**, *2*, 3044.

19.   Zhu, Z.; Espenson, J. H. *J. Am. Chem. Soc.* **1996**, *118*, 9901.

20.   Ho, C.-M.; Zhang, J.-L.; Zhou, C.-Y.; Chan, O.-Y.; Yan, J. J.; Zhang, F.-Y.; Huang, J.-S.; Che, C.-M. *J. Am. Chem. Soc.* **2010**, *132*, 1886.

21.   Galardon, E.; Le Maux, P.; Simonneaux, G. *J. Chem. Soc., Perkin Trans. 1* **1997**, 2455.

22.   Le Maux, P.; Nicolas, I.; Chevance, S.; Simonneaux, G. *Tetrahedron* **2010**, *66*, 4462.

23.   Anding, B. J.; Woo, L. K. In *Handbook of Porphyrin Science*; Kadish, K. M., Guilard, R., Smith, K., Eds.; World Scientific Publishing Company: Hackensack, NJ, 2012; Vol. 21, p 145.

24.   Mbuvi, H.; Klobukowski, E.; Roberts, G.; Woo, L. K. *J. Porphyrins Phthalocyanines* **2010**, *14*, 284.

25.   Nicolas, I.; Roisnel, T.; Le Maux, P.; Simonneaux, G. *Tetrahedron Lett.* **2009**, *50*, 5149.

26. Aviv, I.; Gross, Z. *Chem. Eur. J.* **2008**, *14*, 3995.

27. Baumann, L.; Mbuvi, H.; Du, G.; Woo, L. K. *Organometallics* **2007**, *26*, 3995.

28. Mangion, I. K.; Nwamba, I. K.; Shevlin, M.; Huffman, M. A. *Org. Lett.* **2009**, *11*, 3566.

29. Wang, J.-C.; Xu, Z.-J.; Guo, Z.; Deng, Q.-H.; Zhou, C.-Y.; Wan, X.-L.; Che, C.-M. *Chem. Commun.* **2012**, *48*, 4299.

30. Ichinose, M.; Suematsu, H.; Katsuki, T. *Angew. Chem. Intl. Ed.* **2009**, *48*, 3121.

31. Anding, B. J.; Ellern, A.; Woo, L. K. *Organometallics* **2012**, *31*, 3628.

32. Anding, B. J.; Brgoch, J.; Miller, G. J.; Woo, L. K. *Organometallics* **2012**, *31*, 5586.

33. Suematsu, H.; Katsuki, T. *J. Am. Chem. Soc.* **2009**, *131*, 14218.

34. Lopez Sanchez, C.; Rodríguez García, C.; Lopez, S. *Synlett* **2012**, *23*, 2469.

35. Yasutomi, Y.; Suematsu, H.; Katsuki, T. *J. Am. Chem. Soc.* **2010**, *132*, 4510.

36. Doyle, M. P.; McKervey, M. A.; Ye, T. *Modern Catalytic Methods for Organic Synthesis with Diazo Compounds: From Cyclopropanes to Ylides*; Wiley-Interscience: New York, **1998**.

37. Zhu, B.; Angelici, R. J. *Chem. Commun.* **2007**, 2157.

38. Hong, D.; Zhu, Y.; Li, Y.; Lin, X.; Lu, P.; Wang, Y. *Org. Lett.* **2011**, *13*, 4668.

39. Kadish, K. M.; Cornillon, J. L.; Mitaine, P.; Deng, Y. J.; Korp, J. D. *Inorg. Chem.* **1989**, *28*, 2534.

40. Wang, P.; Adams, J. *J. Am. Chem. Soc.* **1994**, *116*, 3296.

41. Djukic, J.-P.; Young, V. G.; Woo, L. K. *Organometallics* **1994**, *13*, 3995.

42. Zhai, H.; Bunn, A.; Wayland, B. *Chem. Commun.* **2001**, 1294.

43. Wang, H. *Int. J. Electrochem. Sci.* **2011**, *6*, 1720.

44. Godefroi, E. F.; Eycken, C. A. M. v. d.; Janssen, P. A. J. *J. Org. Chem.* **1966**, *31*, 806.

45. Yeung, S. K.; Chan, K. S. *Organometallics* **2005**, *24*, 6426.

46. Ogoshi, H.; Setsune, J.; Yoshida, Z. *J. Organomet. Chem.* **1978**, *159*, 317.

47. Zhao, W.-J.; Yan, M.; Huang, D.; Ji, S.-J. *Tetrahedron* **2005**, *61*, 5585.

48. Wolfe, D. *Eur. J. Org. Chem.* **2007**, *2007*, 2825.

49. Ando, A. *Tetrahedron* **1989**, *45*, 4969.

50. Dan, H.; Guo-Ming, J.; Hong-Xia, C.; Wen-Dong, G. *Synth. Commun.* **2010**, *40*, 229.

51. Hii, K. K.; Thornton-Pett, M.; Jutand, A.; Tooze, R. P. *Organometallics* **1999**, *18*, 1887.

52. Burks, E. *Synlett* **1998**, *1998*, 1285.

53. Saha, M. *Bangladesh J. Sci. Ind. Res.* **1999**, *34*, 149.

54. Kuninobu, Y.; Nishi, M.; Takai, K. *Chem. Commun.* **2010**, *46*, 8860.

55. Wang, Y.; Zhu, Y.; Chen, Z.; Mi, A.; Hu, W.; Doyle, M. P. *Org. Lett.* **2003**, *5*, 3923.

Appendix C

Time-Course of Reactions

In addition to the kinetics investigations discussed in the article, a qualitative rate profile was briefly examined as a function of the electronic nature of the substrate.
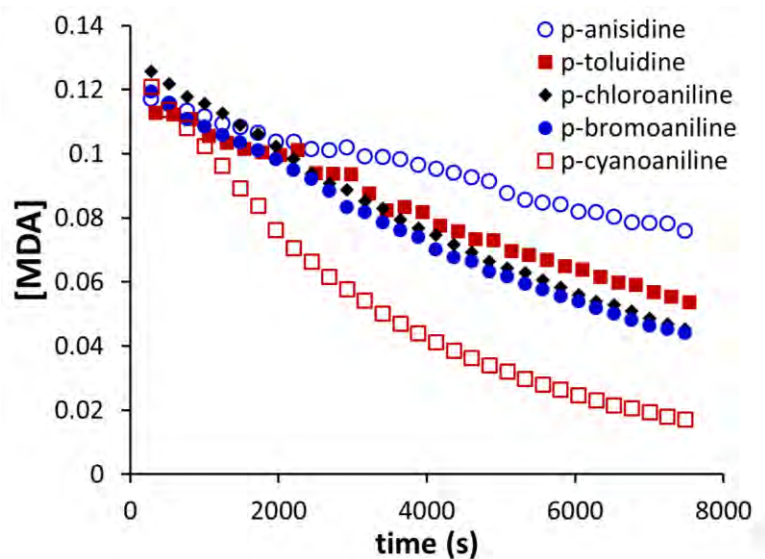
Figure 4.7: The overall loss of MDA over time for substrate competition reactions using different *para*-substituted anilines. Reactions were run using 0.119 M aniline, 0.119 M para-substituted aniline, 0.117 M MDA, and 8.92×10^{-6} M Ir(TTP)CH$_3$.

Equilibrium Binding Studies

Binding studies were explored using an Hewlett-Packard/Agilent Technologies 8453 UV-Vis spectrophotometer. All samples were collected in a 1.0-mm path length cell. Benzene was used as the solvent to prevent photolysis of Ir(TTP)CH$_3$, which will readily form Ir(TTP)Cl(CO) in methylene chloride or chloroform. Equilibrium constants were determined by comparing the Soret bands for solutions containing 1:1 and 2:1 mixtures of ligand to Ir(TTP)CH$_3$ with those of pure Ir(TTP)CH$_3$ and Ir(TTP)CH$_3$(L) (Figures 4.8 – 4.16). The spectra of pure Ir(TTP)CH$_3$(L) was obtained by dissolving Ir(TTP)CH$_3$ in a large excess of ligand (0.1 M solutions).
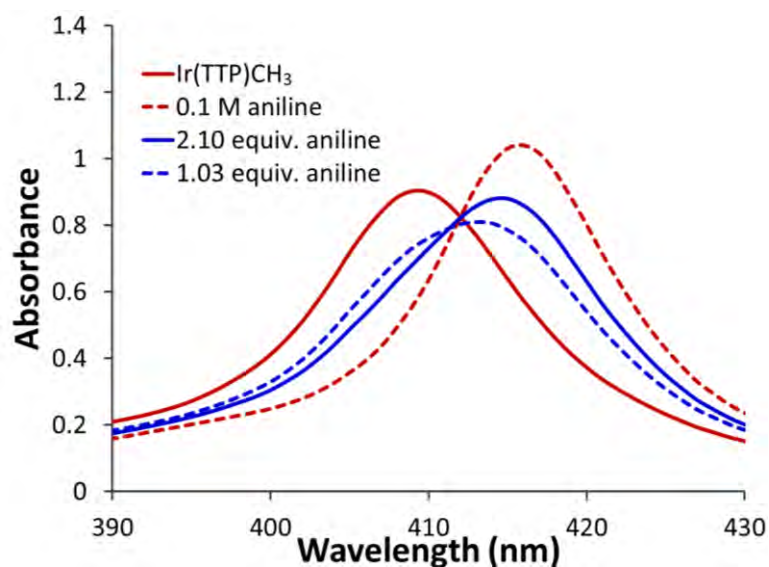
Figure 4.8: Absorbance spectra for 4.59×10^{-5} M Ir(TTP)CH$_3$ in benzene (solid red), in 0.1 M aniline and benzene (dashed red), in 9.64×10^{-5} M aniline in benzene (solid blue), and in 4.81×10^{-5} M aniline in benzene (dashed blue). **K = 2.7 ± 0.2 × 10^4.**
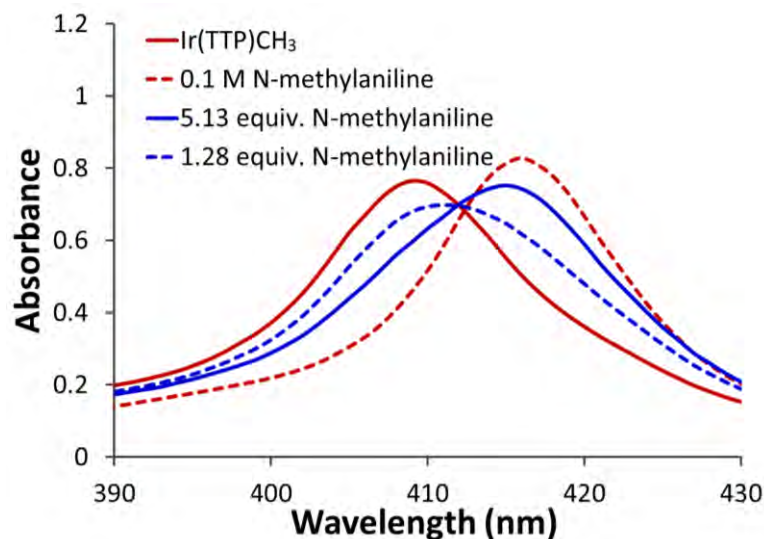
Figure 4.9: Absorbance spectra for 4.00×10^{-5} M Ir(TTP)CH$_3$ in benzene (solid red), in 0.1 M N-methylaniline and benzene (dashed red), in 1.97×10^{-4} M N-methylaniline in benzene (solid blue), and in 4.93×10^{-5} M N-methylaniline in benzene (dashed blue). **K = 1.1 ± 0.2 × 10^4.**
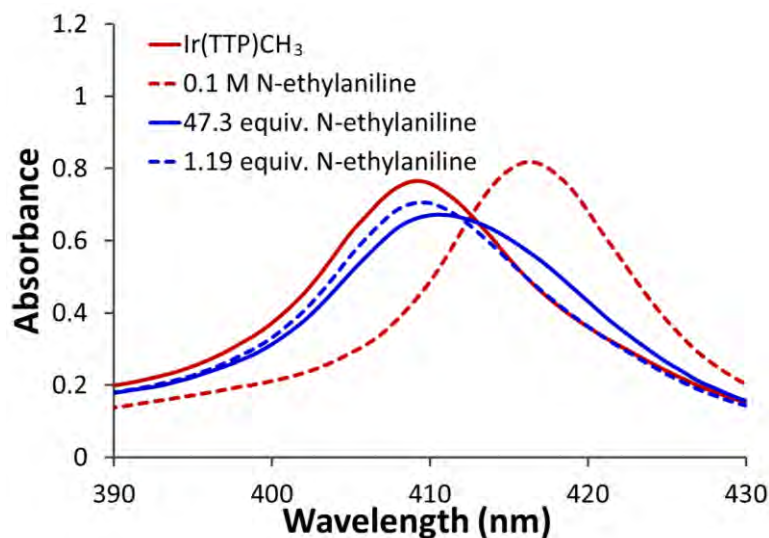
Figure 4.10: Absorbance spectra for 4.00×10^{-5} M Ir(TTP)CH$_3$ in benzene (solid red), in 0.1 M N-ethylaniline and benzene (dashed red), in 1.89×10^{-3} M N-ethylaniline in benzene (solid blue), and in 4.74×10^{-5} M N-ethylaniline in benzene (dashed blue). **K = 5.6 ± 4.9 × 10^2.**
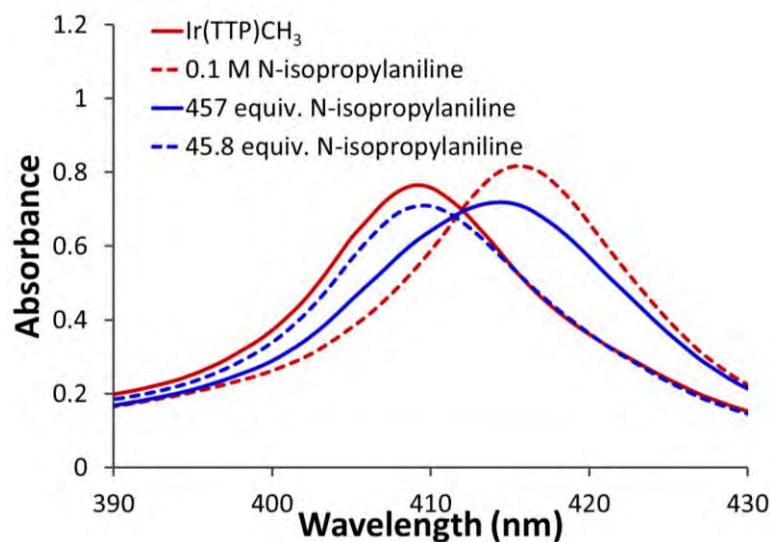
Figure 4.11: Absorbance spectra for 4.00×10^{-5} M Ir(TTP)CH$_3$ in benzene (solid red), in 0.1 M N-isopropylaniline and benzene (dashed red), in 1.83×10^{-2} M N-isopropylaniline in benzene (solid blue), and in 1.83×10^{-3} M N-isopropylaniline in benzene (dashed blue). **K = 92 ± 22.**
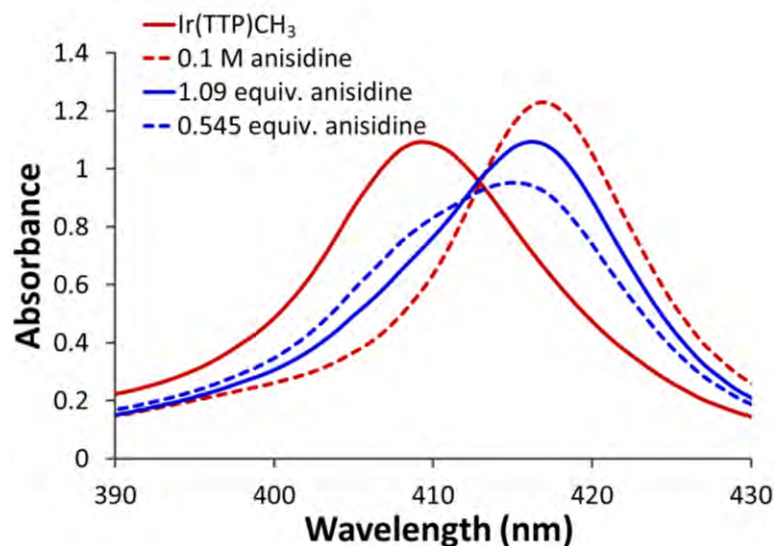
Figure 4.12: Absorbance spectra for 4.95×10^{-5} M Ir(TTP)CH$_3$ in benzene (solid red), in 0.1 M anisidine and benzene (dashed red), in 5.39×10^{-5} M anisidine in benzene (solid blue), and in 2.70×10^{-5} M anisidine in benzene (dashed blue). **K = 2.3 ± 2.3 × 10^5.**
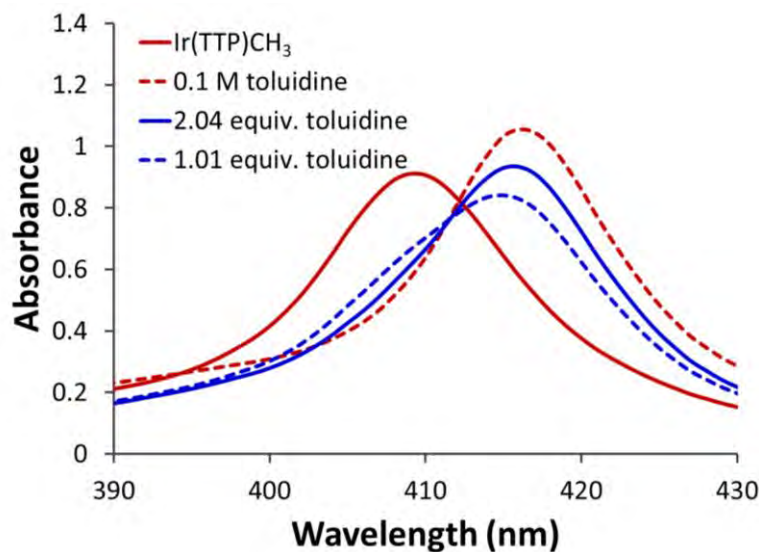
Figure 4.13: Absorbance spectra for 4.63×10^{-5} M Ir(TTP)CH$_3$ in benzene (solid red), in 0.1 M toluidine and benzene (dashed red), in 9.36×10^{-5} M toluidine in benzene (solid blue), and in 4.68×10^{-5} M toluidine in benzene (dashed blue). **K = 2.7 ± 0.2 × 10^4.**
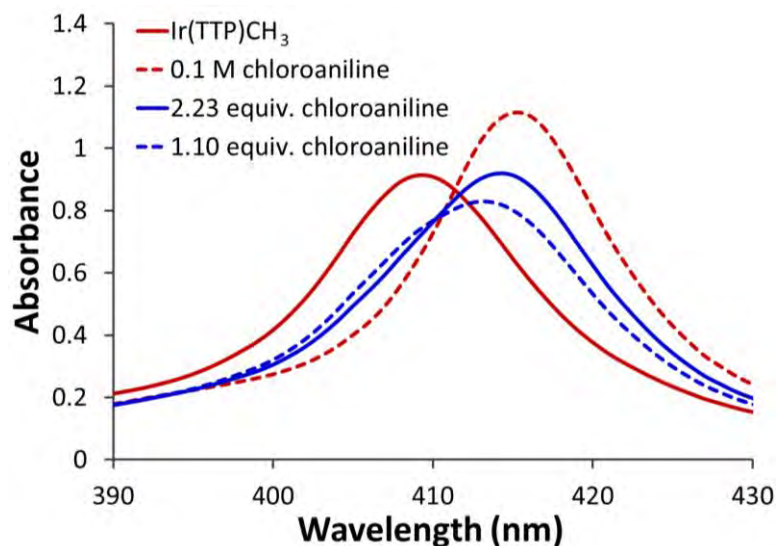
Figure 4.14: Absorbance spectra for 4.64×10^{-5} M Ir(TTP)CH$_3$ in benzene (solid red), in 0.1 M chloroaniline and benzene (dashed red), in 1.02×10^{-4} M chloroaniline in benzene (solid blue), and in 5.11×10^{-5} M chloroaniline in benzene (dashed blue). **K = 9.3 ± 0.7 × 10^4.**
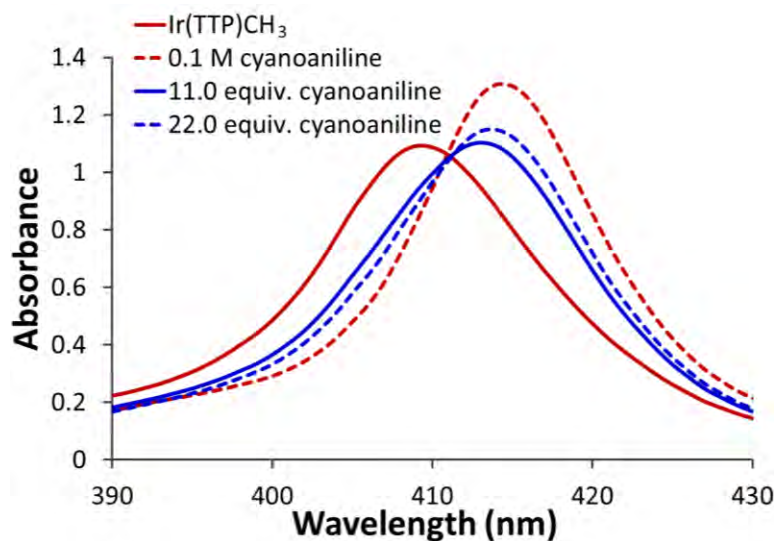
Figure 4.15: Absorbance spectra for 4.95×10^{-5} M Ir(TTP)CH$_3$ in benzene (solid red), in 0.1 M cyanoaniline and benzene (dashed red), in 5.34×10^{-4} M cyanoaniline in benzene (solid blue), and in 1.09×10^{-3} M cyanoaniline in benzene (dashed blue). **K = 2.4 ± 0.4 × 10^3.**
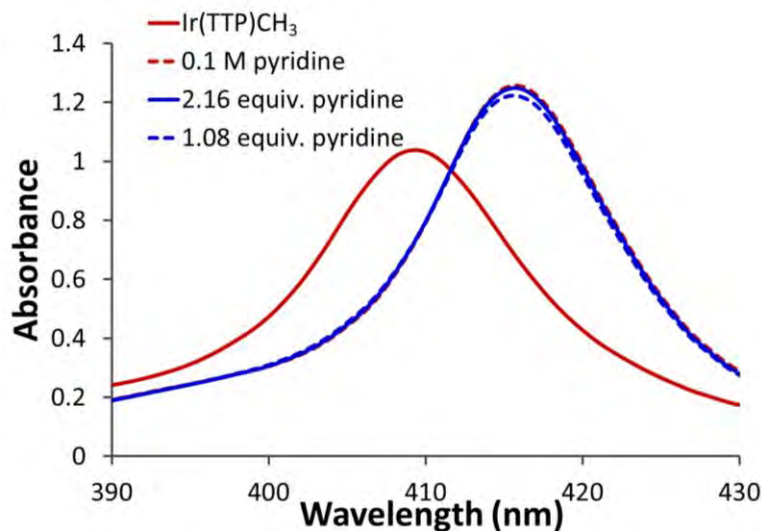
Figure 4.16: Absorbance spectra for 5.27×10^{-5} M Ir(TTP)CH$_3$ in benzene (solid red), in 0.1 M pyridine and benzene (dashed red), in 1.14×10^{-4} M pyridine in benzene (solid blue), and in 5.71×10^{-5} M pyridine in benzene (dashed blue). **K = 2.4 ± 1.8 × 10^6.**

Absorption Spectroscopy Data
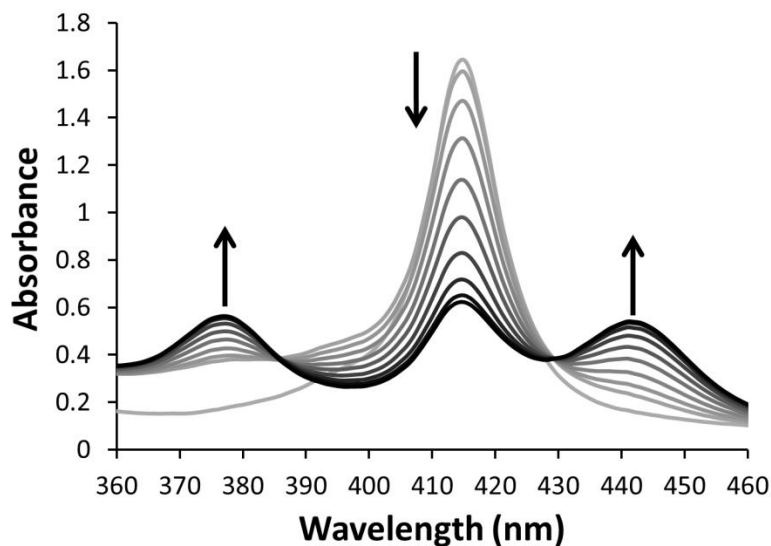
Figure 4.17: Absorbance spectra for the second addition of EDA (105 μmol addition, 210 μmol total) to a CH_2Cl_2 solution of aniline (54 μmol) and Ir(TTP)CH$_3$ (7.46×10^{-2} μmol). Spectra were acquired at 10 second intervals after EDA addition. Reaction progress is represented by a transition from gray to black. The intermediate bands (black) converted back to the lone band representing Ir(TTP)CH3(aniline) (415 nm) over approximately 3 minutes.
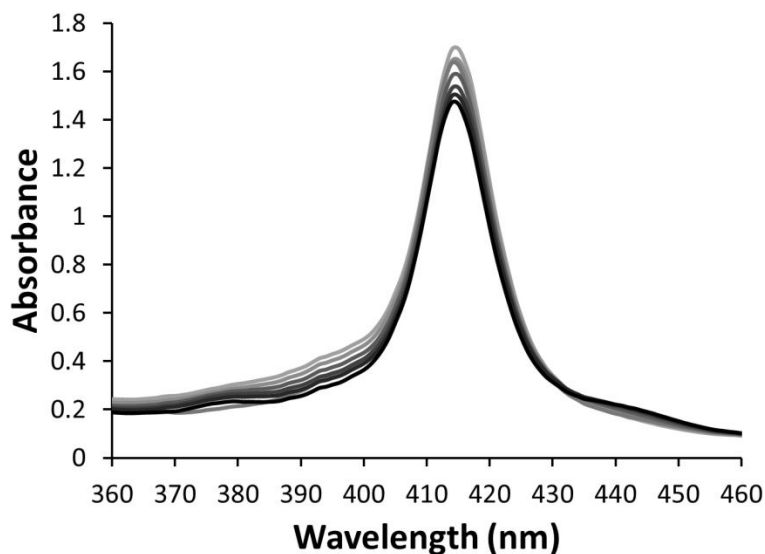
Figure 4.18: Absorbance spectra for the addition of EDA (105 μmol) to a CH_2Cl_2 solution of aniline (54 μmol) and Ir(TTP)CH$_3$ (7.46×10^{-2} μmol). Spectra were acquired at 10 second intervals after EDA addition. Reaction progress is represented by a transition from gray to black.
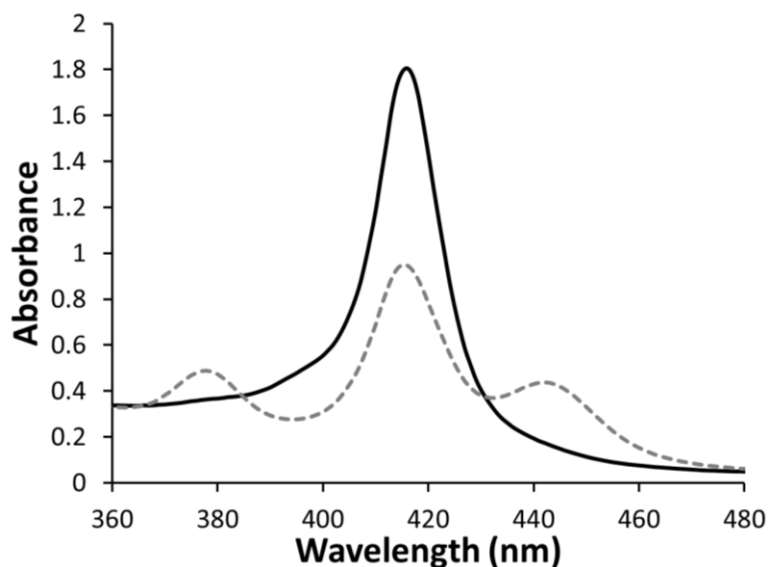
Figure 4.19: Addition of EDA (105 μmol) to a solution of Ir(TTP)CH$_3$ (7.24 × 10^{-2} μmol) and *p*-anisidine (26.0 μmol) in CH$_2$Cl$_2$. The shown spectra depict the Soret band(s) immediately after EDA addition (solid) and at the point of lowest absorbance for the 415 nm band (dashed), which occurred at 243 seconds after EDA addition.
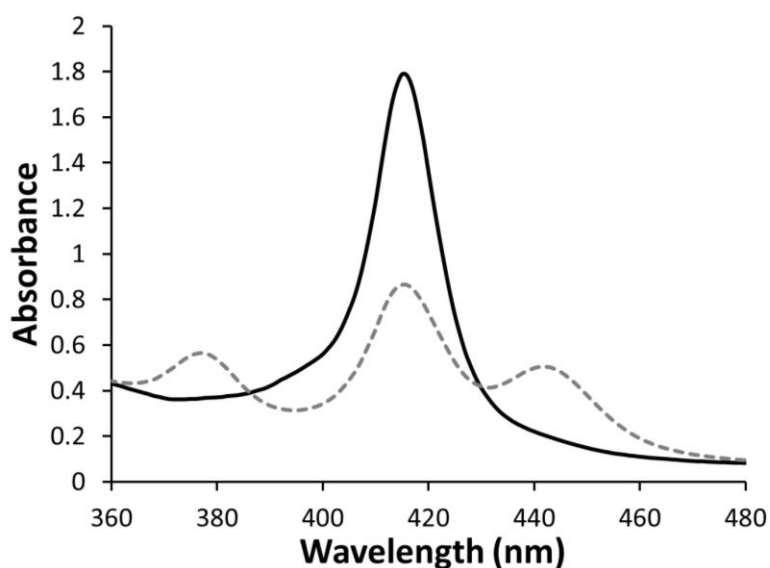
Figure 4.20: Addition of EDA (105 μmol) to a solution of Ir(TTP)CH3 (7.24 × 10^{-2} μmol) and *p*-toluidine (26.0 μmol) in CH$_2$Cl$_2$. The shown spectra depict the Soret band(s) immediately after EDA addition (solid) and at the point of lowest absorbance for the 415 nm band (dashed), which occurred at 123 seconds after EDA addition.
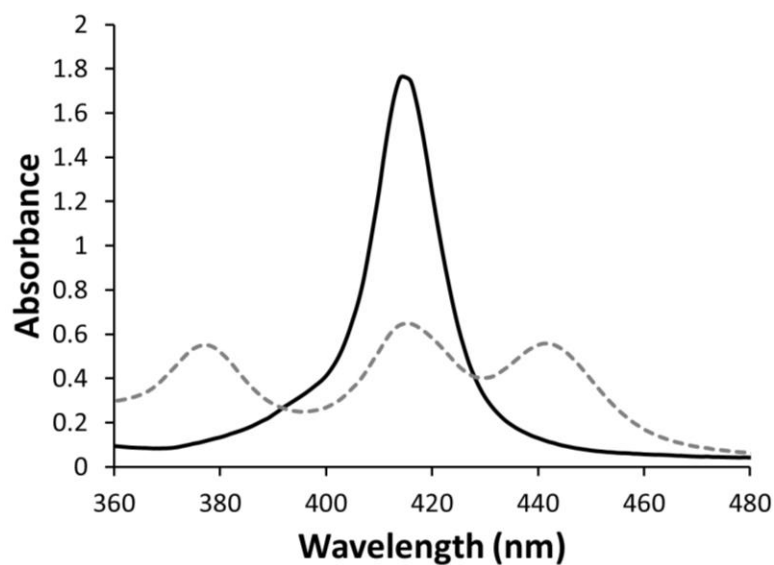
Figure 4.21: Addition of EDA (105 μmol) to a solution of Ir(TTP)CH$_3$ (7.24 × 10^{-2} μmol) and aniline (25.9 μmol) in CH$_2$Cl$_2$. The shown spectra depict the Soret band(s) immediately after EDA addition (solid) and at the point of lowest absorbance for the 415 nm band (dashed), which occurred at 93 seconds after EDA addition.
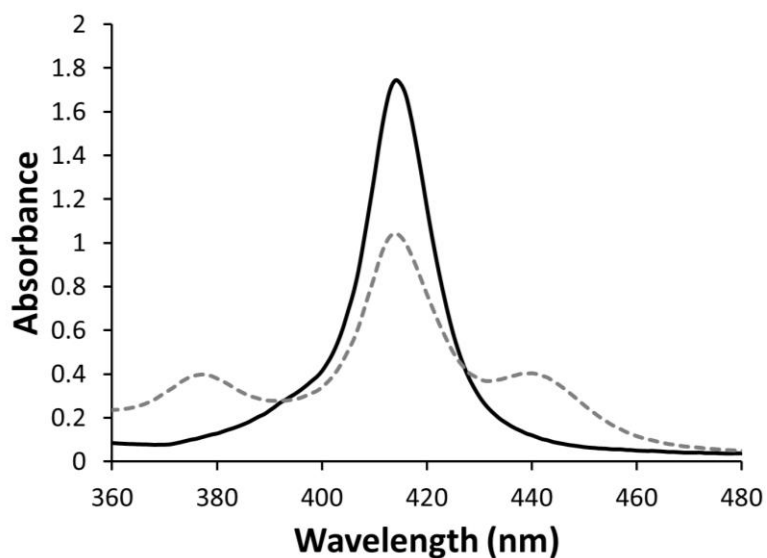
Figure 4.22: Addition of EDA (105 μmol) to a solution of Ir(TTP)CH$_3$ (7.24 × 10^{-2} μmol) and *p*-chloroaniline (26.0 μmol) in CH$_2$Cl$_2$. The shown spectra depict the Soret band(s) immediately after EDA addition (solid) and at the point of lowest absorbance for the 415 nm band (dashed), which occurred at 63 seconds after EDA addition.
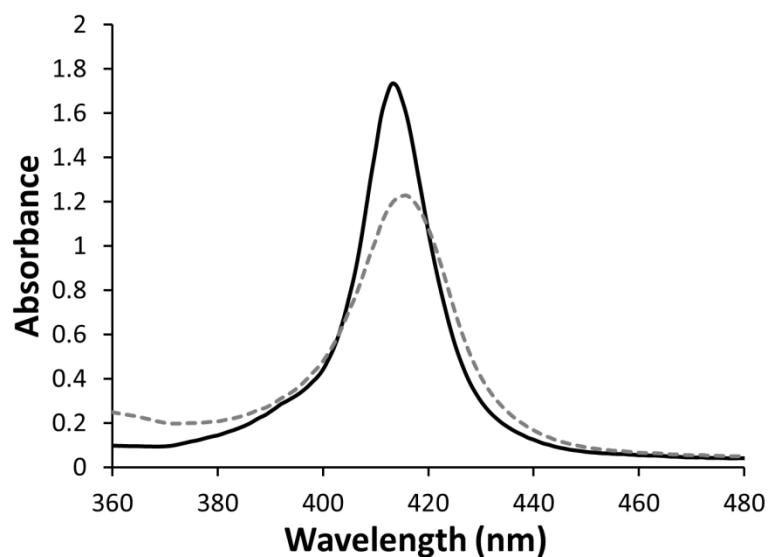
Figure 4.23: Addition of EDA (105 μmol) to a solution of Ir(TTP)CH$_3$ (7.24 × 10^{-2} μmol) and *p*-cyanoaniline (25.9 μmol) in CH$_2$Cl$_2$. The shown spectra depict the Soret band(s) immediately after EDA addition (solid) and at the point of lowest absorbance for the 415 nm band (dashed). Unlike the other samples, the intermediate bands at 375 and 440 nm were never observed, and the 415 nm band continued to decrease in absorbance over time.
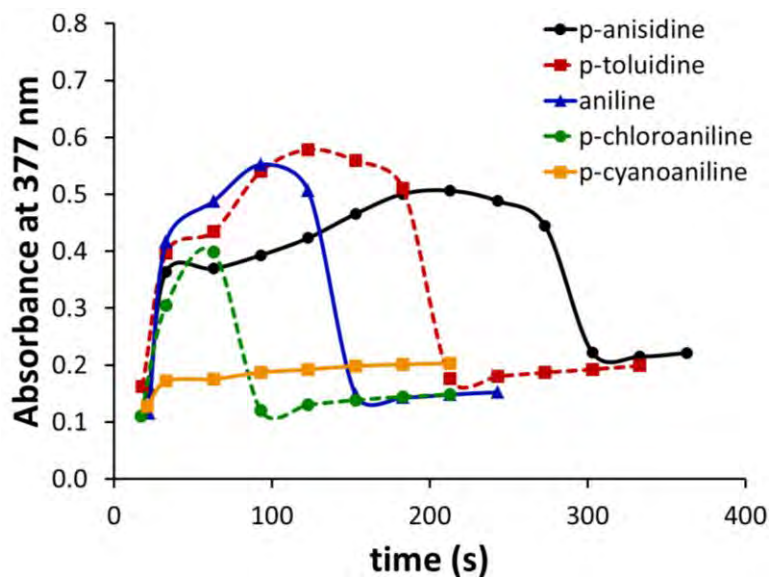
Figure 4.24: Formation of the intermediate after EDA addition, as monitored by the plot of the intermediate band at 377 nm verses time. Although it seems like the intermediate forms immediately after EDA addition for all substrates, a rise in the 377 nm band intensity may also be the result of the loss of isosbestic behavior as shown in Figures 4.5 and 4.25. Reaction conditions: Ir(TTP)CH$_3$ (7.24 × 10^{-5} M), EDA (0.105 M), and various aniline substrates (0.026 M). Data points were collected at 30 second intervals.
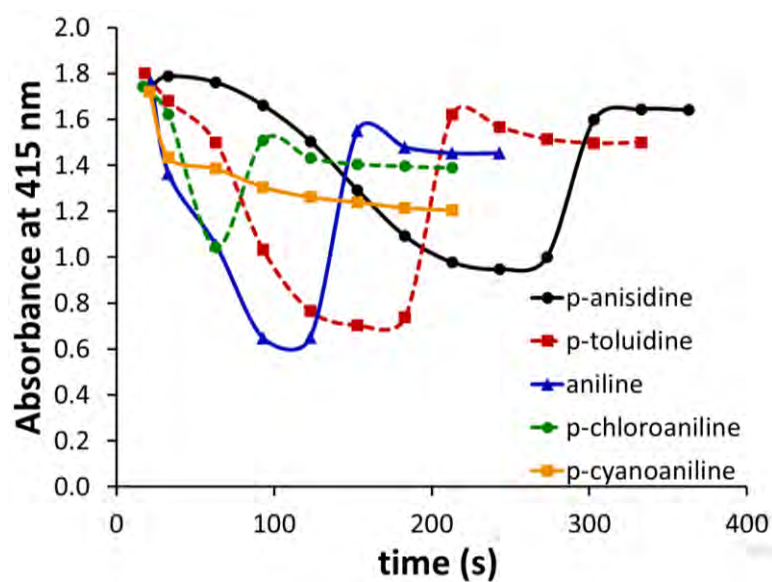
Figure 4.25: Loss of the 415 nm Soret band of Ir(TTP)CH$_3$(L), where L = aniline substrate, after EDA addition. Results match the formation of the intermediate band at 441 nm shown in Figure 5. Reaction conditions: Ir(TTP)CH$_3$ (7.24 × 10^{-5} M), EDA (0.105 M), and various aniline substrates (0.026 M). Data points were collected at 30 second intervals.

Photolysis Experiments
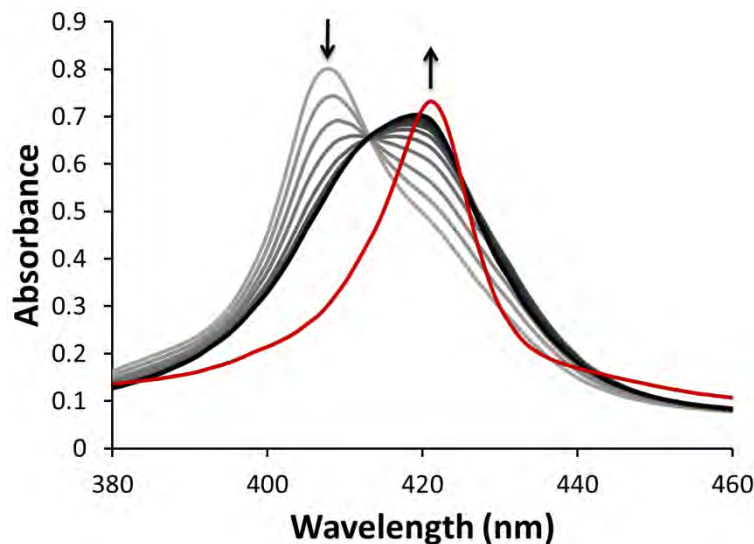
Figure 4.26: A CH$_2$Cl$_2$ solution of Ir(TTP)CH$_3$ (4.29 × 10^{-5} µmol) in a 1-mm path length cell was exposed to ambient room light. Spectra were acquired every 60 seconds, showing a decrease in the Soret band of Ir(TTP)CH$_3$ and an increase in the Soret of Ir(TTP)Cl(CO) (gray to black). After 12 minutes under ambient light, the cell was exposed to a sun lamp for 5 minutes. The resulting spectrum (red) is that of Ir(TTP)Cl(CO).
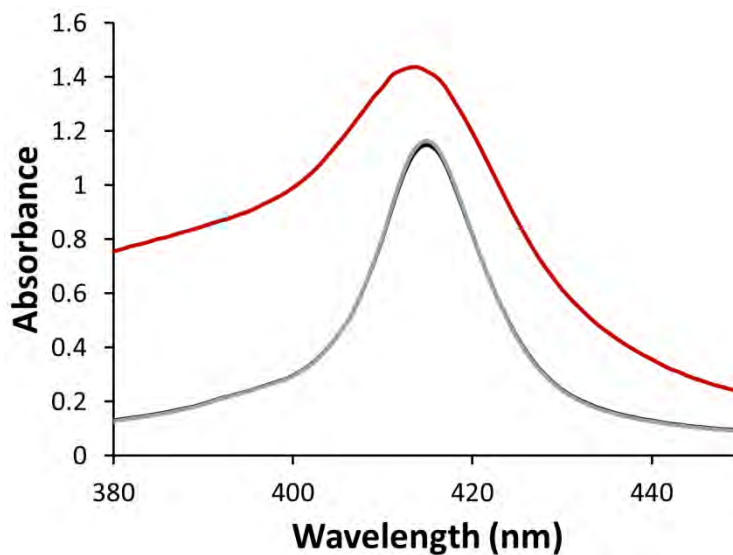
Figure 4.27: A CH$_2$Cl$_2$ solution of Ir(TTP)CH$_3$ (4.29 × 10^{-5} µmol) and aniline (0.1 M) in a 1-mm path length cell was exposed to ambient room light. Spectra were acquired every 60 seconds for 10 minutes, showing no change in the Soret band of Ir(TTP)CH$_3$(aniline). The cell was then exposed to a sun lamp for 5 minutes. The resulting spectrum (red) exhibits a broad absorbance between 310 and 500 nm, but the λ_{max} still corresponds to Ir(TTP)CH$_3$(aniline).

Spectra of Previously Unreported Compounds

400 MHz
CDCl₃

7.24
7.22
7.20
6.74
6.72
6.70
6.68

4.24
4.22
4.20
4.18
4.17
4.15
4.13
3.92

1.29
1.27
1.25
1.22
1.20
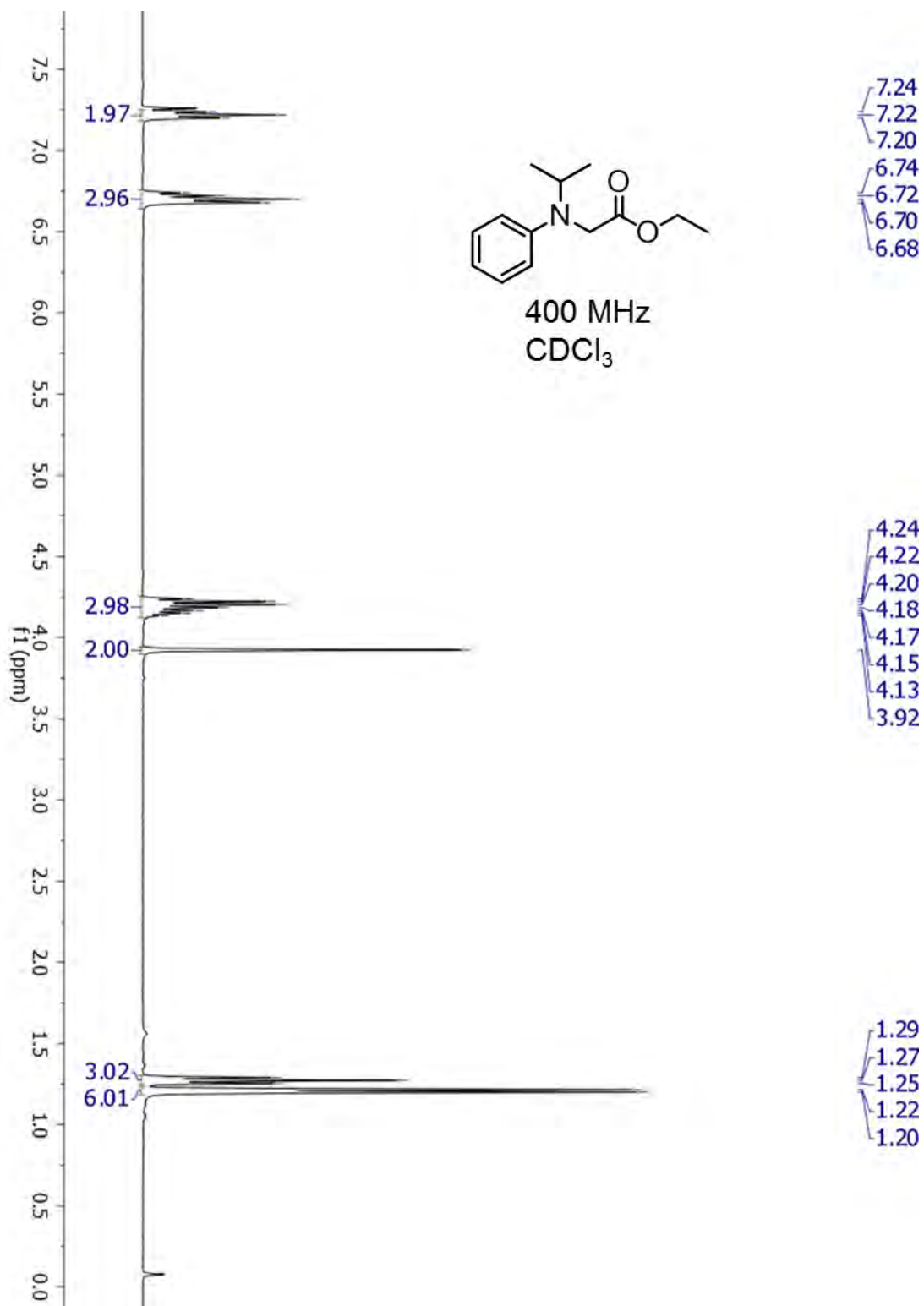
Figure 4.28: ¹H NMR spectrum of ethyl 2-(isopropyl(phenyl)amino)acetate.
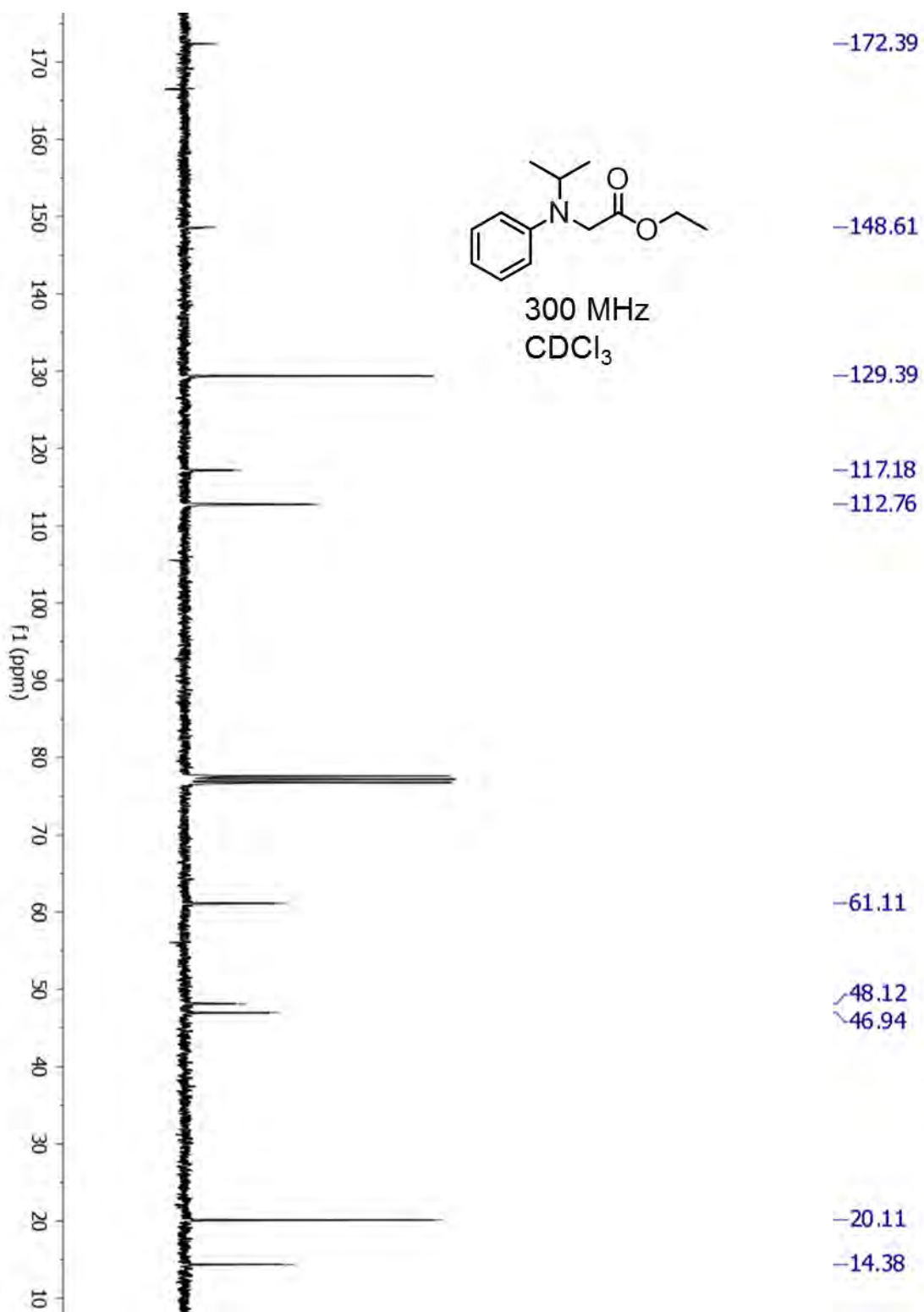
Figure 4.29: 13C NMR spectrum of ethyl 2-(isopropyl(phenyl)amino)acetate.
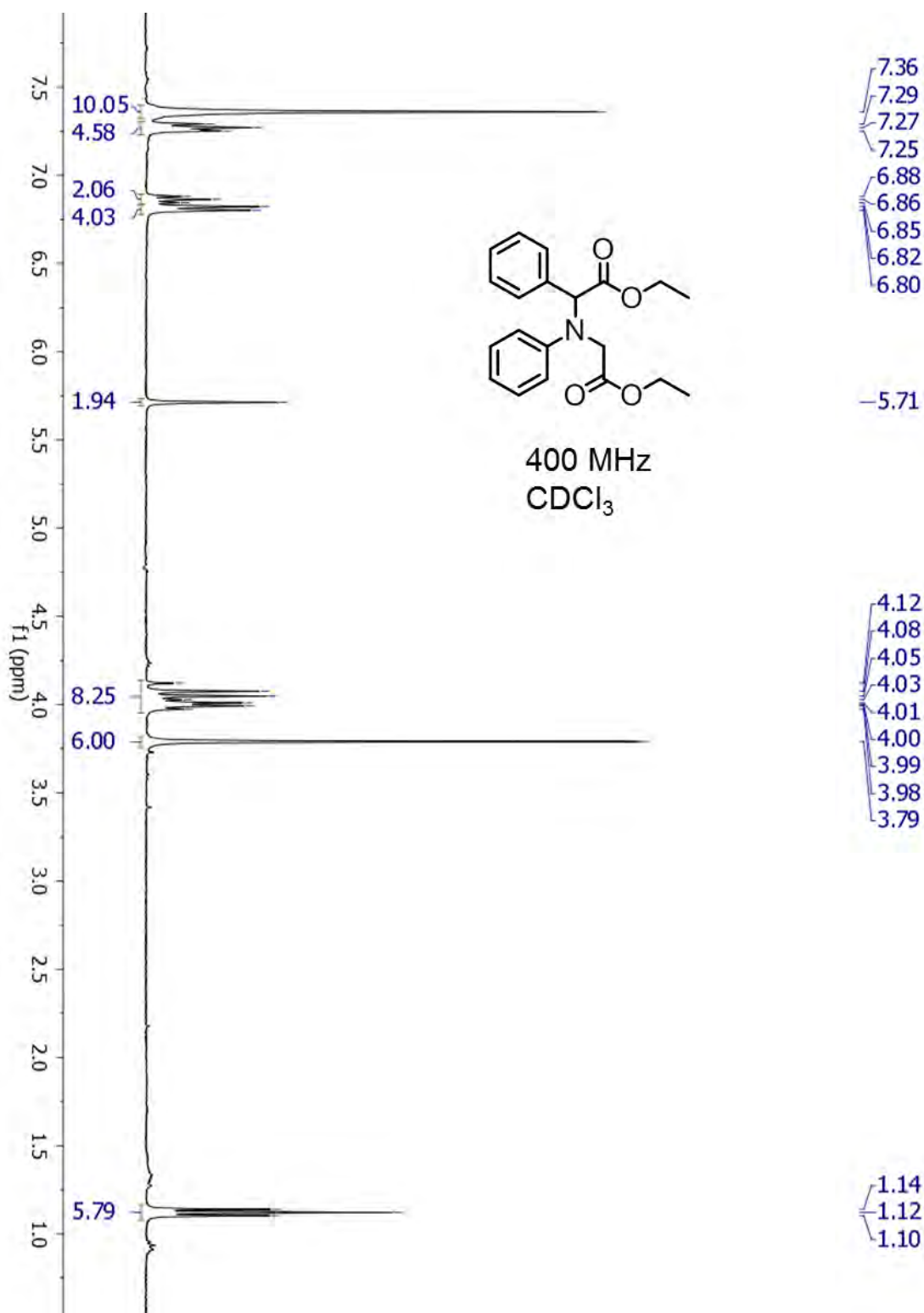
Figure 4.30: ^{1}H NMR spectrum of methyl 2-((2-ethoxy-2-oxoethyl)(phenyl)amino)-2-phenylacetate.
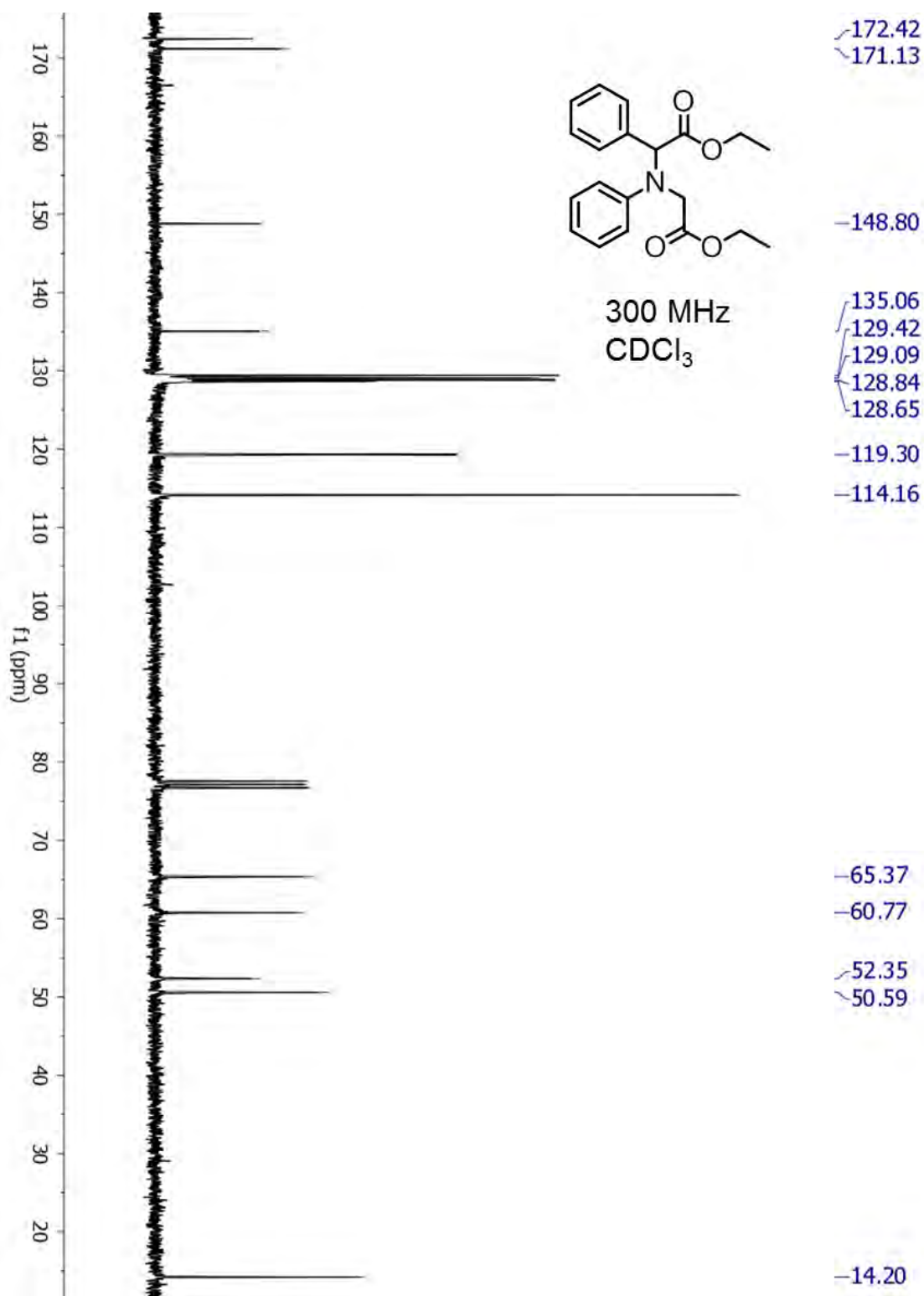
Figure 4.31: ^{13}C NMR spectrum of methyl 2-((2-ethoxy-2-oxoethyl)(phenyl)amino)-2-phenylacetate.
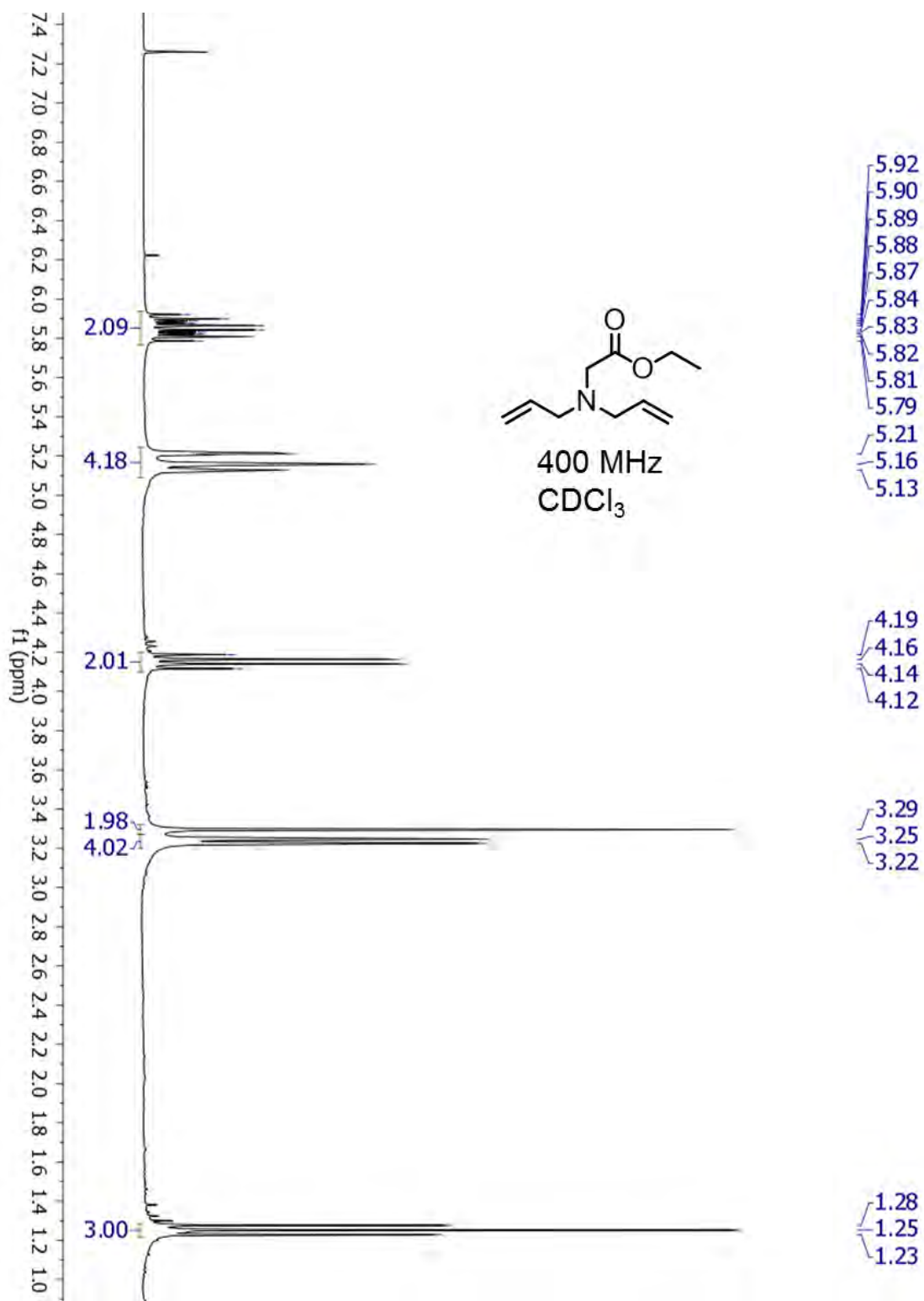
Figure 4.32: ^{1}H NMR spectrum of ethyl 2-(diallylamino)acetate (**19**).
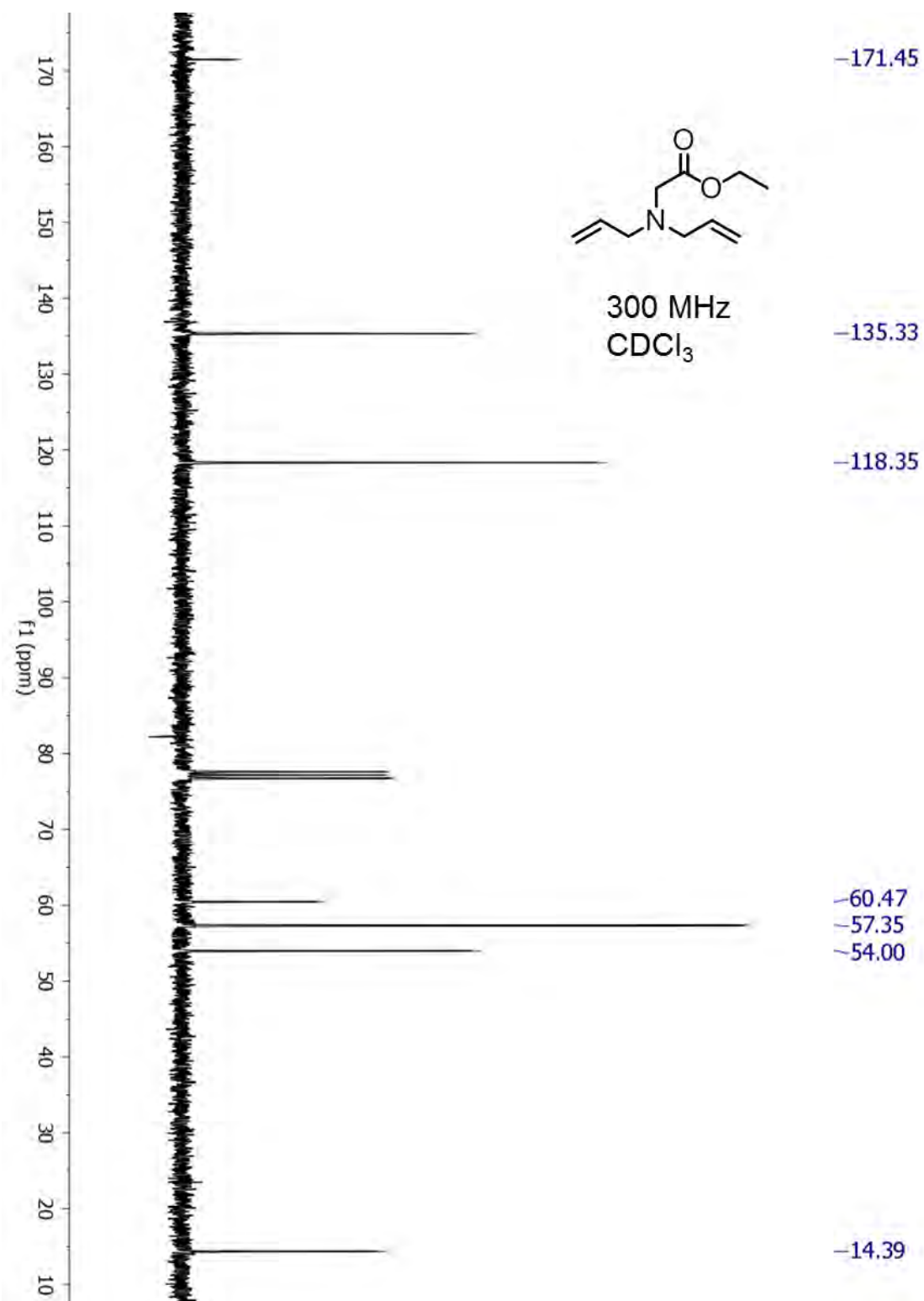
Figure 4.33: ^{13}C NMR spectrum of ethyl 2-(diallylamino)acetate (**19**).
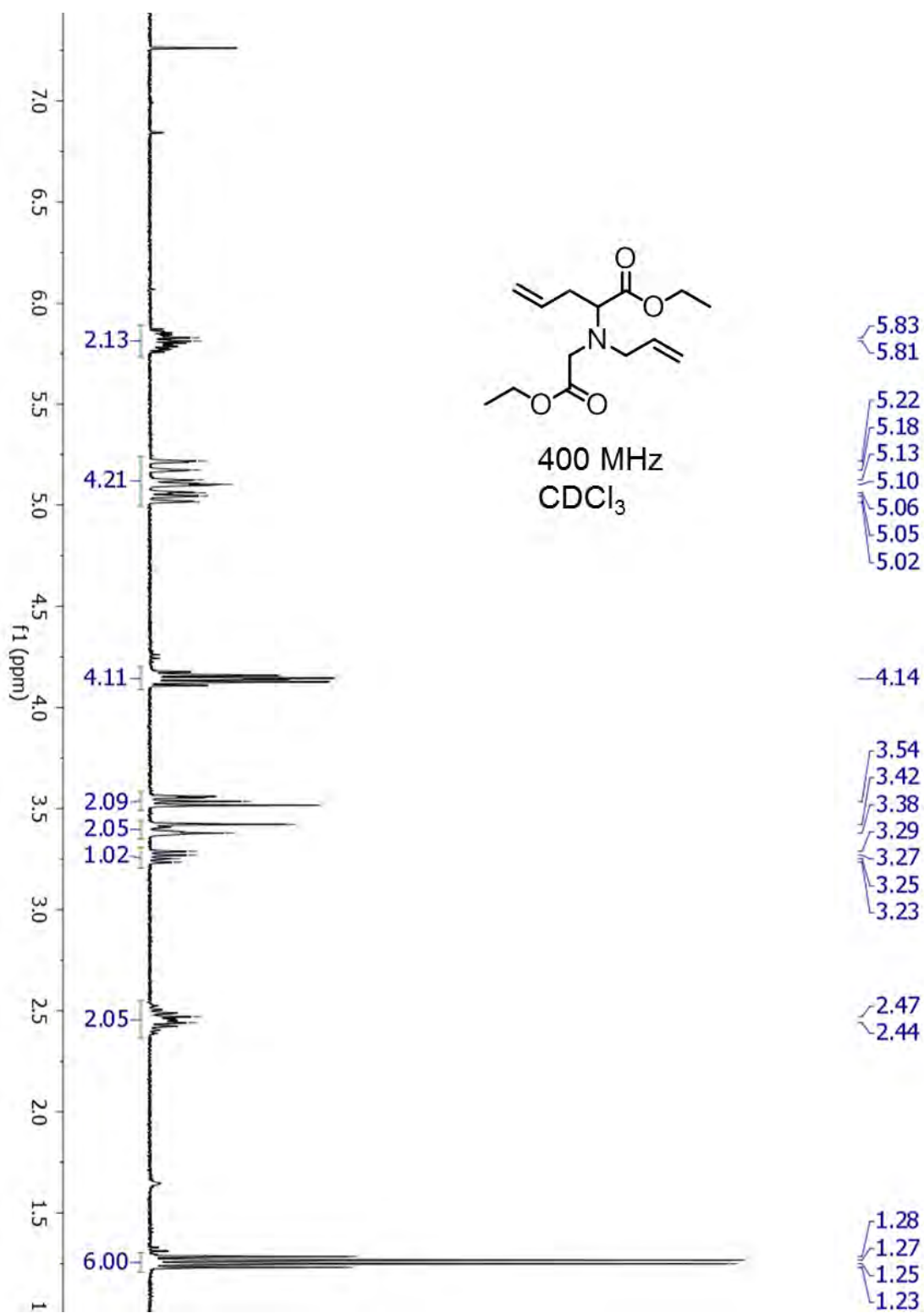
Figure 4.34: ^{1}H NMR spectrum of ethyl 2-(allyl(2-ethoxy-2-oxoethyl)amino)pent-4-enoate (**20**).

172.50
171.85

135.75
134.48

117.99
117.18

300 MHz
CDCl₃

63.64
60.50
60.37
55.53
51.67

34.87

14.49
14.30
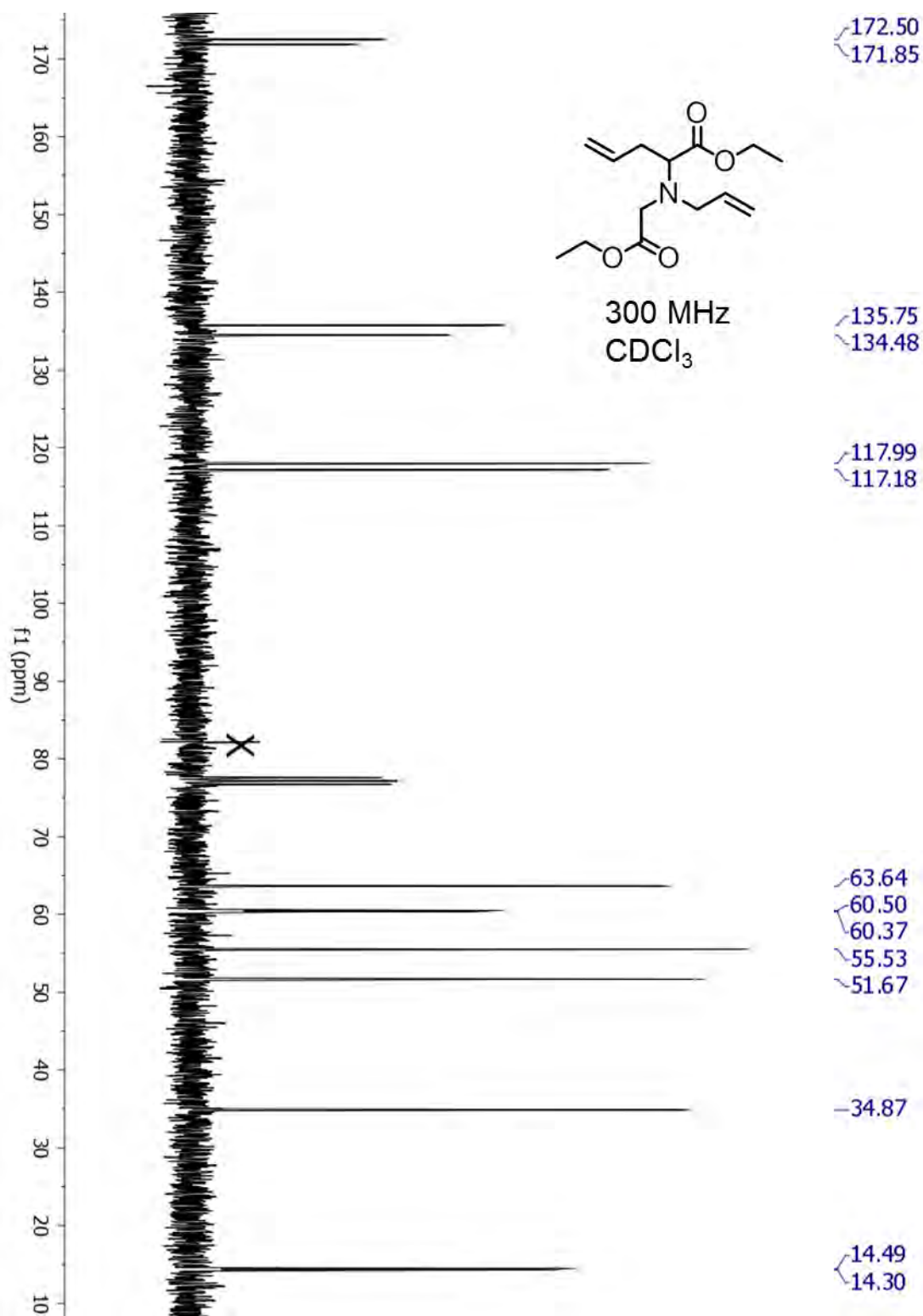
Figure 4.35: 13C NMR spectrum of ethyl 2-(allyl(2-ethoxy-2-oxoethyl)amino)pent-4-enoate (**20**).

CHAPTER 5.   COMPARISON STUDY OF RHODIUM AND IRIDIUM PORPHYRIN DIAMINOCARBENE AND N-HETEROCYCLIC CARBENE COMPLEXES

To be submitted to *Inorg. Chem.*

Bernie J. Anding, Arkady Ellern, and L. Keith Woo

Abstract

Iridium meso-tetratolylporphyrinato (TTP) mono- and bis-diaminocarbene complexes ($[Ir(TTP)[=C(NHBn)(NHR)]]_{2-x}(C\equiv NBn)_x]BF_4$ where R = Bn, *n*-Bu and x = 1, 0) were synthesized by nucleophilic addition of amines to the bis-isocyanide complex $[Ir(TTP)(C\equiv NBn)_2]BF_4$. Rhodium and iridium porphyrinato N-heterocyclic carbene (NHC) complexes ($M(TTP)CH_3(NHC)$ where NHC = 1,3-diethylimidazolylidene (deim) or 1-(*n*-butyl)-3-methylimidazolylidene (bmim)) were generated by direct coordination with the free NHC. Complexes were characterized by IR, NMR, and absorption spectroscopy, and the structures of several complexes were resolved by single-crystal X-ray diffraction. Variable temperature NMR revealed two dynamic processes in the NHC complexes. Rhodium NHC complexes demonstrated fluxional NHC coordination. NMR line-shape analyses on the NHC exchange between 284 K and 296 K revealed rate constants of 3.7 – 35 s^{-1} for deim displacement by bmim (forward reaction) and 2.2 – 19 s^{-1} for bmim displacement by deim (reverse reaction), which corresponded to $\Delta G^{\ddagger}_f$ of 66.4 ± 0.6 kJ mol^{-1} and $\Delta G^{\ddagger}_r$ of 65.6 ± 0.8 kJ mol^{-1}. Rates of NHC exchange with iridium were far slower, with first-order dissociation rate constants of 1.8 ± 0.4 × 10-4 s^{-1} for the forward reaction and 1.2 ± 0.1 × 10-4 s^{-1} for the reverse reaction at 298 K. These rate constants correspond to $\Delta G^{\ddagger}$ values of 94.4 ± 0.6 and 95.4 ± 0.2 kJ mol^{-1}, respectively. Equilibrium constants for the exchange reactions were 1.6 ± 0.2 with rhodium and 1.56 ± 0.04 with iridium, favoring the bmim complex in both cases. The log(K) values for NHC binding to $M(TTP)CH_3$ were 4.5 ± 0.3 (M = Rh) and 5.4 ± 0.5 (M = Ir), which were determined by spectrophotometric titrations at 23 ^{o}C. NHC complexes

also exhibited dynamic NMR features for *meso*-aryl–porphyrin C–C bond rotation in temperatures ranges between 243 and 323 K. Coalescence data for four different complexes revealed $\Delta G^{\ddagger}_{ROT}$ values of 59 – 63 kJ mol-1. These relatively low rotation barriers may result from ruffling distortions in the porphyrin core, which were observed in the molecular structures of the rhodium and iridium bmim complexes. The molecular structures also featured unusually long metal–carbene bonds for the bmim complexes (Rh–C_{NHC}: 2.255(3) Å and Ir–C_{NHC}: 2.194(4) Å).

Introduction

Metalloporphyrin complexes containing Fe, Ru, Os, Co, Rh, and Ir are useful catalysts for carbene transfer reactions including cyclopropanation, X–H insertion (X = C, N, O, and S), and ylide-forming reactions.[1] Particularly noteworthy is the dramatic reactivity differences displayed among the group 9 metalloporphyrin catalysts. For example, cyclopropanation of electron-deficient olefins is achieved with remarkable efficiency using cobalt(II) porphyrin catalysts, whereas yields with the other group 9 metalloporphyrin catalysts are modest.[2,3] This unusual activity was explained by the intermediacy of relatively nucleophilic cobalt-carbene complexes having radical character.[4-6] Unlike cobalt, rhodium and iridium porphyrin catalysts are typically in the +3 oxidation state and are believed to form traditional electrophilic Fischer-type carbene complexes. Despite this similarity, rhodium and iridium catalysts display notably divergent reactivity patterns from each other. Rhodium porphyrins catalyze cyclopropanation and C–H insertion reactions with rare *cis* and primary selectivity, respectively. However, these reactions are often slow and require somewhat forcing conditions. In contrast, iridium complexes do not induce remarkable diastereo- or regioselectivity but are extremely reactive and robust, generating cyclopropanation products rapidly at -78 °C with turnover numbers on the order of 10^5.[7] Additional insight on these reactivity differences may be achieved by further examination of rhodium and iridium porphyrin carbene complexes.

Rhodium and iridium porphyrin carbene complexes derived from alkyldiazoacetate compounds were observed spectroscopically,[8,9] but have not been successfully isolated in pure form. The only group 9 metalloporphyrin carbene complex that has been isolated and

structurally characterized by single-crystal X-ray analysis is a rhodium diaminocarbene complex (**21**).[10] This complex was synthesized via nucleophilic addition of benzylamine to bis(isocyanide)(tetraphenylporphyrinato)rhodium(III) hexafluorophosphate (Figure 5.1). Ease of isolation of diaminocarbene and the related N-heterocyclic carbene (NHC) complexes makes them useful models for metalloporphyrin-carbene studies. Accordingly, the work herein describes the synthesis, characterization, and structural comparison of new rhodium and iridium porphyrin diaminocarbene and NHC complexes.
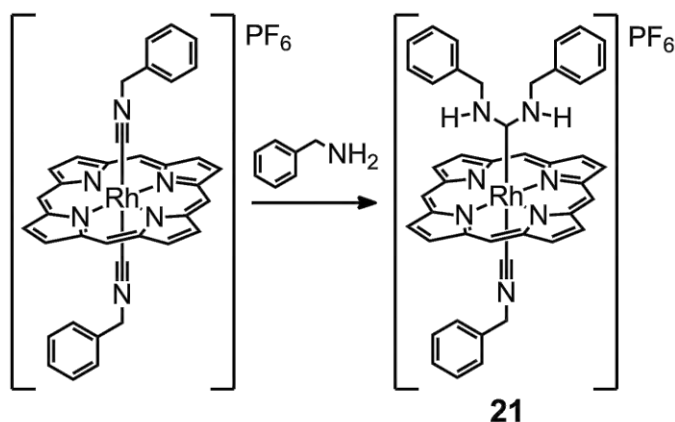
Figure 5.1: Nucleophilic attack on a bis(isocyanide)complex to generate complex **21**. Meso phenyl groups were omitted for clarity.

Results

An iridium diaminocarbene complex was synthesized using a synthetic route similar to that described previously for complex **21** (Figure 5.2).[10,11] Treating Ir(TTP)Cl(CO) (TTP = tetratolylporphyrinato) with silver tetrafluoroborate followed by excess benzyl isocyanide formed the bis(isocyanide) iridium complex (**22**), which was isolated in 61% yield after recrystallization. Complex **22** was characterized by ^{1}H NMR, ^{13}C NMR, and IR spectroscopy. New ^{1}H NMR signals observed at 6.98 (*p*-H, t, 2H), 6.79 (*m*-H, t, 4H), 4.80 (*o*-H, d, 4H), and 2.65 (-CH$_2$-, s, 4H) ppm were attributed to the isocyanide ligands. Significant upfield shifts, especially for the *ortho* and *meta* protons of the isocyanides, were due to the porphyrin ring current effect. Coordination to iridium also caused a shift in the C≡N bond IR stretching mode from 2151 cm^{-1} for the free isocyanide to 2228 cm^{-1}, indicating that the bound isocyanide is susceptible to nucleophilic attack.[12] This stretching frequency is similar to that of Rh(TTP)(C≡NBn)$_2$(PF$_6$) found at 2248 cm^{-1}.[10] The molecular structure of

22 was determined by single-crystal X-ray diffraction analysis (Figure 5.3). Complex **22** crystallized in the *C* 2/*c* space group with half of the molecule in the asymmetric unit. Complex **22** also displayed axial ligand disorder through a mirror plane, which required the atomic positions for the axial ligands to be approximated. Iridium was coordinated in a nearly ideal octahedral environment (Table 5.7; Appendix D), and the porphyrin ring displayed very little distortion from planarity (*vide infra*).
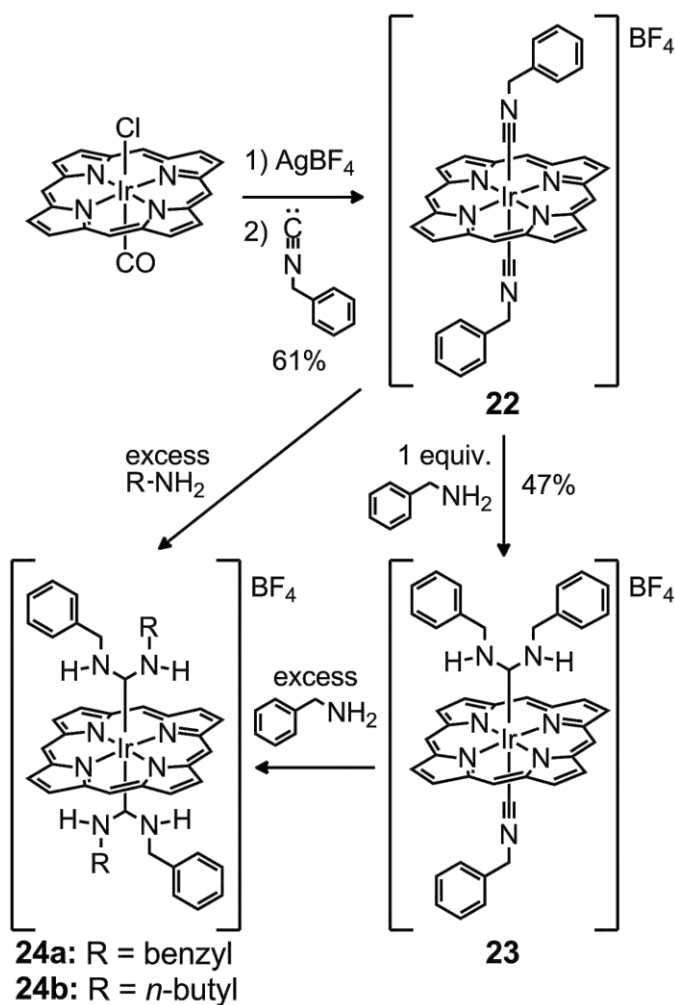

Figure 5.2: Synthesis of diaminocarbene (tetra-*p*-tolylporphyrinato)iridium complexes. *Meso p*-tolyl groups were omitted for clarity.

Nucleophilic addition to one of the coordinated isocyanide carbon atoms with benzylamine afforded the target diaminocarbene complex **23**. Signals corresponding to the diaminocarbene ligand were observed by ^{1}H NMR spectrum at 7.17 (*p*–H, t, 2H), 7.02 (*m*–H,

t, 4H), 5.31 (*o*–H, d, 4H), 2.07 (–CH$_2$–, d, 4H), and -1.89 (br, 2H, NH). The remaining isocyanide ligand displayed shifts similar to those observed in complex **22**. The presence of a bound isocyanide ligand was further confirmed by IR with a C≡N stretching band at 2218 cm^{-1}. A spectral characteristic of complex **23** involved an unusually large separation in chemical shifts of the *o*- and *o*'-protons on the *meso* aryl substituents at 7.91 and 7.53 ppm. The molecular structure of complex **23** was confirmed by single-crystal X-ray diffraction (Figure 5.4). Complex **23** crystallized in a C-centered monoclinic unit cell, in the *C* 2/*c* space group with a half of the molecule in the asymmetric unit. Similar to complex **22**, the axial ligands were disordered through symmetry, and the interatomic distances in those groups were constrained. Iridium inhabited a nearly ideal octahedral environment, and the porphyrin core was planar with very little distortion (*vide infra*).
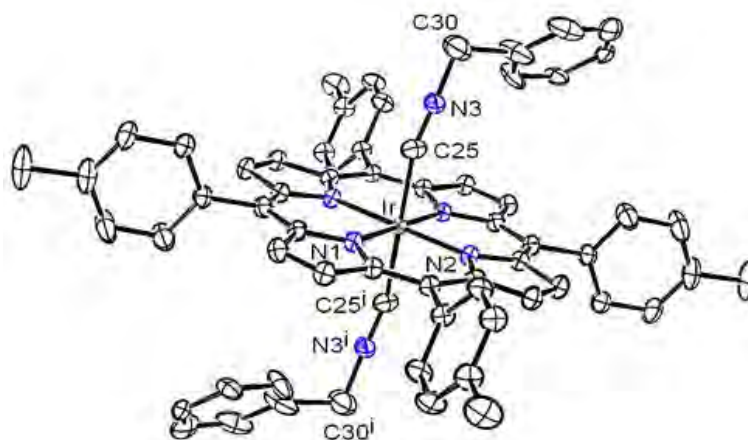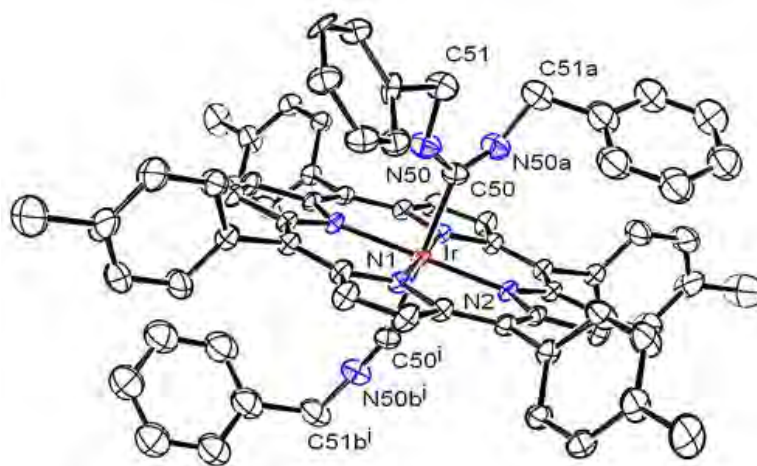

Figure 5.3:[13] ORTEP of complex **22** with 30% probability thermal ellipsoids. Selected bond distances (Å): Ir–N(1) = 2.045(4), Ir–N(2) = 2.044(4). Selected bond angles (°): N(1)–Ir–N(2) = 90.02(14), N(1)–Ir–N(2i) = 89.98(14). Atoms with index *i* are related to the basic atom with transformation 1/2 - x, ½+y, 1 +z.

The 2218 cm^{-1} C≡N stretching band for complex **23** suggested that the remaining coordinated isocyanide was also susceptible to nucleophilic attack. Indeed, addition of excess benzylamine to complex **22** or **23** produced bis(diaminocarbene) complex **24a**. Excess amine (~10 eq) was required for the reaction to proceed at a practical rate; attempts with ≤ 5 equivalents of benzylamine gave no reaction or traces of product in 24 hours. The formation of complex **24a** was established on the basis of its ^{1}H NMR spectrum. Integrations

of the diaminocarbene signals at 7.17 (t, 4H, *p*–H), 7.02 (t, 8H, *m*–H), 5.31 (d, 8H, *o*–H), 2.07 (d, 8H, CH$_2$), -1.72 (br, 4H, NH) ppm were consistent with two equivalent axial ligands. Loss of the coordinated isocyanide was indicated by the disappearance of diagnostic signals at 4.85 – 4.80 ppm (d, *o*–H) and 2.65 – 2.63 ppm (s, CH$_2$). In addition, signals for the *ortho*-protons of the *meso*-tolyl groups appeared to be relatively upfield shifted to *ca.* 7.5 ppm. It was difficult to fully characterize complex **24a** by ^{1}H NMR because other metalloporphyrin impurities were present in substantial amounts, and attempts to purify complex **24a** or obtain single crystals suitable for X-ray diffraction were unsuccessful. However, single crystals were isolated and examined by X-ray diffraction for a similar bis(diaminocarbene) complex **24b** derived from the addition of excess *n*-butylamine to the bis(isocyanide) complex **22** (Appendix D). This structure confirmed the formation of a bis(diaminocarbene) complex, but the axial ligands were disordered through symmetry, prohibiting a thorough metrical analysis of the axial atomic positions. The structure of the porphyrin core was well-defined and exhibited significant ruffling and saddling deformations (*vide infra*).

Figure 5.4:[13] ORTEP of complex **23** with 30% probability thermal ellipsoids. Selected bond distances (Å): Ir–N(1) = 2.044(4), Ir–N(2) = 2.042(4). Selected bond angles (°): N(1)–Ir–N(2) = 90.03(13), N(2)–Ir–N(1) = 89.97(13). Atoms with index *i* are related to the basic atom with transformation 1/2 - x, ½-y, 2 – z.

To compare further rhodium and iridium porphyrin carbene complexes, NHC complexes were examined using 1,3-diethylimidazolylidiene (deim) and 1-(*n*-butyl)-3-methylimidazolylidene (bmim). The two NHC ligands were synthesized by deprotonation of

the corresponding imidazolium salt as reported by Arduengo et al.[14] Compounds **25a,b** and **26a,b** were synthesized by treating the respective alkylmetal porphyrinato complexes with a slight excess of the free NHC (Figure 5.5). In all cases, conversion of the metalloporphyrin was nearly quantitative as indicated by the formation one major β-pyrrole porphyrin signal in the ^{1}H NMR spectrum of the reaction mixture. Pure samples were isolated by recrystallization from THF/hexanes and characterized by absorption spectroscopy, NMR spectroscopy, and X-ray diffraction studies. Compounds **25** and **26** were moisture sensitive, especially in solution, generating M(TTP)CH$_3$ (M = Rh, Ir) along with an imidazolium salt upon exposure to water. Complexes **25** and **26** serve as the first examples of metalloporphyrin NHC complexes.

25a : M = Rh, R^1 = R^2 = Et
25b : M = Rh, R^1 = *n*Bu, R^2 = Me
26a : M = Ir, R^1 = R^2 = Et
26b : M = Ir, R^1 = *n*Bu, R^2 = Me
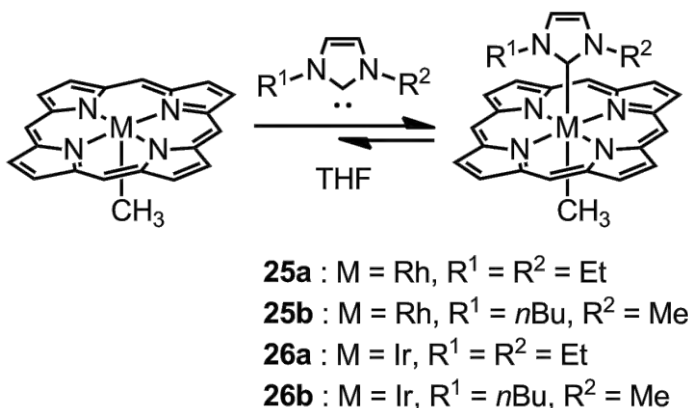
Figure 5.5: Synthesis of (tetra-*p*-tolylporphyrinato)rhodium and iridium NHC complexes. Meso *p*-tolyl groups were omitted for clarity.

Spectroscopic changes accompanied the addition of the free NHC to M(TTP)CH$_3$, producing an immediate color change from orange-red to a dark greenish brown. The resulting absorption spectra displayed "split Soret" bands, characteristic of hyperporphyrins, at 374 and 444 nm for the rhodium NHC complexes and 370 and 438 nm for the iridium NHC complexes (Figure 5.6).[15] Similar hyper spectra were observed previously with the diazoacetate chemistry of iridium porphyrin complexes, including the metal–carbene and metal–ylide intermediates detected in Ir(TTP)CH$_3$-catalyzed C–H insertion and N–H insertion reactions, respectively.[8,16,17] In contrast, the diaminocarbene complexes of rhodium and iridium did not display hyper spectra. This suggests that NHC complexes **25** and **26**

provide a better model for the electronic structure of metal–carbene intermediates involved in catalysis than do the diaminocarbene complexes.
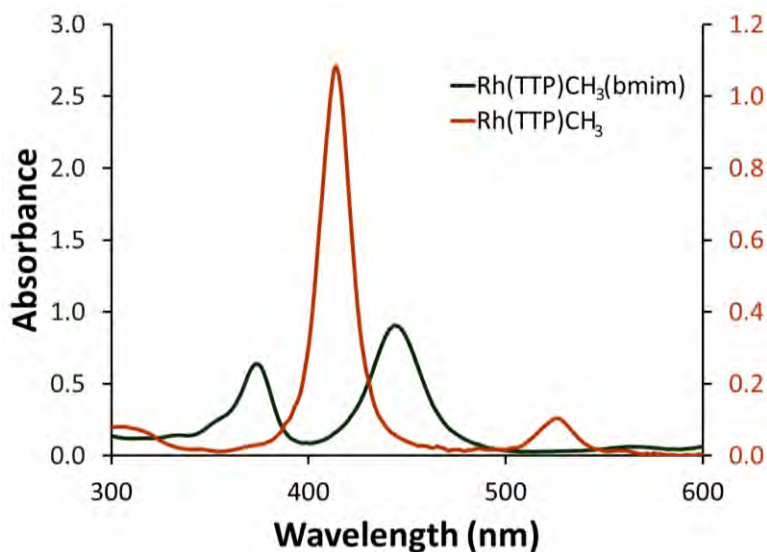

Figure 5.6: The absorption spectra for Rh(TTP)CH$_3$ (4.41×10^{-5} M, orange, right axis) and complex **25b** (1.11×10^{-4} M, green, left axis) in THF. Absorption axes were scaled to demonstrate the actual relative band intensities. Complexes **25a**, **25b**, **26a**, and **26b** all exhibit similar absorption spectra.

Transition metal hyperporphyrin complexes are typically classified as d-type metallopophryins, where the hyper character is the result of charge transfer from porphyrin $a_{1u}(\pi)$, $a_{2u}(\pi)$ orbitals to metal $e_g(d_\pi)$ orbitals.[15,18] Metalloporphyrins with d^6 electron configurations are an unusual case because the metal $e_g(d_\pi)$ orbitals (d_{xz} and d_{yz}, with the z-axis perpendicular to the plane of the porphyrin) are filled in the ground state. Iterative extended Hückel calculations with (OEP)Ru(py)$_2$ and (OEP)Os(py)$_2$ suggested that orbital mixing with relatively low energy doubly excited states, $[e_g(d_\pi)]^3[\,a_{1u}(\pi), a_{2u}(\pi)]^3[e_g(\pi^*)]^2$, may be responsible for the extra absorption bands.[19] A similar phenomenon may be responsible for the hyper spectra displayed here.

NHC coordination to M(TTP)CH$_3$ was confirmed by ^{1}H and ^{13}C NMR spectroscopy. The ^{1}H NMR spectra of **25** and **26** displayed signals corresponding to the coordinated NHCs in the region of 5.3 – 5.1 ppm for the vinylic protons and 0.5 – -0.6 ppm for the aliphatic protons. These signals were strongly upfield shifted 1 – 5 ppm relative to those of the free

NHC. Coordination of the NHC also caused a significant upfield shift in the *trans*-methyl resonances. The *trans*-methyl shifted from -6.56 ppm to -7.44 and -7.38 ppm for rhodium NHC complexes (**25a** and **25b**, respectively) and from -7.01 to -8.03 and -7.97 ppm for the iridium NHC complexes (**26a** and **26b**, respectively). These results are in contrast to the *trans*-methyl signal of Ir(TTP)CH$_3$(=C(Ph)CO$_2$Me) which is shifted downfield to -4.8 ppm.[8] The ^{13}C NMR spectra for complexes **25a**, **25b**, **26a**, and **26b** exhibited carbene α-carbon signals at 180.79 ppm, 181.84 ppm, 164.33 ppm, and 164.86 ppm, respectively. These values are reasonable based on other rhodium and iridium NHC complexes, where carbene α-carbon signals for RhCl(η^2-O$_2$)(IPr)$_2$ and IrCl(η^2-O$_2$)(IPr)$_2$ (IPr = N,N-diisopropyl imidazolylidene) were observed at 180.8 ppm and 167.4 ppm, respectively.[20-22] The carbene α-carbon ^{13}C NMR signals did not seem to be affected substantially by the porphyrin ring current effect.
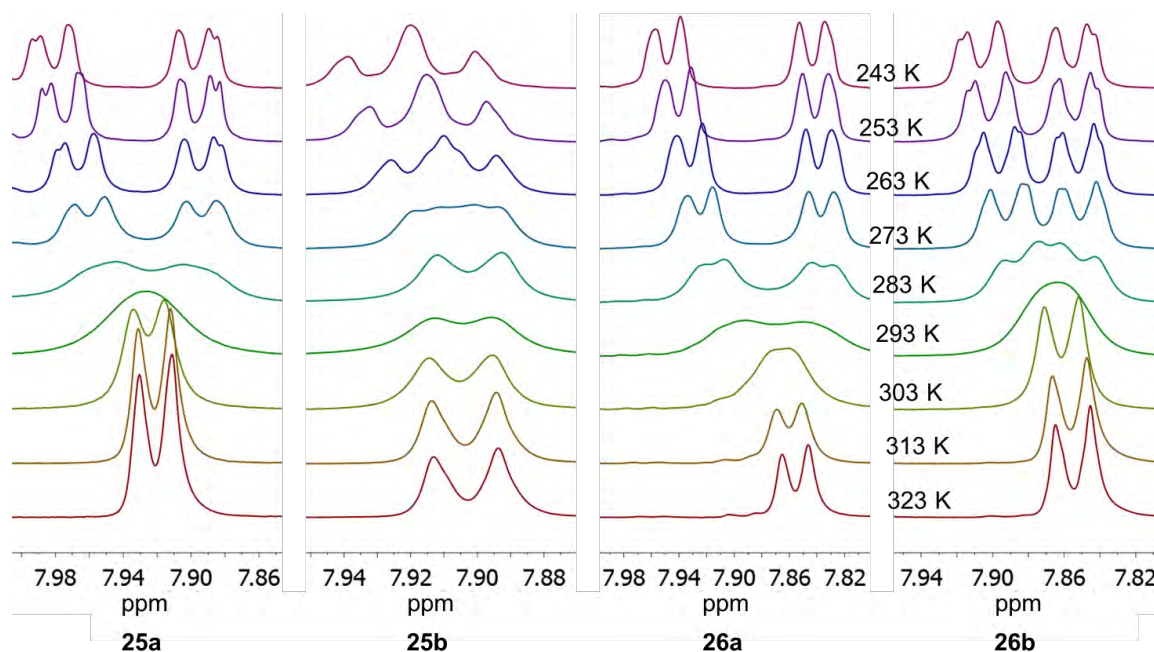
Figure 5.7: Variable temperature ^{1}H NMR spectra of the ortho protons on the *meso* tolyl substituents of complexes **25** and **26**. Dynamic behavior is consistent with aryl–porphyrin rotation.

At ambient temperature, complexes **25** and **26** displayed several broad NMR resonances. Further examination by variable temperature NMR revealed multiple dynamic processes. At 303.0 K, signals corresponding to the *ortho* and *meta* protons on the *meso* tolyl substituents appeared as two doublets at *ca.* 7.9 and 7.5 ppm, respectively. Decreasing the temperature resulted in splitting these signals into a doublet of doublets, which was most evident in the *ortho* signals (Figure 5.7). Numerous dynamic processes of porphyrin complexes have been identified including N–H tautomerism, macrocyclic inversion, and substituent–porphyrin rotation.[23] The behavior exhibited here is consistent with *meso* aryl rotation. Coalescence data gave activation energies ($\Delta G^{\ddagger}_{ROT}$) between 59 and 63 kJ mol^{-1} (Table 5.1), which are within the previously established range of 40 – 78 kJ mol^{-1} for metalloporphyrins.[24-26]

Table 5.1: Kinetic data for the aryl–porphyrin rotation shown by complexes **25a**, **25b**, **26a**, and **26b**.

Complex	$\Delta G^{\ddagger}_{ROT}$ (kJ mol^{-1})	Coalescence T (K)
Rh(TTP)CH$_3$(deim) **(25a)**	61 ± 1	293
Rh(TTP)CH$_3$(bmim) **(25b)**	59 ± 2	273
Ir(TTP)CH$_3$(deim) **(26a)**	63 ± 1	303
Ir(TTP)CH$_3$(bmim) **(26b)**	62 ± 2	288

Dynamic *meso*-aryl–porphyrin C–C bond rotation was observed previously in several metalloporphyrin complexes, including those with Ti, Ru, Ni, Zn, In, and Bi.[24-26] Although aryl–porphyrin rotation has not been reported in rhodium or iridium porphyrin complexes, a study with ruthenium porphyrins measured relatively high barriers for *meso*-aryl rotation at 72 – 78 kJ mol^{-1}.[26] High rotation barriers are typically expected with relatively planar metalloporphyrins, which is usually the case with platinum group metals. Indeed, most axially asymmetric rhodium and iridium complexes typically display sharp inequivalent *ortho* proton signals at ambient temperature, implying that the activation energies for rotation are greater than 70 kJ/mol. Thus it is remarkable that NHC coordination lowers the barrier for aryl rotation to 59 – 63 kJ mol^{-1}. More intriguing is that coordination with acyclic diaminocarbenes as in complexes **23** and **24** does not appear to lower the rotation barrier below 70 kJ mol^{-1}. The nature of the axial ligand is not believed to have a significant impact on *meso*-aryl–porphyrin C–C bond rotation.[26] A more reasonable explanation is that the low

rotation barriers result from deformations in the porphyrin ring, which are caused by coordination with bulky NHC ligands (*vide infra*).[27,28] The relationship between porphyrin deformation and activation energy of aryl–porphyrin rotation was shown previously.[24]

A second dynamic process with larger activation energies was observed for rhodium complexes **25a** and **25b**. At 303.0 K, spectra of these complexes featured broad resonances for the NHC and the *trans* methyl protons. As the temperature was decreased to 243.0 K, these signals sharpened considerably (Figure 5.8), suggesting that NHC binding was fluxional and exchange was rapid on the NMR timescale. In contrast, iridium complexes **26a** and **26b** did not display rapid NHC fluxional behavior at temperatures ranging from 243.0 to 323.0 K. Decomposition became significant at temperatures above 323 K, prohibiting high temperature studies.
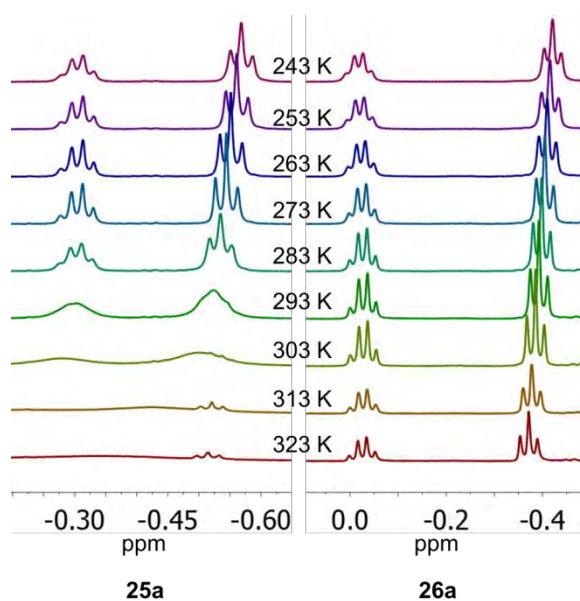
Figure 5.8: Variable temperature ^{1}H NMR spectra of the coordinated NHC protons of complex **25a** compared to complex **26a**. NHC binding is more fluxional with rhodium than with iridium.

The fluxionality of the NHC ligand was further established by an NHC exchange reaction. In the initial studies, deim complexes **25a** or **26a** were treated with bmim and NHC exchange (Eq. 5.1) was monitored by ^{1}H NMR. The ratio of $M(TTP)CH_3(deim)$ to

M(TTP)CH$_3$(bmim) was determined by proton integration of the cleanly separated *trans* methyl proton signals. At 263 K, signals for the rhodium complexes resonated at -7.43 ppm (**25a**) and -7.36 ppm (**25b**), and those for the iridium complexes appeared at -8.00 ppm (**26a**) and -7.92 ppm (**26b**). NHC exchange was observed for all complexes, but the rates of exchange were dramatically different for Rh vs. Ir. For a mixture of **25a** and **25b** produced by combining Rh(TTP)CH$_3$ (18 μmol), deim (32 μmol), and bmim (39 μmol), the coordinated NHC signals were broad and unresolved at 303 K. Cooling the sample to 253 K produced sharp Rh-CH$_3$ signals, with integrations that indicated the sample contained a mixture of **25a** and **25b** in a ratio of 1:1.7. This ratio did not change after repeated cycles of heating and cooling, suggesting that the sample had reached equilibrium before the initial cooling, which took place within five minutes of mixing. Rate constants for NHC exchange, under conditions with a *ca.* 10-fold excess of both bmim and deim, were calculated by line shape analysis using the slow exchange approximation for temperatures between 284 K and 296 K (Figure 5.42; Appendix D). Using the reaction direction defined in Eq. 5.1, rate constants for the forward reaction ranged between 3.7 s^{-1} (284 K) and 26.7 s^{-1} (296 K), which correspond to a $\Delta G^{\ddagger}$ of 65.6 ± 0.8 kJ mol^{-1}. Rate constants for the reverse reaction were 2.9 s^{-1} (284 K) to 17.3 s^{-1} (296 K), with $\Delta G^{\ddagger}$ of 66.4 ± 0.6 kJ mol^{-1}. Although these activation barriers are unresolved within the error limits, the equilibrium constant at these temperatures, as determined by NMR, was 1.6 ± 0.2, indicating that k_f is indeed greater than k_r. Rate constants were similar under a variety of different NHC concentrations, indicating that these first-order rate constants are representative of rate-limiting ligand dissociation. As expected for this rate limiting step, the pentacoordinate intermediate, Rh(TTP)CH$_3$, was not observed under these conditions.

(5.1)
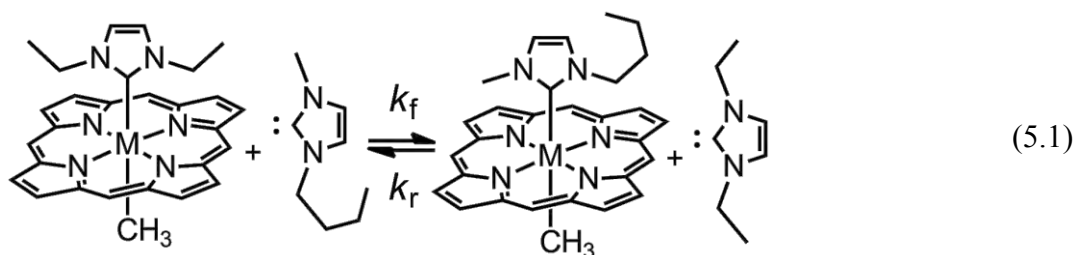
NHC exchange with Ir(TTP)CH$_3$ was much slower and was examined by kinetics. Preliminary experiments under saturated, reversible conditions demonstrated that the system was well-behaved and gave second-order exchange rate constants (Appendix D). First-order rate constants for NHC exchange were determined by initial rate kinetics under pseudo irreversible conditions, which were created by using *ca.* 1 equivalent of the dissociating NHC (NHC$_d$) and a large excess of the incoming NHC (NHC$_i$) (Figure 5.9). To limit the influence of the reverse reaction, only the initial kinetics data were used for rate determination. A steady state approximation was applicable since the pentacoordinate intermediate was not present in observable amounts. Under these pseudo irreversible conditions, the steady state approximation follows the limiting case where $k_2 \gg k_{-1}$. Thus, the reaction rate depended only on the rate constant for NHC dissociation (k_1) and the concentration of the starting iridium NHC complex (Eqs. 5.6 and 5.7; Appendix D).
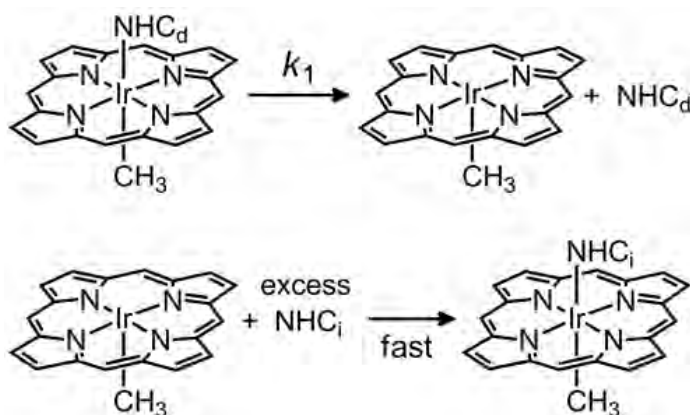
Figure 5.9: Pseudo irreversible NHC exchange with Ir(TTP)CH$_3$.

The first series of kinetics reactions examined the exchange of deim in complex **26a** with bmim as NHC$_i$ at 298.0 K. Reactions with varying concentrations of bmim ([0.0227 – 0.0629] M, 8.3 – 21.6 equiv. relative to the metalloporphyrin) showed little change with respect to reaction rate (Figure 5.47; Appendix D), as expected for rate-limiting ligand dissociation. A second series of reactions used varying concentrations of Ir(TTP)CH$_3$(deim). Plotting the initial rate of these reactions verses [Ir(TTP)CH$_3$(deim)] gave a line with a slope of $1.8 \pm 0.4 \times 10^{-4}$ s^{-1}, representing the rate constant of dissociation for the forward reaction (k_{1f}). The same treatment for the reverse reaction starting with Ir(TTP)CH$_3$(bmim) gave a

dissociation rate constant for the reverse reaction (k_{1r}) equal to $1.2 \pm 0.1 \times 10^{-4}$ s^{-1}. Rate constants k_{1f} and k_{1r} at 298.0 K correspond to $\Delta G^{\ddagger}$ values of 94 and 95 kJ mol^{-1}, respectively, which is much higher than the $\Delta G^{\ddagger}$ values observed for NHC exchange with rhodium (65.6 and 66.4 kJ mol^{-1}). Overall, the rate of NHC exchange is much slower for iridium than for rhodium, consistent with previously reported findings.[29-31]

Equilibrium binding constants for NHC coordination to M(TTP)CH$_3$ were determined using a UV/vis titration method similar to that reported previously (Table 5.2).[16,17] Binding constants were nearly an order of magnitude smaller with Rh(TTP)CH$_3$ compared to Ir(TTP)CH$_3$. Binding constants with deim were similar to those for bmim, within error. Considering the relative equilibrium constants determined during kinetics studies (*vide supra*), the binding constant with bmim is expected to be slightly larger than that with deim. Overall, the equilibrium binding constants are reasonable compared to previous binding studies with rhodium and iridium porphyrin complexes.[17,32,33] Values for log(K) ranged between 1.6 and 8.2 for various L-type ligands. In particular, binding constants found for the coordination of PPh$_3$, N-methylimidazole (N-MeIm), and CO with Ir(OEP)C$_3$H$_7$ were very similar to the values observed for NHC ligands. In contrast, the binding constant previously reported for Rh(OEP)CH$_3$ and PPh$_3$ was lower than those with NHC ligands by an order of magnitude.

Table 5.2: Equilibrium binding constants for the coordination of NHC to M(TTP)CH$_3$ at 296 K.

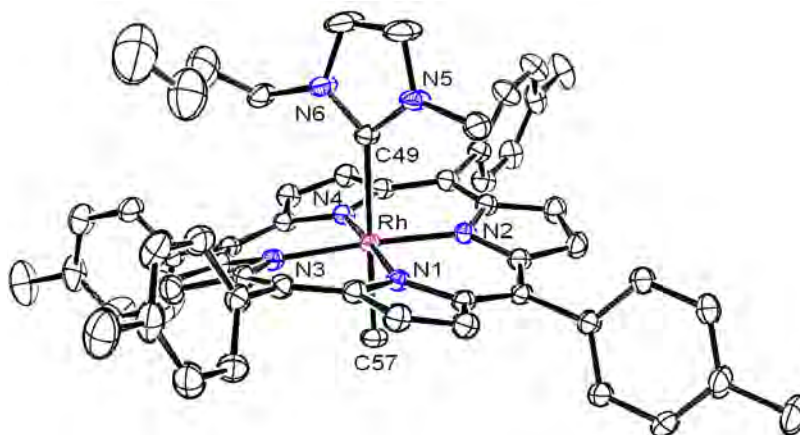| Metalloporphyrin	L	log(K)	Ref.
Rh(TTP)CH$_3$	deim	4.6 ± 0.2	this work
Rh(TTP)CH$_3$	bmim	4.4 ± 0.3	this work
Ir(TTP)CH$_3$	deim	5.5 ± 0.2	this work
Ir(TTP)CH$_3$	bmim	5.3 ± 0.5	this work
Ir(OEP)(C$_3$H$_7$)	PPh$_3$	6.1 ± 0.4	22
Ir(OEP)(C$_3$H$_7$)	N-MeIm	5.6 ± 0.4	22
Ir(OEP)(C$_3$H$_7$)	CO	5.0 ± 0.4	22
Rh(OEP)CH$_3$	PPh$_3$	3.3[a]	37

a) Error was not reported.

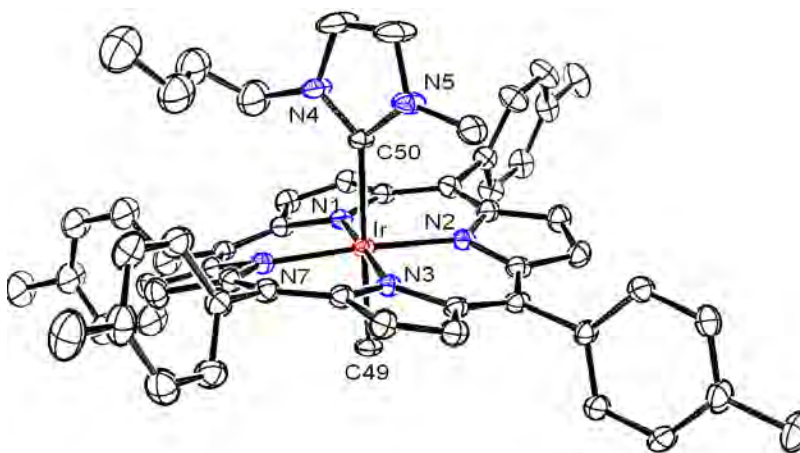**Figure 5.10:** ORTEP[19] of complex **25b** with 30% probability thermal ellipsoids.

Figure 5.11: ORTEP[19] of complex **26b** with 30% probability thermal ellipsoids.

Structures of complexes **25b** and **26b** were determined unambiguously by single crystal X-ray diffraction (Figures 5.9 and 5.10). Both complexes crystallized in the P$\bar{1}$ space group, a triclinic unit cell, and displayed distorted octahedral geometry about the metal center. Selected bond distances and angles are listed in Table 5.3. Complexes **25b** and **26b** feature very long metal–C$_{\alpha-carbene}$ bonds at 2.255(3) Å and 2.194(4) Å, respectively. These bonds are longer than any previously reported rhodium or iridium M–C$_{\alpha-carbene}$ bonds, which typically range from 1.96 to 2.10 Å.[34-37] Moreover, the Rh–C$_{\alpha-carbene}$ bond is considerably longer than that for the iridium analog, which in conjunction with carbene binding equilibrium constants, suggests that the rhodium carbene complex is more electrophilic than the iridium analog.

This hypothesis is consistent with the transition state model proposed for metalloporphyrin-catalyzed cyclopropanation.[7,38]

Table 5.3: Selected bond distances and angles for complexes **25b** and **26b**.

Rh(TTP)CH$_3$(bmim) **25b**		Ir(TTP)CH$_3$(bmim) **26b**	
Rh–C(49)[a]	2.255(3) Å	Ir–C(50)[a]	2.194(4) Å
Rh–C(57)[b]	2.068(3) Å	Ir–C(49)[b]	2.097(4) Å
Rh–N(1)	2.021(3) Å	Ir–N(1)	2.028(3) Å
Rh–N(2)	2.019(3) Å	Ir–N(2)	2.023(3) Å
Rh–N(3)	2.015(3) Å	Ir–N(3)	2.207(3) Å
Rh–N(4)	2.022(3) Å	Ir–N(7)	2.024(3) Å
C(49)–Rh–C(57)	178.11(14)	C(50)–Ir–C(49)	178.15(15)
C(49)–Rh–N(1)	92.81(12)°	C(50)–Ir–N(1)	91.40(11)°
C(49)–Rh–N(2)	90.75(12)°	C(50)–Ir–N(2)	91.01(12)°
C(49)–Rh–N(3)	91.35(12)°	C(50)–Ir–N(3)	92.83(12)°
C(49)–Rh–N(4)	93.39(12)°	C(50)–Ir–N(7)	93.42(12)°
C(57)–Rh–N(1)	88.34(13)°	C(49)–Ir–N(1)	87.59(14)°
C(57)–Rh–N(2)	87.75(13)°	C(49)–Ir–N(2)	87.44(14)°
C(57)–Rh–N(3)	87.50(13)°	C(49)–Ir–N(3)	88.18(14)°
C(57)–Rh–N(4)	88.12(13)°	C(49)–Ir–N(7)	88.13(14)°
Rh–C(49)–N(5)[c]	128.0(3)°	Ir–C(50)–N(5)[c]	128.2(3)°
Rh–C(49)–N(6)[d]	128.9(3)°	Ir–C(50)–N(4)[d]	129.1(3)°
N(5)–Rh–N(6)	102.7(3)°	N(5)–Ir–N(4)	102.5(3)°

[a] carbene carbon. [b] *trans* methyl carbon. [c] Imidazolylidene nitrogen bound to the methyl substituent. [d] Imidazolylidene nitrogren bound to the *n*-butyl substituent.

M–C bond distances for the *trans* methyl carbons of **25b** and **26b** were 2.068(3) Å and 2.097(4) Å, respectively. These bonds were significantly longer than those of the pentacoordinate complexes Rh(TPP)CH$_3$ (1.968(12) Å) and Ir(TTP)CH$_3$·H$_2$O (2.059(11) Å).[39,40] In addition, multiple structural deformations were observed in complexes **25b** and **26b**. Distortion in the bonding angle of the NHC ligand is described by pitch (out-of-plane tilting) and yaw (in-plane tilting) angles (Figure 5.12).[41] While both complexes display a trivial yaw angle (< 1°), the pitch angle was 7.9° in **25b** and 6.4° in **26b**. This distortion may result from steric interactions with the porphyrin as pitch angles up to 23° have been reported with sterically hindered NHC complexes.[42,43] Considerable distortion was also observed in the porphyrin ligand. Deformations of the porphyrin core are quantitatively described using

the normal-coordinate structural decomposition (NSD) analysis.[44,45] This method describes the total out-of-plane (D_{oop}) and in-plane (D_{ip}) displacements as a function of the twelve lowest-frequency normal modes of the porphyrin core. Minimal basis calculations for complexes **25b** and **26b** are shown in Table 5.4. Deformations in the related diaminocarbene, bis-isocyanide, and pentacoordinate complexes are also included as a comparison. NHC complexes **25b** and **26b** contain substantial out-of-plane distortions, which primarily involve a ruffling mode (B_{1u}). The calculated D_{oop} values of 1.2165 and 1.2097 are moderate as compared to the values for other metalloporphyrins complexes, where highly distorted complexes have D_{oop} values above 3.[45] Similar deformations are observed with the bis-diaminocarbene complex **24b**, albeit with a larger saddling displacement (B_{2u}). Small D_{oop} values were measured for Rh(TTP)CH$_3$, Ir(TTP)CH$_3$, complex **22**, complex **23**, and the rhodium analog of complex **23**, Rh(TPP)(=C(NHBn)$_2$)(C≡NBn)(PF$_6$). These complexes show large in-plane displacements relative to **24b**, **25b**, and **26b**, but these D_{ip} values are still small relative to other metalloporphyrin complexes.[45]
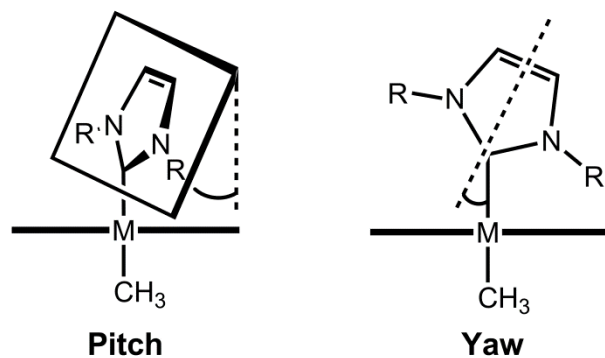
Figure 5.12: Graphical representations of pitch and yaw angles.

Porphyrin deformations are ubiquitous in natural and synthetic systems,[46] and systematic analysis of heme complexes demonstrated that coordination with π-accepting ligands especially increases deformation in the ruffling mode.[47] Multiple studies have examined the importance of ring distortion on enzyme catalysis.[48-50] A recent study examined the effect of ruffling and doming deformations on the N$_4$ cavity of the porphyrin.[51] While doming expands the cavity, ruffling contracts it, resulting in up to a 24 nm red shift in the Soret band

of the porphyrin. Such a shifting is consistent with the 444 nm and 438 nm Soret bands for complexes **25b** and **26b**, respectively (*vide supra*). Furthermore, the N_4 cavity contraction was suggested to increase the electron cloud density of a complexed metal ion, which was suggested to drive the formation of higher valent iron species.[52] While it is unclear how these factors influence catalysis, the present and previous studies indicate that significant deformations are present during carbene transfer. DFT optimization of $Ir(TTP)CH_3(=C(Ph)CO_2CH_3)$ revealed notable porphyrin distortion in the ruffling (-0.4513) and doming (-0.2309) modes, with an overall D_{oop} of 0.5154.[8]

Medforth et al. previously proposed a deformability model, which suggests that the barrier for *meso* aryl–porphyrin rotation lowers upon increasing ruffling of the metalloporphyrin.[24] Rotation barriers and NSD data for complexes **25b** and **26b** are consistent with this model. However, given the similar displacements in the B_{1u} ruffling mode, it is surprising that complex **24b** does not show dynamic aryl–porphyrin rotation ($\Delta G^{\ddagger}_{ROT} > 70$ kJ mol^{-1}) in the temperature range between 243 and 323 K. Complex **24b** displays slightly more saddling, but previous studies suggest that increasing saddling deformations does not have a large impact on the *meso* rotation barrier.[24] Perhaps added steric bulk from the bis-diaminocarbene ligands relative to the NHCs raises the rotation barrier. The relationship between aryl–porphyrin bond distances and meso rotation barriers were also considered. Aryl–porphyrin bond lengths for complexes **25b** and **26b** ranged from 1.491(5) Å to 1.506(7) Å. These bond distances are not significantly longer than other metalloporphyrin complexes, including **22** and **24b** (1.487(6) – 1.501(7) Å), which did exhibit dynamic aryl–porphyrin rotation. The low $\Delta G^{\ddagger}_{ROT}$ values displayed by complex **25** and **26** cannot be explained by aryl–porphyrin bond lengths.

Table 5.4: NSD analysis of selected rhodium and iridium metalloporphyrins.[a]

Out-of-Plane Displacements (Å)

Complex	D_{oop}	δ_{oop}[b]	B_{2u}, *sad*	B_{1u}, *ruf*	A_{2u}, *dom*	$E_g(x)$, *wav(x)*	$E_g(y)$, *wav(y)*	A_{1u}, *prop*
22	0.0590	0.0214	-0.0001	-0.0003	0.0000	-0.0587	0.0056	-0.0003
23	0.0185	0.0180	0.0006	-0.0004	-0.0004	0.0171	0.0070	0.0002
Rh(TPP)(=C(NHBn)$_2$)(C≡NBn)(PF$_6$)[53]	0.1803	0.0222	0.1425	-0.0602	-0.0445	-0.0242	-0.0773	0.0074
24b	1.4937	0.0182	-0.9857	1.1223	-0.0005	0.0000	0.0000	0.0005
25b	1.2165	0.0119	-0.2479	1.1705	-0.2108	-0.0057	0.0613	0.0088
26b	1.2097	0.0119	0.2521	1.1551	0.2493	-0.0046	-0.0568	0.0094
Rh(TPP)CH$_3$[39]	0.0000	0.0000	0.0000	0.0000	0.0000	0.0000	0.0000	0.0000
Ir(TTP)CH$_3$·H$_2$O[40]	0.1124	0.0053	0.0681	-0.0115	0.0754	-0.0234	0.0355	0.0192

In-Plane Displacements (Å)

Complex	D_{ip}	δ_{ip}[b]	B_{2g}, *m-str*	B_{1g}, *n-str*	A_{2g}, *rot*	$E_u(x)$, *trn*	$E_u(y)$, *trn*	A_{1g}, *bre*
22	0.1840	0.0110	-0.0080	0.0190	0.0002	0.0005	0.1826	-0.0084
23	0.1430	0.0151	-0.0034	-0.0064	0.0001	-0.0006	0.1428	0.0038
Rh(TPP)(=C(NHBn)$_2$)(C≡NBn)(PF$_6$)[53]	0.1716	0.0215	-0.0017	0.0481	-0.0063	-0.0240	0.1626	-0.0102
24b	0.0361	0.0235	0.0000	0.0001	-0.0005	0.0003	0.0035	-0.0360
25b	0.0613	0.0199	0.0518	0.0211	0.0193	0.0010	-0.0034	-0.0157
26b	0.0665	0.0198	-0.0570	0.0195	-0.0144	0.0011	0.0163	0.0178
Rh(TPP)CH$_3$[39]	0.1154	0.0090	0.0000	0.0000	0.0000	0.0003	0.1154	0.0036
Ir(TTP)CH$_3$·H$_2$O[40]	0.0922	0.0158	0.0044	-0.0105	0.0018	0.0097	0.0910	-0.0005

Structures for referenced complexes were resolved previously. [a] Displacements were calculated from the minimum basis set of core atoms in the porphyrin ring. [b] Mean deviations.

Conclusion

Several metalloporphyrin diaminocarbene and NHC complexes were prepared and characterized. Iridium diaminocarbene complexes **23** and **24** were synthesized by nucleophilic addition of an amine to the bis-isocyanide complex, [Ir(TTP)(C≡NBn)$_2$](BF$_4$). Characterization data for **23** appears similar to that for the previously reported rhodium diaminocarbene complexes, [Rh(por)(=C(NHBn)$_2$)(C≡NBn)](PF$_6$). However, axial ligand disorder in the crystal structures of **23** and **24b** prohibited a thorough metrical comparison. More direct comparisons were observed between rhodium and iridium NHC complexes. Equilibrium binding constants and ligand exchange rate constants demonstrated that NHCs were bound more strongly to iridium than rhodium. This was further established by examining metal–C$_{\alpha–carbene}$ bond lengths, which revealed that the rhodium–C$_{\alpha–carbene}$ bond was *ca.* 0.06 Å longer than the iridium–C$_{\alpha–carbene}$ bond. These data are consistent with the transition state model proposed for rhodium porphyrin-catalyzed cyclopropanation where the selectivity of rhodium catalysts was proposed to arise from a relatively high energy rhodium–carbene complex, leading an earlier transition state for carbene transfer. In addition, isolated NHC complexes exhibited significant porphyrin ring distortions. As has been shown repeatedly in biological systems, porphyrin distortion plays an important role in catalysis, and should be considered for the continuing development of synthetic metalloporphyrin catalysts.

Experimental

General Considerations: 1,3-diethylimidazolylidiene (deim) and 1,3-*n*-butylmethylimidazolylidene (bmim) were synthesized following the procedure described by Arduengo, et al.[14] Crude samples of deim and bmim were dissolved in a known volume of THF and stored in the freezer. Stock solution concentrations were in the range of 0.10 to 0.50 M. Attempts to purify deim and bmim by distillation decomposed the free NHC. Ir(TTP)Cl(CO) was generated by a known procedure for metalation of H$_2$TTP.[54] Rh(TTP)CH$_3$ and Ir(TTP)CH$_3$ were synthesized similar to previously described methods for reductive alkylation of the corresponding metal halogenato porphyrin complex.[55] Methylene chloride and tetrahydrofuran were deoxygenated and dried by passage through columns of

reduced copper and alumina. Hexanes and benzene-d_6 were dried over sieves, deoxygenated by successive freeze-pump-thaw cycles, and passed through a plug of activated alumina in the glovebox. All other chemicals were purchased as reagent grade and used without further purification. General NMR spectra were collected using Bruker DRX 400 MHz and AVIII 600 MHz spectrometers. Carbene ^{13}C signals for the NHC complexes were verified with a 700 MHz instrument equipped with a cryoprobe. Variable temperature and kinetics studies were done using the Bruker DRX 400 MHz spectrometer. ^{1}H and ^{13}C NMR peak positions were referenced against residual proton resonances of deuterated solvents (δ,ppm: CDCl$_3$, 7.26 and 77.16; THF, 3.58 and 67.57; C$_6$D$_6$, 7.16). Absorption spectra were collected using a Hewlett-Packard/Agilent Technologies 8453 UV-Vis spectrophotometer.

X-Ray Single Crystal Structure Determination: The crystal evaluation and data collection were performed at 173 K on a Bruker APEX II CCD diffractometer using Mo K_α($\lambda = 0.71073$ Å). Full sphere data with 0.3° frame width were collected until a resolution of 0.74 Å. The absorption correction was based on a fit of a spherical harmonic function to the empirical transmission surface as sampled by multiple equivalent measurements.[56] Structures were solved using direct methods and were refined using a full-matrix anisotropic approximation for all non-hydrogen atoms. All hydrogen atoms were placed in the structure factor calculation at idealized positions and refined using a "riding model." The U_{iso}(H) values were set at 1.5 times the U_{eq} value of the carrier atom. All calculations were performed using the APEX II software package.[57,58] CCDC 943042-943046 contains the supplementary crystallographic data for this paper. These data can be obtained free of charge from The Cambridge Crystallographic Data Centre via www.ccdc.cam.ac.uk/data_request/cif.

NHC Exchange with Rh(TTP)CH$_3$: Stock-solutions of bmim (6.0 mL from a 0.027 THF-stock solution, 0.16 mmol) and deim (1.0 mL from a 0.18 M THF-stock solution, 0.18 mmol) were collected in a vial and THF was removed quickly *in vacuo*. Immediately after THF removal, the residue was treated with a THF-d_8 solution of Rh(TTP)CH$_3$(deim) (32.0 mg, 0.0351 mmol). This solution was transferred to an NMR tube fitted with a Teflon stopcock, charged with mesitylene as an internal standard (2.0 µL, 0.01437 mmol), diluted to

a final volume of 750 μL, and analyzed by ^{1}H NMR. As verification, the same procedure was executed with Rh(TTP)CH$_3$(bmim) (16.7 mg, 0.0180 mmol) under varying conditions with increasing amounts of bmim (0.039 mmol to 0.26 mmol) and deim (0.032 mmol to 0.58 mmol).

Reversible NHC exchange with iridium porphyrins: An NMR tube fitted with a Teflon stopcock was charged with 450 μL of a stock solution of Ir(TTP)CH$_3$ (3.14×10^{-3} M, 1.41 μmol). The solution was taken to dryness and the NMR tube was brought into a glovebox. The NMR tube was charged with mesitylene standard (20 μL from a 5.16×10^{-2} M C$_6$D$_6$ stock solution, 1.03 μmol), deim (108 μL from a 0.144 M C$_6$D$_6$ stock solution, 15.5 μmol), and enough C$_6$D$_6$ to attain a final solution volume of 420 μL. After mixing for 5 – 10 min, the solution was treated with varying amounts of bmim (140 – 292 μL from a 0.0798 M C$_6$D$_6$ stock solution, 11.2 – 23.3 μmol). The tube was sealed and transferred to an NMR instrument, where the temperature was raised to 308.0 K and reaction progress was monitored at 40 – 120 second intervals. This procedure was used for additional experiments where [bmim] was varied in order to determine k_f. The same procedure, except switching the order of NHC additions and varying only [deim], was extended to a second set of experiments to determine k_r. One of these sets was discarded as a statistical outlier.

Pseudo irreversible NHC exchange with iridium porphyrins: A medium-walled NMR tube was charged with Ir(TTP)CH$_3$ (300 to 600 μL from a 3.60×10^{-3} M CH$_2$Cl$_2$ stock-solution, 1.08 to 2.16 μmol). The tube was taken into a glovebox and loaded with NHC$_d$ (deim: 16 to 23 μL from a 0.141 M C$_6$D$_6$ stock-solution, 2.3 to 3.2 μmol; bmim: 20 to 34 μL from a 0.0764 M C$_6$D$_6$ stock-solution, 1.5 to 2.6 μmol), mesitylene (20 μL from a 5.16×10^{-2} M C$_6$D$_6$ stock-solution, 1.0 μmol), and enough C$_6$D$_6$ to reach a final volume of 420 μL. The tube was sealed with a septum and taken to the NMR spectrometer. Spectrometer settings were prepared and temperature was equilibrated to 298.0 K. Finally, the solution was treated with NHC$_i$ (deim: 110 μL from a 0.141 M C$_6$D$_6$ stock-solution, 15.1 μmol; bmim: 200 μL from a 0.0764 M C$_6$D$_6$ stock-solution, 15.3 μmol) and data collection began *ca.* 2 min after addition.

Ir(TTP)(C≡NBn)₂(BF₄) (22): Following a procedure similar to that described previously for Rh(TPP)(C≡N*t*Bu)(PF₆)[11] and Ir(TTP)(BF₄)/Ir(TTP)(CO)(BF₄),[59] Ir(TTP)Cl(CO) (44.8 mg, 0.0485 mmol) and silver tetrafluoroborate (16.9 mg, 0.0868 mmol) were collected in a vial under glovebox atmosphere, wrapped with aluminum foil, dissolved in CH₂Cl₂, and stirred at ambient temperature for 2 days. Solids were removed by filtration through a pad of celite. The filtrate was treated with benzyl isocyanide (25.0 µL, 0.205 mmol) and stirred at ambient temperature overnight. Volatiles were removed *in vacuo*, and the crude sample was evaluated by ¹H NMR. If conversion to complex **22** was incomplete, the residue was recollected in CH₂Cl₂ (5.0 mL) under air and treated with additional portions of benzyl isocyanide until ¹H NMR signals corresponding to Ir(TTP)(BF₄)/Ir(TTP)(CO)(BF₄) were completely consumed. Complex **22** was isolated by recrystallization from CH₂Cl₂/hexanes (33.3 mg, 0.0295 mmol, 61% yield), though benzene was also a suitable recrystallization solvent. ¹H NMR (CDCl₃, 300 MHz): δ 8.96 (s, 8H, β-porphyrin), 7.96 (d, J = 7.8 Hz, 8H, *meso-o*-tolyl), 7.56 (d, J = 7.8 Hz, 8H, *meso-m*-tolyl), 6.98 (t, J = 7.5 Hz, 2H, *p*-phenyl), 6.79 (t, J = 7.5 Hz, 4H, *m*-phenyl), 4.80 (d, J = 7.5 Hz, 4H, *o*-phenyl), 2.72 (s, 12H, tolyl -CH₃), 2.65 (s, 4H, -CH₂-). ¹³C{¹H} NMR (CDCl₃, 300 MHz): δ 183.07, 141.72, 138.18, 137.77, 134.26, 132.43, 128.51, 128.02, 127.81, 124.16, 122.55, 45.16, 21.67. UV-Vis (CH₂Cl₂): nm (log ε) 419 (5.44), 531 (4.36), 566 (3.86). IR (KBr): C≡N 2228 cm⁻¹.

[Ir(TTP)(=C(NHBn)₂)(C≡NBn)](BF₄), 23: Complex **22** (26.1 mg, 0.0221 mmol) was collected in a 20-mL scintillation vial and dissolved in CH₂Cl₂ (3.5 mL) under air. The solution was treated with benzylamine (5.40 × 10² µL from a 0.0411 M CDCl₃ stock solution, 0.0222 mmol) and heated to 40 °C overnight in a tightly closed container sealed with a poly-lined cap. Volatiles were removed in vacuo. Single crystals suitable for X-ray diffraction were obtained by slow evaporation from a CH₂Cl₂/hexanes solution (20.7 mg, 0.0161 mmol, 73% yield). ¹H NMR (CDCl₃, 400 MHz): δ 8.80 (s, 8H, β-porphyrin), 7.91 (d, J = 7.6 Hz, 4H, meso-*o*-tolyl), 7.53 (m, 12H, meso-*o*-tolyl and meso-*p*-tolyl), 7.17 (t, J = 7.6 Hz, 2H, *p*-phenyl(carbene)), 7.04 – 6.96 (m, 5H, *p*-phenyl(isocyanide) and *m*-phenyl(carbene)), 6.81 (t, J = 7.6 Hz, 2H, *m*-phenyl(isocyanide)), 5.31 (d, J = 7.6 Hz, 4H, *o*-phenyl(carbene)), 4.85 (d, J = 7.6 Hz, 2H, *o*-phenyl(isocyanide)), 2.70 (s, 12H, tolyl -CH₃), 2.63 (s, 2H, -CH₂-(isocyanide)), 2.07 (d, J = 3.2 Hz, 4H, -CH₂- (carbene)), -1.98 (br, 2H, -

NH). $^{13}C\{^{1}H\}$ NMR (CDCl$_3$, 600 MHz): δ 162.92, 141.56, 138.20, 137.58, 134.43, 134.09, 134.05, 132.50, 129.47, 129.00, 128.48, 128.21, 127.89, 127.85, 127.73, 126.17, 124.18, 122.66, 48.12, 44.85, 21.65. UV-Vis (CH$_2$Cl$_2$): nm (log ε) 419 (5.38), 530 (4.34), 564 (3.85). IR (KBr): C $^{\circ}$ N 2218 cm^{-1}

General procedure for synthesis and isolation of NHC complexes: A 20-mL scintillation vial was charged with M(TTP)CH$_3$ and transferred into the glovebox. The metalloporphyrin was dissolved in 1 – 3 mL THF and treated with the NHC complex (*ca.* 1.5 equiv.). The resulting solution was layered with hexanes (*ca.* 3x greater volume than THF) and stored in the freezer overnight. Dark crystals were collected by filtration and physical separation. To isolate high purity complexes, separation was rather selective, which resulted in artificially low yields.

Rh(TTP)(deim)(CH$_3$), 25a: Rh(TTP)CH$_3$ (58.0 mg, 73.7 µmol) was treated with bmim (0.30 mL from a 0.40 M stock solution, 120 µmol). Dark green crystals (16.7 mg, 18.0 µmol, 24% yield) were collected after drying *in vacuo*. ^{1}H NMR (THF-d_8, 400 MHz, 243.0 K): δ 8.53 (s, 8H, β-porphyrin), 7.93 (dd, J = 30.4, 7.6 Hz, 8H, meso-*o*-tolyl), 7.52 (d, J = 7.6 Hz, 8H, meso-*m*-tolyl), 5.27 (s, 2H, vinyl -CH), 2.65 (s, 12H, tolyl -CH$_3$), -0.31 (q, J = 7.0 Hz, 4H, ethyl -CH$_2$-), -0.56 (t, J = 7.0 Hz, 6H, ethyl -CH$_3$), -7.44 (d, J_{Rh-H} = 2.0 Hz, 3H, axial methyl -CH$_3$). $^{13}C\{^{1}H\}$ NMR (THF-d_8, 600 MHz, 263 K): δ 179.98 (d, J = 88.2 Hz), 143.07, 140.45, 137.35, 134.69, 134.57, 131.79, 127.96, 127.59, 121.44, 117.89, 40.19, 21.38, 15.32, -4.55. ^{13}C signals, especially those for the carbene and axial methyl carbons, were verified by HMQC experiments and in a separate acquisition with a 700 MHz instrument using Cr(acac)$_3$. UV-Vis (THF): nm (log ε) 374 (4.80), 444 (4.94).

Rh(TTP)(bmim)(CH$_3$), 25b: Rh(TTP)CH$_3$ (40.0 mg, 50.8 µmol) was treated with bmim (0.350 mL from a 0.18 M stock solution, 65 µmol). Dark green crystals (32.0 mg, 35.1 µmol, 69% yield) were collected after drying *in vacuo*. ^{1}H NMR (THF-d_8, 400 MHz, 243.0 K): δ 8.53 (s, 8H, β-positions), 7.92 (dd, J = 7.6 Hz, 7.6 Hz, 8H, meso-*o*-tolyl), 7.52 (d, J = 7.6 Hz, 8H, meso-*m*-tolyl), 5.20 (d, J = 1.2 Hz, 1H, vinyl -CH), 5.13 (d, J = 1.2 Hz, 1H, vinyl -CH), 2.65 (s, 12H, tolyl -CH$_3$), 0.44 (t, J = 7.4 Hz, 3H, butyl -CH$_3$), 0.20 (m, 2H, butyl -CH$_2$-), -0.20 (s, 3H, methyl -CH$_3$), -0.31 (m, 2H, butyl -CH$_2$-), -0.42 (m, 2H, butyl -CH$_2$-), -7.38 (d,

J_{Rh-H} = 1.6 Hz, 3H, axial methyl -CH$_3$). ^{13}C{^{1}H} NMR (THF-d_8, 600 MHz, 263.0 K): δ 181.84 (br), 143.00, 140.41, 137.35, 134.61, 134.46, 131.74, 127.97, 127.57, 121.41, 120.31, 117.16, 45.12, 32.88, 32.47, 21.39, 19.57, 13.79, and -5.01. The axial methyl carbon at -5.01 ppm was observed only by HMQC. The carbene signal at 181.84 ppm (br) was observed only in a separate acquisition using Cr(acac)$_3$ and a 700 MHz NMR instrument. UV-Vis (THF): nm (log ε) 374 (4.80), 444 (4.94).

Ir(TTP)(deim)(CH$_3$), 26a: Ir(TTP)CH$_3$ (17.7 mg, 20.2 μmol) was treated with bmim (0.15 mL from a 0.18 M stock solution, 27 μmol). Dark brown crystals (11.0 mg, 11.0 μmol, 55% yield) were collected after drying *in vacuo*. ^{1}H NMR (THF-d_8, 400 MHz, 243.0 K): δ 8.30 (s, 8H, β-porphyrin), 7.89 (dd, J = 34.4, 7.2 Hz, 8H, meso-o-tolyl), 7.51 (dd, J = 7.2, 7.2 Hz, 8H, meso-m-tolyl), 5.32 (s, 2H, vinyl -CH), 2.63 (s, 12H, tolyl -CH$_3$), -0.02 (q, J = 6.8 Hz, 4H, ethyl -CH$_2$-), -0.42 (t, J = 6.8 Hz, 6H, ethyl -CH$_3$), -8.03 (s, 3H, axial methyl -CH$_3$). ^{13}C{^{1}H} NMR (THF-d_8, 600 MHz, 298 K): δ 164.33, 143.43, 139.92, 137.31, 134.64-134.44, 131.51, 127.99-127.60, 123.71, 118.03, 40.16, 21.30, 15.12, -21.97. ^{13}C signals, especially those for the carbene and axial methyl carbons, were verified by HMQC experiments. UV-Vis (THF): nm (log ε) 370 (4.54), 438 (4.94).

Ir(TTP)(bmim)(CH$_3$), 26b: Ir(TTP)CH$_3$ (27.9 mg, 31.8 μmol) was treated with bmim (0.10 mL from a 0.40 M stock solution, 40 μmol). Dark brown crystals (10.1 mg, 10.0 μmol, 31% yield) were collected after drying *in vacuo*. ^{1}H NMR (THF-d_8, 400 MHz, 243.0 K): δ 8.30 (s, 8H, β-porphyrin), 7.88 (dd, J = 20.0, 8.0 Hz, 8H, meso-o-tolyl), 7.50 (d, J = 8.0 Hz, 8H, meso-m-tolyl), 5.22 (d, J = 1.2, 1H, vinyl -CH), 5.15 (d, J = 1.2, 1H, vinyl -CH), 2.63 (s, 12H, tolyl -CH$_3$), 0.52 (t, J = 7.2 Hz, 3H, butyl -CH$_3$), 0.40 (m, 2H, butyl -CH$_2$-), 0.05 (s, 3H, methyl -CH$_3$), -0.03 (t, J = 7.2 Hz, 2H, butyl -CH$_2$-), -0.32 (m, 2H, butyl -CH$_2$-), -7.94 (s, 3H, axial methyl -CH$_3$). ^{13}C{^{1}H} NMR (THF-d_8, 600 MHz, 298 K): δ 164.86, 143.40, 139.91, 137.31, 134.66-134.34, 131.47, 127.96- 127.58, 123.74, 120.61, 117.23, 45.15, 32.70, 32.68, 21.30, 19.61, 13.67, -21.92. ^{13}C signals, especially those for the carbene and axial methyl carbons, were verified by HMQC experiments. UV-Vis (THF): nm (log ε) 370 (4.49), 438 (4.89).

References

1.   Anding, B. J.; Woo, L. K. In *Handbook of Porphyrin Science*; Kadish, K. M., Guilard, R., Smith, K., Eds.; World Scientific Publishing Company: Hackensack, NJ, 2012; Vol. 21, p 145.

2.   Chen, Y.; Ruppel, J. V.; Zhang, X. P. *J. Am. Chem. Soc.* **2007**, *129*, 12074.

3.   Doyle, M. P. *Angew. Chem. Intl. Ed.* **2009**, *48*, 850.

4.   Lu, H.; Dzik, W. I.; Xu, X.; Wojtas, L.; de Bruin, B.; Zhang, X. P. *J. Am. Chem. Soc.* **2011**, *133*, 8518.

5.   Belof, J. L.; Cioce, C. R.; Xu, X.; Zhang, X. P.; Space, B.; Woodcock, H. L. *Organometallics* **2011**, *30*, 2739.

6.   Dzik, W. I.; Xu, X.; Zhang, X. P.; Reek, J. N. H.; de Bruin, B. *J. Am. Chem. Soc.* **2010**, *132*, 10891.

7.   Anding, B. J.; Ellern, A.; Woo, L. K. *Organometallics* **2012**, *31*, 3628.

8.   Anding, B. J.; Brgoch, J.; Miller, G. J.; Woo, L. K. *Organometallics* **2012**, *31*, 5586.

9.   Maxwell, J. L.; Brown, K. C.; Bartley, D. W.; Kodadek, T. *Science* **1992**, *256*, 1544.

10.   Boschi, T.; Licoccia, S.; Paolesse, R.; Tagliatesta, P.; Pelizzi, G.; Vitali, F. *Organometallics* **1989**, *8*, 330.

11.   Boschi, T.; Licoccia, S.; Tagliatesta, P. *Inorg. Chim. Acta* **1987**, *126*, 157.

12.   Joo, S.-W.; Kim, W.-J.; Yun, W. S.; Hwang, S.; Choi, I. S. *App. Spec.* **2004**, *58*, 218.

13.   Farrugia, L. J. *J. Appl. Cryst.* **1997**, *30*, 565.

14.   Arduengo, A. J.; Dias, H. V. R.; Harlow, R. L.; Kline, M. *J. Am. Chem. Soc.* **1992**, *114*, 5530.

15.   Gouterman, M. *The Porphyrins: Physical Chemistry, Pt. A*; Academic Press, Inc.: New York, **1978**; Vol. 3.

16.   Anding, B. J.; Woo, L. K. *Organometallics* **2013**, *32*, 2599.

17.   Kadish, K. M.; Cornillon, J. L.; Mitaine, P.; Deng, Y. J.; Korp, J. D. *Inorg. Chem.* **1989**, *28*, 2534.

18.   Gouterman, M.; Hanson, L. K.; Khalil, G. E.; Leenstra, W. R.; Buchler, J. W. *J. Chem. Phys.* **1975**, *62*, 2343.

19.   Antipas, A.; Buchler, J. W.; Gouterman, M.; Smith, P. D. *J. Am. Chem. Soc.* **1978**, *100*, 3015.

20.   Praetorius, J. M.; Allen, D. P.; Wang, R.; Webb, J. D.; Grein, F.; Kennepohl, P.; Crudden, C. M. *J. Am. Chem. Soc.* **2008**, *130*, 3724.

21.   DeBoef, B.; Pastine, S. J.; Sames, D. *J. Am. Chem. Soc.* **2004**, *126*, 6556.

22.   *N-Heterocyclic Carbenes in Transition Metal Catalysis and Organocatalysis*; Springer: New York, **2011**; Vol. 32.

23.   Medforth, C. J. In *The Porphyrin Handbook*; Kadish, K. M., Smith, K. M., Guilard, R., Eds.; Academic Press: Boston, 2000; Vol. 5, p 1.

24.   Medforth, C. J.; Haddad, R. E.; Muzzi, C. M.; Dooley, N. R.; Jaquinod, L.; Shyr, D. C.; Nurco, D. J.; Olmstead, M. M.; Smith, K. M.; Ma, J.-G.; Shelnutt, J. A. *Inorg. Chem.* **2003**, *42*, 2227.

25.   Barbour, T.; Belcher, W. J.; Brothers, P. J.; Rickard, C. E. F.; Ware, D. C. *Inorg. Chem.* **1992**, *31*, 746.

26.   Eaton, S. S.; Eaton, G. R. *J. Am. Chem. Soc.* **1977**, *99*, 6594.

27.   Song, Y.; Haddad, R. E.; Jia, S.-L.; Hok, S.; Olmstead, M. M.; Nurco, D. J.; Schore, N. E.; Zhang, J.; Ma, J.-G.; Smith, K. M.; Gazeau, S.; Pécaut, J.; Marchon, J.-C.; Medforth, C. J.; Shelnutt, J. A. *J. Am. Chem. Soc.* **2005**, *127*, 1179.

28.   Jia, S.-L.; Jentzen, W.; Shang, M.; Song, X.-Z.; Ma, J.-G.; Scheidt, W. R.; Shelnutt, J. A. *Inorg. Chem.* **1998**, *37*, 4402.

29.   Deeming, A. J.; Proud, G. P.; Dawes, H. M.; Hursthouse, M. B. *J. Chem. Soc., Dalton Trans.* **1986**, 2545.

30.   Dadci, L.; Elias, H.; Frey, U.; Hoernig, A.; Koelle, U.; Merbach, A. E.; Paulus, H.; Schneider, J. S. *Inorg. Chem.* **1995**, *34*, 306.

31.   Cusanelli, A.; Nicula-Dadci, L.; Frey, U.; Merbach, A. E. *Inorg. Chem.* **1997**, *36*, 2211.

32.   Kadish, K. M.; Araullo, C.; Yao, C. L. *Organometallics* **1988**, *7*, 1583.

33.   Aoyama, Y.; Asakawa, M.; Yamagishi, A.; Toi, H.; Ogoshi, H. *J. Am. Chem. Soc.* **1990**, *112*, 3145.

34.   Chen, L.; Liu, Y.; Hou, G.; Song, H.; Zi, G. *Inorg. Chem. Commun.* **2013**, *29*, 141.

35.   Meredith, J. M.; Robinson, R.; Goldberg, K. I.; Kaminsky, W.; Heinekey, D. M. *Organometallics* **2012**, *31*, 1879.

36.   Dastgir, S.; Coleman, K. S.; Cowley, A. R.; Green, M. L. H. *Dalton Trans.* **2009**, 7203.

37.   Poyatos, M.; Sanaú, M.; Peris, E. *Inorg. Chem.* **2003**, *42*, 2572.

38.   Wolf, J. R.; Hamaker, C. G.; Djukic, J.-P.; Kodadek, T.; Woo, L. K. *J. Am. Chem. Soc.* **1995**, *117*, 9194.

39.   Stulz, E.; Scott, S. M.; Bond, A. D.; Otto, S.; Sanders, J. K. M. *Inorg. Chem.* **2003**, *42*, 3086.

40.   Song, X.; Chan, K.-S. *J. Chin. Chem. Soc.* **2009**, *56*, 667.

41.   Kühl, O. *Coord. Chem. Rev.* **2009**, *253*, 2481.

42.   Mungur, S. A.; Liddle, S. T.; Wilson, C.; Sarsfield, M. J.; Arnold, P. L. *Chem. Commun.* **2004**, *0*, 2738.

43.   Fegler, W.; Spaniol, T. P.; Okuda, J. *Dalton Trans.* **2010**, *39*, 6774.

44.   Sun, L.; Jentzen, W.; Shelnutt, J. A.   The Normal Coordinate Structural Decomposition   Engine. http://jasheln.unm.edu/jasheln/content/nsd/NSDengine/start.htm.

45.   Jentzen, W.; Song, X.-Z.; Shelnutt, J. A. *J. Phys. Chem. B* **1997**, *101*, 1684.

46.   A. Shelnutt, J.; Song, X.-Z.; Ma, J.-G.; Jia, S.-L.; Jentzen, W.; J. Medforth, C. *Chem. Soc. Rev.* **1998**, *27*, 31.

47.   Maes, E. M.; Roberts, S. A.; Weichsel, A.; Montfort, W. R. *Biochemistry* **2005**, *44*, 12690.

48.   Pang, J.; Li, X.; Morokuma, K.; Scrutton, N. S.; Sutcliffe, M. J. *J. Am. Chem. Soc.* **2011**, *134*, 2367.

49.   Shi, Z.; Franco, R.; Haddad, R.; Shelnutt, J. A.; Ferreira, G. C. *Biochemistry* **2006**, *45*, 2904.

50.   Yin, J.; Andryski, S. E.; Beuscher, A. E.; Stevens, R. C.; Schultz, P. G. *Proc. Natl. Acad. Sci.* **2003**, *100*, 856.

51.   Zhou, Z.; Shen, M.; Cao, C.; Liu, Q.; Yan, Z. *Chem. Eur. J.* **2012**, *18*, 7675.

52.   Zhou, Z.; Liu, Q.; Yan, Z.; Long, G.; Zhang, X.; Cao, C.; Jiang, R. *Org. Lett.* **2013**, *15*, 606.

53.   Boschi, T.; Licoccia, S.; Paolesse, R.; Tagliatesta, P.; Pelizzi, G.; Vitali, F. *Organometallics* **1989**, *8*, 330.

54.   Yeung, S. K.; Chan, K. S. *Organometallics* **2005**, *24*, 6426.

55.   Ogoshi, H.; Setsune, J.; Yoshida, Z. *J. Organomet. Chem.* **1978**, *159*, 317.

56.   Blessing, R. *Acta Crystallogr., Sect. A* **1995**, *51*, 33.

57.   ; APEX2 Version 2.2. Bruker AXS Inc.: Madison, WI, USA, 2007.

58.   Sheldrick, G. M. *Acta. Cryst.* **2008**, *A64*, 112.

59.   Song, X.; Chan, K. S. *Organometallics* **2007**, *26*, 965.

Appendix D

Absorption Spectroscopy
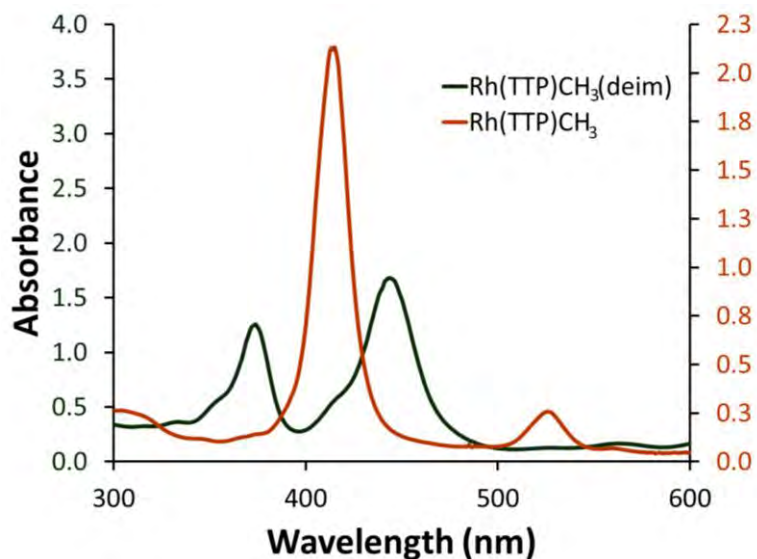
Figure 5.13: The absorption spectra for Rh(TTP)CH$_3$ (1.12 × 10^{-4} M, orange, right axis) and complex **25a** (2.01 × 10^{-4} M, green, left axis) in THF. Absorption axes were scaled to demonstrate the actual relative band intensities.
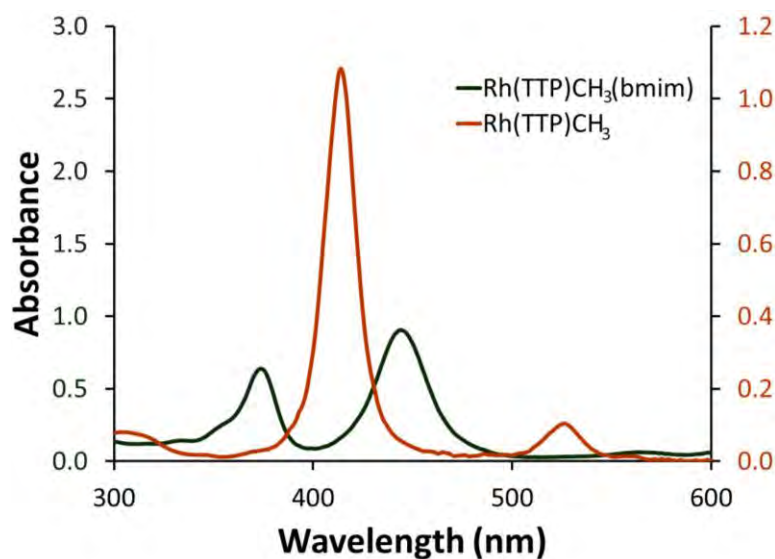
Figure 5.14 The absorption spectra for Rh(TTP)CH$_3$ (4.41 × 10^{-5} M, orange, right axis) and complex **25b** (1.11 × 10^{-4} M, green, left axis) in THF. Absorption axes were scaled to demonstrate the actual relative band intensities.
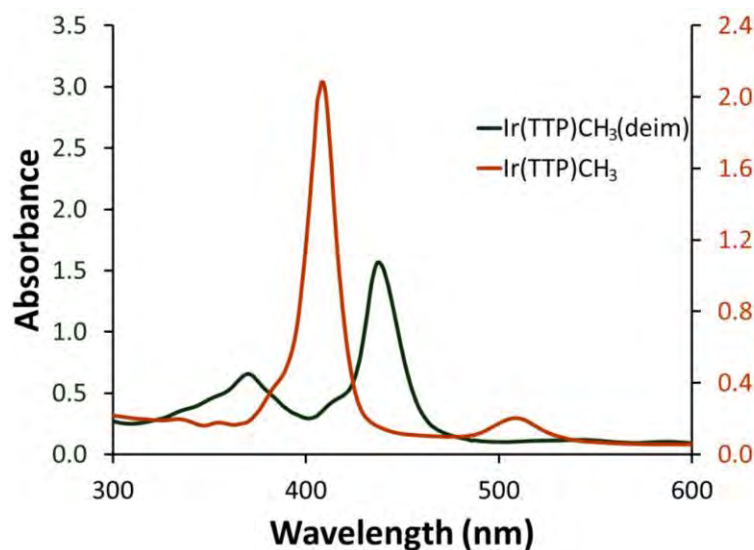
Figure 5.15: The absorption spectra for Ir(TTP)CH$_3$ (1.09 × 10^{-5} M, orange, right axis) and complex **26a** (1.55 × 10^{-4} M, green, left axis) in THF. Absorption axes were scaled to demonstrate the actual relative band intensities.
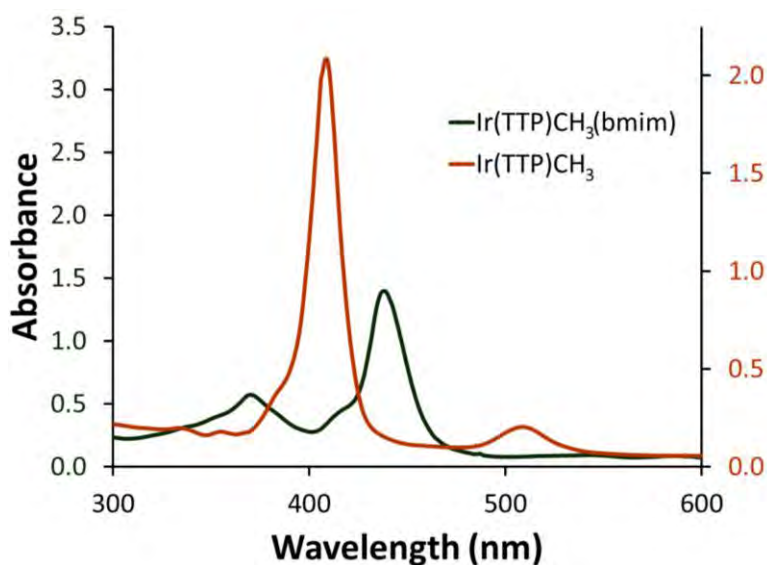
Figure 5.16: The absorption spectra for Ir(TTP)CH$_3$ (1.09 × 10^{-5} M, orange, right axis) and complex **26b** (1.71 × 10^{-4} M, green, left axis) in THF. Absorption axes were scaled to demonstrate the actual relative band intensities.

NMR Characterization Data

Figure 5.17: [1]NMR spectrum of complex **22**.

Ir(TTP)(C≡NBn)$_2$(BF$_4$)
^{13}C NMR
300 MHz
CDCl$_3$
ambient temperature

−183.07

141.72
138.18
137.77
134.26
132.43
128.85
128.51
128.02
127.81
124.16
122.55

CDCl$_3$

−45.16

−21.67

f1 (ppm)
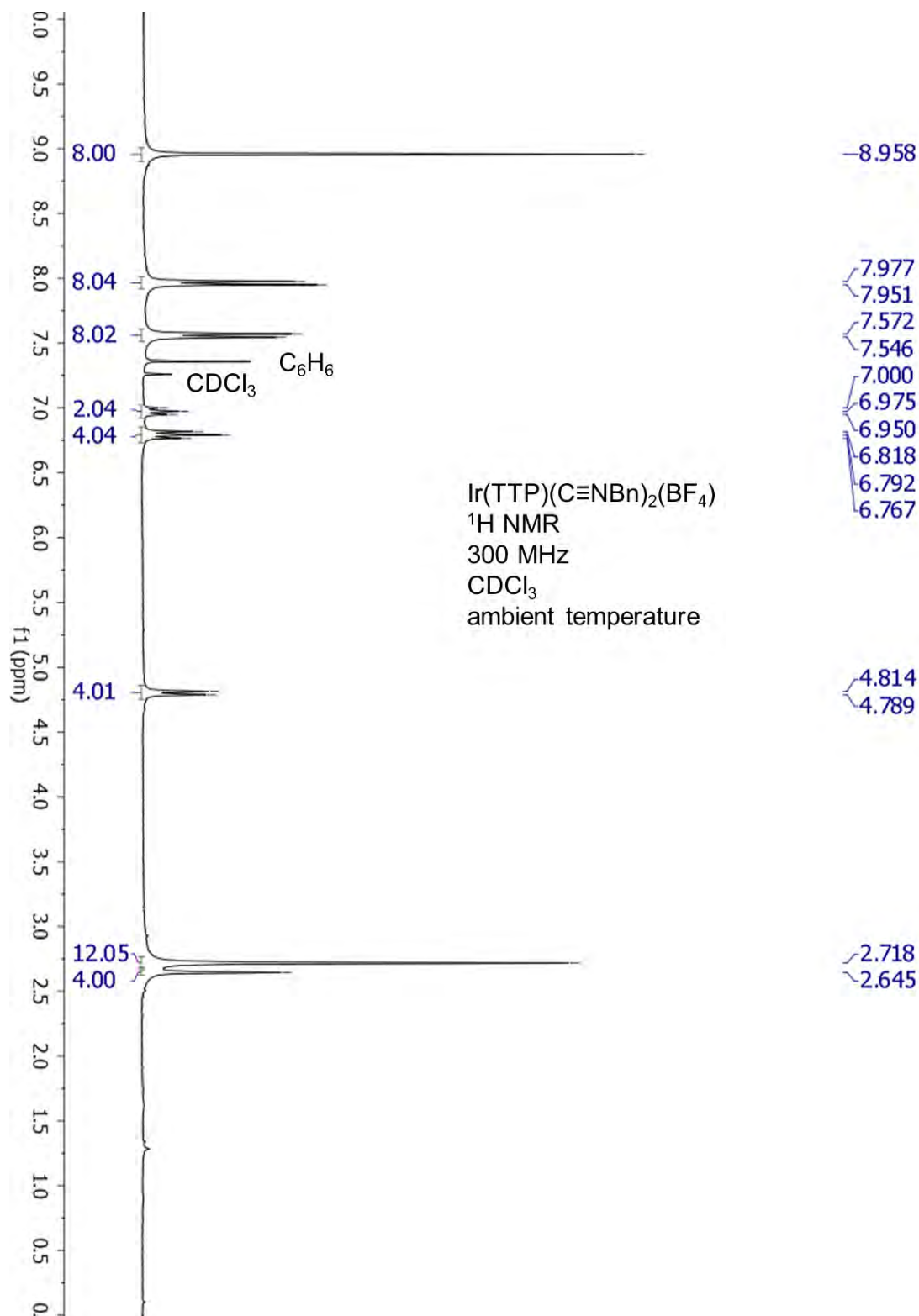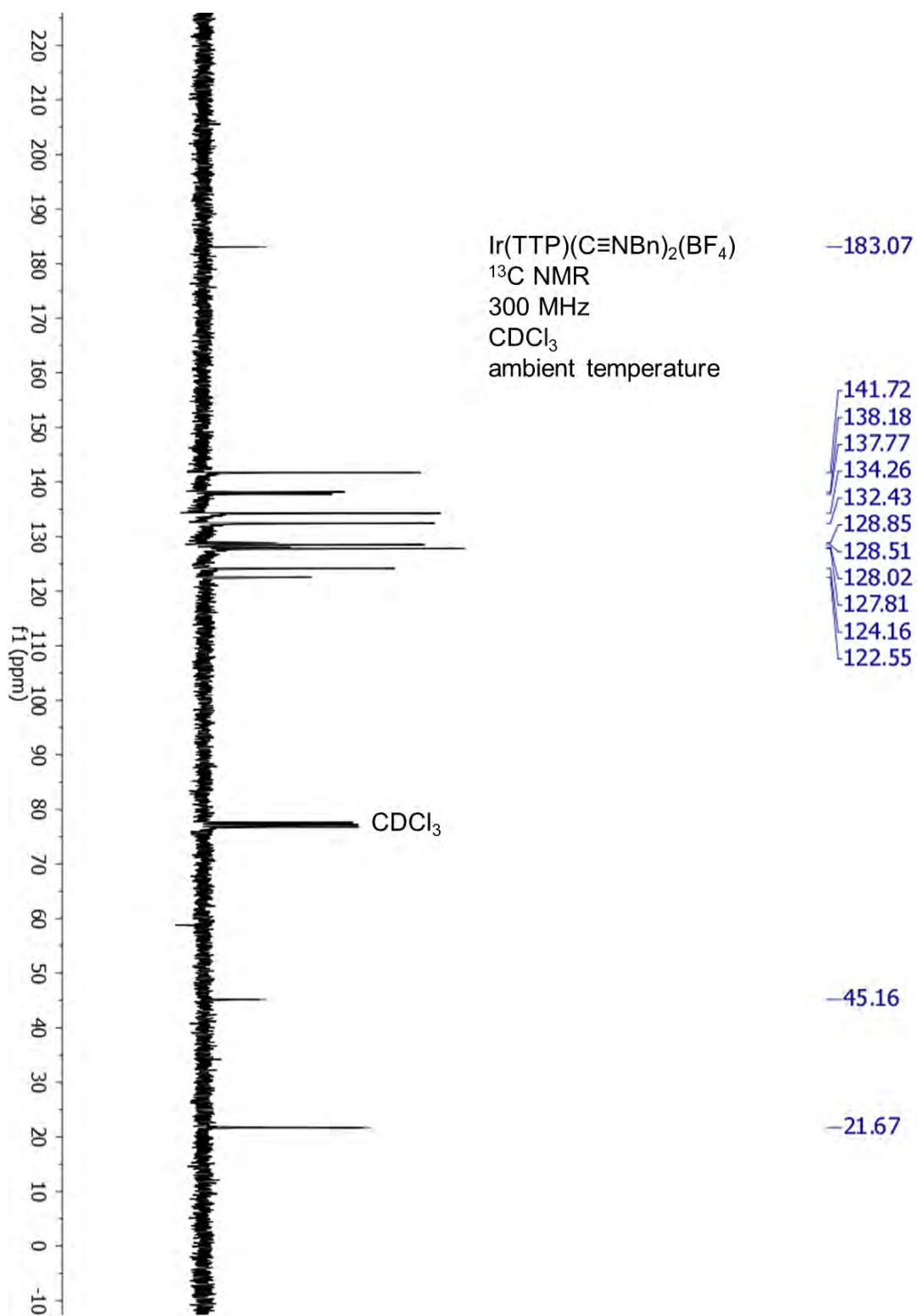
Figure 5.18: ^{13}C NMR of complex **22**.

Ir(TTP)(C=(NHBn)$_2$)(CNBn)(BF$_4$)
^{1}H NMR
400 MHz
CDCl$_3$
ambient temperature
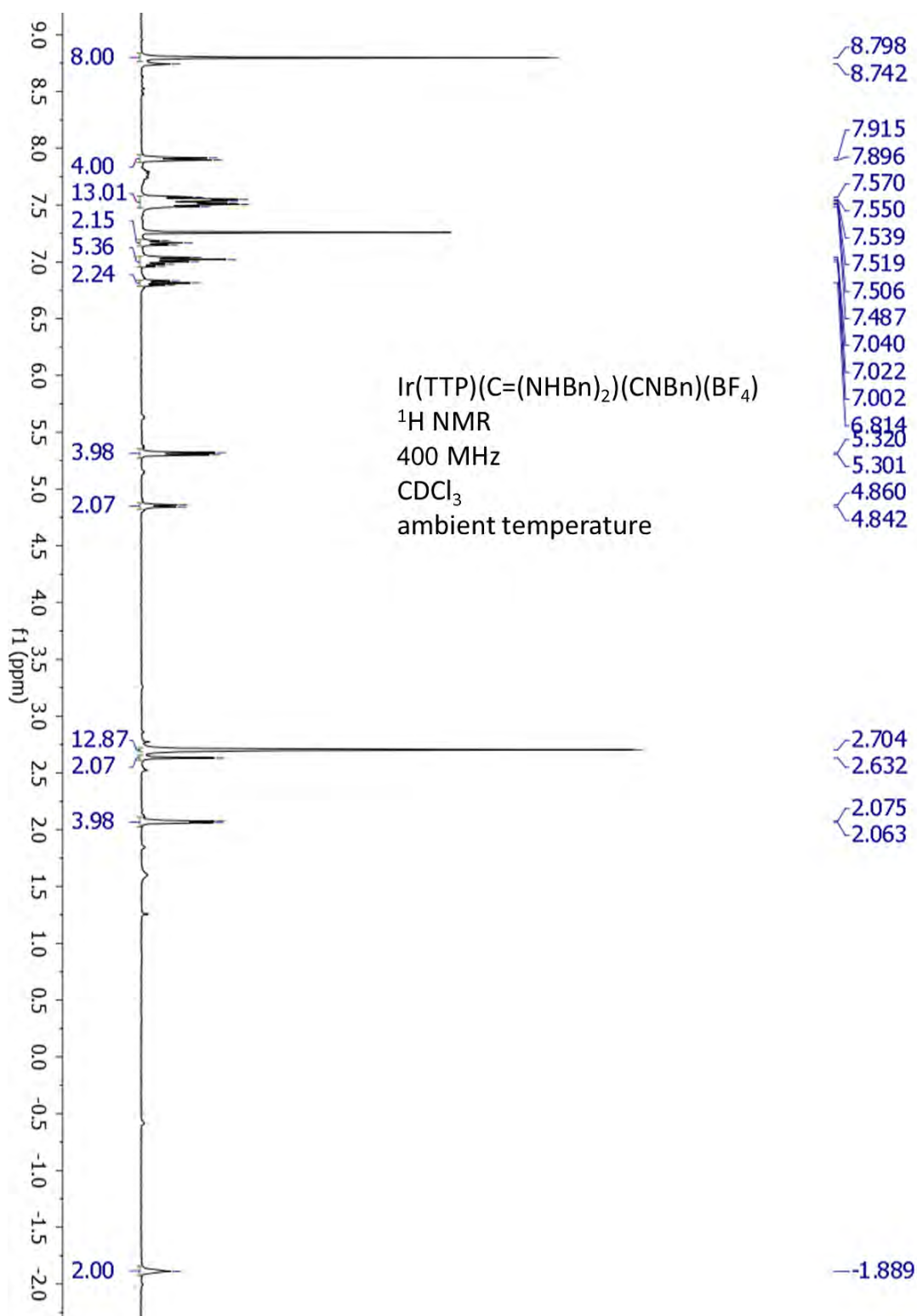
Figure 5.19: ^{1}H NMR spectrum of complex **23**.

Ir(TTP)(C=(NHBn)₂)(CNBn)(BF₄)
¹³C NMR
600 MHz
CDCl₃
ambient temperature

−162.92
141.56
138.20
137.58
134.43
134.09
134.05
132.50
129.47
129.00
128.48
128.21
127.89
127.85
127.73
126.17
124.18
122.66

−48.12
~44.85

−21.65
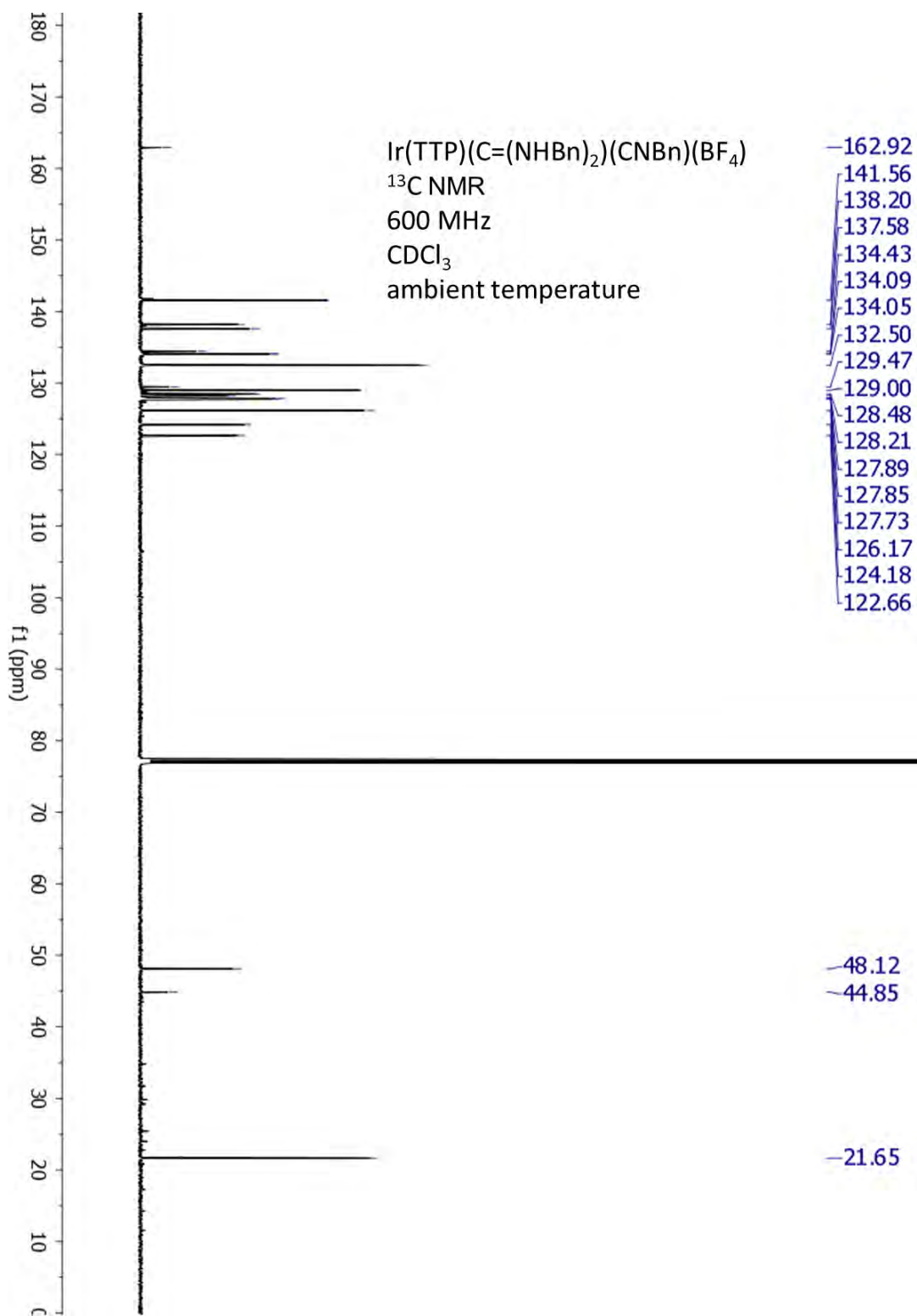
Figure 5.20: ¹³C NMR spectrum of complex **23**.

Rh(TTP)CH$_3$(deim)
^{1}H NMR
400 MHz
THF d$_8$
303.0 K

THF

THF
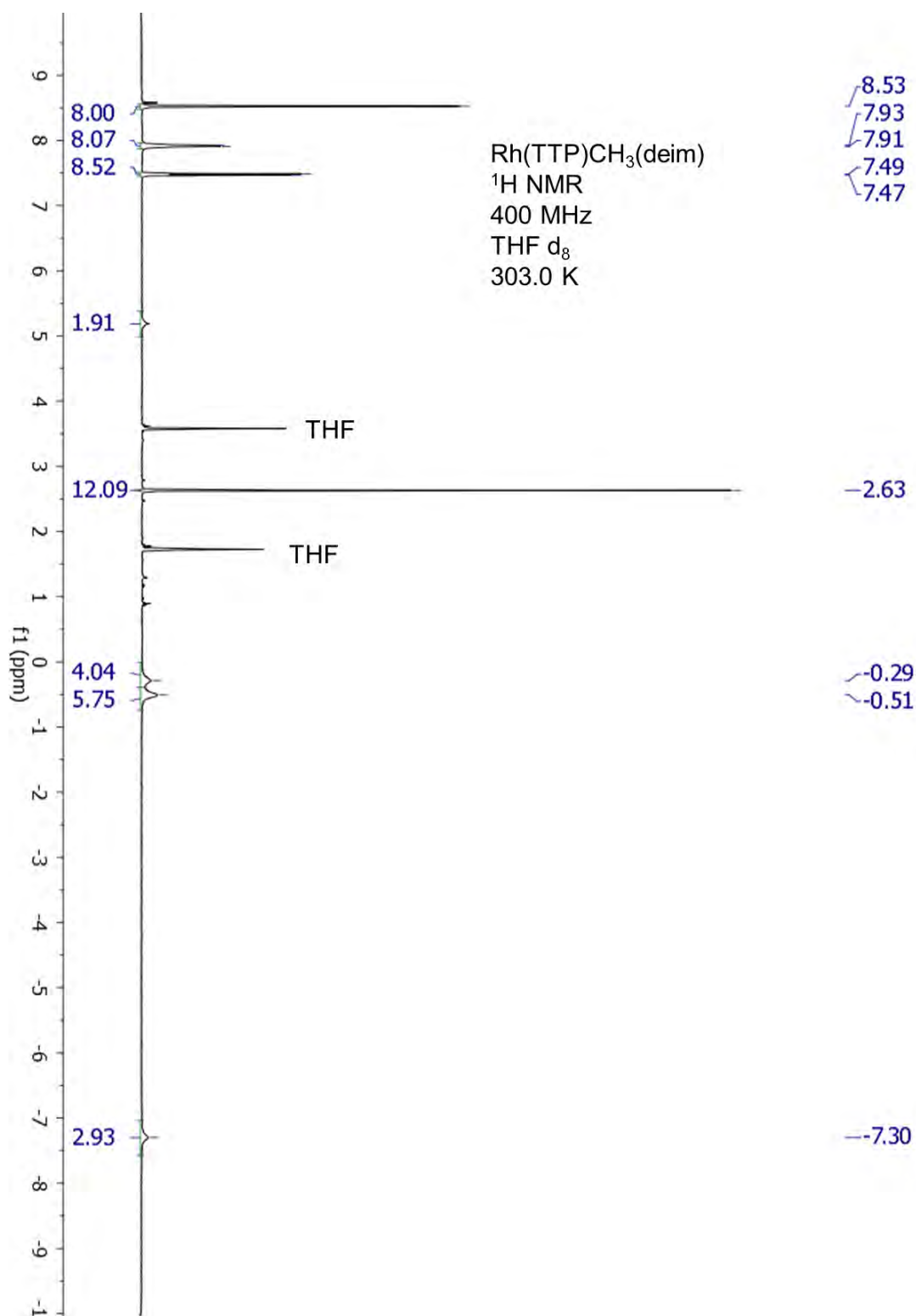
Figure 5.21: ^{1}H NMR spectrum of complex **25a**.

Rh(TTP)CH$_3$(deim)
^{13}C NMR
600 MHz
THF d$_8$
263.0 K

180.06
179.91

143.07
140.45
137.35
134.69
134.57
131.79
127.96
127.59
121.44
117.89

40.19

21.38
15.32

−4.55
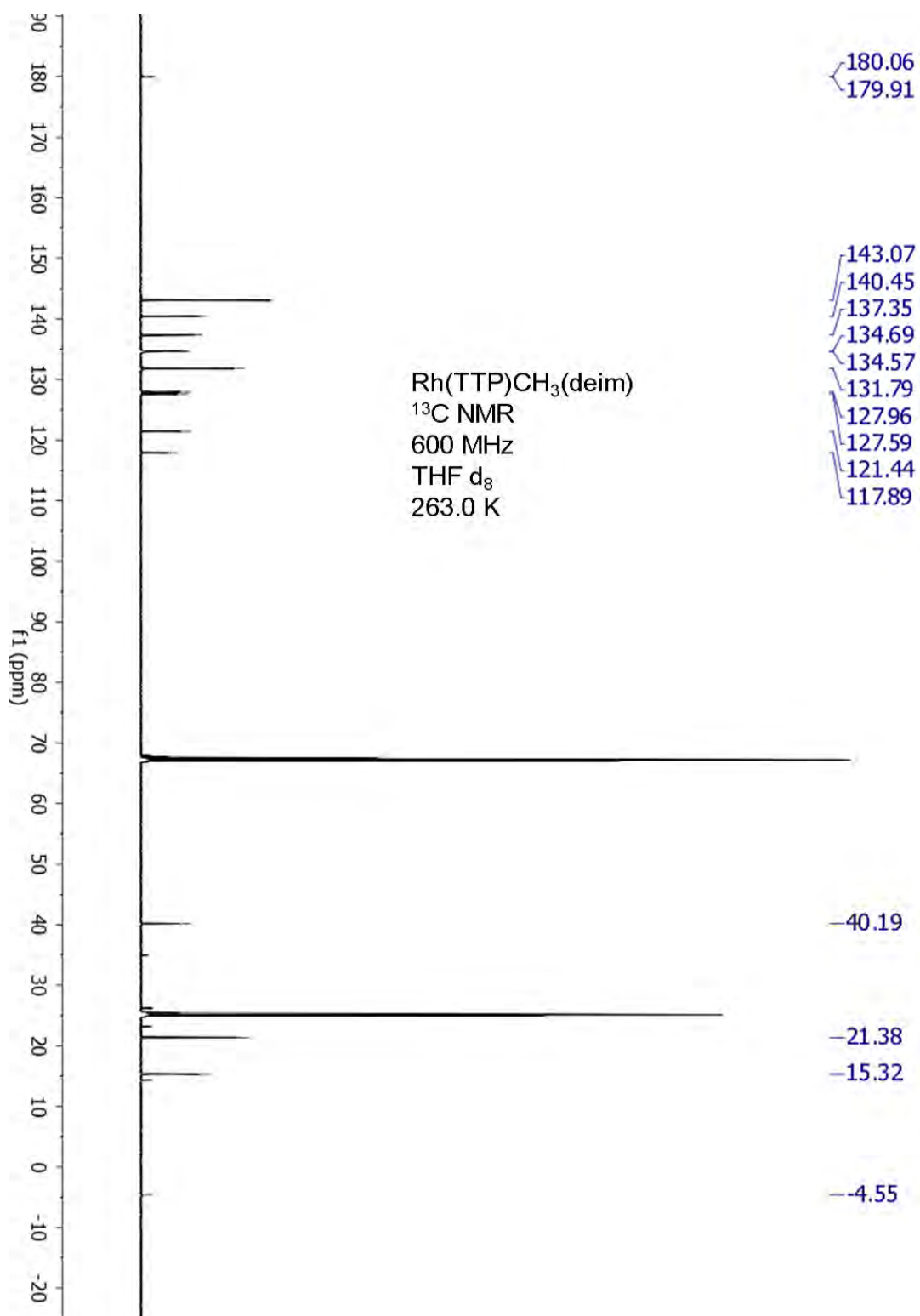
Figure 5.22: ^{13}C NMR spectrum of complex **25b**.
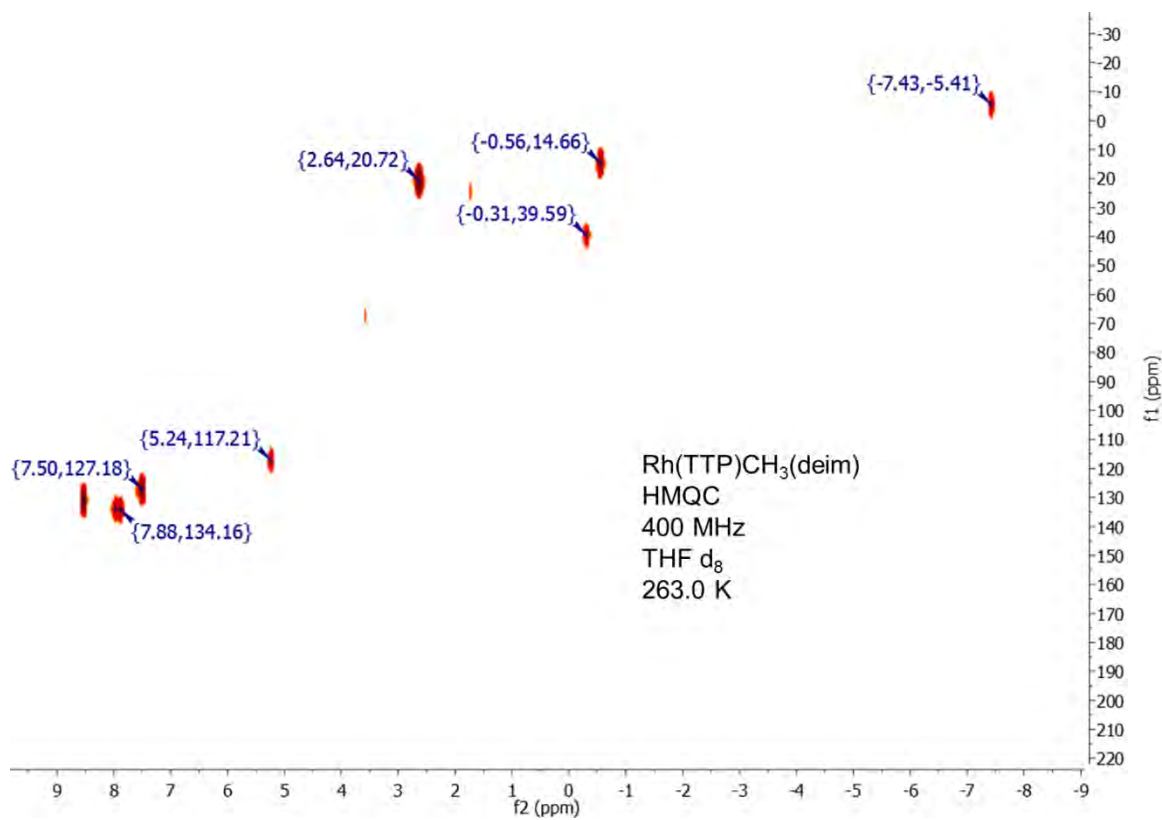
Figure 5.23: HMQC spectrum of complex **25b**.

Rh(TTP)CH$_3$(bmim)
^{1}H NMR
400 MHz
THF d$_8$
303.0 K
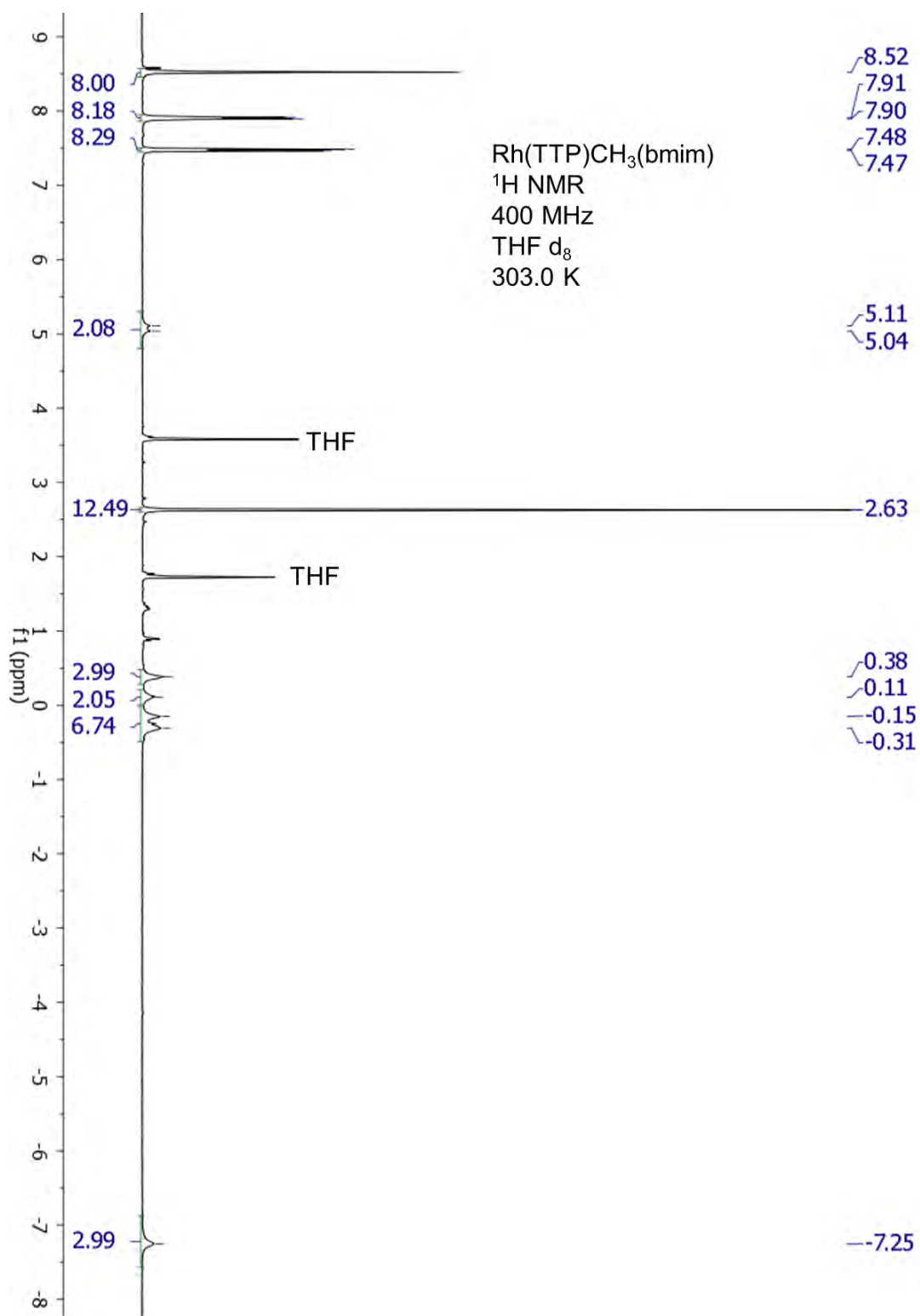
Figure 5.24: ^{1}H NMR of complex **25b**.

Rh(TTP)CH$_3$(bmim)
^{13}C NMR
600 MHz
THF d$_8$
263.0 K

143.00
140.41
137.35
134.61
134.46
131.74
127.97
127.57
121.41
120.31
117.16

45.12

32.88
32.47
26.20
21.39
19.57
13.79
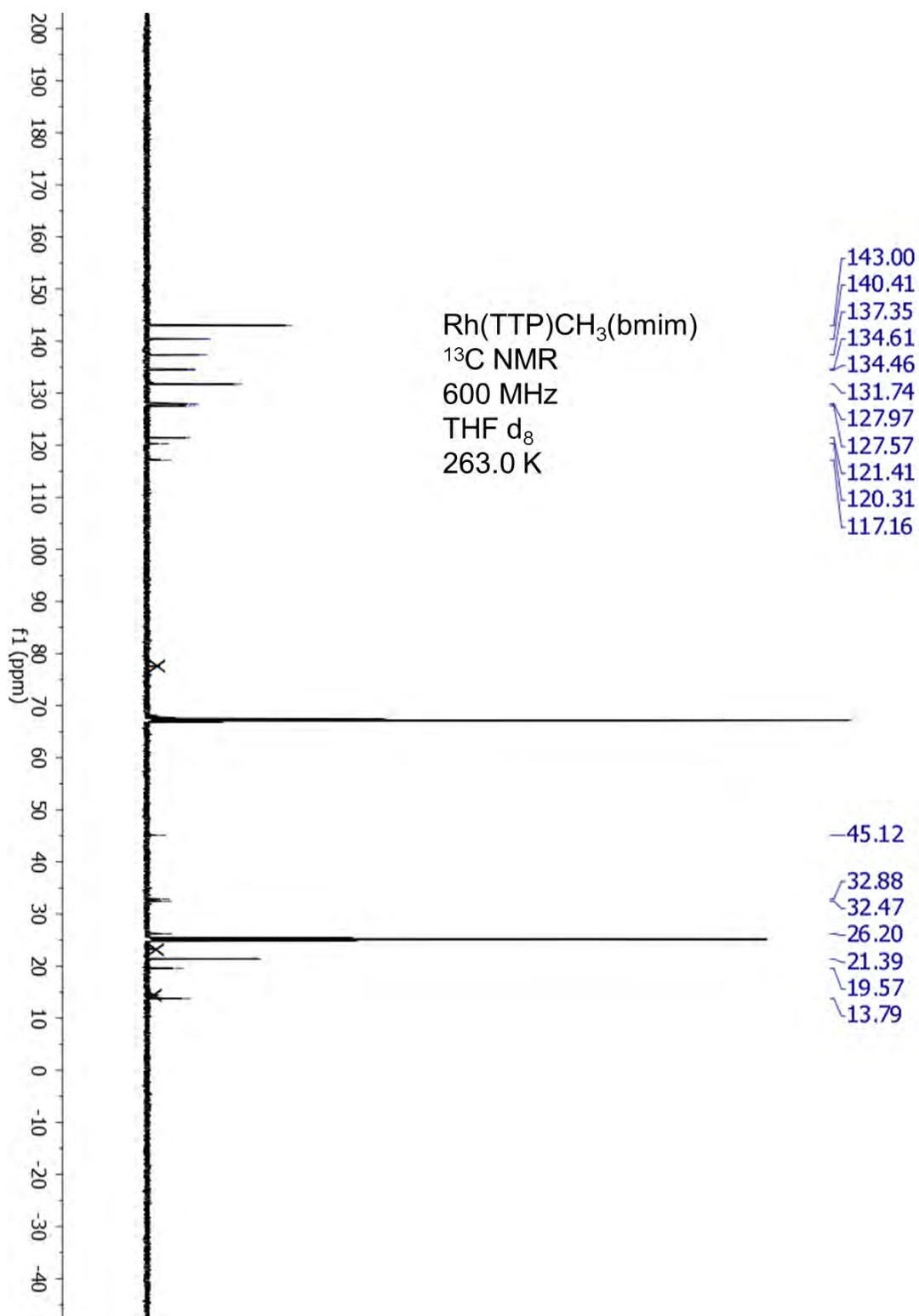
Figure 5.25: ^{13}C NMR of complex **25b**.

Rh(TTP)CH$_3$(deim)
^{13}C NMR
700 MHz
THF d$_8$
ambient temperature
with Cr(acac)$_3$

−180.79

143.03
140.47
−137.28
134.51
131.62
127.87
127.66

−121.39

−117.85
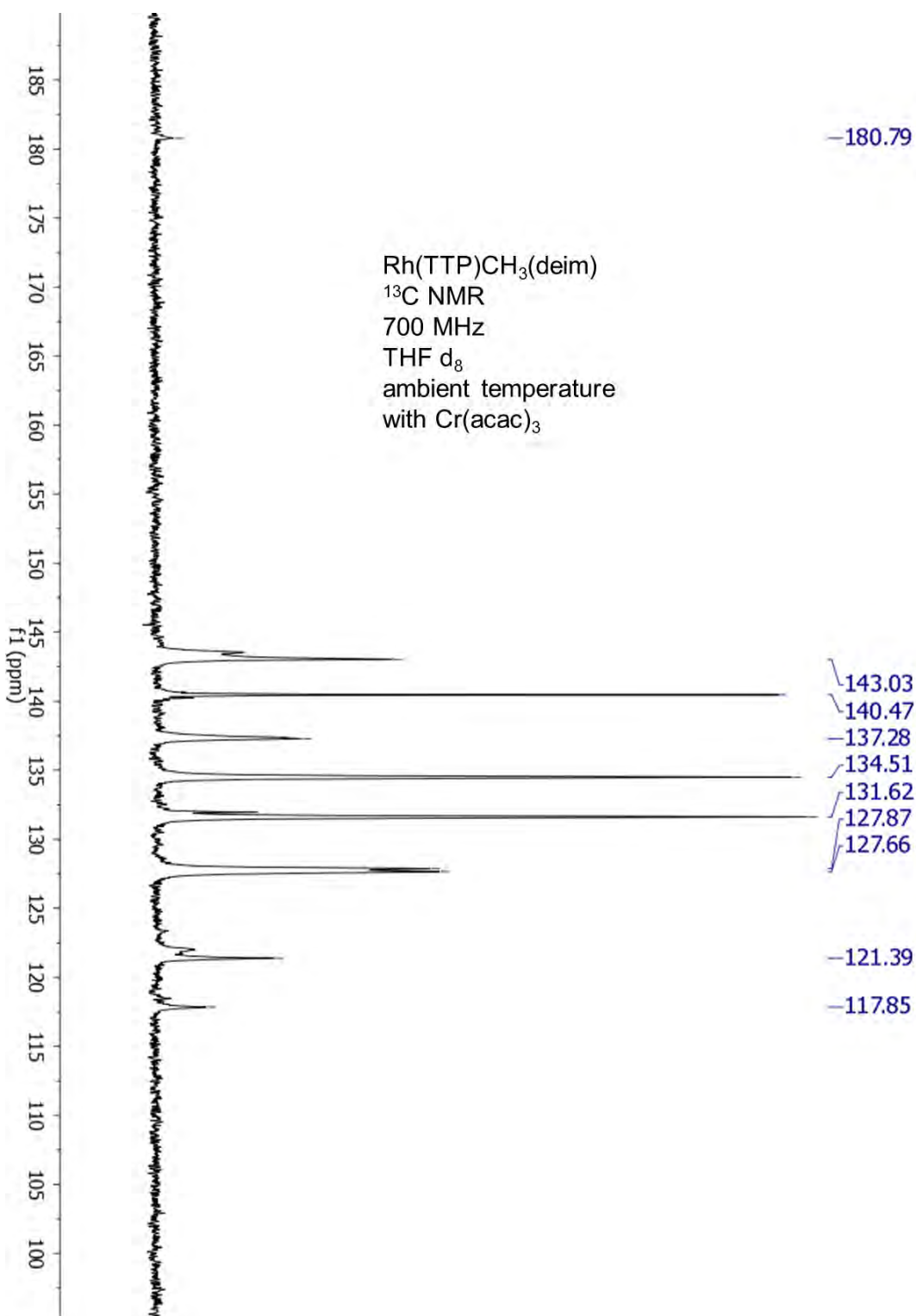
Figure 5.26: ^{13}C NMR spectrum of complex **26b**. Sample contains Cr(acac)$_3$ (*ca.* 13 mg), which induces faster relaxation of the signals and allows for easier observation of the carbene carbon signal.
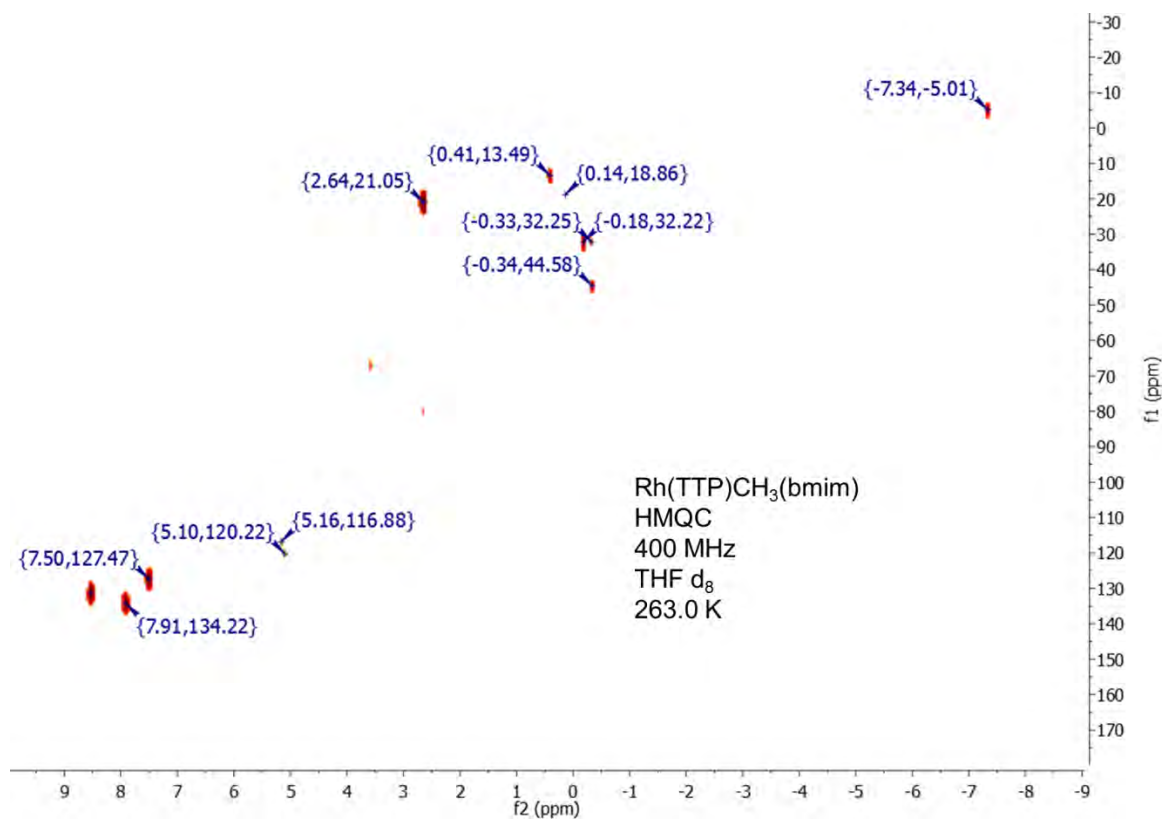
Figure 5.27: HMQC spectrum of complex **25b**.
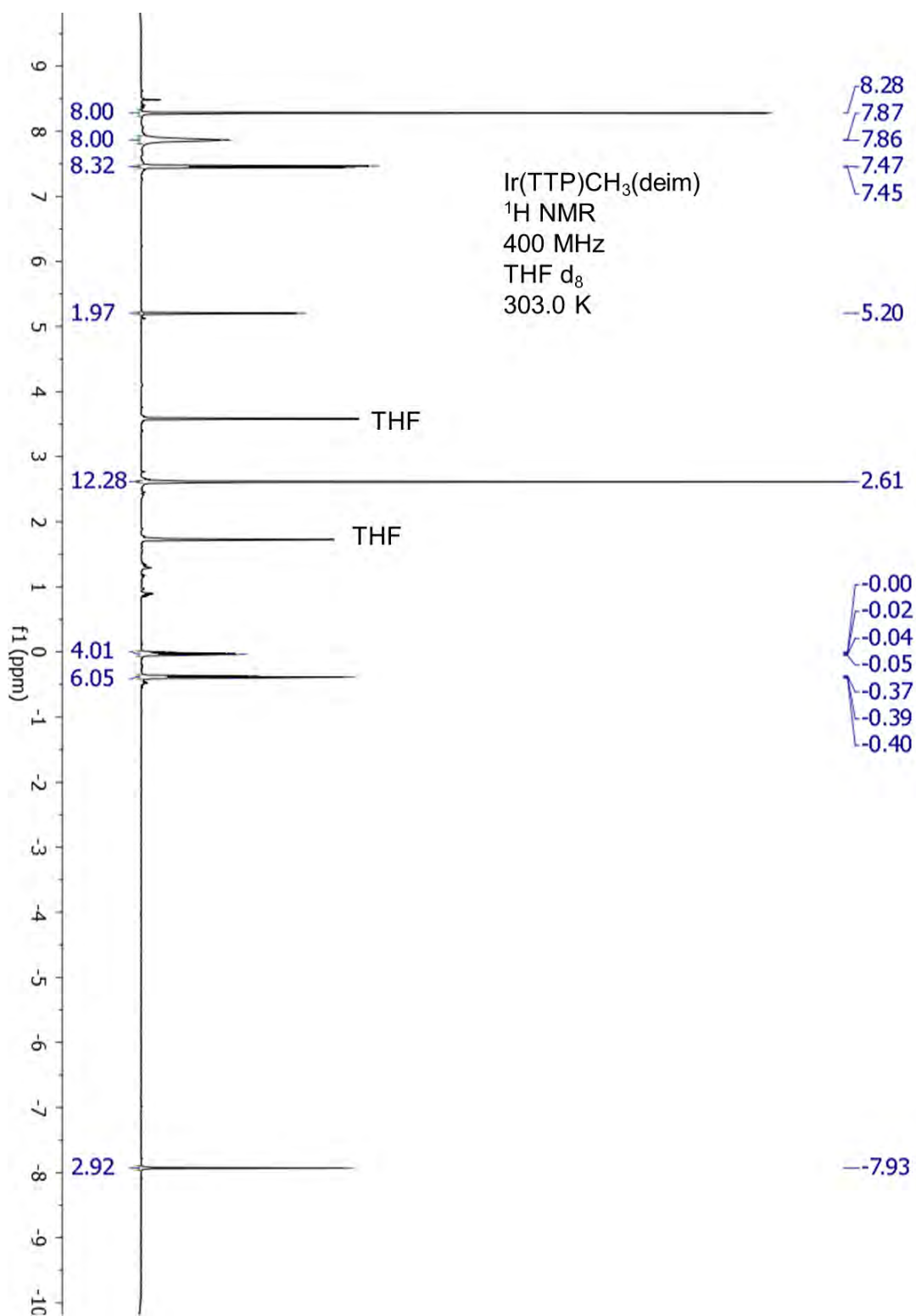
Figure 5.28: ^{1}H NMR spectrum of complex **25a**.

Ir(TTP)CH$_3$(deim)
^{13}C NMR
600 MHz
THF d$_8$
298 K

210 200 190 180 170 160 150 140 130 120 110 100 90 80 70 60 50 40 30 20 10 0 -10 -20 -30 -40 -50 -60
f1 (ppm)

—164.33
143.43
139.92
137.31
134.64
134.44
131.51
127.99
127.60
123.71
118.03

—40.16

—21.30
—15.12

—-21.97
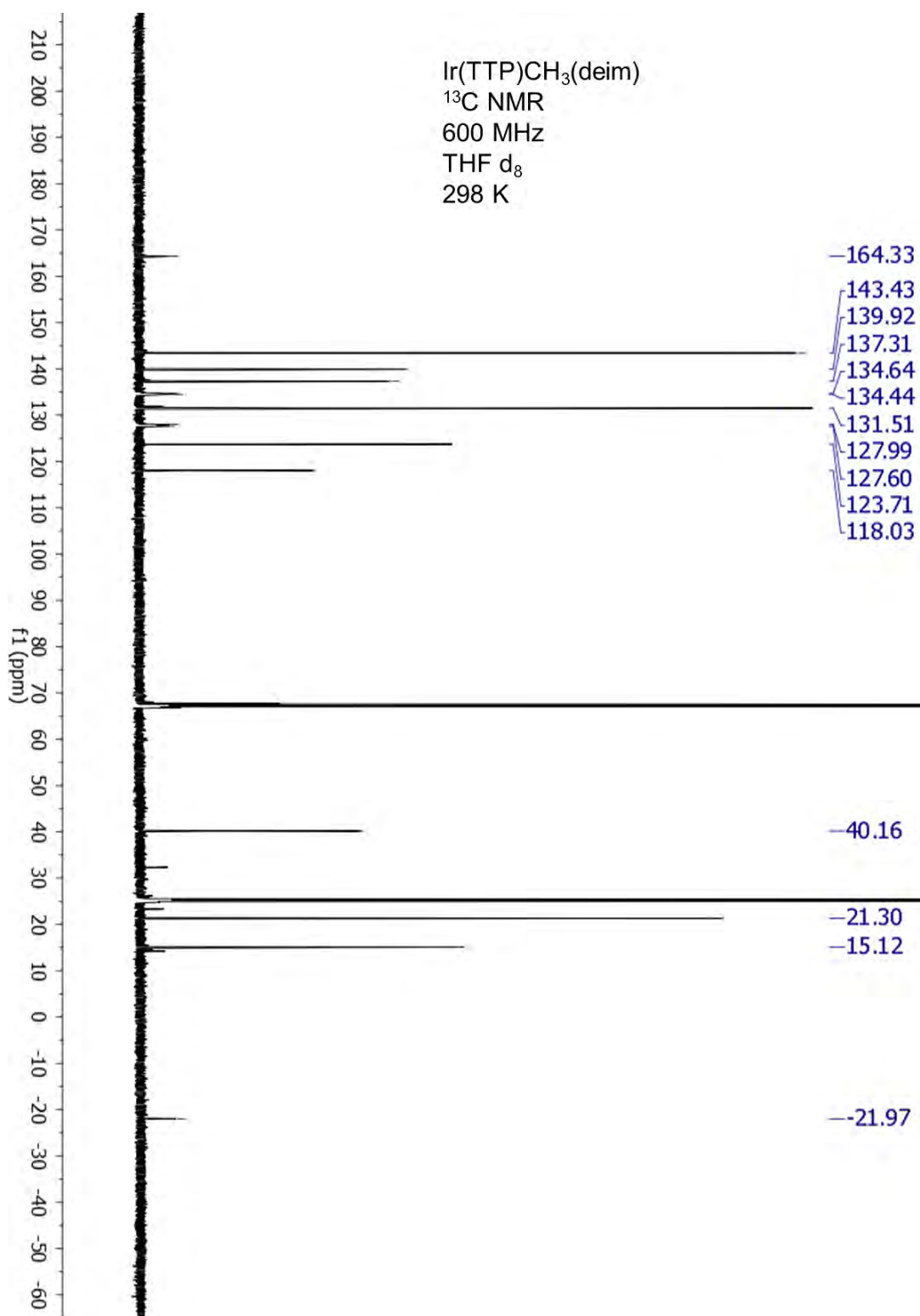
Figure 5.29: ^{13}C NMR spectrum of complex **26a**.
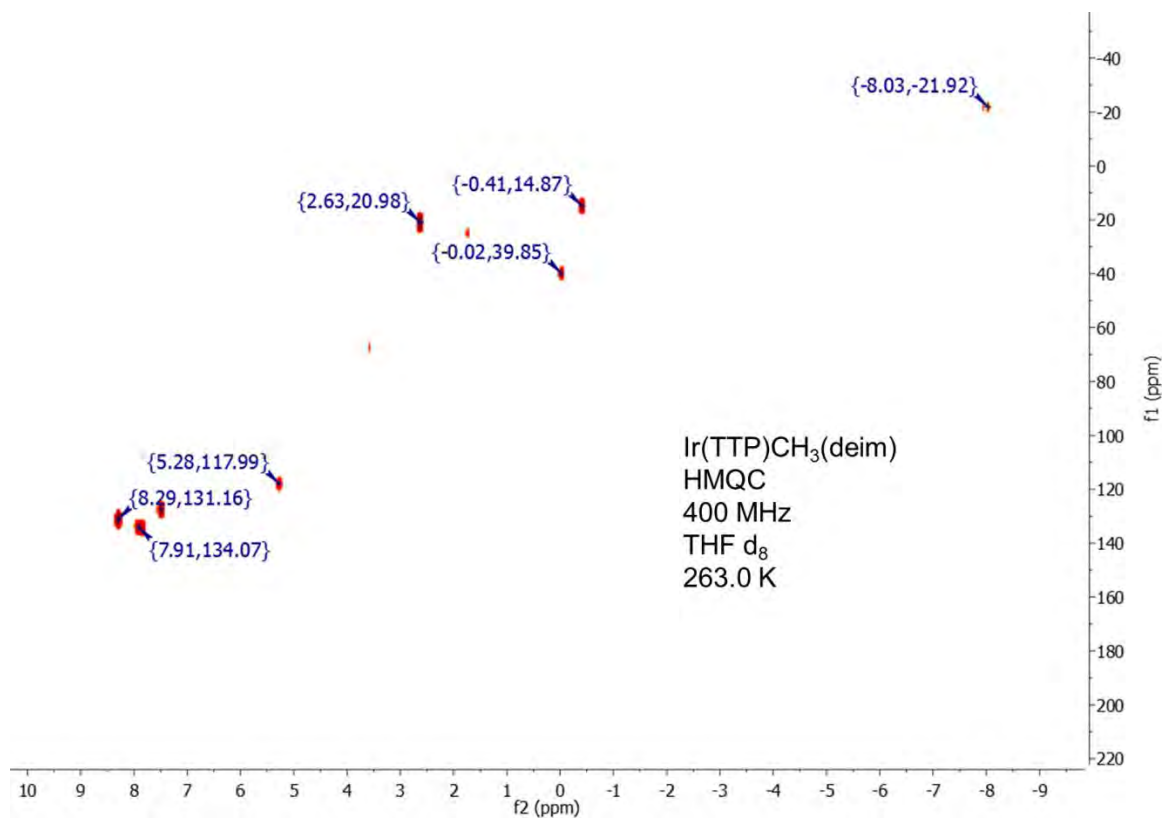
Figure 5.30: HMQC spectrum of complex **26a**.
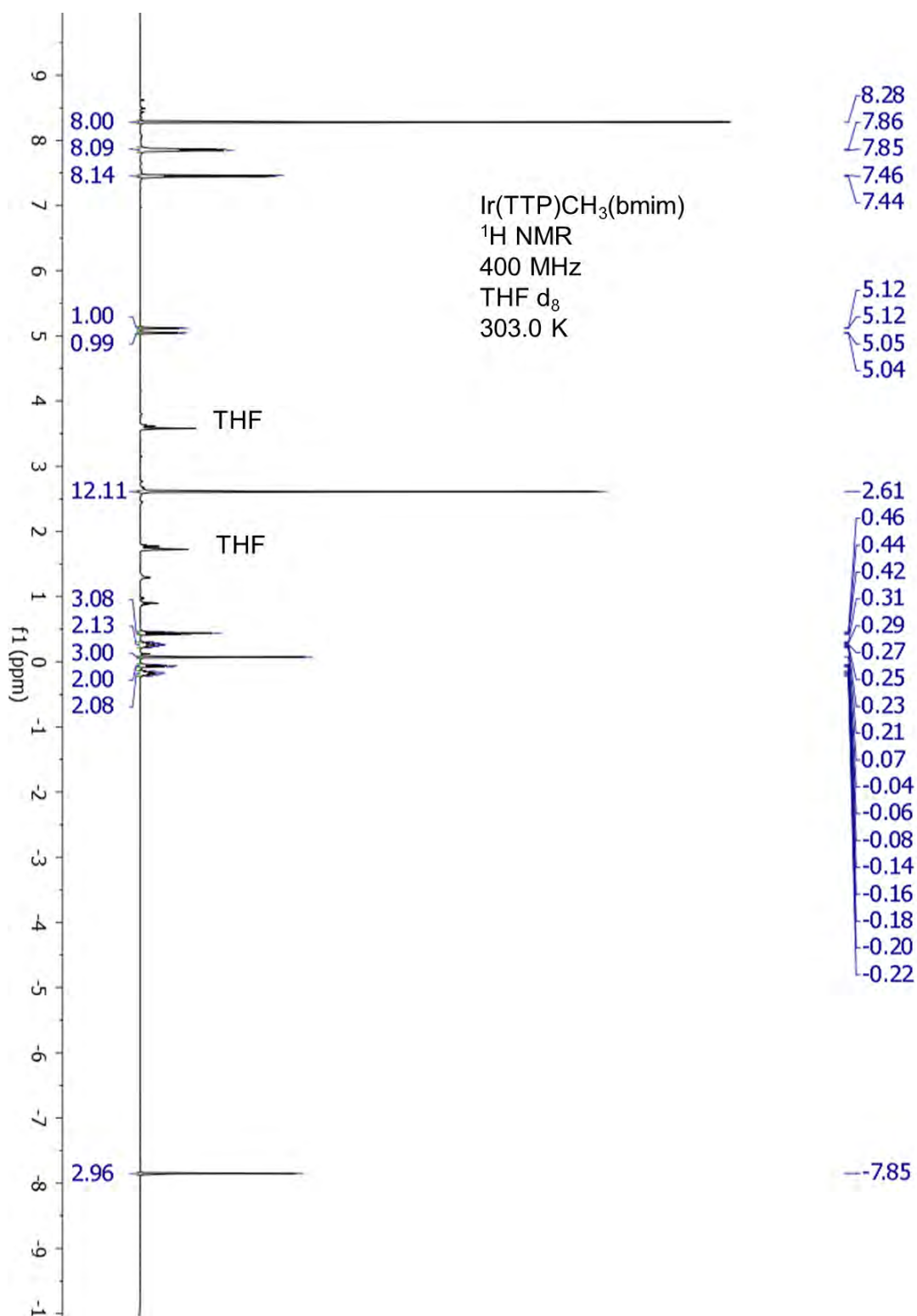
Figure 5.31: ^{1}H NMR spectrum of complex **26b**.

Ir(TTP)CH$_3$(bmim)
^{13}C NMR
600 MHz
THF d$_8$
298 K

—164.86
143.40
139.91
137.31
134.66
134.34
131.47
127.96
127.58
123.74
120.61
117.23

—45.15

32.70
32.68
21.30
19.61
13.67

-21.76
-21.92
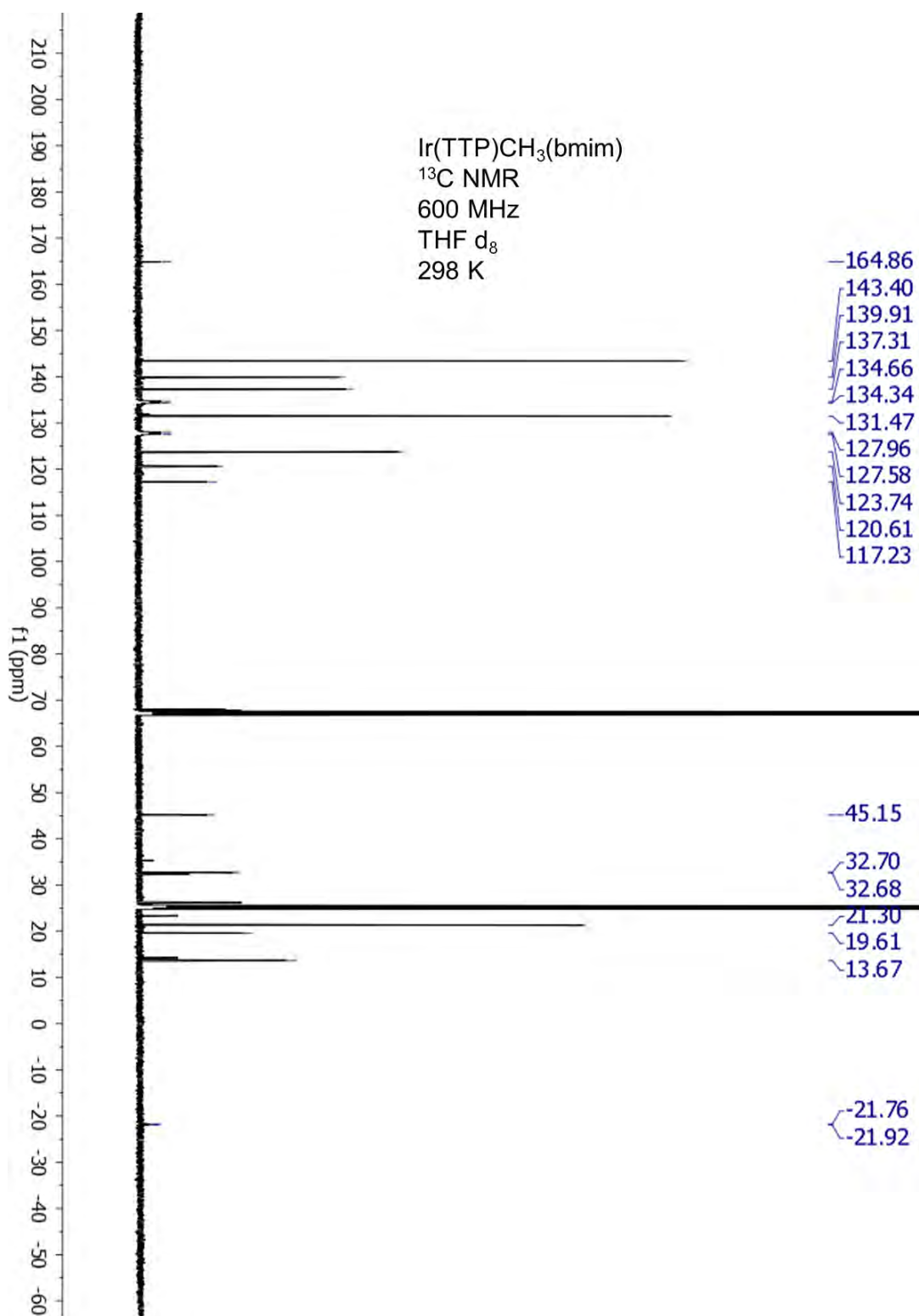
Figure 5.32: ^{13}C NMR spectrum of complex **26b**.
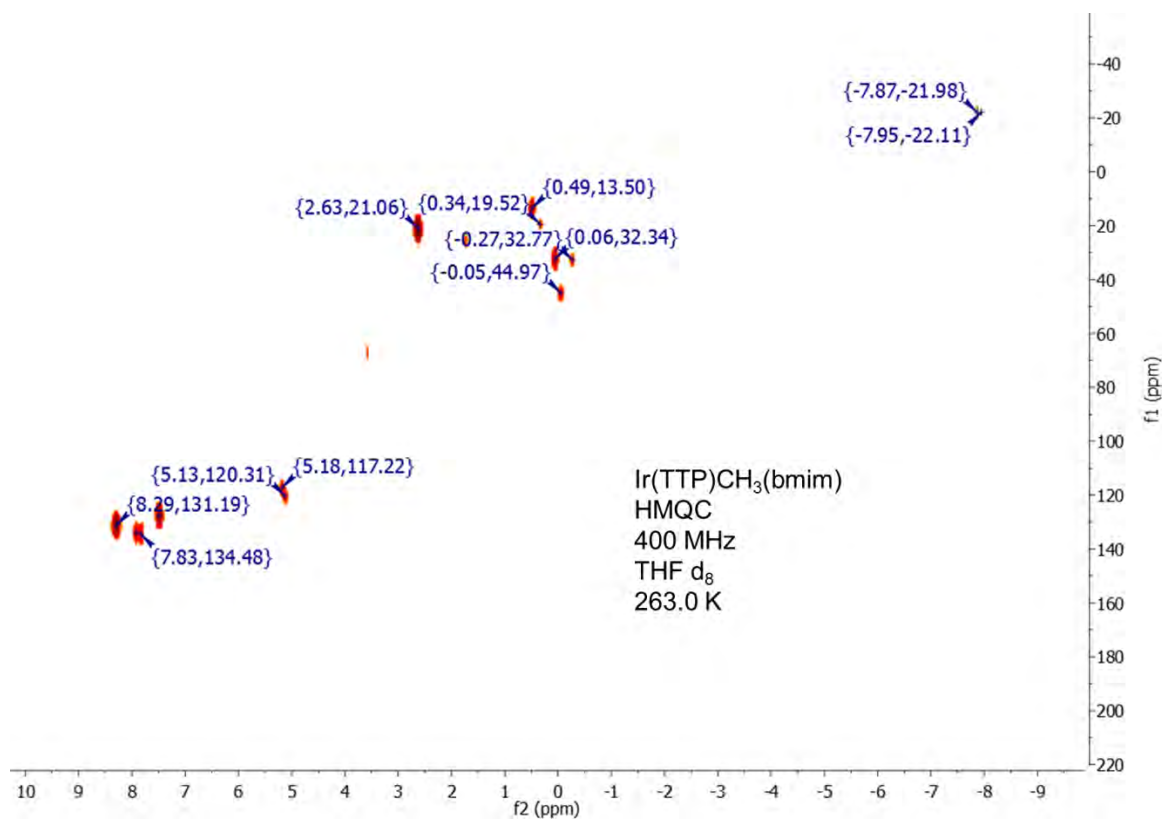
Figure 5.33: HMQC spectrum of complex **26b**.

Variable Temperature 1H NMR Studies
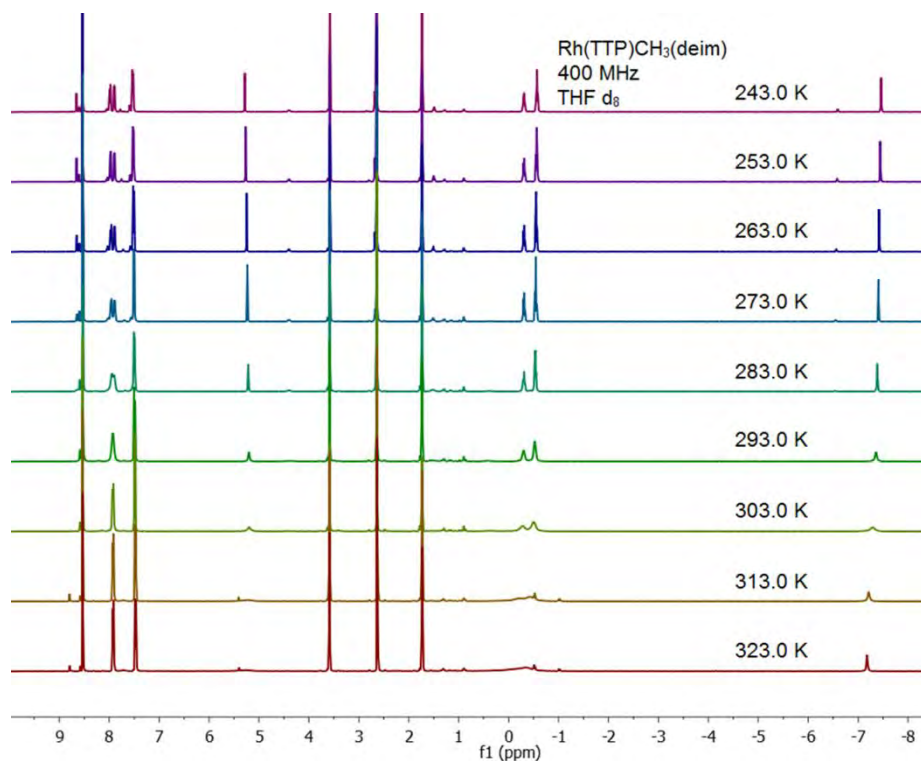
Figure 5.34: Variable temperature ^{1}H NMR spectra of complex **25a**.
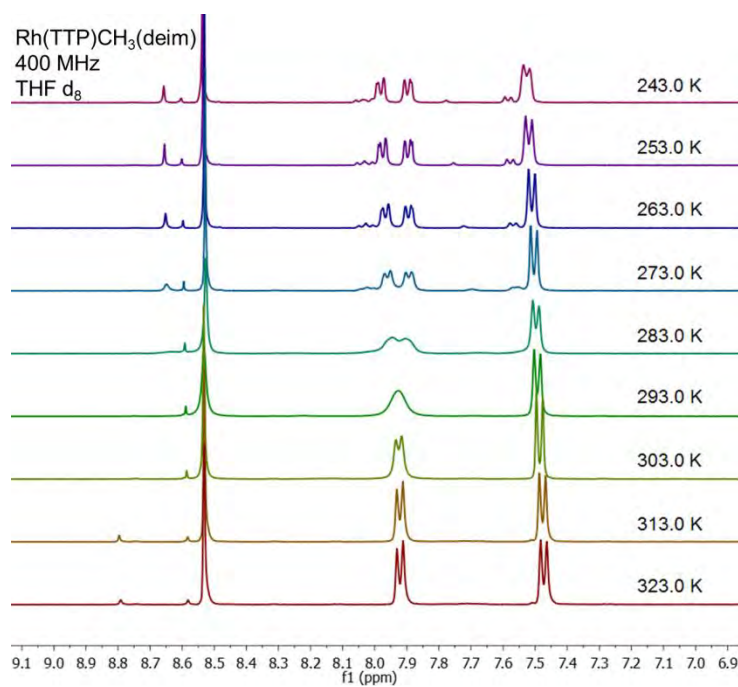
Figure 5.35: Expanded view of the aromatic region for complex **25a**.
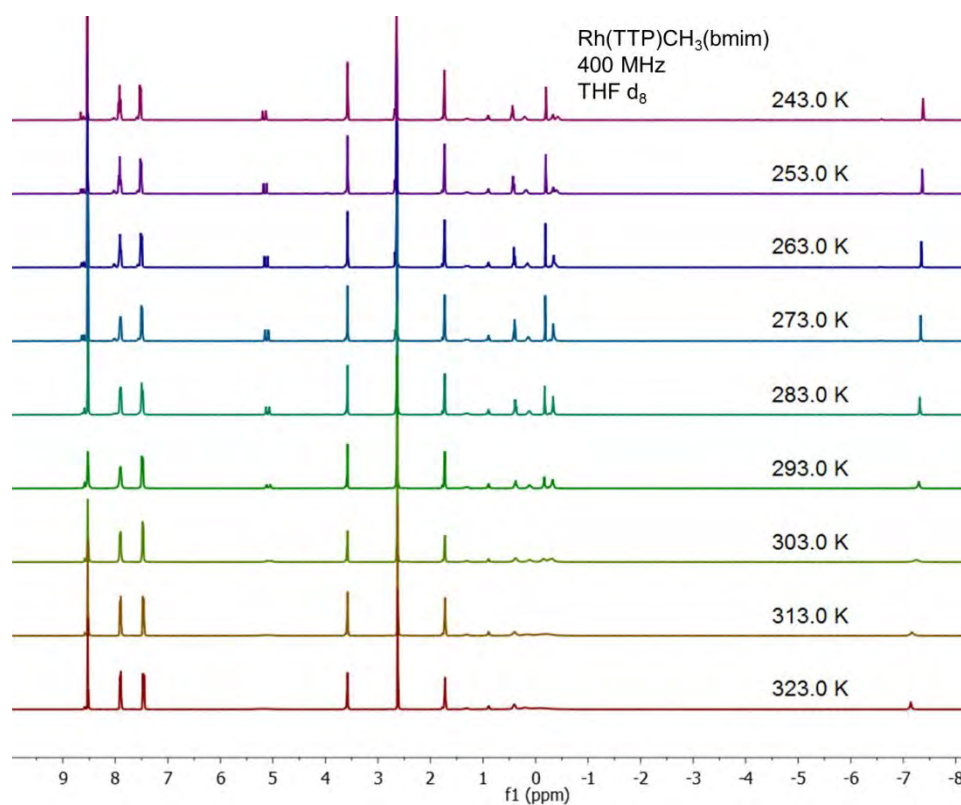
Figure 5.36: Variable temperature ^{1}H NMR spectra of complex **25b**.
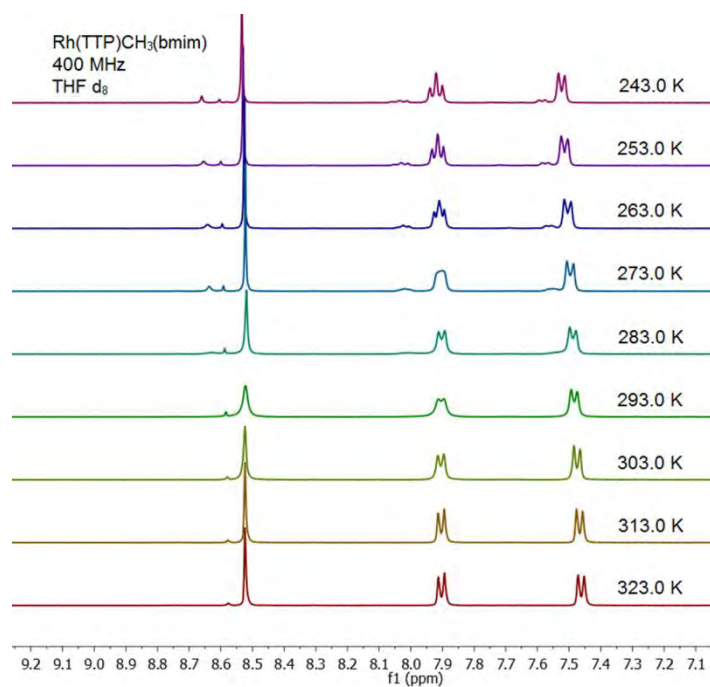
Figure 5.37: Expanded view of the aromatic region for complex **25b**.
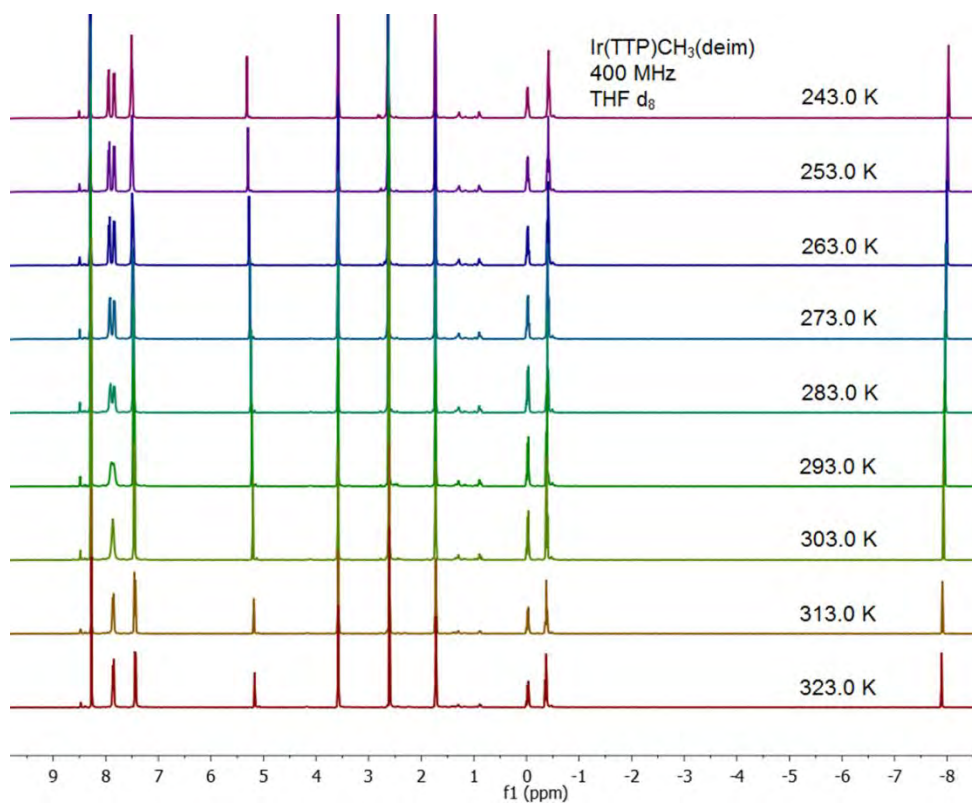
Figure 5.38: Variable temperature ^{1}H NMR spectra of complex **26a**.
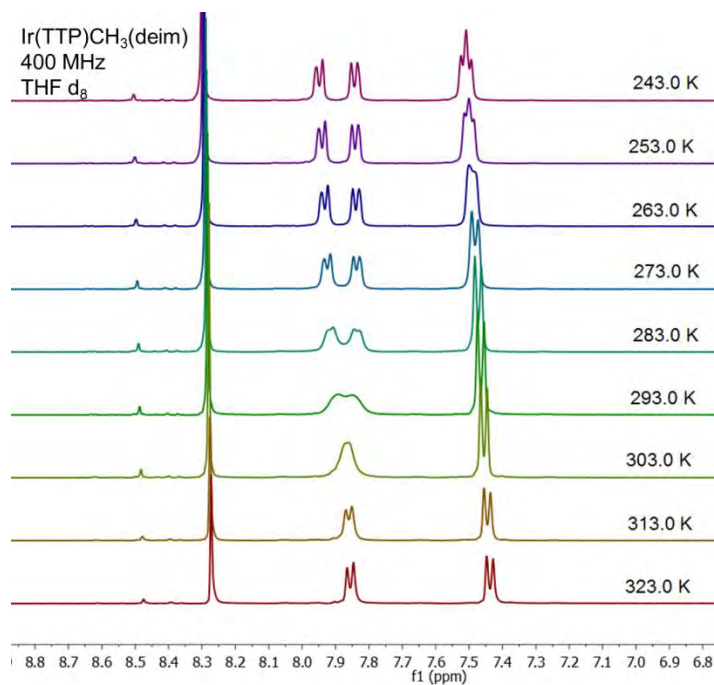
Figure 5.39: Expanded view of the aromatic region for complex **26a**.
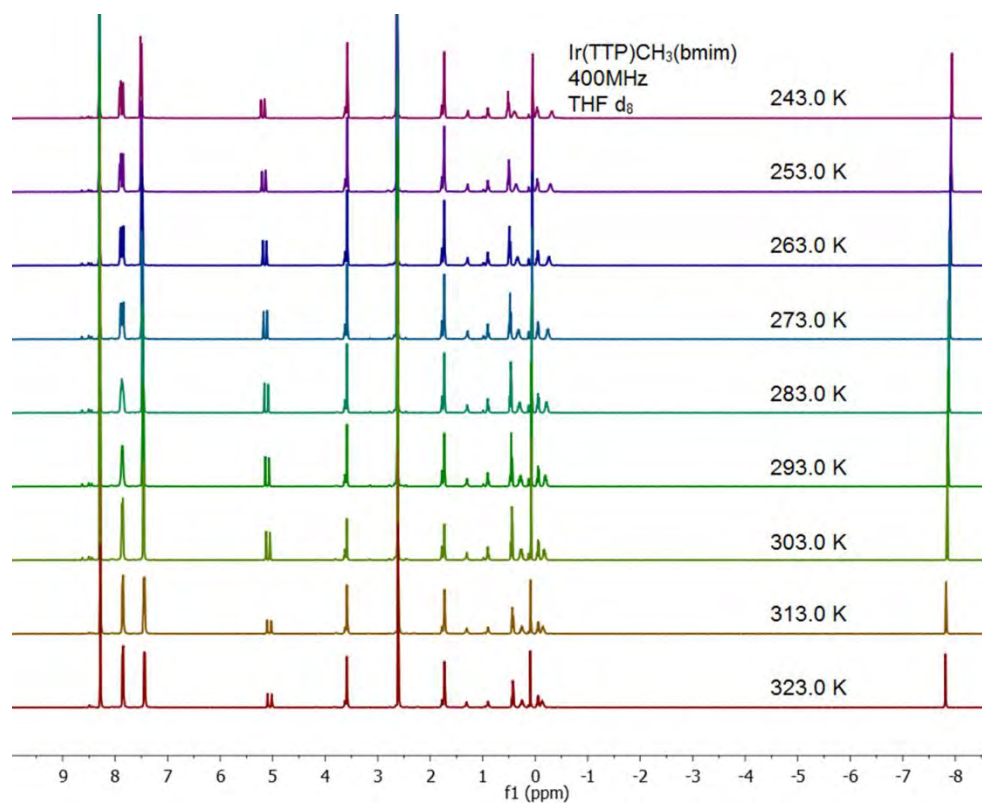
Figure 5.40: Variable temperature ^{1}H NMR spectra of complex **26b**.
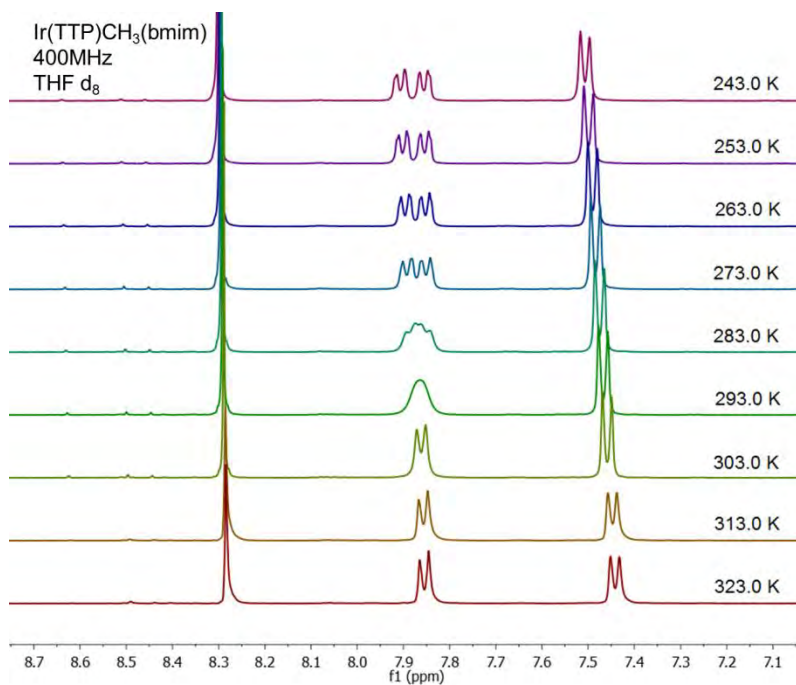
Figure 5.41: Expanded view of the aromatic region for complex **26b**.

Ligand Exchange with Rh(TTP)CH₃
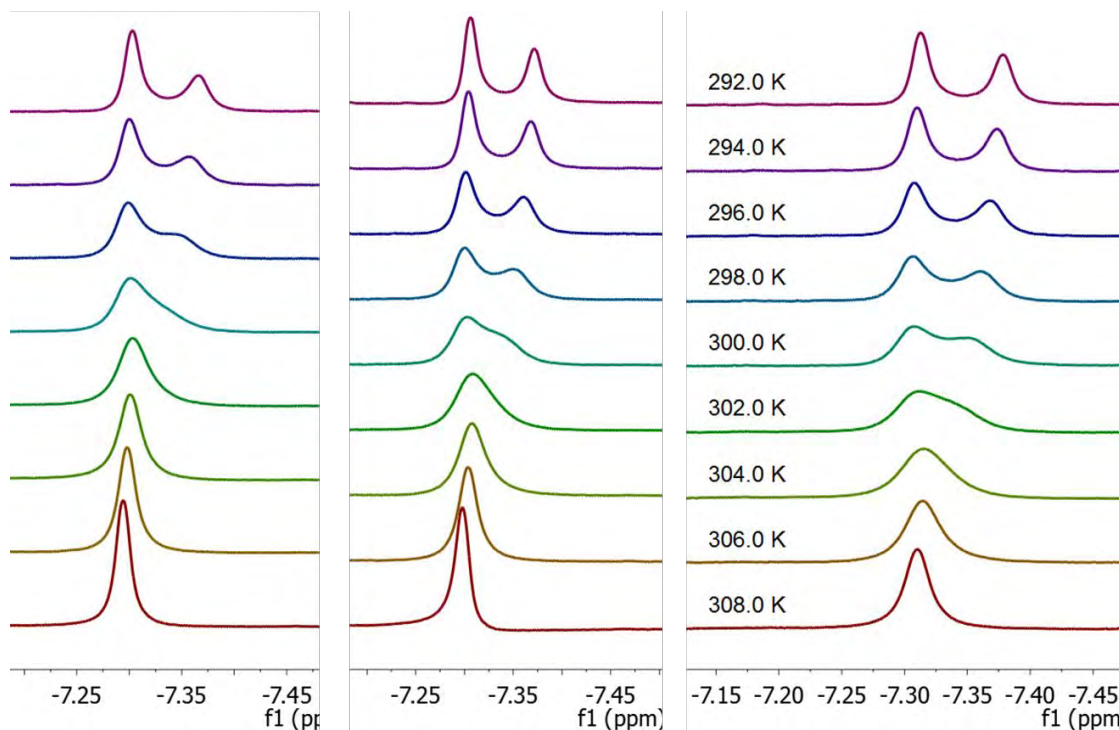
Figure 5.42: Variable temperature ^{1}H NMR spectra of Rh(TTP)CH$_3$ in the presence of both bmim and deim. Exchange rates were determined by examination of the trans methyl proton signals of Rh(TTP)CH$_3$(bmim) (downfield) and Rh(TTP)CH$_3$(deim) (upfield).Conditions: (left) [Rh(TTP)CH$_3$] = 0.045 M, [bmim] = 0.098, [deim] = 0.080; (middle) [Rh(TTP)CH$_3$] = 0.045 M, [bmim] = 0.098 M, [deim] = 0.10 M; (right) [Rh(TTP)CH$_3$] = 0.045 M, [bmim] = 0.76, [deim] = 1.6. Rate constants were determined by the slow exchange approximation; the approximation was applied to the *trans* methyl signals for temperatures between 284 and 296 K.
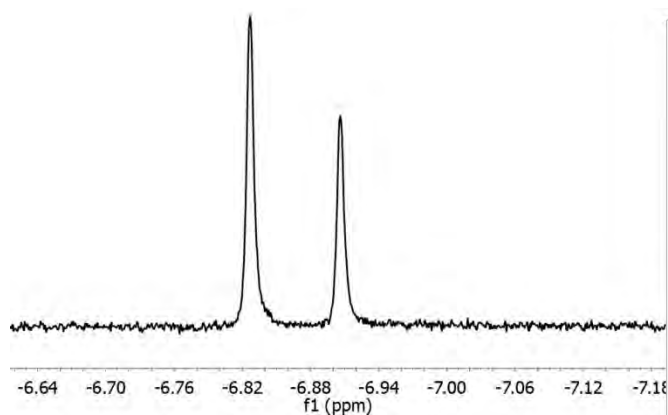
Figure 5.43: ^{1}H NMR spectra of Ir(TTP)CH$_3$ in the presence of excess bmim and deim at 308 K.

Kinetics Data

NHC exchange was much slower with iridium than with rhodium; line broadening was not observed by ^{1}H NMR at 308 K. To verify that NHC exchange with Ir(TTP)CH$_3$ is reversible, preliminary kinetics studies were performed under pseudo first-order according to Eqs. S1-S4. Second-order exchange rate constants k_f and k_r were determined by setting up two different series of experiments where the concentration of one of the NHC compounds was changed while the concentration of the other was kept constant (Eq. S3). Observed rate constants (k_{obs}) for these reactions were measured at 308.0 K with 7 − 30 fold excesses of NHCs relative to Ir(TTP)CH$_3$. For reactions with varying concentrations of bmim, a plot of [bmim] verses k_{obs} containing two points had a slope (k_f) of 0.034 ± 0.020 (estimated error) M^{-1}·s^{-1}. Due to the difficulty in performing these experiments, the plot contained just two points, producing a large error in the slope and a very approximate rate constant value. The same treatment of the reactions with three different concentrations of deim afforded a k_r of 0.0113 ± 0.0006 M^{-1}·s^{-1}. Values for k_f and k_r were verified for each reaction with the equilibrium binding constant (1.56 ± 0.04) and k_{obs} according to Eqs. S3 and S4. This treatment estimated that k_f = 0.028 ± 0.005 M^{-1}s^{-1} and k_r = 0.018 ± 0.003 M^{-1}s^{-1}, which is consistent with the values determined by linear regression.

Relevant equations for pseudo first-order kinetics for reversible reactions:

$$\frac{-d[IrL]}{dt} = k_f{}'[IrL] - k_r{}'[IrL'] \tag{5.2}$$

$$\ln([IrL]_t - [IrL]_{eq}) = -k_{obs}t + \ln([IrL]_o - [IrL]_{eq}) \tag{5.3}$$

$$k_{obs} = k_f' + k_r' = k_f[bmim] + k_r[deim] \tag{5.4}$$

$$K = \frac{k_f}{k_r} \tag{5.5}$$

Plots to determine k_{obs}:

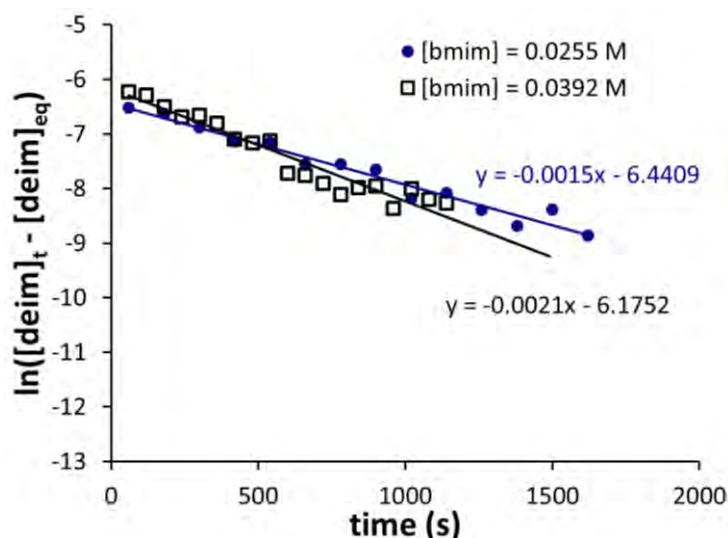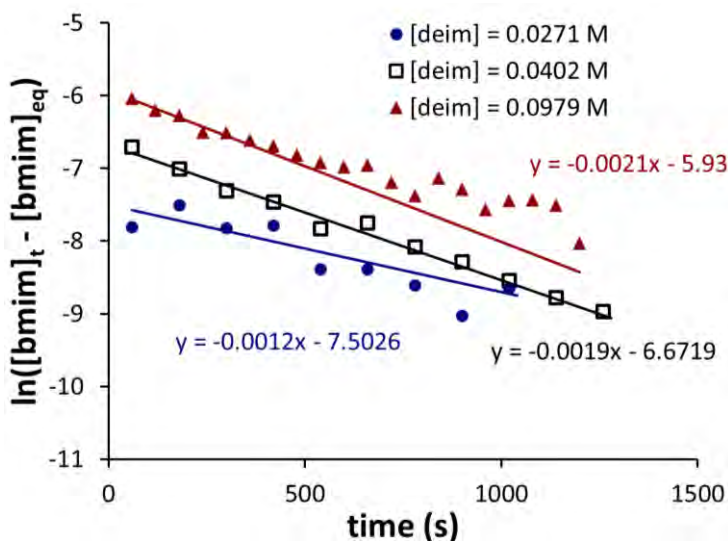**Figure 5.44:** A plot of reaction progress versus time for a series of experiments at 308.0 K with $[Ir(TTP)CH_3] = 3.36 \times 10^{-3}$ M, [deim] = *ca.* 0.0369 M, and varying amounts of bmim (0.0255-0.0392 M). Reaction progress was monitored as a the consumption of $Ir(TTP)CH_3(deim)$ toward equilibrium. As shown in equation S2, the slope of each line equals k_{obs}. A third reaction, where [bmim] = 0.0515 M, was acquired but the data was removed as a statistical outlier (outside of 2 standard deviations from the mean).

Figure 5.45: A plot of reaction progress versus time for a series of experiments at 308.0 K with $[Ir(TTP)CH_3] = 3.36 \times 10^{-3}$ M, [deim] = *ca.* 0.0380 M, and varying amounts of deim (0.0271-0.0979 M). Reaction progress was monitored as a the consumption of $Ir(TTP)CH_3(deim)$ toward equilibrium. As shown in equation S2, the slope of each line equals k_{obs}.
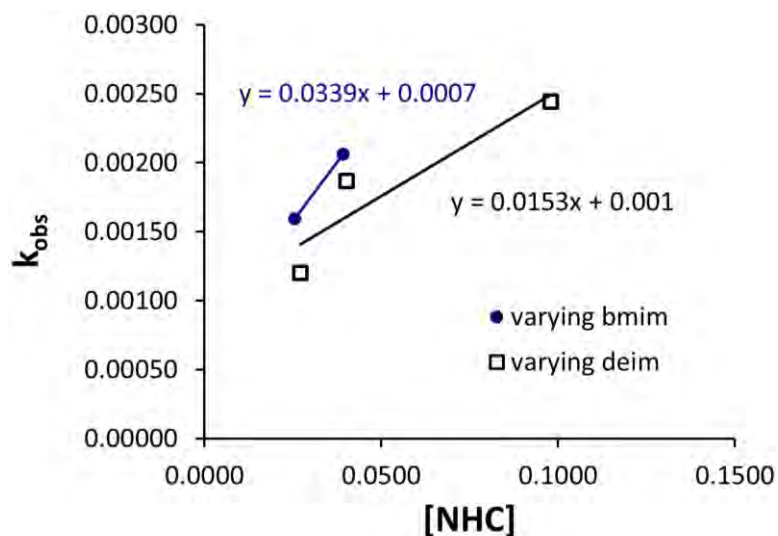
Figure 5.46: Plots of k_{obs} versus [NHC] at 308.0 K. The plot representing varying concentrations of bmim (solid blue circles) gives a linear regression with slope equal to k_f. The linear regression for the plot of varying deim concentrations (black squares) has a slope equal to k_r. Linear-least squares regression gives an error of 0.0063 for k_r.

Table 5.5: Data for the calculation of k_f and k_r using equations 5.4 and 5.5.

Entry	[deim]	[bmim]	k_{obs} (s^{-1})	K	k_f	k_r
1	0.0369	0.0255	1.60×10^{-3}	1.55	0.0324	0.0209
2	0.0385	0.0392	2.06×10^{-3}	1.62	0.0327	0.0202
5	0.0271	0.0372	1.20×10^{-3}	1.61	0.0222	0.0138
4	0.0402	0.0375	1.87×10^{-3}	1.55	0.0294	0.0190
5	0.0979	0.0402	2.44×10^{-3}	1.52	0.0234	0.0154

Equations relevant for pseudo irreversible exchange reactions (using excess amounts of only the incoming NHC compound):

$$Rate = \frac{-d[IrL]}{dt} = \frac{k_1 k_2 [IrL]}{k_{-1}[deim] + k_2[bmim]} \qquad (5.6)$$
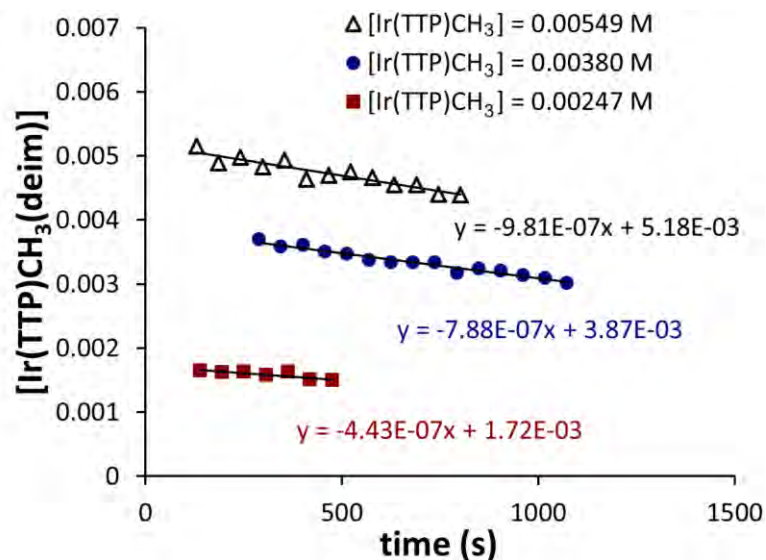
$$Rate = \frac{-d[IrL]}{dt} = k_1[IrL] \qquad (5.7)$$
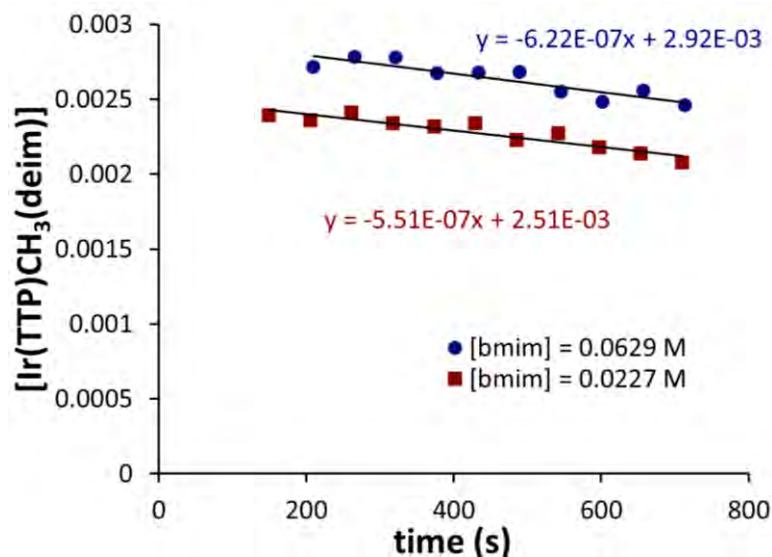
Figure 5.47: The rate of exchange, measured as the loss of Ir(TTP)CH$_3$(deim), versus time under pseudo irreversible conditions at 298.0 K with varying amounts of bmim. Ir(TTP)CH$_3$(deim) was generated *in situ* from Ir(TTP)CH$_3$ (0.0028 M) and deim (0.0044 M). This NHC complex was treated with bmim (0.0227 to 0.0629 M). Rates were determined using data from only the first 20% of the reaction. Changing the concentration of NHC$_d$ did not have an effect on rate. The observed difference between the two lines represents procedural errors.

Figure 5.48: The rate of exchange, measured as the loss of Ir(TTP)CH$_3$(deim), versus time under pseudo irreversible conditions at 298.0 K with varying amounts of Ir(TTP)CH$_3$(deim). Ir(TTP)CH$_3$(deim) was generated *in situ* from Ir(TTP)CH$_3$ (0.00247 to 0.00549 M) and deim (0.0049 to 0.0061 to M). This NHC complex was treated with bmim (0.034 M). Rates were determined using initial rate data, though the reaction with [Ir(TTP)CH$_3$] = 0.00247 M was 30% complete before the first data point.
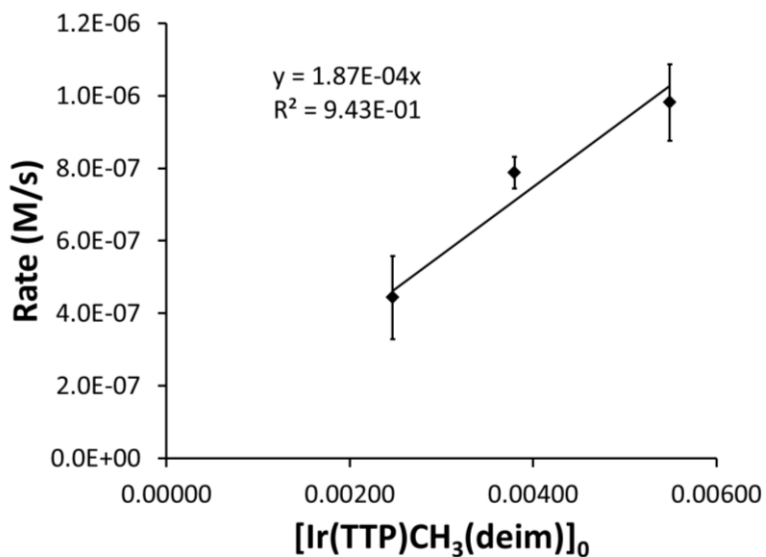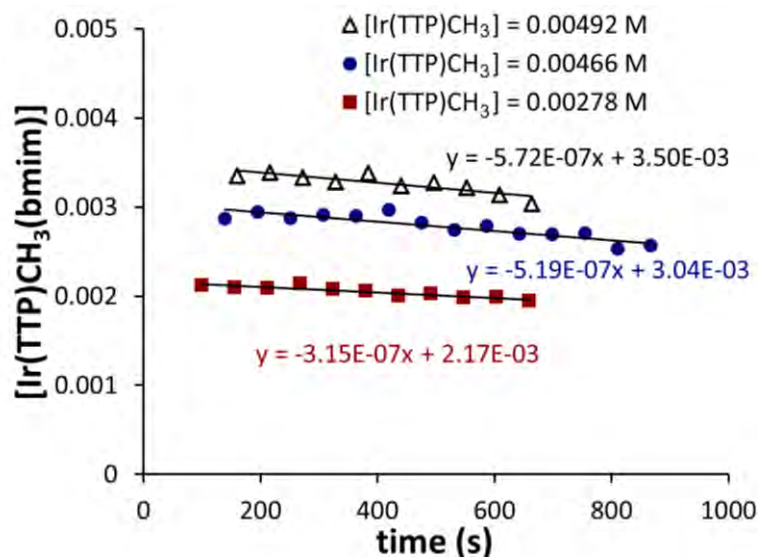

Figure 5.49: A plot of reaction rate versus [Ir(TTP)CH$_3$(deim)] at 298.0 K according to Eq. S6. The slope represents the rate constant of dissociation for the forward reaction (k_{1f}). Linear-least squares regression gave an error of 4.1×10^{-5} s^{-1}.

Figure 5.50: The rate of exchange, measured as the loss of Ir(TTP)CH$_3$(bmim), versus time under pseudo irreversible conditions at 298.0 K with varying amounts of Ir(TTP)CH$_3$(bmim). Ir(TTP)CH$_3$(bmim) was generated *in situ* from Ir(TTP)CH$_3$ (0.00278 to 0.00492 M) and bmim (0.0041 to 0.0054 to M). This NHC complex was treated with deim (0.033 M). Rates were determined using initial rate data, though all the reactions were 30% complete before the first data point.
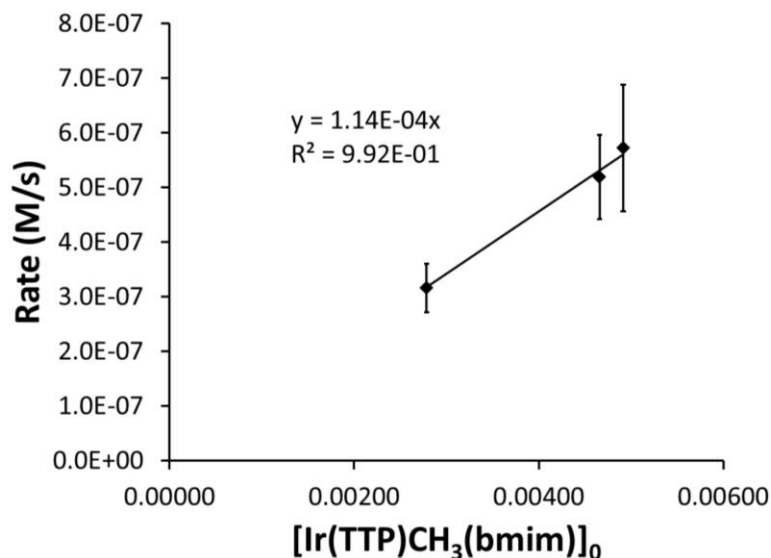

Figure 5.51: A plot of reaction rate versus [Ir(TTP)CH$_3$(bmim)] at 298.0 K according to Eq. S6. The slope represents the rate constant of dissociation for the reverse reaction (k_{1r}). Linear-least squares regression gave an error of 9.9×10^{-6} s^{-1}

Crystal and Structure Refinement Data

Table 5.6: Structure refinement data for complexes **22**, **23**, and **24b**.

	22	23	24b
empirical formula	$C_{68}H_{58}IrN_6OBF_4$	$C_{71}H_{59}IrN_7BF_4 \cdot 2H_2O$	$C_{72}H_{72}IrN_8BF_4$
formula weight	1254.21	1325.29	1328.39
temperature	173(2) K	173(2) K	173(2) K
wavelength	0.71073 Å	0.71073 Å	0.71073 Å
cryst. syst., space group	monoclinic, $C\,1\,2/c\,1$	monoclinic, $C\,1\,2/c\,1$	tetragonal, $I\,41/a$
unit cell dimensions	a = 21.1990(10) Å b = 13.6732(10) Å c = 22.5583(13) Å $\alpha = 90°$ $\beta = 94.6880(10)°$ $\gamma = 90°$	a = 21.1330(13) Å b = 13.6335(8) Å c = 22.5007(13) Å $\alpha = 90°$ $\beta = 95.8960(10)°$ $\gamma = 90°$	a = 20.7502(16) Å b = 20.7502(16) Å c = 14.3770(11) Å $\alpha = 90°$ $\beta = 90°$ $\gamma = 90°$
volume	6516.8(7) $Å^3$	6448.5(7) $Å^3$	6190.3(8) $Å^3$
Z, calculated density	4, 1.278 Mg/m^3	4, 1.365 Mg/m^3	4, 1.425 Mg/m^3
absorption coefficient	2.104 mm^{-1}	2.132 mm^{-1}	2.219 mm^{-1}
F(000)	2536	2688	2712
crystal size	0.17 x 0.15 x 0.08 mm^3	0.25 x 0.21 x 0.21 mm^3	0.34 x 0.32 x 0.27 mm^3
θ range for data collection	1.77 to 30.57°	1.78 to 28.74°	2.6142 to 25.6734°
limiting indices	$-30 \leq h \leq 29$ $-19 \leq k \leq 19$ $-32 \leq l \leq 31$	$-28 \leq h \leq 28$ $-18 \leq k \leq 18$ $-30 \leq l \leq 30$	$-27 \leq h \leq 27$ $-27 \leq k \leq 26$ $-19 \leq l \leq 19$
reflections collected/unique	36132/9612 [R(int) = 0.0265]	34138/8336 [R(int) = 0.0346]	31117/3853 [R(int) = 0.0251]
completeness to θmax	96.2 %	99.8 %	99.8 %
absorption correction	multi-scan	multi-scan	multi-scan
max and min transmission	0.85 and 0.72	0.66 and 0.62	0.59 and 0.45
data/restraints/parameters	9621/336/412	8336/395/480	3853/201/252

Table 5.5 (continued)

goodness-of-fit on F^2	1.142	1.149	1.137
final R indices [I > 2σ(I)]	R1 = 0.0409 wR2 = 0.1396	R1 = 0.0600 wR2 = 0.1812	R1 = 0.0376 wR2 = 0.1009
R indices (all data)	R1 = 0.0601 wR2 = 0.1563	R1 = 0.0770 wR2 = 0.1926	R1 = 0.0484 wR2 = 0.1175
largest diff. peak and hole	1.477 and -0.701 e Å^{-3}	3.707 and -0.848 e Å^{-3}	0.986 and -0.866 e Å^{-3}
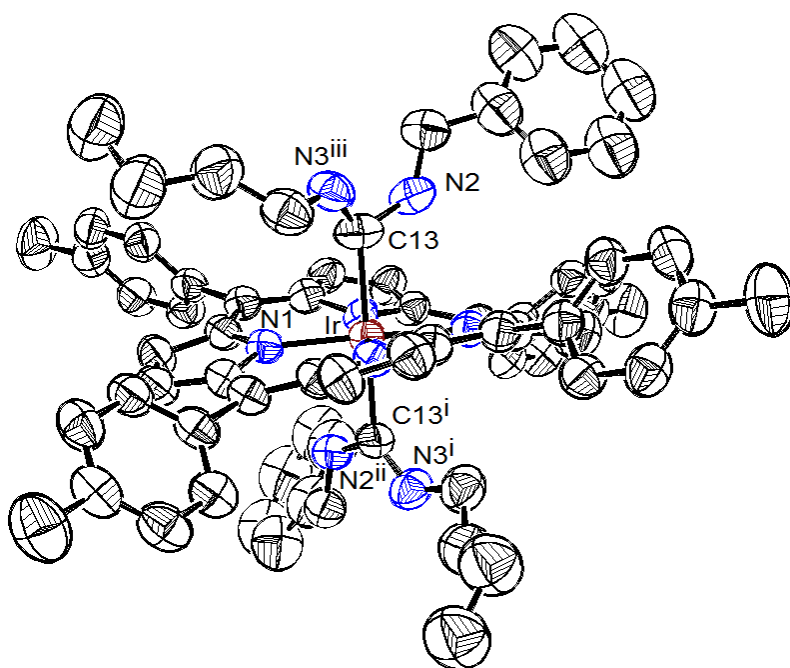
Figure 5.52: Full ORTEP[19] of complex **24b** with 50% probability ellipsoids.
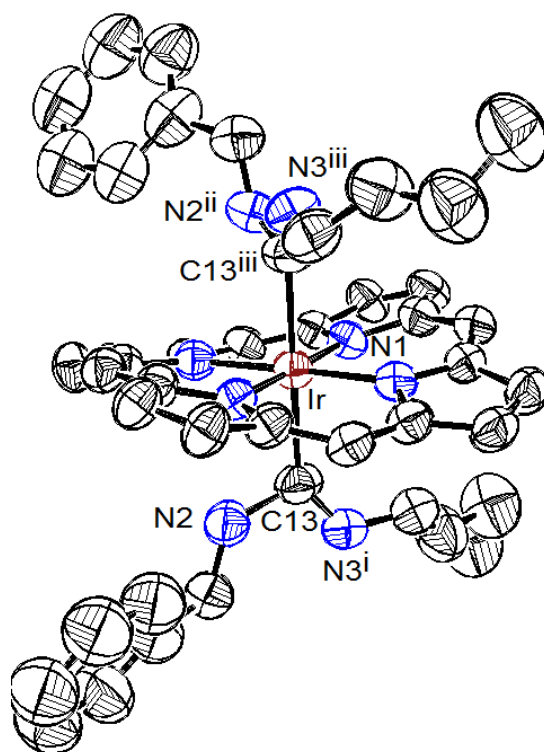
Figure 5.53: ORTEP[19]of complex **24b** with 50% probability ellipsoids. *Meso* tolyl substituents omitted for clarity.

Table 5.7: Metrical parameters for the crystal structures of complexes **22**, **23**, and **24b**.

Complex **22**[a]		Complex **23** [a]		Complex **24b** [a]	
Ir–N(1)	2.045(4) Å	Ir–N(1)	2.044(4) Å	Ir–N(1)	2.029(4) Å
Ir–N(2)	2.044(4) Å	Ir–N(2)	2.042(4) Å	N(1)–Ir–N(1)	90.00(12)°
N(1)–Ir–N(2)	90.02(13)°	N(1)–Ir–N(2)	90.03(13)°		
N(2)–Ir–N(1)	89.98(13)°	N(2)–Ir–N(1)	89.97(13)°		

[a] Metrical parameters involving the axial ligands were not included. Due to disorder, atomic positions of the axial ligands were approximated.

Table 5.8: Structure refinement data for complexes **25b** and **26b**.

	25b	26b
empirical formula	$C_{65}H_{69}RhN_6O_2$	$C_{122}H_{116}\,Ir_2N_{12}O_2$
formula weight	1069.17	2166.67
temperature	173(2) K	173(2) K
wavelength	0.71073 Å	0.71073 Å
cryst. syst., space group	triclinic, $P\bar{1}$	triclinic, $P\bar{1}$
unit cell dimensions	a = 9.9009(7) Å b = 16.5931(11) Å c = 18.1728(12) Å α = 107.2440(10)° β = 96.9950(10)° γ = 90.0620(10)°	a = 9.8727(11) Å b = 16.6107(19) Å c = 18.1540(20) Å α = 107.208(20)° β = 96.7300(20)° γ = 90.3540(20)°
volume	2827.9(3) Å^3	2821.6(5) Å^3
Z, calculated density	2, 1.256 Mg/m^3	1, 1.275 Mg/m^3
absorption coefficient	0.351 mm^{-1}	2.409 mm^{-1}
F(000)	1124	1102
crystal size	0.19 x 0.17 x 0.08 mm^3	0.22 x 0.18 x 0.18 mm^3
θ range for data collection	2.6124 to 25.6734°	2.4665 to 30.3686°
limiting indices	$-13 \leq h \leq 14$ $-23 \leq k \leq 22$ $-25 \leq l \leq 25$	$-14 \leq h \leq 14$ $-22 \leq k \leq 22$ $-25 \leq l \leq 25$
reflections collected/unique	31721/15941 [R(int) = 0.0310]	31402/15795 [R(int) = 0.0187]
completeness to θmax	92.4 %	92.2 %
absorption correction	multi-scan	multi-scan
max and min transmission	0.97 and 0.94	0.76 and 0.67
data/restraints/parameters	15941/104/674	15795/170/673
goodness-of-fit on F^2	1.051	1.035
final R indices [I > 2σ(I)]	R1 = 0.0641 wR2 = 0.1764	R1 = 0.0440 wR2 = 0.1223
R indices (all data)	R1 = 0.0854 wR2 = 0.1934	R1 = 0.0495 wR2 = 0.1264
largest diff. peak and hole	1.328 and -1.314 e Å^{-3}	2.756 and -2.046 e Å^{-3}

GENERAL CONCLUSION

Carbene transfer catalysis was demonstrated with iridium porphyrin complexes for the first time. With diazoacetate carbene precursor reagents, iridium porphyrin catalysts were extremely robust and reactive. Cyclopropanation and N–H insertion reactions proceeded rapidly at temperatures as low as -78 °C, with yields commonly above 80%, and with turnover numbers on the order of 10^5. The highest yields were typically observed with sterically unhindered aryl olefin or amine substrates, but several aliphatic and bulky substrates were converted in good yields. Attempts to catalyze C–H insertion reactions with diazoacetate reagents failed due to rapid carbene dimerization. However, using more robust aryl diazoacetate reagents, C–H insertion reactions proceeded in modest to good yields with little carbene dimerization. Aryl diazoacetate reagents were also effective precursors for cyclopropanation and N–H insertion, though reactions were considerably slower than those with diazoacetate precursors. In addition, preliminary results indicated that iridium porphyrin complexes are effective catalysts for cyclopropenation, O–H insertion, and sigmatropic rearrangement reactions.

Thorough mechanistic studies supported the intermediacy of metal-carbene complexes for cyclopropanation and C–H insertion as well as metal-ylide complexes for N–H insertion. Indirect evidence for these intermediates was obtained with Hammett correlation, kinetic isotope effect, and other substrate competition studies, which generally indicated that the intermediates were electrophilic. More definitive evidence of metal-carbene and metal-ylide intermediates was established by direct observation of these species by ^{1}H NMR and absorption spectroscopy. Under the C–H insertion and N–H insertion conditions where these intermediates were observed, the rate-limiting step of the catalytic cycle was carbene transfer. Kinetics investigations supported this hypothesis and also indicated that carbene transfer is rate-limiting for cyclopropanation, despite that the proposed metal-carbene intermediate reacted too quickly to be observed spectroscopically. However, the lack of a kinetic isotope effect for N–H insertion reactions with EDA suggests that the rate-limiting step may change depending on the conditions.

In general, iridium porphyrin catalysts are attractive for being robust and reactive. This contrasts previous studies with rhodium porphyrin catalysts, which are known for imparting unique selectivity in cyclopropanation and C–H insertion reactions. A systematic analysis of rhodium and iridium porphyrin diaminocarbene and NHC complexes revealed distinct differences between the two metals. Equilibrium binding studies and ligand exchange reactions demonstrated that NHC ligands bind more favorably and more inertly to iridium than to rhodium. This deduction was supported further by the solid state structures of the metal–NHC complexes, which featured a rhodium-carbene bond that was *ca.* 0.061 longer than the analogous iridium–carbene bond. Overall, these data are consistent with the transition state model proposed previously by Woo, Kodadek, and co-workers; rhodium porphyrin carbene complexes are higher in energy, which results in an earlier carbene transfer transition state that is more heavily influenced by the porphyrin ligand.

This work provides the foundation for the future development of iridium porphyrin carbene transfer catalysts. Due to their high reactivity and stability, iridium porphyrin catalysts are extremely promising. In particular, mechanistic results indicated that chiral iridium porphyrin catalysts should be active and general for enantioselective N–H insertion reactions, which is traditionally difficult for most carbene transfer catalysts. Additionally, structural studies of NHC complexes, in conjunction with computational studies on the iridium porphyrin carbene intermediate, suggest that the intermediate potentially contain significant distortion in the porphyrin ligand. Understanding the influence of this porphyrin distortion on catalysis may be critical to the eloquent design of more sophisticated catalysts.

ACKNOWLEDGEMENTS